Scuola Internazionale Superiore di Studi Avanzati - Trieste

Area of Physics
Ph.D. in Astroparticle Physics

A glimpse on Dark Matter particles shining through the gamma-ray Sky

Candidate
Mauro Valli

Supervisor
Prof. **Piero Ullio**

Thesis submitted in partial fulfillment of the requirements
for the degree of Doctor Philosophiæ Academic Year 2015/2016

SISSA - Via Bonomea 265 - 34136 TRIESTE - ITALY

Zwei Dinge erfüllen das Gemüt mit immer neuer
und zunehmender Bewunderung und Ehrfurcht, je öfter und
anhaltender sich das Nachdenken damit beschäftigt:
Der bestirnte Himmel über mir, und das moralische Gesetz in mir.

– **I. Kant**, *Kritik der praktischen Vernunft* (1788) –

Foreword

The work presented in this thesis is based on the following four publications [1–4]:

- *"Gamma-ray sky points to radial gradients in cosmic-ray transport"*,
  D. Gaggero, A. Urbano, M. Valli and P. Ullio,
  Phys. Rev. D 91, no. 8, 083012 (2015),
  arXiv:1411.7623 [astro-ph.HE],
- *"The gamma-ray and neutrino sky: A consistent picture of Fermi-LAT, Milagro, and IceCube results"*,
  D. Gaggero, D. Grasso, A. Marinelli, A. Urbano and M. Valli,
  Astrophys. J. 815 (2015) 2, L25,
  arXiv:1504.00227 [astro-ph.HE],
- *"Towards a realistic astrophysical interpretation of the Galactic center excess"*,
  D. Gaggero, M. Taoso, A. Urbano, M. Valli and P. Ullio,
  JCAP 1512 (2015) no.12, 056,
  arXiv:1507.06129 [astro-ph.HE],
- *"A critical reassessment of Particle Dark Matter limits from dwarf satellites"*,
  P. Ullio and M.Valli,
  JCAP 1607 (2016) no.07, 025,
  arXiv:1603.07721 [astro-ph.GA],

plus some additional material presented in three conference proceedings [5–7].

During his Ph.D., the candidate has been also working on Particle Physics phenomenology, with a particular focus on Flavor Physics. Moreover, he has contributed to the development of `HEPfit` [8], a code to perform precision tests in the Standard Model of Particle Physics and Beyond.

This additional research activity has lead to the following publication [9]:

- *"$B \to K^* \ell^+ \ell^-$ decays at large recoil in the Standard Model: a theoretical reappraisal"*,
  M. Ciuchini, M. Fedele, E. Franco, S. Mishima,
  A. Paul, L. Silvestrini and M. Valli,
  JHEP 1606 (2016) 116,
  arXiv:1512.07157 [hep-ph].

Abstract

In an era of unprecedented sensitivity to cosmic gamma rays, it is timely to study possible signatures rising from Dark Matter (DM) particle interactions. The aim of the present thesis is precisely devoted to that. We start by presenting a broad study on physically motivated Galactic diffuse emission models. These derive from the interaction of Galactic cosmic rays with the interstellar medium and describe the bulk of photons imprinted in the observed gamma-ray sky. We show how gamma-ray data offer a complementary deep diagnostic of the standard paradigm for Galactic cosmic-ray propagation, usually tuned on local cosmic-ray observables. We present a self-contained discussion about the inferred radial gradients in the gamma-ray data relative to the Galactic plane region, and interpret them as a strong hint in favor of a spatially varying diffusion rate for cosmic rays in the Galaxy. We corroborate this study with a set of distinctive predictions, embracing the available information on TeV high-energy photon data and the expectations for a detection of Galactic neutrino fluxes on the basis of current and future neutrino observatory sensitivities. We, then, scrutinize the claim of a gamma-ray signal from DM particle annihilation observed in the innermost central part of our Galaxy, analyzing the gamma-ray data coming from few tens of degrees around the Galactic center. We show that a spherical excess – interpretable as the annihilation of weakly interacting massive particles in the Galactic halo – does not stand out in the data any longer when the effect of the observationally inferred high star-formation rate in this complex astrophysical environment is considered. Accounting properly for that in the injection source distribution of cosmic rays, we show that most of the "GeV excess" has a simple explanation in terms of well-motivated cosmic-ray physics. We remark, in particular, that with this correction, counts in the residual map are not only drastically reduced, but also do not spatially correlate anymore with an approximately spherical morphology. Finally, we critically reassess the DM content in the satellites of the Milky Way. In order to do that, we develop a new method, mainly based on the kinematics of the stars in these galaxies, that in the end provides a conservative estimate of the line-of-sight integrated halo profile squared for these objects, the so-called J-factor. After carrying out in detail the study case of Ursa Minor, we present here – as last original contribution in the thesis – a similar conservative analysis of the J-factor for the whole set of classical satellites of the Milky Way. In light of our novel approach, we conclude that these galaxies offer to us a reliable "DM laboratory" where we can probe the freeze-out mechanism of cold thermal relics in a robust and unique way.

Contents

List of Figures

List of Tables

Preface

In the Galaxy where we are living – the Milky Way – there is much more than what can be simply perceived at naked eye. There is in particular much more matter than what we can observe with the most powerful telescopes, and it seems to be not of a common kind, i.e. it is not made of stars, planets, comets, or ordinary gas. According to our state-of-the-art knowledge about Astrophysics and Cosmology, what we are referring to must be made of something completely different at fundamental level, that for instance cannot be found in any other substance ever observed or produced so far in our laboratories. This matter component is actually not a peculiarity of our Galaxy, but it is believed to permeate the whole Universe, characterizing the evolution history of the latter, allowing for the formation and growth of structures to happen, at the origin of our existence of today.

Probably mentioned for the first time by Henri Poincaré already in 1906 [10], this kind of matter has been historically dubbed "Dark Matter" since it does not shine or absorb light as ordinary baryonic matter does. One of the first historical inferences about an additional large amount of gravitating matter of different kind from the stars and gas present in ordinary astrophysical objects, such as galaxies and clusters of galaxies, dates back to the 1930s. In those years, a pioneer of the field like Fritz Zwicky had the chance to observe the Coma cluster with unprecedented detail for the time. These observations were at the basis of his revolutionary study of the dynamics of galaxies in the Coma, with an innovative approach leading him to conclude that most of the mass of the system was not in the form of ordinary bright and luminous matter [11]. Thanks to the tremendous experimental and technological progress in a lapse of time covering more than 80 years from the original observations of Zwicky, nowadays we have at our disposal a multitude of different evidences in favor of the existence of this relevant matter component. The set of current data in favor of the Dark Matter hypothesis spans a huge range of scales in orders of magnitude, going from the smallest size of known galaxies, about hundred million larger than the size of our Solar System, up to the largest clustered structures we can observe in the Universe today with dedicated forefront surveys, corresponding to scales ten thousand times larger than the former one.

In spite of this sensational collection of observations, the main ingredient at the basis of our ability to detect the presence of Dark Matter today remains the same of 80 years ago: the laws of gravity applied to macroscopic massive systems. At this point, one may start to be suspicious of how much we have really understood about free falling apples from trees or Einstein elevators moving upwards and downwards

in the back of our minds. While doubting possibly represents a good attitude for a scientist to seriously progress in his own field of research, most of the scientific community is not really inclined to think that the fundamental explanation to these puzzling observations should rely on the modification of the known standard laws of gravity. Indeed, these are precisely tested in the neighborhood of the Solar System, and seem also to work pretty well at describing the evolution history of our Universe. In general, when we try to modify gravity at cosmological scales, we usually obtain a completely altered distribution of matter than the one traced by galaxies and larger clustered structures that we observe today in the Universe.

At present, the most likely option for Dark Matter is to have as building blocks some degrees of freedom coming from the world of Particle Physics. Then, it is probably true that the elementary constituents of Dark Matter must be quite different from standard known particles. In fact, Dark Matter particles should not be electrically charged as for instance electrons are, and, more in general, they should not talk that much with ordinary matter constituents such as protons and/or neutrons. According to some of the most important informative pictures we have from rare and very energetic events in the outer-space like the collision of two galaxy clusters, Dark Matter particles should not even interact too much with each other. All this already gives us some intuition that the identikit we are looking for does not match the bulk of known particles discovered so far. The only exception may be neutrinos that, however, as in the case of modified gravity, would drive a structure formation history which does not match observations.

As we are going to discuss extensively in the whole thesis, against the odds of the name, today we really hope to meet the opportunity of detecting some kind of interaction of Dark Matter particles, in order to learn something more about them and possibly about the "big picture" behind them. In particular, in astrophysical objects we do expect a very high concentration of these particles and, hence, it may be plausible that once in a while two of them may interact yielding, for example, very energetic radiation as a result of this interaction. The work in this thesis is actually related to the study of such kind of signals in promising astrophysical targets, that leave room for a potential indirect detection of Dark Matter particles through the emission of very energetic photons. Note, however, that this chance of detection is crucially pending on the fundamental properties that distinguish Dark Matter from ordinary matter, and as already said before, we still know very little about them. Therefore, just by chance, the name "Dark Matter" may be also considered quite appropriate these times for its not-yet revealed microscopic nature and this thesis may be simply taken as a very modest attempt to shed some new light on such a dark name.

Chapter 1

1 The Dark Matter problem

1.1 Evidences in favor of a long-standing puzzle

The seminal papers of Fritz Zwicky have been among the first works pointing quantitative and methodological evidence for Dark Matter (DM). In its pioneering study of the Coma Cluster in 1933 [11], he guessed the total mass of the system to be given as the average mass of a galaxy, $\langle m \rangle \sim 10^9$ $M_\odot$, times the number of tracers, $N \sim 800$, while approximating the physical volume of the cluster with a sphere of radius $\langle R \rangle \sim 300$ kpc. Then, assuming the system to be in equilibrium, Zwicky applied for the first time the virial theorem to galaxy clusters:

$$2\langle T \rangle + \langle U \rangle = 0 \;\Rightarrow\; \langle \sigma \rangle = \sqrt{\frac{G_N N \langle m \rangle}{2\langle R \rangle}} \sim 70 \text{ km/s} \,, \tag{1.1}$$

obtaining a dynamical estimate of the averaged velocity dispersion of the Coma members much smaller than what inferred from the Doppler shift of the measured galaxy spectra, $\langle \sigma \rangle \sim 1000$ km/s. From the comparison he reached the conclusion:

> *« If this would be confirmed, we would get the surprising result that dark matter is present in much greater amount than luminous matter. »*

The above observation has set up the stages for what we refer today as the "Dark Matter problem", namely what is the nature of this gravitationally inferred matter component.

More recent studies of galaxy clusters including Coma have actually shown that most of the baryonic mass in these systems is in the form of hot intergalactic gas, emitting X rays by bremsstrahlung. Consequently, informations on the main baryonic component comes from the X-bolometric luminosity, that can be converted in gas density maps, and from X-ray spectra, that give us access to the gas temperature profile, to be translated into the gas pressure. Assuming the hot gas to be in hydrostatic equilibrium within the underlying gravitational well, we can

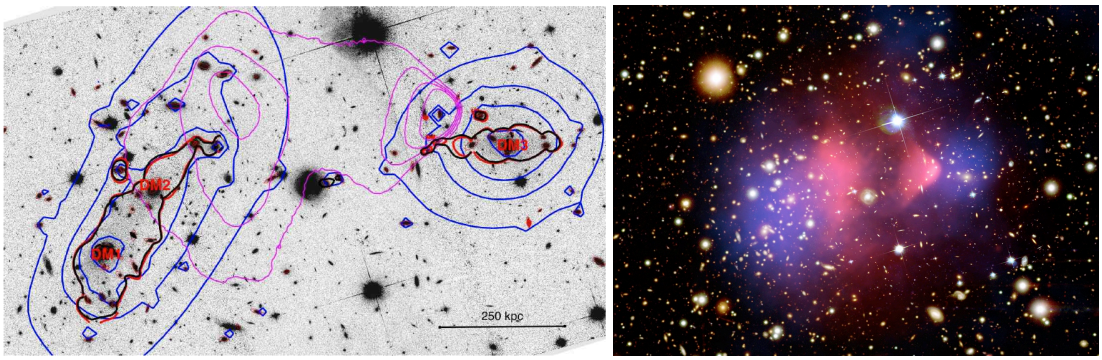

Figure 1.1: *Composite image of the Bullet Cluster. In the left (right) panel, X-ray emission in magenta (pink), and strong (weak) lensing contour in blue. Image Credit: Fig. 7 from Ref. [14] (left panel). X-ray: NASA/CXC/CfA/ M.Markevitch et al.; Lensing Map: NASA/STScI; ESO WFI; Magellan/U.Arizona/ D.Clowe et al.; Optical: NASA/STScI; Magellan/U.Arizona/D.Clowe et al. (right panel).*

then infer the mass profile of the system by:

$$\frac{dP_{\rm gas}}{dr} = G_N \frac{M(r)\rho_{\rm gas}}{r^2} \ . \tag{1.2}$$

For instance, for the Coma Cluster we obtain $M_{\rm gas}/M \simeq 14\%$ [12], i.e. $\sim$7 times more mass than the one expected from the traced hot gas. Interestingly, this is not the only modern proof of DM in galaxy clusters. Nowadays we have at our disposal gravitational lensing techniques that allow us to perform a precise tomography of the gravitating mass distribution within the system, showing among galaxy mass peaks the presence of a smoothly distributed DM component that dominates the total potential well [13]. Even more spectacularly, we can perform a multi-level mapping of galaxy cluster merging events like in the case of the Bullet Cluster (see, e.g., [14]). As displayed in Fig. 1.1, in this impressive event, the baryonic hot gas gets shocked in the collision and gets displaced from the bulk of the gravitating mass as inferred by different lensing techniques. This segregation of the non-dissipative DM component from the dissipative baryonic counterpart offers to us a quite unique probe of DM existence.

Another historical piece of evidence in favor of DM falls actually around the 1970s, when the first explicit statements arguing that additional mass was needed in the outer parts of some galaxies began to appear in the literature. These claims were based on comparisons of the rotation curves from 21 cm observations and those computed from luminous mass profiles measured in photometric analyses, as for the case of the seminal work on the dynamics of M31 carried out by Kent Ford

and Vera Rubin [15]. Applying Newtonian gravity, the circular velocity v_c of stars in a galaxy is simply given by:

$$v_c(r) = \sqrt{\frac{G_N M(r)}{r}} \,, \tag{1.3}$$

where r is the radial distance from the center of the object and M is the corresponding enclosed mass. Assuming that most of the mass is associated to the galactic stellar disk, for distances beyond the size of the latter M would be constant, and one would expect a Keplerian fall-off, $v_c \propto r^{-1/2}$. Therefore, the observational evidence in favor of flat rotation curves in the outermost region of galaxies has immediately captured the attention of the community. Indeed, on one hand, the puzzling observation was pointing to the existence of an additional matter component, clearly extending to distances much greater than the visible mass scale, with a density profile falling off as $\rho \propto r^{-2}$ in the outer region of the system in order to reproduce the "asymptotic" flatness of the measured rotation curves. On the other hand, this explanation was putting down roots in the regime of validity of Newton's law, as firstly noticed by Mordehai Milgrom in 1983 [16]. The phenomenological recipe he proposed more than 30 years ago, namely an ad hoc modification of Newton's law on the basis of an acceleration threshold parameter to be fixed by data – the so-called MOdified Newtonian Dynamics (MOND) – is still reliable to fit hundreds of rotation curve data sets and to explain empirical scaling relation laws as well. The successful prediction of MOND at the galactic scale motivated further studies aiming at extending Einstein's General Relativity (GR) in order to present a serious competitor to the DM hypothesis. For instance, in 2004 Jacob Bekenstein has proven the existence of a fully covariant extension of GR able to reproduce MOND phenomenology at galactic scales, while accommodating post-Newtonian tests of gravity and taking into account standard results from gravitational lensing as well [17].

While the interplay between modified gravity theories and the DM-like phenomenology is still an active area of research also in light of the issues risen by the Dark Energy component of the Universe, see e.g. [19], nowadays cosmological precision tests point to the existence of a dominant matter component of non-baryonic type. In fact, as a byproduct of linearly perturbed Einstein's field equations and a homogeneous and isotropic space-time background, a simple framework as linear cosmological perturbation theory allows us to make solid and detailed predictions about the temperature anisotropies in the cosmic microwave background (CMB). State-of-the-art measurements by the Planck satellite of the temperature anisotropies, which are at the level $(\delta T/T)_{\rm rec} \sim 10^{-5}$, are shown in terms of an angular power

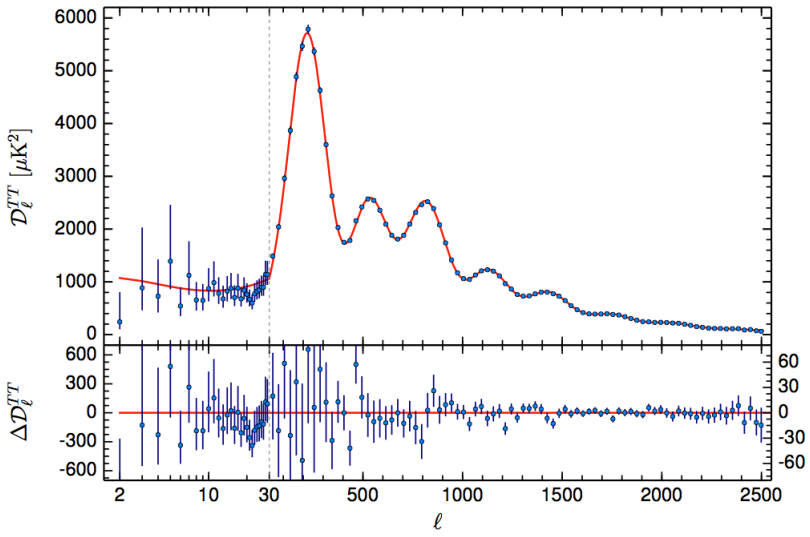

Figure 1.2: *Planck 2015 temperature power spectrum. The best-fit base* ΛCDM *theoretical spectrum fitted to the temperature × temperature Planck likelihood + low angular multiple polarization data is plotted in the upper panel. Residuals with respect to this model are shown in the lower panel. The error bars show* $\pm 1\sigma$ *uncertainties.*
Image Credit: Fig. 1 from Ref. [18].

spectrum, as the one reported in Fig. 1.2. The fit to such a set of data strongly points to a "cosmological concordance model" – the so-called ΛCDM [20] – where, in particular, the energy budget associated to the Universe matter content of today must be dominated by a pressureless fluid component, $\Omega_{\rm DM}h^2 = 0.1197 \pm 0.0022$ [18], with $\Omega_X \equiv 8\pi G_N \rho_X/(3H_0^2)$ and $h = H_0/(100\,\text{km s}^{-1}\,\text{Mpc}^{-1}) \simeq 0.7$. This value is indeed much greater than the baryonic counterpart $\Omega_b h^2 = 0.02222 \pm 0.00023$ [18], which is in very good agreement, e.g., with the total baryon density required to match measured primordial light element abundances as predicted in standard Big Bang nucleosynthesis [21].

The existence of this cosmological pressureless matter fluid – what we may refer to as the cold DM (CDM) paradigm – is of fundamental importance for the evolution of the Universe. Indeed, baryons and photons in the Early Universe until recombination, i.e. for redshifts greater than $z_{\rm rec} = 1090$ were tightly coupled, sharing the same perturbations. If we would not include the presence of some uncoupled fluid component baryons would not have got enough time to form the structures we see today. Indeed, in the analogous cosmological picture without DM, the matter density contrast, $\delta \equiv \delta\rho/\rho$, would be small even today [20, 22]:

$$\delta_0 = (1 + z_{\rm rec})\delta_{\rm rec} \;\Rightarrow\; \delta_0 \sim 10^{-2}\,, \tag{1.4}$$

where $\delta_{\rm rec} \sim (\delta T/T)_{\rm rec}$. The $\mathcal{O}(1)$ over-densities we see populating our local observable Universe clearly rule out this scenario. Pending on the right amount of CDM abundance, after recombination baryons can quickly fall into deeper DM gravitational wells and, tracing the growth of the DM density contrast, can reach $\mathcal{O}(1)$ over-densities at the suitable time to explain the distribution of galaxies and galaxy clusters we see nowadays. Therefore, the detailed picture of the evolution history of our Universe depicted from, e.g., the temperature anisotropies of the CMB and the linear matter power spectrum of galaxy distribution catalogues, is in firm support of CDM. The same picture also suggests that a change in the laws of gravity in place of CDM is likely a scenario poorly supported by data. Indeed, a modification of the laws of gravity qualitatively implies a substantial change in the playground shared by all the cosmological species present in the Universe. As pedagogically illustrated in Ref. [23], even if candidates like Bekenstein's Tensor-Vector-Scalar theory may be tuned to get the right "boost" in the growth of amplitudes, all modified gravity theories known at present systematically fail at reproducing the correct shape of, e.g., the matter power spectrum, as well as the peaks in Fig. 1.2 of the CMB temperature power spectrum, providing an inconsistent description of up-to-date cosmological data.

1.2 Educated guesses on Dark Matter properties

Given the set of observational evidences presented above, if we still stick to GR and we leave also aside quite radical options such as, e.g., very early time collapsed objects like primordial black holes [24], it is certainly true that DM is needed and it is likely in the form of some kind of particle. In this respect, one may list a set of rules that can, at most, be very mildly violated:

1) *DM is optically dark and dissipationless.* Its electromagnetic coupling must be suppressed to not spoil e.g. the shape and amplitude observed in the matter power spectrum already at the linear level, and to not contribute significantly to background radiation at any frequency. Moreover, evidences in favor of extended triaxial DM halos [25] suggest that DM cannot cool radiating photons (or in any other way). This is in net contrast to baryons, that can efficiently cool sinking in the inner regions of galaxies, possibly forming axial-symmetric structures as for the case of the Milky Way (MW).

2) *DM is collisionless*, at least on galaxy cluster scales. If DM-DM interaction is too strong, spherical structures would be obtained rather than triaxial. The observed ellipticity in galaxy clusters may imply constraints on the

self-scattering DM cross section, hinting to $\sigma_{\rm DM} \lesssim 0.02$ cm^2 g^{-1} [26]. More robust analyses on the morphology of several merger systems like the Bullet Cluster have been recently obtained, yielding $\sigma_{\rm DM} < 0.47$ cm^2 g^{-1} at 95% C.L. [27]. Note, however, that if DM self-scattering turns out to be velocity dependent such as in the case of very light force carriers mediating the interaction [28–30], these constraints apply only on large scales. Moreover, controversial observations in tension with the bound coming from merging systems like the Bullet do exist, see the puzzling case of Abell 520 [31]. A deeper understanding of this merging cluster system may actually lead to a new fundamental paradigm concerning the nature of DM [32].

3) DM is smoothly distributed, i.e. it does not have a granular structure in known astrophysical systems. Indeed, a granular distribution would provide time-dependent gravitational potentials, affecting the stability of astrophysical systems. Several searches for micro-lensing events towards the Large Magellanic Cloud have excluded a dominant granular component in DM halos for massive compact objects in the range of 10^{-7} - 10 M$_\odot$ [33], while from the study of wide binary stars it is possible to extract an upper bound close to 40 M$_\odot$ [34].

4) DM must behave like a classical fluid at least down to galactic scales, namely where we have evidence for it to be confined. If we suppose DM to be a boson with mass m and velocity v, we can then require to behave classically down to the typical size of MW satellites and obtain the following condition:

$$\lambda_{\text{De Broglie}} = \frac{h}{mv} \lesssim 1 \text{ kpc} \;\Rightarrow\; m \gtrsim 10^{-22} \text{ eV} \left(\frac{120\,\text{km/s}}{v}\right) . \tag{1.5}$$

For a kpc-sized halo of total mass $M \sim 10^9$ M$_\odot$, we expect a virial velocity $v \sim \sqrt{G_N M/R} \sim 70$ km/s, which implies a lower limit for the mass of bosonic DM of about 10^{-22} eV. Thanks to its ultra-light mass, the bosonic DM saturating the lower bound in Eq. (1.5) – known as Fuzzy DM [35] – represents a viable solution to the tensions that seemingly arise when the standard CDM paradigm is probed into the deep non-linear regime at redshift $z \sim 0$ [36, 37] (see the last section of Chapter 4 for further details). A similar argument holds also for fermionic DM [38], where the lower bound turns out to be more severe due to Pauli exclusion principle:

$$M \sim m\,\frac{4\pi}{3}R^3 \int d^3p\, f(\vec{p}) \lesssim m\frac{4\pi}{3}R^3 \int \frac{d^3p}{h^3} \sim m\left(\frac{R\,mv}{h}\right)^3 , \tag{1.6}$$

where f, m and v are the phase-space distribution, the mass and the velocity

of the particle, R the size of halo and M the corresponding enclosed mass. In the chain above, we have used $0 \leq f(\vec{p}) \lesssim h^{-3}$ (h being the Planck constant) due to Fermi-Dirac statistics. Therefore, plugging in the same reference values as before:

$$m^2 \gtrsim \sqrt{M \left(\frac{h}{R\,v}\right)^3} \;\Rightarrow\; m \gtrsim 0.3 \text{ keV} \,, \tag{1.7}$$

which is in the ballpark of more refined recent estimates for fermionic DM [39].

5) DM is not hot, namely it cannot be relativistic (roughly) at matter-radiation equality, since as previously discussed matter perturbations need to grow at that time. Indeed, as long as the kinetic energy dominates over the potential one, the free streaming of DM particles washes out the formation of structures. We can introduce the free-streaming length as the comoving distance between DM production at time t_i and the onset of structure formation, $\sim t_{\rm eq}$:

$$\lambda_{\rm FS} = \int_{t_i}^{t_{\rm eq}} dt' \frac{v(t')}{a(t')} \,, \tag{1.8}$$

and use it as a standard ruler for the typical length scale at which collisionless particles feel gravitational clustering. The integral in Eq. (1.8) is dominated by the time interval when the particle is fully relativistic, i.e. $v(t) \sim 1\,,\, \forall\, t \lesssim t_{\rm nr}$. Assuming $t_{\rm nr} \leq t_{\rm eq}$ and setting $T_{\rm nr}$ as the temperature saturating $3k_{\rm B}T \lesssim mc^2$, typical values for $t_{\rm nr}$ yield [40]:

$$\lambda_{\rm FS} \sim 2\frac{t_{\rm nr}}{a_{\rm nr}} \sim 0.4 \text{ Mpc } \frac{\text{keV}}{m} \frac{T_{\rm nr}}{T} \;\Rightarrow\; \lambda^{\nu}_{\rm FS} \sim 40 \text{ Mpc } \frac{30 \text{ eV}}{m_\nu} \,, \tag{1.9}$$

where we have considered to be in radiation domination and we have traded in the last step $T_{\rm nr}/T$ for $T_\nu/T = (4/11)^{1/3}$, valid for light neutrino species in a standard cosmological scenario. From the estimate in Eq. (1.9) we can see that neutrinos with eV masses are "hot" DM candidates, i.e. $\lambda_{\rm FS} \simeq \lambda_{\rm eq} \sim 10$ Mpc, which would imply the erasing of all small scale structures at first and top-down formation history where large structures are supposed to fragment into smaller ones. Since cosmological measurements support instead the opposite bottom-up picture with hierarchical growth of structures, Standard Model neutrinos cannot be the bulk of the DM component. Interestingly, in "warm" DM scenarios, where $\lambda_{\rm FS} \sim 1$ Mpc, small-scale perturbations can be washed out and, therefore, candidates such as sterile neutrinos [41] may alleviate the apparent difficulties of CDM at reproducing the low-mass end of the halo mass function [42]. However, strong constraints apply to this class of models as well, e.g., from the Ly-α forest data [43], limiting

the phenomenological viability of warm DM candidates. This also probably suggests that CDM ($\lambda_{\rm FS} \ll$ Mpc) is still today the most robust framework where model predictions meet an overall good agreement with a broad variety of astrophysical and cosmological measurements [44].

To conclude, a multitude of observations is clearly pointing to the need of some degrees of freedom, gravitating as ordinary matter, but with otherwise suppressed couplings. On the basis of the five points listed above, it turns out that these degrees of freedom cannot fit in the spectrum of elementary particles of the Standard Model (SM). Therefore, up to possibly not-yet detected exotic bound states of quarks [45], addressing the DM problem likely represents today one of the most compelling patterns towards a foreseeable New Physics (NP) discovery.

1.3 The Lee-Weinberg proposal and New Physics

According to Eq. (1.5) - (1.6) it is possible to gain some general, (almost) model-independent statement about the mass range of DM particles by the simple observation that DM must form galactic halos. As we are going to see in what follows, folding in assumptions about the evolution of the DM density in the Early Universe allows us to motivate more specific mass scales, possibly meeting NP expectations rising from mere theoretical arguments in Physics Beyond the SM (BSM).

1.3.1 The (not-so) WIMP miracle

Let us consider a new massive particle species χ in the thermal bath of the very Early Universe, with a lifetime $\tau_\chi \gtrsim \tau_{\rm Universe} \sim 13.8 \cdot 10^9$ yrs. If χ would not be interacting with any of the other species present in the bath, its number density n_χ in an expanding homogenous and isotropic Universe would be conserved in a comoving volume:

$$\frac{dn_\chi}{dt} + 3Hn_\chi = 0 \;\Rightarrow\; n_\chi \propto a^{-3} \,, \tag{1.10}$$

with H the Hubble parameter, $da/dt = a\,H$, and a the scale factor. Of course, the picture gets modified if we allow χ particles to annihilate and be produced in pairs by $2 \to 2$ interactions with the thermal plasma. The r.h.s. of Eq. (1.10) is no longer vanishing and it must contain a term of "particle loss" due to $\chi\overline{\chi}$ annihilation, hence proportional to n_χ^2, as well as a term of "particle gain", proportional to the number density of the species A and B producing χ . Moreover, if we assume A, B and χ to be in thermal equilibrium at the very early stages of the Universe

expansion history, detailed balance implies:

$$n_{\rm A}^{\rm eq.} n_{\rm B}^{\rm eq.} = (n_\chi^{\rm eq.})^2 \ , \tag{1.11}$$

where $n_{\rm S}^{\rm eq.}$ is denoting the thermal equilibrium distribution of the species S.
On physical grounds, the proportionality constant we expect to appear in Eq. (1.10) must be related to the cross section characterizing the annihilation rate of χ ,

$$\Gamma_\chi = n_\chi \langle \sigma v \rangle \ . \tag{1.12}$$

The thermally averaged annihilation cross section introduced above can be computed according to the following relativistic single-integral expression [46]:

$$\langle \sigma v \rangle = \frac{x}{8 m_\chi^5 K_2^2(x)} \int_{4m_\chi^2}^\infty d\tilde{s} \, \left(\tilde{s} - 4m_\chi^2\right) \sqrt{\tilde{s}} \, K_1\left(x \frac{\sqrt{\tilde{s}}}{m_\chi}\right) \sigma(\tilde{s}) \simeq C^{(0)} + \frac{3}{2} C^{(1)} \, x^{-1} + \dots \tag{1.13}$$

where $\sqrt{\tilde{s}}$ is the center of mass energy of the process, $x \equiv m_\chi / T$, and K_n is the modified Bessel function of the second kind. In the case of non-relativistic species, $\langle \sigma v \rangle$ may be expanded taking the non-relativistic limit: the S-wave contribution then proceeds through $C^{(0,1,\dots)}$, the P-wave through $C^{(1,2,\dots)}$ and so forth, with velocity $v = \sqrt{3/x}$ in natural units ($k_{\rm B}, c = 1$). Given the all set of arguments, we can heuristically justify the Boltzmann equation governing the evolution of n_χ ,

$$\frac{dn_\chi}{dt} + 3Hn_\chi = \langle \sigma v \rangle \left[(n_\chi^{\rm eq.})^2 - n_\chi^2\right] \ \Rightarrow \ \frac{x}{Y_\chi^{\rm eq.}} \frac{dY_\chi}{dx} = \frac{\Gamma_\chi^{\rm eq.}}{H} \left[\left(\frac{Y_\chi}{Y_\chi^{\rm eq.}}\right)^2 - 1\right] \ , \tag{1.14}$$

where in the last step $Y_\chi \equiv n_\chi / s$ – with s being the entropy density of the thermal bath – and we have exploited the entropy conservation per comoving volume, assuming that the Universe can be approximated to be an iso-entropic system. In the early stages of the radiation dominated era, we can assume the temperature to be much larger than the mass of thermal bath states as well as $x \ll 1$. Hence, according to Eq. (1.14), the evolution of χ in the primordial Universe must be first of all characterized by a phase where the species number density is tracking its original relativistic equilibrium distribution:

$$\Gamma_\chi^{\rm eq.} \sim \mathcal{O}(10^{-1}) \times T^3 \langle \sigma v \rangle \gg H \sim \mathcal{O}(10) \times \frac{T^2}{M_{\rm Pl}} \ \Rightarrow \ Y_\chi = Y_\chi^{\rm eq.} \ , \tag{1.15}$$

where we have reported also the typical order of magnitude of numerical pre-factors which include the internal degrees of freedom of χ and of the relativistic species active at very high temperatures. As time goes by, the Universe expands and cools

down, so that, depending on the mass and interaction strength of χ, the above condition may not be satisfied anymore. In particular, let us assume the existence of a temperature $T_{\rm nr}^{(\chi)}$ such that for $T \lesssim T_{\rm nr}^{(\chi)}$, $x \gtrsim 1$. Here, χ follows a second phase of evolution: as a non-relativistic species, its density features an exponential Boltzmann suppression. Physically, for $T \lesssim T_{\rm nr}^{(\chi)}$ χ annihilation still takes place, but the typical forward reaction creating χ pairs is now kinematically forbidden. At this point, pending on the value of $\langle\sigma v\rangle$, the particle χ may decouple from the thermal plasma before its complete extinction. Indeed, as the Universe expands, it becomes increasingly harder for a χ particle to find a partner to annihilate with. As a consequence of that, its yield Y_χ may freeze out. From Eq. (1.14), the condition of freeze-out for χ requires $x_{\rm f.o.}$ such that:

$$\Gamma_\chi^{\rm eq.} \sim H \;\Leftrightarrow\; \sqrt{x_{\rm f.o.}}e^{-x_{\rm f.o.}} \sim \mathcal{O}(10^2) \times \frac{1}{m_\chi \langle\sigma v\rangle M_{\rm Pl}} \,. \tag{1.16}$$

Plugging this expression into the definition of the yield of χ at freeze-out gives:

$$Y_\chi\Big|_{x_{\rm f.o.}} \sim \mathcal{O}\left(10^{-3}\right) \times x_{\rm f.o.}\sqrt{x_{\rm f.o.}}e^{-x_{\rm f.o.}} \sim \mathcal{O}\left(10^{-1}\right) \times \frac{x_{\rm f.o.}}{m_\chi \langle\sigma v\rangle M_{\rm Pl}} \,. \tag{1.17}$$

Eventually, assuming again to be in an iso-entropic Universe, the last estimate allows us to compute the relic abundance that χ has today:

$$\begin{aligned} \Omega_\chi h^2 \;\equiv\; \frac{\rho_\chi^0}{\rho_{\rm crit.}^0 h^{-2}} &= \left(\frac{s_0}{\rho_{\rm crit.}^0 h^{-2}}\right) m_\chi Y_\chi\Big|_{x_{\rm f.o.}} \simeq \frac{10^{11}}{3}\left(\frac{m_\chi}{10^2\,\text{GeV}}\right) Y_\chi\Big|_{x_{\rm f.o.}} \\ &\sim \mathcal{O}\left(10^{-1}\right) \times \left(\frac{x_{\rm f.o.}}{30}\right)\left(\frac{10^{18}\,\text{GeV}}{M_{\rm Pl}}\right)\left(\frac{10^{-8}\,\text{GeV}^{-2}}{\langle\sigma v\rangle}\right) \,, \end{aligned} \tag{1.18}$$

where we have used the typical values $s_0 \simeq 3000$ cm^{-3}, $\rho_{\rm crit.}^0 \simeq 10^{-5} h^2$ GeV cm^{-3}.

Remarkably, if for the species χ the assumption of cold relic comes together with a thermally averaged cross section in the ballpark of the one for weak interactions – where $\sigma_{\rm EW}/m^2 \sim G_F^2 \simeq 10^{-10}\,\text{GeV}^{-4}$ – the corresponding estimate of its relic abundance can return the known density of DM today. If we restrain to $20 \lesssim x_{\rm f.o.} \lesssim 40$ (a range we may justify a posteriori), we can estimate through Eq. (1.16) the corresponding typical range of masses:

$$m_\chi \sim \mathcal{O}(10^2) \times \left(\frac{10^{-16} - 10^{-9}}{\sqrt{x_{\rm f.o}}e^{-x_{\rm f.o}}}\right)\left(\frac{10^{18}\,\text{GeV}}{M_{\rm Pl}}\right)\left(\frac{10^{-8}\,\text{GeV}^{-2}}{\langle\sigma v\rangle}\right)\,\text{GeV} \,, \tag{1.19}$$

that for the nominal values above corresponds to $10\,\text{GeV} \lesssim m_\chi \lesssim 10^2\,\text{TeV}$. The lower extreme of this range becomes effectively a lower bound on the mass of χ if the species is charged under $SU(2)_L \otimes U(1)_Y$ of the SM. This phenomenologically

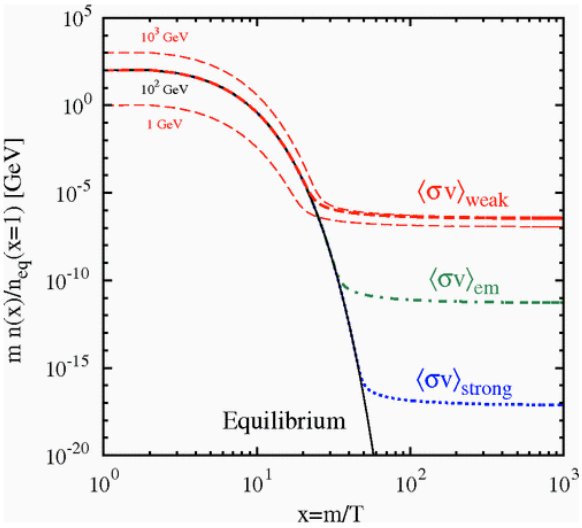

Figure 1.3: *Evolution of the abundance of a non-relativistc species as a function of $x = m/T$. The thick curves show the number density normalized to the initial equilibrium value, for different choices of annihilation cross section $\langle\sigma v\rangle$ and mass m. Results for $m = 100$ GeV are shown for weak interactions, $\langle\sigma v\rangle \simeq 10^{-8}$ GeV^{-2}, (dashed red), electromagnetic interactions, $\langle\sigma v\rangle \simeq 10^{-3}$ GeV^{-2} (dot-dashed green), and strong interactions, $\langle\sigma v\rangle \simeq 10^{3}$ GeV^{-2} (dotted blue). For the weak cross section the thin dashed curves show the mass dependence for $m_\chi = 103$ GeV (upper dashed curve) and $m = 1$ GeV (lower dashed curve). The solid black curve shows the evolution of the equilibrium abundance for $m = 100$ GeV. Image Credit: Fig. 1 from Ref. [47].*

interesting scenario has been historically explored in 1977 by Benjamin W. Lee and Steven Weinberg in their seminal study on cosmological heavy neutrinos [48][1]. The upper extreme of the mass interval corresponds instead to the upper limit one can set from unitarity arguments on the cross section of χ, since it cannot be arbitrarily large as a function of energy [50]. Such a bound, however, may be model-dependent on the basis of the underlying UV theory [51].

The fact that a cold relic in the Early Universe, with $\langle\sigma v\rangle$ of about the weak interaction cross section, is able to explain the observed $\Omega_{\rm DM}h^2$ and, moreover, has a mass that can be accommodated close to the electroweak scale $\Lambda_{\rm EW} \sim 10^2\,{\rm GeV}$,

$$\langle\sigma v\rangle \sim G_{\rm F}^2\, T_{\rm f.o.}^2 \;\Leftrightarrow\; m_\chi \sim \sqrt{\frac{\langle\sigma v\rangle}{10^{-8}\,{\rm GeV}^{-2}}}\left(\frac{x_{\rm f.o.}}{30}\right)\left(\frac{10^{-5}\,{\rm GeV}^{-2}}{G_{\rm F}}\right) 300\,{\rm GeV}\ , \quad (1.20)$$

is commonly referred to as "weakly interactive massive particle (WIMP) miracle".

[1] The cosmological lower bound on heavy neutrinos was originally obtained in Ref. [49], few months before Lee-Weinberg's paper. I thank Subir Sarkar to have made me aware of that.

In Fig. 1.3 we show the number density normalized to the initial equilibrium value for a non-relativistic species as a function of $x = m/T$, where m has been set to be $\mathcal{O}(\Lambda_{\rm EW})$. As displayed in the figure, the freeze-out yield of the species is inversely proportional to the value of the thermally averaged annihilation cross section. According to Eq. (1.18) and Fig. 1.3, weak-scale non-relativistic species with typical cross section of electromagnetic or strong interactions would annihilate too efficiently in the Early Universe to explain the whole DM relic density we measure today (besides not being a reliable DM candidate, see the five rules in the previous section).

As we are going to recap in what follows, the weak-scale "WIMP miracle" has become one of the most influential paradigm for DM as well-motivated theoretical models can embed such candidates, while an ongoing broad experimental effort is currently probing larger and larger portions of the corresponding parameter space. However, despite an intensive program targeting expectations like the one in Eq. (1.20), it is worth noting that the relation obtained in Eq. (1.18) is not really peculiar to the electroweak scale. Indeed, using e.g. the nominal values of $\langle\sigma v\rangle$ and $M_{\rm Pl}$ reported above, it is possible to obtain from Eq. (1.16) $x_{\rm f.o.} \sim \mathcal{O}(10)$ with a large range of values for m_χ. As a consequence, the relic abundance computation in Eq. (1.18) is essentially sensitive to $\langle\sigma v\rangle$. This fact actually opens up the possibility to play with a much wider band of allowed masses for thermal DM than the one suggested in Eq. (1.19). For instance, assuming a dominant s-wave contribution, the thermally averaged cross section can be parametrized on dimensional grounds as $\langle\sigma v\rangle \sim \alpha_\chi^2/m_\chi^2$, where α_χ is the dimensionless coupling characterizing the strength of χ interactions. Then, looking back to Eq. (1.18), one can take α_χ arbitrarily small while keeping the ratio α_χ^2/m_χ^2 fixed to get the desired DM relic density [52].

1.3.2 WIMPs and the hierarchy problem

In quantum field theory, order of magnitude estimates of dimensionless couplings and dimensionful ones turn out to be very different on simple dimensional grounds. Indeed, if no symmetry principle is at hand, dimensionless couplings may be expected to be generically of $\mathcal{O}(1)$ [53]. On the other hand, dimensionful couplings should be of the order of the largest mass scale in the theory, to the appropriate power [54]. However, when a symmetry is restored in the limit of a coupling (dimensionless or not) going to 0, it is "natural" to expect for the value of this coupling an arbitrarily small number. These considerations are at the basis of what we refer today as "naturalness" and the intimately related "hierarchy problem" of scales in High Energy Physics [55].

To see this guiding principle at work, let us suppose to have as a UV complete model the Yukawa theory in 4 space-time dimensions:

$$\mathscr{L}_{\rm UV} = \bar{\psi}(i\partial\!\!\!/ - m_\psi)\psi + \frac{1}{2}\partial_\mu\phi\,\partial^\mu\phi - \frac{m_\phi^2}{2}\phi^2 + g_{\rm Y}\phi\bar{\psi}\psi \ , \tag{1.21}$$

where a massive fermion ψ is coupled to a massive scalar ϕ with a trilinear interaction of strength $g_{\rm Y}$. We have assumed a Z_2 symmetry, $\phi \to -\phi$, for the scalar, and ignored the renormalizable ϕ^4 term, which is not important for the discussion that follows. Setting the highest scale of the theory to be $\Lambda_{\rm UV} \equiv \max(m_\psi, m_\phi)$, we can integrate out the heavy degrees of freedom and study Eq. (1.21) in the full IR regime. It is easy to see that in the limit where $m_\phi \gg m_\psi$, we end up at low energy with a Fermi-like theory of four-fermion interactions with coupling g^2/m_ϕ^2, whereas in the opposite situation we get (at dimension 4) an ordinary ϕ^4 scalar theory. Matching at 1-loop level the (1-particle irreducible) 2-point functions of UV and IR theories, the IR spectrum of the Yukawa theory is characterized by [56]:

$$\begin{aligned}
\Lambda_{\rm IR} &= m_\psi(\Lambda_{\rm UV})\left[1 - \frac{g_{\rm Y}^2}{16\pi^2}\left(\frac{5}{4} + \frac{m_\psi^2}{2\Lambda_{\rm UV}^2}\right)\right] \qquad \text{if} \ \ m_\phi \gg m_\psi \ , \\
\Lambda_{\rm IR}^2 &= m_\phi^2(\Lambda_{\rm UV}) - \frac{g_{\rm Y}^2}{16\pi^2}\left(20\,\Lambda_{\rm UV}^2 - \frac{64}{3}m_\phi^2\right) \qquad \text{if} \ \ m_\psi \gg m_\phi \ ,
\end{aligned} \tag{1.22}$$

where we have used dimensional regularization (note that all power-like divergences in this regularization method identically vanish) and the $\overline{MS}$ subtraction scheme. We have set the matching scale at $\Lambda_{\rm UV}$ and introduced the IR energy scale, $\Lambda_{\rm IR}$, as the physical mass of the particle present in the low energy spectrum of the theory.

From Eq. (1.21) above, we can note that in the case of the light fermion the UV sensitivity of the IR scale is pretty mild: the quantum correction to the mass of the fermion is proportional to the mass itself, and, hence, in the limit $m_\psi \to 0$ it is stable under quantum corrections. Indeed, a symmetry originally lying in the UV theory, namely the invariance under chiral transformations, $\psi \to e^{i\gamma_5\theta}\psi$ (combined with the Z_2 invariance of the scalar), is restored in the massless limit: consequently, fermion masses can be naturally small. This fact stands out in net contrast to the opposite scenario where the scalar is the light degree of freedom in the IR. The quantum correction in $\Lambda_{\rm IR}$ is now of $\mathcal{O}(\Lambda_{\rm UV}^2 g_{\rm Y}^2/(16\pi^2))$, which implies that any small fluctuation $g + \delta g$ in the UV theory is reflected in the IR by a large radiative effect. This extreme UV sensitivity follows from the lack of an underlying symmetry when in the Yukawa Lagrangian, Eq. (1.21), we take the limit $m_\phi \to 0$.

The SM Higgs boson falls in this unpleasant situation: its mass, $m_h \sim \mathcal{O}(\Lambda_{\rm EW})$, is quadratically sensitive to any NP scale $\Lambda_{\rm NP} \gtrsim \Lambda_{\rm EW}$. While state-of-the-art

experimental measurements of electroweak and strong couplings, supplemented by the SM renormalization group evolution, offer an important hint for NP existence already at $\sim 10^{16}$ GeV [57], we may (naively) expect quantum gravity effects to become non-negligible at $\sim M_{\rm Pl}$. This would suggest $\Lambda_{\rm NP} \sim 10^{18}$ GeV, implying a very fine-tuned Higgs mass against large UV radiative corrections. While from the mere theory side hierarchy problems do not lead to real inconsistencies in a quantum field theory, the quest for naturalness has been historically the main driving force to motivate BSM physics at $\Lambda_{\rm NP} \sim \Lambda_{\rm EW}$, providing a guide line for extensions of the SM where the Higgs mass turns out to be technically natural.

One of the most elegant solutions to the hierarchy problem in BSM physics is certainly provided by Supersymmetry (SUSY). In SUSY theories, the Poincaré group is enlarged to contain transformations generated by anti-commuting fermionic operators mapping bosons to fermions and viceversa [58]. For instance, promoting ϕ to be complex in order to match the number of degrees of freedom of ψ, the SUSY version of the Lagrangian in Eq. (1.21) would require fermionic and bosonic pairs to share the same energy mass scale, being one the super-partner of the other. Hence, the enhancement of space-time symmetries in SUSY theories allow the scalars to inherit the chiral symmetry of the fermions. As a straightforward consequence, the exact manifestation of SUSY in Nature would ensure the mass of scalar particles to be radiatively stable under quantum corrections.

It is easy to see that SM bosons and fermions cannot be the super-partner of each other, since they do not show any degeneracy in mass and, moreover, they carry different quantum numbers. Hence, even in its most economical realization – the Minimal Supersymmetric Standard Model (MSSM) – any SUSY extension of the SM predicts the existence of SM super-partners, with (at least) some of them expected to be found around the scale of SUSY breaking, $\Lambda_{\rm SUSY}$. Up-to-date searches at the Large Hadron Collider (LHC) put severe constraints, e.g., on the mass of squarks and gluinos, the super-partners of quarks and gluons, starting to probe $\Lambda_{\rm SUSY}$ above the TeV, i.e. $\Lambda_{\rm SUSY} \gtrsim 10\,\Lambda_{\rm EW}$. Therefore, even if SUSY would be a symmetry chosen by Nature, current null results at colliders imply a mild hierarchy problem – the so-called "little hierarchy problem" [59] – forcing the Higgs mass in SUSY extensions of the SM to be tuned (at least) at the % level [60].

In spite of any hierarchy problem, SUSY remains a very welcome opportunity for BSM models [61, 62]. Indeed, it allows for an exact unification of the SM gauge couplings, possibly accounting also for current bounds on the lifetime of proton decay. Moreover, the typical spectrum of these models quite remarkably contain viable DM candidates. For instance, if we take the general MSSM, we can see that phenomenologically dangerous terms allowing for baryon and lepton

number violating processes arise already at the renormalizable level. In a bottom-up approach, to avoid unsuppressed $\Delta B, \Delta L \neq 0$ operators we may invoke the conservation of a discrete symmetry like R-parity [63]:

$$R = (-1)^{2j+3(B-L)} \ , \tag{1.23}$$

where j is the spin of the particle with baryonic charge B and leptonic charge L. According to Eq. (1.23), SM particles have positive R quantum number, while their super-partners have $R = -1$. Consequently, this Z_2 symmetry distinguishes SM particles from SUSY counterparts, and implies that the lightest supersymmetric particle (LSP) of the MSSM is stable. Interestingly, in many MSSM realizations one of the four neutralinos can usually be identified as the LSP of the theory. Neutralinos are mass eigenstates of a linear superposition of the super-partners of the Higgs and of the $SU(2)_L \otimes U(1)_Y$ neutral gauge bosons, namely the two neutral higgsinos, the neutral wino and the bino:

$$\widetilde{\chi}_i^0 = h_{ui}\, \widetilde{H}_u^0 + h_{di}\, \widetilde{H}_d^0 + w_i\, \widetilde{W}^0 + b_i\, \widetilde{B}^0 \ . \tag{1.24}$$

So, in the framework of the R-parity conserving MSSM the lightest neutralino typically corresponds to a stable particle with electroweak quantum numbers. Therefore, it represents a very appealing WIMP DM candidate [64].

Neutralinos in the Early Universe can decouple from the primordial plasma as cold thermal relics, following the picture drawn in detail in the previous section. They can reproduce the DM measured abundance of today even in the simplest phenomenological versions of the MSSM [65, 66]. Looking back at Eq. (1.24), if we wish to identify the DM candidate with a pure state neutralino, while in the case of bino DM the annihilation rate in the Early Universe is usually too small and easily overcloses the Universe, a pure higgsino with mass ~ 1 TeV and a pure wino with mass ~ 3 TeV are typical benchmark scenarios that correctly yield the right DM abundance. Interestingly enough, the latter may be phenomenologically disfavored by DM indirect searches [67–69]. Eventually, one may look for more complicated situations, motivated by the desire that the LSP mass should be as close as possible to $\Lambda_{\rm EW}$. In this case, the DM neutralino should contain mostly a bino component, and an additional ingredient that allows to increase the corresponding annihilation cross section $\langle \sigma v \rangle$ is required. Mechanisms such as co-annihilation (e.g. with a stop or a stau) and resonant annihilation through on-shell mediators (e.g. the Z^0 or the Higgs) [70] make the bino-like neutralino generally able to reproduce Planck's value of the current cosmological DM density. Finally, it is worth noting that the right DM relic abundance may also be obtained through an appropriate balance of

bino and higgsino and/or wino mixtures, corresponding to the phenomenological window of the so-called "well-tempered" neutralino [71].

Eventually, we wish to remark that many other alternatives to the WIMP paradigm may be considered to account for the fundamental origin of DM, and some of them may be found to be as well-motivated as WIMPs in relation to open problems in Particle Physics [72]. In particular, we would like to mention the gravitino as other viable DM candidate in SUSY models [73, 74]; composite DM in non-minimal realization of composite Higgs models [75, 76], where the dynamically emergent scale of compositeness is supposed to address/alleviate the hierarchy problem [77]; the sterile neutrino in relation to the mechanisms at the origin of SM neutrino masses and baryon asymmetry of the Universe [78, 79]; the axion, namely a naturally light massive scalar [80, 81] that elegantly accounts for the absence of CP violating processes in Quantum Chromodynamics [82, 83], such as the neutron electric dipole moment, and that, at the same time, offers a rich cosmological picture where it may behave as cold DM [84].

1.4 Looking for thermal relics in the sky

In the LHC era, high energy proton-proton collisions allow us to look for possible production of new stable (or long-lived) massive particles that may be potentially identified as DM. Dedicated searches at collider exploit the tag on events, e.g., with a single jet or photon plus missing transverse energy, possibly related to a boosted pair of undetected colorless and electrically neutral massive particles [85]. While being an important complementary "DM tool", collider searches, according to this kind of signatures, cannot really assess the DM nature of the missing energy and, hence, must be supplemented by more targeted experiments on DM detection.

After 30 years from its original proposal [86], today we are looking for DM imprints in underground labs with an unprecedented level of sensitivity, in the attempt to measure the recoil energy from elastic/inelastic scattering of local DM particles with nucleon constituents of apposite target nuclei. Notable examples on the experimental side are detectors based on cryogenic technologies [87], sensitive to the excitations of, e.g., germanium or silicon crystals, and noble liquid experiments [88], that are monitoring scintillation signals in, e.g., liquid argon and xenon.

Unfortunately, no clear evidence in favor of a positive detection has been singled out so far neither at the LHC nor in the underground labs designed for a DM direct detection. These null results have been translated into a relevant set of limits for the mass and the coupling of DM particles in many BSM proposals. For

instance, concerning SUSY model building, bounds from direct detection signals definitely exclude sneutrinos, scalar super-partners of SM neutrinos, as viable DM candidates in the MSSM (but not in its extensions, see e.g. [89,90]). With the most notable exception of a detected event rate in favor of a DM annual modulation signal, claimed by the DAMA/LIBRA collaboration already few years back [91] and possibly soon confirmed/disproved by next-generation facilities [92], direct detection searches are currently setting very strict limits on the strength of DM-nucleon interactions, excluding at 90% C.L. weak-scale DM with spin independent scattering cross section $\gtrsim 10^{-45}$ cm^2 [93].

Very intriguingly, the quest for a DM discovery may potentially undertake a different path than the one beaten by the two techniques just mentioned. Indeed, since we have inferred so far the existence of DM only on astrophysical and cosmological scales, it may be reasonable to expect a DM particle signal arising from astrophysical systems and/or cosmological measurements. In particular, astrophysical objects or peculiar regions of the sky characterized by the indirect (gravitational) evidence of large DM densities may be of fundamental phenomenological relevance. In fact, they may represent "natural boost factories", potentially able to strengthen typically faint signals as the ones expected from "collisionless" particles.

Mostly targeting the picture of thermal relics described in Section 1.3.1, indirect searches for DM are based on the challenge of detecting possible yields from DM particles annihilating (or decaying), in correspondence of DM overdense regions. If we assume DM pairs to annihilate in the final state f with a thermally-averaged cross section $\langle \sigma_f v \rangle$, the corresponding annihilation differential rate consists in the annihilation rate per particle times the number of pairs annihilating in a differential volume dV :

$$d\Gamma_{\rm ann}^{(f)} = \frac{\rho\left[r(\psi,\ell)\right]}{m_\chi}\langle\sigma_f v\rangle \times \frac{\rho\left[r(\psi,\ell)\right]}{2\,d_\chi\,m_\chi}\,\ell^2 d\ell\,d\Omega(\psi)\ , \tag{1.25}$$

where we have assumed a spherical DM density ρ, and r can be taken as the radial distance between the annihilation event and the center of the system, and here it is a function of the line-of-sight distance of the observer, ℓ, and the angular aperture, ψ, away from the center direction. The factor $d_\chi = 1\,(2)$ reflects the possibility that DM particles may (not) correspond to their own antiparticles. From Eq. (1.25) we can easily compute, e.g., the total flux of the prompt photons related to the annihilation of DM thermal relics:

$$\frac{d\phi_\gamma}{dE_\gamma} = \sum_f \int \frac{d\Gamma_{\rm ann}^{(f)}}{4\pi\ell^2}\,\frac{dN_\gamma^{(f)}(E_\gamma, m_\chi)}{dE_\gamma} = P(E_\gamma, m_\chi) \times J(\Delta\Omega)\ , \tag{1.26}$$

where in the last step we have conveniently grouped together factors closer to Particle Physics and those instead pertaining more to the Astrophysics community.

The "particle factor" in Eq. (1.26) includes the spectral emissivity $dN^{(f)}/dE_\gamma$ of the annihilation final state f as a function of the photon energy and the mass of the DM together with the total velocity-averaged annihilation cross section $\langle\sigma_{\rm tot}v\rangle$ and the branching ratio $b_f \equiv \langle\sigma_f v\rangle/\langle\sigma_{\rm tot}v\rangle$:

$$P(E_\gamma, m_\chi) = \frac{\langle\sigma_{\rm tot}v\rangle}{8\pi\, d_\chi m_\chi^2} \sum_f b_f \frac{dN_\gamma^{(f)}(E_\gamma, m_\chi)}{dE_\gamma} \ . \tag{1.27}$$

Note that the above result holds as long as $\langle\sigma v\rangle$ does not depend strongly on the velocity, as it is the case for S-wave production according to the expansion shown in Eq. (1.13). The typical mean velocity of the DM particles today in the halo of our Galaxy can be roughly estimated to be $\langle v\rangle \sim \sqrt{G_N M_{\rm MW}/R_{\rm MW}} \sim 200\,{\rm km/s}$, which implies that P-wave thermal relics will not give in general any detectable indirect detection signal due to the suppressed velocity in comparison to the one at freeze-out, $\langle v\rangle \sim c/3$. On the other hand, a velocity dependence in Eq. (1.27) may be an important particle boost factor in the case of models featuring Sommerfeld enhancement [94], namely a quantum non-relativistic effect due to the modification of the wave-function of DM particles that can self-interact via long-range mediator exchanges before annihilating. For instance, in the MSSM Sommerfeld enhancement can play an important role both in the computation of the DM relic density as well as in the study of indirect signals of pure wino DM [69, 95].

The "astrophysical factor", also known as J-factor, is the line-of-sight integral within an angular aperture $\Delta\Omega$ of the DM halo density profile squared:

$$J(\Delta\Omega) = \int_{\Delta\Omega} d\Omega \int_{\rm l.o.s.} d\ell\, \rho^2\left[r(\psi,\ell)\right] \ . \tag{1.28}$$

As expected on physical grounds, Eq. (1.26) tells us that to maximize the chance of a detection of photons from DM annihilation we have to conveniently choose astrophysical targets with high J-factors, i.e. with a high Dark Matter concentration. Note that analogous formulæ can be derived also in the case of decaying DM, where the "astrophysical factor" will be only linearly sensitive to the halo density profile. Of course, the signal-to-noise ratio of the sample chosen for a possible DM particle discovery does not depend critically only on the J-value, but also on the astrophysical processes characterizing the sample background/foreground relative to the wavelength investigated. In Chapter 3 and 4 we will study two of the most promising targets for DM indirect detection according to their corresponding J-factors, namely the innermost degrees surrounding the Galactic Center and

the MW dwarf spheroidal galaxies. Dwarf spheroidals are milestone examples of DM-dominated objects that contain few stars and low gas densities and, hence, are potentially ideal DM laboratories, leaving also room, together with galaxy clusters, for possibly broad multi-wavelength analyses [96]. In contrast, the region around the center of our Galaxy is a very complicated astrophysical environment. Despite the promising J-value (3 - 5 orders of magnitude bigger than the typical ones for MW dwarfs) due to the high DM content and the proximity to us, the Galactic Center region is generally polluted by large systematic uncertainties stemming from multi-wavelength backgrounds and foregrounds that are hard to estimate precisely.

Among the possible messengers for indirect searches, gamma rays play a leading role as they propagate essentially unperturbed to us, retaining the directionality from the origin of their emission. This allows us to potentially extract both morphological and spectral informations from gamma-ray emitting sources. Remarkably, any DM signal in the gamma-ray band should show a spatial correlation with the gravitationally inferred DM halo distribution. Weak-scale DM particles as WIMPs are supposed to yield such kind of signals [97]. Indeed, weak-scale thermal relics, being non-relativistic, may annihilate even today in galactic halos with typical center of mass energy $E_{\rm C.M.} \simeq 2m_\chi \sim 2\Lambda_{\rm EW}$, which turns out to be a sufficient energy budget for DM final states f to open up a gamma-ray window of secondary emitted photons with $E_\gamma \gtrsim$ MeV and sharply cut off at $E_\gamma \sim m_\chi$.

So, the kinematics related to today's thermal relic annihilation actually determines the properties of the photon energy spectrum. In Fig. 1.4 we show typical spectral features expected from the annihilation of weak-scale DM. For instance, in the case where DM annihilates into two-body final state channels containing at least one photon (e.g., $\gamma\gamma$, γZ^0, γh), we have that the spectrum of the signal is simply mono-energetic line,

$$\frac{dN}{dE_\gamma} \propto \delta(E_\gamma - E) \ , \ \text{with} \ \ E \leq m_\chi \ . \tag{1.29}$$

A hint of such a peculiar signature, implying $E_\gamma = m_\chi$ in the $\gamma\gamma$ channel, was found a few years back in the publicly available data of the Fermi Large Area Telescope – currently surveying the sky in the gamma-ray band since 2008 – at the photon energy $E_\gamma \sim 130$ GeV, from the analysis of an extended region containing also the Galactic Center [99, 100]. Unfortunately, up-to-date analyses, including the one of the Fermi collaboration itself [101], do not find any evidence for this spectral feature in the data anymore, suggesting probably a statistical fluctuation (for very recent studies on the impact of statistical flukes in Particle Physics see, e.g., Ref. [102, 103]). From the theoretical point of view, photon spectral lines

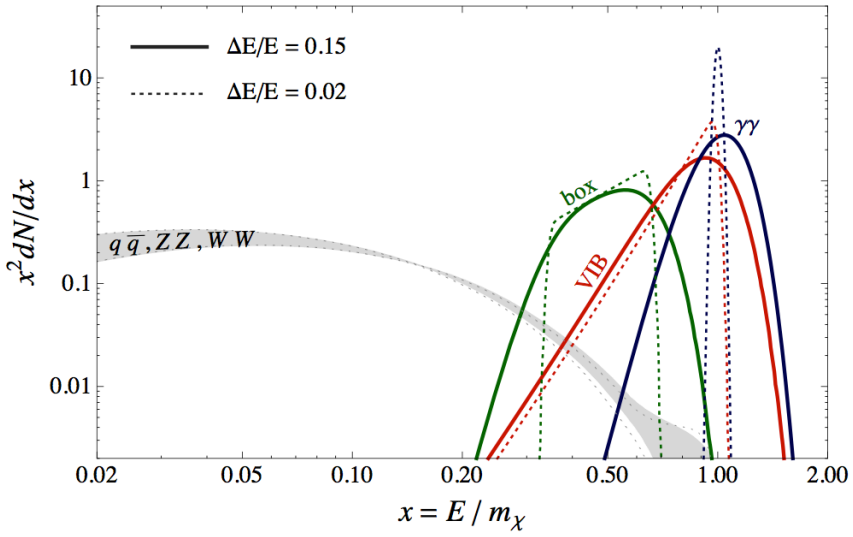

Figure 1.4: *From Ref. [98], various gamma-ray spectra expected from weak-scale DM annihilation, all normalized to $N(x > 0.1) = 1$. Prompt emission spectra from quarks, $W^\pm$ and Z^0 DM final states (gray band) look very similar. In the same figure, for two different energy resolutions $\Delta E/E$, a box-shaped spectrum due to DM cascade decays, a bump-like spectrum due to virtual internal bremsstrahlung from charged mediators, and the spectral line from DM annihilation into $\gamma\gamma$.*

arise only at loop level for a (supposedly) neutral DM particle, with a relative suppression factor typically of the size of $\alpha^2_{\text{e.m.}}/(4\pi)^2 \sim \mathcal{O}(10^{-7})$ (for an explicit computation in the MSSM see Ref. [104]).

Falling in a different energy range than the one targeted for a WIMP detection – the observation of a sharp spectral emission peaked around ~ 3.5 keV, observed by two independent groups in the analysis of X-ray spectra of several galaxy clusters [105, 106] – has recently triggered a renewed interest on spectral line signatures in BSM scenarios. However, the interpretation of this signal in terms of a genuine DM signature has been iteratively criticized in literature due to the generally complex analysis of all the de-excitation atomic lines falling in the energy range of the observed X-ray spectra [107, 108]. At present, the true origin of the signal is still a matter of ongoing debate, but the recent null findings from the observation of Draco dwarf spheroidal with the deep XMM-Newton survey [109, 110] reasonably disfavor the DM interpretation of the signal detected, instead, in galaxy clusters.

Depending on the exact energy resolution of the instrument, gamma-ray spectral lines may not be further distinguished from other peculiar spectral features yield by annihilating DM. Among these distinct signatures, we can consider, for example,

virtual internal bremsstrahlung, which results in a broadening of the spectral line signal towards lower masses [99]. Another highlighted possibility in literature has been the box-like spectrum [111], that arise in scenarios where the DM particles annihilate into a pair of final states that subsequently decay into $\gamma\gamma$. The two situations are respectively reported in Fig. 1.4 with red and blue lines. Recently, it has been shown that DM self-annihilating into two Dirac fermions, which then decay into another fermion and a photon, offers a quite characteristic triangular spectral feature to possibly be searched for as well in the gamma-ray sky [112].

Most commonly, thermal relics will likely annihilate into ordinary SM particles such as leptons, gauge bosons, and/or quarks. These yields may produce a secondary photon component either through final-state radiation or in the shower of their decay products, such as π^0 decays into $\gamma\gamma$ coming from hadronic showers. Looking at Fig. 1.4, we can see that, to first approximation, the secondary photon spectrum so produced is essentially featureless, with a rather soft cutoff at the kinematical limit $E_\gamma = m_\chi$, and it is very similar in shape for all the channels, without a strong dependence on the value of m_χ. Note, however, that refinements to this general picture do exist. For instance, model-independent electroweak corrections apply to all the SM final states when $m_\chi \gtrsim \Lambda_{\rm EW}$, giving an important imprint on the spectral shape of the single SM final state f [113]. Moreover, in the case of leptonic final states, radiated high-energy photons related to the energy losses of the particles propagating in the astrophysical medium may be relevant as well [114]. State-of-the-art predictions for these spectra can be found in the encyclopedic work of Ref. [115]. As shown in Fig. 1.4, the signature of secondary photon emission coming from SM yields of DM usually shows up as a broad bump-like excess to be detected on top of the expected astrophysical gamma-ray background. We will see in Chapter 2 how much, in general, we understand about this astrophysical background. Interestingly, a gamma-ray continuum excess has been reported in several gamma-ray analyses of the inner few tens of degrees around the Galactic Center, with a statistically strong evidence in favor of a spectrally and morphologically WIMP-like signature exactly like the one just discussed here. We will dedicate the entire Chapter 3 on this exciting claim about a potential DM particle discovery.

Another very promising indirect messenger of the nature of the DM particle may be neutrinos. They, indeed, can offer a diagnostics for DM annihilation very similar to the one presented for gamma-ray photons. In particular, Eq. (1.26) holds also for neutrinos, with the obvious substitution in Eq. (1.27) of the neutrino spectral emissivity from SM yields. In contrast to the case of gamma rays, a DM signal of high-energy neutrinos is not expected to have many astrophysical background counterparts. However, the typical cross section related to neutrino interactions is

relatively small, the reason why it is very challenging to detect a signal from them. The current null results of up-to-date dedicated searches with gigantic neutrino observatories such as ANTARES and IceCube set upper limits on $\langle \sigma v \rangle$ that are competitive with gamma-ray ones only for few final states and for DM masses above the TeV [116, 117]. Remarkably, neutrinos offer another peculiar diagnostics for DM particle interactions. In fact, the orbit of DM particles populating the halo of our Galaxy may have the chance to pass through a massive celestial body, like the Sun or the Earth. This would give a small probability to have a scattering of DM particles on ordinary matter, possibly diverting the orbit of the DM particle to one which is gravitationally bound to the massive body, and hence via subsequent scatterings, allowing the DM particle to sink at its center and build up a local DM overdensity there. Therefore, the annihilation rate into Standard Model particles of putative DM concentrations at the center of the Sun or of the Earth may give rise eventually to distinctive high-energy neutrino fluxes, representing one of the most peculiar signatures of DM particle interactions [118–121]. Indeed, this kind of DM signature not only involves the knowledge of the DM halo density profile, but also requires the particle velocity distribution, as it also needed by direct detection experiments. The most updated searches for DM annihilation in the Sun, operated by the IceCube collaboration, provide at present the strongest available upper limits on the spin-dependent scattering cross section of DM on a proton [122], excluding weak-scale DM with scattering cross sections greater than $\sim 10^{-40}$ cm^2 ($\sim 10^{-38}$ cm^2) for an assumed W^-W^+ ($b\bar{b}$) annihilation channel.

Finally, the other tool we may want to consider for indirect searches are the fluxes of charged particle we can detect in our local environment. At first glance, charged particle yields may seem much less appealing than high-energy photons and neutrinos as indirect messengers of the nature of DM. Since they are charged, their propagation is affected by the structure of magnetic fields in the Galaxy. Therefore, these messengers do not retain the directionality from their emission, and, hence, cannot provide any precise morphological information on a DM signal. Moreover, high-energy electrons and protons are copiously produced in the outer-space by a large amount of standard astrophysical processes/sources. However, the amount of antimatter we find in our local observable Universe is notably tiny in comparison to ordinary baryonic matter. This opens up the possibility to search in our local environment for antimatter yields [123–126], given the expected low astrophysical background. At the same time, DM thermal relics will be, in general, democratic in the production of yields of matter and antimatter. Hence, DM is expected to have a good signal-to-noise in antimatter channels. Today, thanks to current facilities, such as PAMELA and AMS, we can measure with satisfactory precision

the local flux, e.g., of positrons and antiprotons, two data set on antimatter that are leaving us room for a possible concrete detection of some DM particle signal. The interpretation of these data depends, however, crucially on our knowledge about the production and the propagation mechanisms of charged particles in the Galaxy, which bring us directly to one of the main topics of next chapter.

Chapter 2

2 Diffusion in the GeV-TeV gamma-ray and neutrino sky

2.1 Cosmic rays as particle discovery tools

Some of the historically most important steps in Particle Physics have certainly deep roots in the field of Cosmic-ray (CR) Physics: cosmic rays have been the initial playground that allowed particle physicists to make discoveries of fundamental relevance.
One of the first pioneer studies in CR physics needs to be addressed to Victor Hess, at the beginning of the last century: his historical balloon flight allowed the measurement of an ionized radiation in the atmosphere, whose intensity was increasing with greater altitude. Subsequent studies pointed to the fact that this radiation was of a high-energy kind, and it was penetrating the atmosphere while getting partially absorbed by the latter. The lack of a day/night variation and the absence of a correlation with the position of the Sun suggested in the end that the origin of such a radiation was of a "cosmic" kind. A following set of observations highlighted the correlation of locally measured CR intensities with the dipolar structure of the Earth magnetic field, leading to the conclusion that CRs should have been mainly composed of charged particles. The outstanding discoveries that followed those years revolutionized the knowledge of Particle Physics: the experimental evidence in favor of antimatter with the first detection of antiprotons and positrons, the measurement of heavier replica like the muon, the birth of hadron spectroscopy, and the contemporary validation of theoretical milestone proposals like e.g. the Dirac equation and the Yukawa theory. Such a prolific series of discoveries set up the stages for the advent of particle accelerators and, consequently, starting from the second half of the last century, the study of CR physics has been gradually pertaining to a more Astrophysics-inclined audience.

Interestingly, nowadays we are back to a renewed interest on the interplay between CRs and Particle Physics. At present, the state-of-the-art measurements of CR observables on one side and the progressing theoretical development of CR theory

modeling on the other one, may offer to us a unique window to study possible indirect imprints of Dark Matter (DM) particle interactions. As already discussed in Chapter 1, the possible identification of yields from the annihilation or decay of DM particles is currently one of the most valuable opportunities in the challenge of a New Physics discovery. Several controversial signals are in support of these exciting times, e.g. the rise at high energy in the positron fraction firstly measured by PAMELA [127,128], the very recent antiproton to proton ratio in the preliminary data set of the AMS-02 collaboration [129], and last, but absolutely not least, the debated anomaly observed in the gamma-ray wavelength at the center of the Galaxy, that we will be discussing extensively in Chapter 3.

In this Chapter we briefly overview some of the salient CR features known at present for what concerns in particular the transport of these high-energy particles in the Galaxy. Then, we present a novel phenomenological model for Galactic CR propagation that takes into account all up-to-date measurements of local CR fluxes and constitutes at the same time a new reference scenario in the field. Indeed, the model we propose is able to provide for the first time a coherent picture of the gamma-ray sky we map today with unprecedented level of precision thanks to the spectacular reconstruction done by the Fermi Large Area Telescope (Fermi-LAT) survey. We close this chapter describing the interesting predictions that our Galactic propagation model features for TeV gamma rays, and discussing in a multi-messenger approach the smoking-gun predictions of the model for high-energy neutrino events morphologically correlated with the Galactic plane.

2.2 A brief overview on Galactic Cosmic-ray Physics

A qualitative picture of what we know at present about CRs is well drawn by the all-particle spectrum displayed in Fig. 2.1, as a joint effort of a multitude of particle detectors mounted on flying balloons or in spacecrafts, and of ground-based experiments as well.

The plot shows in particular the cumulative intensity of all CR species as a function of the kinetic energy per particle. Despite the several orders of magnitudes ranging along the y-axis and the x-axis, the flux is to a first approximation described by a single power law, namely $\sim E^{-3}$. Such a power law description starts to do a good job at energies above $\sim$1 GeV, i.e. when the effects arising from the modulation potential of the Sun start to be less important in our local environment. It goes all the way up to very high energies, $\sim 10^{20}$ eV, that should be considered a high-energy cutoff for a twofold reason, because of the so-called GZK cutoff [130,131] –

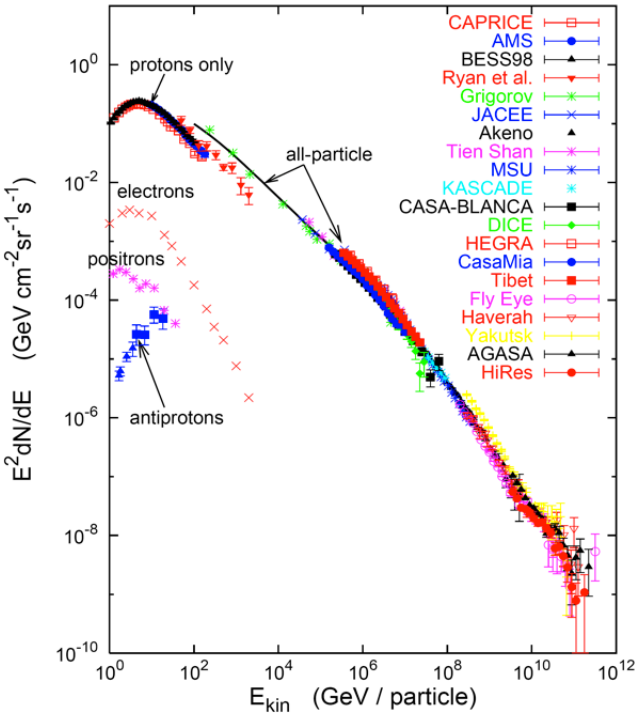

Figure 2.1: *Spectrum of several cosmic-ray species as a function of the kinetic energy per particle. Over a very broad energy interval the flux of the all-particle spectrum falls off approximately proportional to* E^{-3}*. Around* $E \sim 0.5 \times 10^{20}$ *eV an abrupt flux reduction is predicted, the GZK cutoff.*

a theoretical upper limit on the energy of CRs experimentally acknowledged almost a decade ago [132] – and also for the known sources and mechanisms at the basis of CR acceleration. On closer inspection, the all-particle spectrum shows at least two main features: a softening (i.e. a steepening of the spectral index) of the power-law spectrum around 10^{15} eV – the so-called "knee" – and a hardening (i.e. a shallower spectral index) roughly above 5×10^{18} eV – the "ankle", that nowadays we believe to be connected to a change in the cosmic-ray species contribution – not all the species contribute in fact in the same way at a given energy – and even more importantly to a change in the origin of the cosmic-ray population. Looking at Fig. 2.1, it is indeed commonly retained that below the knee CRs are merely of Galactic origin, while above the ankle they are purely extra-Galactic.

A zoom on each species contributing to the all-particle spectrum of Fig. 2.1 teaches us that great part of these high-energy particles corresponds to relativistic protons, while the rest is constituted of heavier nuclei (mostly Helium). It is important to notice that all these particles do not propagate in the vacuum, but in an environment that can provide many back-reactions. So, in the study of CR physics it is of primary importance to characterize all the different components making up

such an environment. For Galactic CRs, the environment polluting CR propagation corresponds to the so-called interstellar medium (ISM) [133]. The ISM can roughly be defined as a relatively dense ($\sim$1 atom per cm^{-3}) material between stars, composed mainly of atomic and molecular Hydrogen, with a smaller percentage $\sim$10% of large grains made of heavier elements. On top of this gas and dust components, the ISM features a notable population of low frequency photons, with typical energy density of $\sim$ eV cm^{-3}, the so-called interstellar radiation field (ISRF), which is made of UV, visible and infrared light components together with the cosmic microwave background (CMB). Moreover, there is a magnetic field permeating the whole Galaxy [134] – i.e. the ISM is magnetized – with a strength of a few μG on average, even though in molecular clouds its value may be order of magnitude larger. As a crucial consequence of that, CR cannot propagate ballistically from their emitting sources, but are subject to the effects of the magnetized medium they travel through, as we are going to discuss in the following.

Interactions with the Galactic ambient components will also lead to important imprints in CR phenomenology. For instance, very high-energy electrons will lose energy mainly in the vicinity of the injection sources through synchrotron radiation, and up-scatter low energy photons from the ISRF. MeV-GeV electrons can eventually radiate energetic photons via bremsstrahlung while traveling in the ionized medium. Relativistic protons, on the other hand, while lose a negligible fraction of energy in the ISM, via radiative emission undergo hadronic proto-reaction with σ_{pp} $\sim$30 mb in a chain e.g. like $p + N \rightarrow X + N + \pi$ (most often $p + p \rightarrow p + p + \pi^0$, $p + p + \pi^0 + \pi^+ + \pi^-$). As we are going to see in the next sections, the presence of pions as final states gives us a diagnostics in favor of both hadronic accelerators and propagation. Indeed, the corresponding pion decay channels, manly

$$\pi^0 \rightarrow \gamma\gamma \quad , \quad \pi^+ \rightarrow \mu^+ \nu_\mu \rightarrow e^+ \, \nu_e \, \bar{\nu}_\mu \, \nu_\mu \ , \tag{2.1}$$

offer to us the unique opportunity of a detailed multi-messenger approach in CR studies through gamma-ray and neutrino observations operated with unprecedented accuracy by current facilities. Finally, from heavier nuclei we have hadronic processes of spallation and/or fragmentation kind: heavier target nuclei can either interact with the ambient field or radioactively decay, producing lighter daughter nuclei as secondary components. The existence of such secondary components on top of primary ones bring us directly to next topic, that is the evidence in favor of CR diffusion in the Galaxy.

2.2.1 Hints for diffusive propagation in the Galaxy

Focussing on CR energies lower than 10^{15} eV, i.e. Galactic CRs, the chemical composition we observe from local CR measurements is very similar to the abundances we can trace back for the elements in the Sun, looking at the absorption lines in the ambient gas. As shown in Fig. 2.2, there is a fair good match between the two sets of abundances that suggests a stellar origin for Galactic CRs.

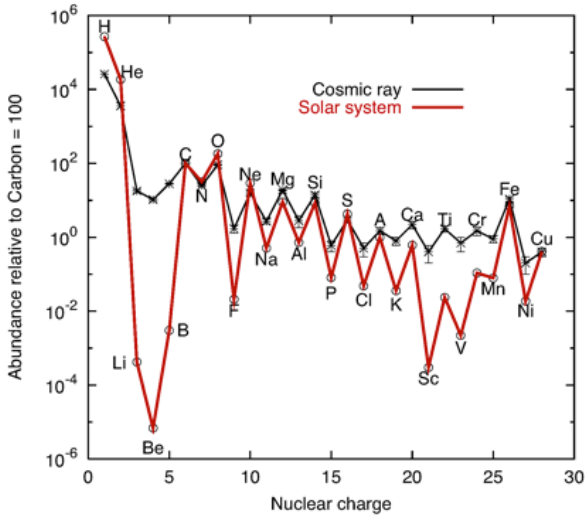

Figure 2.2: *Relative abundances of cosmic-ray species (black line) compared against the Solar system ones (red line).*

However, a closer look at Fig. 2.2 shows some dramatic discrepancies as well. E.g., the enormous enrichment in the CR abundances of Lithium, Beryllium and Boron with respect to the Solar counterparts. Today, we read this mismatch not only as a proof of the interaction of CRs with the ambient components, but also as a strong indirect hint in favor of a diffusive motion of these relativistic particles in the Galaxy. Suppose that the ambient around the Sun is the typical ambient for a star, i.e. the typical ambient which reflects stellar nucleosynthesis. Then, a source is evolving and polluting its environment with its own yields, and, eventually, through some acceleration mechanism injecting these yields out in the interstellar medium as CRs: these species of CR are what we call primary CRs, namely cosmic rays that are synthesized and accelerated in the sources. According to Fig. 2.2, there is however a component that is initially not much present in the sources. This kind of species we dub it a "secondary", since it is supposed to get important contribution along the propagation of the primaries, via their interactions with the ISM. The final result is the more democratic distribution we observe for Galactic CR, represented by the black line in Fig. 2.2.

As we are now going to discuss in some detail, the existence of secondary CRs on

top of primaries support the hypothesis of a diffusive mode for CR propagation. For the purpose, let us introduce the concept of grammage, namely the amount of traversed material by a CR species along its propagation:

$$X \equiv \int d\ell \, \rho_{\rm ISM}(\ell) \ , \tag{2.2}$$

and let us assign to the primary (secondary) species a density n_p (n_s). Introducing the interaction depth $\lambda_{p,s} = m/\sigma_{p,s}$ (neglecting the mismatch in mass between the two species), we can write an equation of evolution for the two densities along the trajectory parametrized by the grammage:

$$\begin{aligned} \frac{dn_p}{dX} &= -\frac{n_p}{\lambda_p} \ , \\ \frac{dn_s}{dX} &= -\frac{n_s}{\lambda_s} + \mathcal{P}_{p\to s}\frac{n_p}{\lambda_p} \ , \end{aligned} \tag{2.3}$$

where in the second line we considered the reaction $p + N \to s + N'$, introducing the probability associated to the secondary production, $\mathcal{P}_{p\to s} \equiv \sigma_{p+\ldots\to s+\ldots}/\sigma_p$. We have obtained a set of two coupled differential equations, whose solution yields the following secondary to primary ratio

$$\frac{n_s}{n_p} = \mathcal{P}_{p\to s}\frac{\lambda_s}{\lambda_s - \lambda_p}\left[\exp\left(-\frac{X}{\lambda_s} + \frac{X}{\lambda_p}\right) - 1\right] \tag{2.4}$$

Looking again at Fig. 2.2, we can now use Eq. (2.4) to study the Li-Be-B cycle of secondaries against the C-N-O cycle of primary species. From nuclear physics [135] we can borrow the estimate of the interaction depth for the two sets of species, $\lambda_{C-N-O} \simeq 6.7$ g/cm^2 and $\lambda_{Li-Be-B} \simeq 10$ g/cm^2, together with the spallation probability $\mathcal{P}_{p\to s} \simeq 0.35$ for energies around the GeV. Taking into account the measurement carried out for local CR observables like B/C we know also that $n_{Li-Be-B}/n_{C-N-O} \simeq 0.2$. So, we are in the position to infer the total grammage related to the conversion of C-N-O into Li-Be-B, that is $X_{p\to s} \simeq 4.3$ g/cm^2.
Now, the estimate of such grammage can be compared with the typical value one would expect from the propagation of CRs in the Galaxy. The disk of the Milky Way (MW) is characterized by a gas density $n_H \sim 1$ cm^{-3}, and it has a thickness of about $h \sim 100$ pc. Now, if CRs would travel ballistically, one would have a primary component that is transversing the thin disk of gas only once, yielding a corresponding grammage of $X_{1\,\rm cross} \sim m_p\, n_H\, h \simeq 10^{-3}$ g/cm^2. This is three orders of magnitude smaller than what needed to correctly match the measured abundance of secondaries over primaries. This result suggests that CRs are likely to cross the Galactic disk multiple times.

As we will try to address in the next paragraph, CR propagation around the disk pretty resembles Brownian motion, due to the random walk triggered by the magnetic irregularities present in the Galactic environment. A lower bound on the timescale associated to the propagation of the primary components through the ISM can be estimated as the number of times the primary species cross the disk times the single crossing time interval, $t_{\rm prop} \gtrsim X_{p\to s}/X_{1\,\rm cross} \times h/c$, yielding roughly $t_{\rm prop} \gtrsim 5 \cdot 10^6$ years. Note that we have derived this as a lower bound since the time that the particle spends only in the thin disk is likely shorter than the Galactic timescale of CR propagation, supposed to be at least an order of magnitude greater. Indeed, the effective propagation region is correlated with the extension of the magnetic field in the Galaxy, usually thought as a magnetized halo of height $\sim 30 - 70\,h$.

2.2.2 Charged particles in magnetic inhomogeneities

As already anticipated, the turbulence glued to the ambient magnetic field is supposed to be at the basis of CR diffusive motion. We expect the influence of the ambient magnetic field on CRs to lead us to an equation of the following kind:

$$\frac{\partial n}{\partial t} + \vec{\nabla} \cdot \vec{\mathcal{J}} = \mathcal{Q} \ , \tag{2.5}$$

where the condition of diffusive regime implies the vector current to be $\vec{\mathcal{J}} = -\vec{\nabla} n$.

In order to derive the diffusion equation of the kind of Eq. (2.5), let us start from the simple study of a charged relativistic particle moving in an environment like our Galaxy, characterized by a regular large scale magnetic field component, $\vec{B} = (0, 0, B)$, on top of which are also present magnetic inhomogeneities, $\delta\vec{B}$. For a particle of charge q and momentum $\vec{p} = m\gamma\vec{v}$, the dynamics is dictated by the Lorenz force:

$$\frac{d\vec{p}}{dt} = q\left[\frac{\vec{v}}{c} \wedge \left(\vec{B} + \delta\vec{B}\right)\right] \ . \tag{2.6}$$

Switching off the irregular component, the particle spirals along the direction of the regular magnetic field and the solution to the equation of motion is simply:

$$\begin{aligned} v_z &= v_\parallel^{(0)} \ , \\ v_x &= v_\perp^{(0)} \cos(\Omega_L t) \ , \\ v_y &= v_\perp^{(0)} \sin(\Omega_L t) \ , \end{aligned} \tag{2.7}$$

where Ω_L corresponds to the Larmor frequency of the paticle, $\Omega_L = q\,B/(mc\gamma)$. If

we now switch on the stochastic fluctuation $\delta\vec{B}$, in the limit where $|\vec{B}| \gg |\delta\vec{B}|$, the so-called quasi-linear approximation, the motion of the particle is sizably affected by this perturbation only along the direction of the regular magnetic field:

$$\frac{dp_{\parallel}}{dt} = p\frac{d\mu}{dt} = q\left(\frac{\vec{v}}{c} \wedge \delta\vec{B}\right) \cdot \hat{p}_{\parallel} \,, \tag{2.8}$$

where $p \equiv |\vec{p}\,|$, which is a constant of motion, and we have introduced for the purpose the pitch angle as $\mu \equiv \cos\left(\hat{p} \wedge \hat{B}\right)$. The perturbation above is intimately related to the effect of the turbulence present in the ISM, manifested by the so-called Alfvén waves, propagating in the intergalactic plasma. These magnetohydrodynamic waves are characterized by a velocity v_A of the order of $\sim B/\sqrt{4\pi\rho_{\rm medium}}$: plugging in the typical value for the Galactic regular magnetic field of order $\sim \mu$G and a reference value for the density of the gas in the ISM, $\sim$cm^{-3}, we estimate v_A to be $\sim 2 \times 10^6$ cm s^{-1}, i.e. Galactic Alfvén waves are non-relativistic. This consideration allows us to undertake the static limit for $\delta\vec{B}$, and write for a single mode k in the rest frame of the waves:

$$\begin{aligned} \delta B_x &= \delta B \, \sin(k\, z + \varphi) \,, \\ \delta B_y &= \delta B \, \cos(k\, z + \varphi) \,, \end{aligned} \tag{2.9}$$

where φ is an arbitrary phase. Exploiting the definition of the pitch angle and inserting Eq. (2.9) into the expression of Eq. (2.8), one gets the master equation for the diffusion in pitch angle:

$$\frac{d\mu}{dt} = \frac{q}{c}\frac{\sqrt{1-\mu^2}}{m\gamma}\delta B \cos\left[(\Omega_L - kv\mu - \varphi)\, t\right] \,, \tag{2.10}$$

where $v\mu$ is the velocity of the particle in the z direction along which particle motion is not influenced by the regular magnetic field component (see Eq. (2.8)). Integrating Eq. (2.10) in time, a small variation $\Delta\mu$ has 0 mean with respect to an average on the random phase ψ. At the same time, the corresponding variance is not vanishing and after a few steps of integration reads as:

$$\langle\frac{\Delta\mu\,\Delta\mu}{\Delta t}\rangle_{\psi} = \frac{q^2(1-\mu^2)}{m^2c^2\gamma^2}(\delta B)^2 \int_{-\Delta t}^{\Delta t} d\tilde{t} \cos\left[(\Omega_L - kv\mu)\,\tilde{t}\right] \,, \tag{2.11}$$

so that for a large time interval Δt the above expression collapses to

$$\langle\frac{\Delta\mu\,\Delta\mu}{\Delta t}\rangle_{\psi} = \pi(1-\mu^2)\Omega_L \left(\frac{\delta B}{B}\right)^2 k_{res}\, \delta\left(k - k_{res}\right) \,, \tag{2.12}$$

where we have defined the resonance wavenumber $k_{res} \equiv \Omega_L/(\mu v) = 1/(\mu\, r_L)$. From Eq. (2.12) we conclude that the variance of the pitch angle is not vanishing when the Alfvén wave mode k is resonating on k_{res}. This result indicates that modes matching the Larmor radius size of the particle are of particular importance. For scales k^{-1} much greater than r_L, the particle spirals around a slightly bended magnetic field with a small gyroradius, "surfing" the perturbation. In the opposite limit, the particle does not see at all the perturbation, spiraling along the direction of the regular magnetic field. In both cases, the particle propagates without experiencing any significant change in the directionality of its motion. When $k^{-1} \sim r_L$, we are instead in a resonant limit where the incoming direction of the particle gets significantly affected by the presence of the ambient magnetic inhomogeneities. Going beyond the single mode study, we have to consider a power spectrum of modes $\mathcal{P}(k) \equiv 8\pi k^2 (\delta B(k)/B)^2$, that after an integration over all the Alfvén wave modes leads to a generalization of Eq. (2.11):

$$\langle \frac{\Delta\mu\, \Delta\mu}{\Delta t} \rangle_\psi = \frac{\pi}{2}(1-\mu^2)\, \Omega_L\, k_{res}\, \mathcal{P}(k_{res}) \ . \tag{2.13}$$

The expression obtained above is intimately related to the definition of the diffusion coefficient in pitch angle, namely

$$D_{\mu\mu} \equiv \frac{1}{2}\langle \frac{\Delta\theta\Delta\theta}{\Delta t} \rangle_\psi = \frac{\pi}{4}\, \Omega_L\, k_{res}\, \mathcal{P}(k_{res}) \ , \tag{2.14}$$

where θ is denoting the angle between the momentum of the particle and the direction of the regular magnetic field.

In the rest frame of the Alfvén waves the diffusion coefficient in Eq. (2.14) characterizes the resonant response of the charged particle to the presence of magnetic inhomogeneities in the medium: the net effect we find is an isotropization of the pitch angle, which happens to be on a timescale $\tau \sim D_{\mu\mu}^{-1}$. This result can be easily translated in the lab frame as a sort of resonant scattering of the charged particle with the Alfvén waves, with an associated scattering length $\lambda \sim (v \pm v_A) \cdot \tau \simeq v \cdot \tau$. By simple dimensional analysis, also in real space the propagation of the particle must be characterized by a (spatial) diffusion coefficient:

$$D_{zz} \equiv \frac{1}{2}\langle \frac{\Delta z \Delta z}{\Delta t} \rangle_\psi \sim \frac{\lambda^2}{\tau} \sim \frac{v^2}{D_{\mu\mu}} \simeq \frac{v^2}{\Omega_L\, k_{res}\, \mathcal{P}(k_{res})} \ . \tag{2.15}$$

We can conclude that the isotropization of the pitch angle in the rest frame of the Alfvén waves is effectively described by a Brownian-like motion of the particle in the lab frame, where the observed spatial diffusion is intimately related to the non-zero variance of the pitch angle, as computed in Eq. (2.13).

2.2.3 The cosmic-ray transport equation

As of now, we have focussed our attention on the motion of a single particle. We can generalize the previous discussion considering now an ensemble of particles described by a phase space distribution function $\mathscr{f}(\vec{x},\vec{p},t)$, and supported by a probability density function $\Psi(\vec{p},\Delta\vec{p})$ related to the transition from momentum $\vec{p}$ to $\vec{p}+\Delta\vec{p}$ due to the interaction with the stochastic fluctuations in the ambient magnetic field. Note that, from detailed balance, the probability density for a transition $\vec{p}\to\vec{p}-\Delta\vec{p}$, represented by $\Psi(\vec{p},-\Delta\vec{p})$, should be equal to $\Psi(\vec{p}-\Delta\vec{p},\Delta\vec{p})$, describing the transition $\vec{p}-\Delta\vec{p}\to\vec{p}$. Implementing the quasi-linear approximation in momentum space, i.e. requiring $|\Delta\vec{p}|/|\vec{p}|\ll 1$, at second order in $|\Delta\vec{p}|$ detailed balance implies:

$$\langle \Delta p_i \rangle_{\Delta\vec{p}} = \frac{1}{2}\sum_j \frac{\partial}{\partial p_j}\langle \Delta p_i \Delta p_j\rangle_{\Delta\vec{p}} \,, \tag{2.16}$$

where $\langle\ldots\rangle_{\Delta\vec{p}}$ involves an average with measure $d\Delta\vec{p}\;\Psi(\vec{p},\Delta\vec{p})$. Exploiting the definition of Ψ, the evolved phase space density in a time lapse Δt must be:

$$\mathscr{f}(\vec{x}+\vec{v}\cdot\Delta t,\vec{p},t+\Delta t) = \int d\Delta\vec{p}\,\Psi(\vec{p}-\Delta\vec{p},\Delta\vec{p})\,\mathscr{f}(\vec{x},\vec{p}-\Delta\vec{p},t) \,, \tag{2.17}$$

where $\vec{v}$ denotes the charged particle velocity in the rest frame of the Alfvén waves. The above expression can be expanded again at second order in $|\Delta\vec{p}|$ according to the quasi-linear approximation. Moreover, we can take the static limit and expand it at linear order for $\Delta t/t\ll 1$ as well. With the help of Eq. (2.16), after simple algebra we get to an evolution equation of the following kind:

$$\frac{\partial \mathscr{f}}{\partial t} + \sum_i v_i \frac{\partial \mathscr{f}}{\partial x_i} = \sum_{j,k}\frac{\partial}{\partial p_j}\left[D_{p_j p_k}\frac{\partial \mathscr{f}}{\partial p_k}\right], \tag{2.18}$$

where we introduced the diffusion coefficient in momentum space as

$$D_{p_i p_j} \equiv \frac{1}{2}\langle \frac{\Delta p_i \Delta p_j}{\Delta t}\rangle_{\Delta\vec{p}} \,. \tag{2.19}$$

Assuming as before $\vec{B} = B\cdot\hat{z}$ and trading the previous average on ψ for an equivalent average on the momentum variation $\Delta\vec{p}$, the diffusion coefficient in the pitch angle is $D_{\mu\mu} = \delta_{iz}\delta_{jz}D_{p_ip_j}/p^2$. Then, isotropization in the pitch angle yields:

$$\frac{\partial \mathscr{f}}{\partial t} + \sum_i v_i \frac{\partial \mathscr{f}}{\partial x_i} = \frac{\partial}{\partial \mu}\left[D_{\mu\mu}\frac{\partial \mathscr{f}}{\partial \mu}\right] \,. \tag{2.20}$$

The expression obtained is a Boltzmann equation: the left-hand side corresponds to the classical Liouville operator acting on $\mathscr{f}$, while the right-hand side is indeed a

sort of collisional operator establishing for ℓ diffusive motion in the pitch angle. Moving to the Galactic rest frame, we can obtain a differential equation for ℓ that closely resembles the structure just derived in the Alfvén wave rest frame [136, 137]:

$$\frac{\partial \ell}{\partial t} + \sum_i u_i \frac{\partial \ell}{\partial x_i} - \frac{1}{3}\left(\vec{\nabla}\cdot\vec{u}\right) p \frac{\partial \ell}{\partial t} = \sum_{j,k} \frac{\partial}{\partial x_j}\left[D_{x_j x_k}\frac{\partial \ell}{\partial x_k}\right] \ . \tag{2.21}$$

Comparing with Eq. (2.20), the drift term in the Liouville operator is now characterized by a velocity $\vec{u}$ which is the result of the sum of the Alfvén wave velocity $\vec{v}_A$ and an overall velocity component associated to the bulk motion of the plasma in the lab frame. Such a term comes together with an adiabatic energy loss term, mainly due to possible convective effects in the Galactic plasma. On the right-hand side, the isotropization in pitch angle is again translated into spatial diffusion, in the same fashion of Eq. (2.15). In particular, taking the propagation of the Alfvén waves to be along the direction of the regular component $\vec{B} = B \cdot \hat{z}$, the following relation between diffusion coefficient in pitch angle and in real space holds [136, 137]:

$$D_{zz} = \frac{v^2}{8}\int_{-1}^{+1} d\mu \frac{(1-\mu^2)^2}{D_{\mu\mu}} \ . \tag{2.22}$$

The transport equation in Eq. (2.21) describes the evolution of Galactic CRs according to a diffusive motion in an environment characterized by a large scale magnetic field and stochastic fluctuations on top of it, possibly supplemented also by non-negligible convective winds. The rich physics of convective-diffusive transport encoded in this theoretical framework can be expanded to take into account other important physical effects for Galactic CRs. The most notable one is probably related to the non-zero velocity $\vec{v}_A$ that magnetic inhomogeneities have in the plasma, resulting in a time-varying magnetic field impacting CR motion as a net acceleration effect, different from the main acceleration of CR injection sources. Such an effect can be shown to yield a diffusion term in momentum space [136, 137]:

$$\frac{1}{p^2}\frac{\partial}{\partial p}\left(p^2 D_{pp}\frac{\partial \ell}{\partial p}\right) \ , \tag{2.23}$$

where $D_{pp} \propto v_A^2 \ p^2/D_{zz}$ [138] for Alfvén waves propagating along the regular magnetic field component. On general grounds, we need to have also a term representative of net energy losses, particularly relevant for CR species like electrons:

$$-\frac{1}{p^2}\frac{\partial}{\partial p}\left[p^2 \frac{dp}{dt}\ell\right] \ , \tag{2.24}$$

where the continuous loss rate dp/dt depends on the kind of process (for instance, synchrotron and inverse Compton rates are $\propto p^2$). In the end, an evolution equation for CRs must feature also a source term, $q(\vec{x}, \vec{p}, t)$, capturing the CR injection mechanism of the species, and a loss term, denoted here simply as $-\not{f}/\tau_{loss}$, to take into account the loss of the species due to possible spallation processes and/or radiative decays [139].
Eventually, we can write such a generalized transport equation for Galactic CR propagation in terms of the particle density per unit of momentum and volume [140]:

$$\begin{aligned} \frac{\partial \mathcal{N}}{\partial t} &+ \vec{\nabla} \cdot (\vec{u}\,\mathcal{N}) - \frac{1}{3}\frac{\partial}{\partial p}\left[p\left(\vec{\nabla}\cdot\vec{u}\right)\mathcal{N}\right] - \vec{\nabla}\cdot\left(D_{\vec{x}\vec{x}}\vec{\nabla}\mathcal{N}\right) \\ &- \frac{\partial}{\partial p}\left[p^2 D_{pp}\frac{\partial}{\partial p}\left(\frac{\mathcal{N}}{p^2}\right)\right] + \frac{\partial}{\partial p}\left(\frac{dp}{dt}\mathcal{N}\right) = \mathcal{Q} - \frac{\mathcal{N}}{\tau_{loss}} \,, \end{aligned} \tag{2.25}$$

where by definiton $\mathcal{N} \equiv p^2 \int d\Omega_{\vec{p}}\, \not{f}(\vec{x}, \vec{p}, t)$ and $\mathcal{Q} \equiv p^2 \int d\Omega_{\vec{p}}\, q(\vec{x}, \vec{p}, t)$.

A solution of Eq. (2.25) generally requires a detailed numerical study. Several dedicated codes for the purpose are available in the literature [141–146]. However, it is illustrative to discuss some simplified version of Eq. (2.25) that provides useful physical insights. For instance, we can trade the spatial diffusion operator for an effective time of confinement and treat the whole Galaxy as a sort of box, in which CRs are randomly walking up to the point where they hit one of the box boundaries and consequently they leak out. In this simple framework, we can get an estimate of the typical time of CR diffusion in the Galaxy. Such a drastic simplification of Eq. (2.25) is the so-called leaky box approximation, that allows us to write:

$$\frac{\partial \mathcal{N}}{\partial t} + \frac{\mathcal{N}}{\tau_{diff}(p)} = \mathcal{Q}(p) \,, \tag{2.26}$$

assuming we are in a regime of pure diffusion. If we further assume that equilibrium has been reached between the injected CRs and the ones escaping from the box, we can neglect time dependence in $\mathcal{N}$, i.e. we can work in the steady state limit, and trivially solve Eq. (2.26):

$$\mathcal{N} = \mathcal{Q}(p)\,\tau_{diff}(p) \,. \tag{2.27}$$

Since the number density of a secondary component will be sourced by the primary one, the secondaries over primaries ratio can be easily predicted to be:

$$\mathcal{N}_s = \mathcal{Q}_s\,\tau_{diff} \propto \mathcal{N}_p\,\tau_{diff} \;\Rightarrow\; \frac{\mathcal{N}_s}{\mathcal{N}_p} \propto \tau_{diff} \,. \tag{2.28}$$

From Eq. (2.28) we conclude that the relative abundance of secondaries over

primaries probes the timescale for confinement of CRs in the Galaxy, or equivalently the spatial diffusion coefficient in the CR transport equation, Eq. (2.26), since by dimensional analysis $\tau_{diff} \sim H^2/D$, where H captures the typical size of the box. On physical grounds, particles with greater rigidities should escape more easily from the Galaxy given their greater Larmor radius: this suggests that the spatial diffusion coefficient must be a monotonic increasing function of rigidity. Supplementing Eq.(2.28) with such expectation, we have a theoretical prediction that nicely fits the trend of available experimental data: at energies above few GeV, data points of local CR observables like B/C show indeed a power-law behavior decreasing with increasing kinetic energy per nucleon (see e.g. Fig. 2.6 and the discussion below). Taking the diffusion coefficient to be a power-law in rigidity, $D(R) = D_0 (R/3 \text{ GV})^{\delta}$, – an ansatz supported on the theory side by analytical approaches to magnetohydrodynamics turbulence [137] – state-of-the-art measurements of this observable points to $\delta \simeq 0.5$, with a normalization $D_0 \simeq 10^{28}$ cm^2 s^{-1}. The sort of flattening we can instead observe in B/C data at lower energies stems from the fact that diffusion stops to be the dominant effect, and other timescales reasonably come into the game, e.g. the one associated to the presence of convective winds, $\tau_{cov} \sim H/u$, and/or also the one related to momentum dependent re-acceleration effects, $\tau_{re-acc}(p) \sim p^2/D_{pp}$.

Doing such a "clock setting" using different indicators is, of course, an opportunity we would not want to miss: according to Fig. 2.2, different patterns of secondaries over primaries allow to check out the same CR transport properties. At present, measurements of CR transport properties from heavier elements are affected by larger error bars than those in B/C data, but they will likely improve in the forthcoming years thanks to the operating AMS-02 magnetic spectrometer. Remarkably, we have other kind of secondaries at our disposal, namely the ones corresponding to antimatter CR species. Notable examples of this kind are antiprotons, a component in local CRs that is roughly at the level of 10^{-4} compared to the measured proton flux, mainly originating from the inelastic collision of primary protons with the ISM according to the reaction $p + H \rightarrow \bar{p} + 3p$. Such inelastic scattering see antiproton production kinematically disfavored at low kinetic energies, while an expected peak at production falls around $E_{\bar{p}} \simeq 1$ GeV. While these features are nicely reproduced by data, the local $\bar{p}$ over p ratio does not really feature at high energies the expected depletion due to the CR diffusive regime, but is rather compatible with a flat $\bar{p}/p$ flux [129] While such a trend still falls withi the several uncertainties plaguing the theoretical prediction [147, 148], next high-energy measures of this observable may provide a clearer indirect evidence of some exotica injecting antiprotons in our local environment.

A slightly different discussion is required for positrons, the other interesting kind of antimatter we can locally observe. Indeed, high-energy leptons feature large energy losses, which imply a new timescale competing with the diffusion one. The transport equation governing $e^{\pm}$ propagation is of the kind

$$\frac{\partial \mathcal{N}}{\partial t} - D\,\Delta\mathcal{N} - \frac{\partial}{\partial p}\left(\frac{dp}{dt}\mathcal{N}\right) = \mathcal{Q} \tag{2.29}$$

where inverse Compton scattering on the photon background and synchrotron radiation define the typical timescale for energy losses, $\tau_{E_{loss}}(p) \sim p/|dp/dt| \propto p^{-1}$. The solution of Eq. (2.29) is given by a Green function that boils down to:

$$\mathcal{N} \simeq \frac{\mathcal{Q}(p)\,\tau_{E_{loss}}}{\sqrt{D(p)\,\tau_{E_{loss}}}}\ . \tag{2.30}$$

For primary electrons this result implies a scaling $\mathcal{N} \propto \mathrm{p}^{\alpha_e - \frac{\delta}{2} - \frac{1}{2}}$, where $\alpha_{\rm CR}$ is the spectral index of the injected CR species. On the other hand, positrons in the Galaxy are believed to originate as a secondary component arising from the collisions of relativistic protons with the ISM gas according to a chain like $p + H \to \ldots \to \pi^{\pm} \to \mu^{\pm} + \ldots \to e^{\pm} + \ldots$. The source function of positrons is then expected to scale as:

$$\mathcal{Q}_{e^+} \propto \mathcal{N}_p\, n_H\, \sigma_{p\to e^+} \propto \mathcal{Q}_p\, \tau_{diff} \propto p^{-\alpha_p - \delta}, \tag{2.31}$$

where we have implemented the rather simplistic approximation of an energy independent cross section $\sigma_{p\to e^+}$, and used the fact that the relevant timescale for propagation of high-energy protons is the diffusion timescale, and defined α_p the spectral index for the proton injection source function. Plugging this result in Eq. (2.31), we can predict the scaling of the propagated positron flux over the electron one:

$$\frac{\mathcal{N}_{e^+}}{\mathcal{N}_{e^-}} \propto p^{-\alpha_p + \alpha_e - \delta}\ , \tag{2.32}$$

with α_e the spectral index at injection for the electron source distribution. In the hypothesis that CR primaries are accelerated in the same kind of environment, the injected spectral index should not differ much going from one species to another. Consequently, the ratio of secondary positrons over primary electrons is predicted to scale down in the same way as for the B/C case, probing in a similar fashion local CR diffusion. The rise at high energy in the positron fraction originally detected by PAMELA in 2009 [127], and subsequently confirmed by Fermi-LAT [149] and AMS collaborations [150], constitutes a substantial deviation from the prediction of Eq. (2.32). While the origin of this anomaly generated an exciting brainstorming

in the DM community (see e.g. [151, 152]), this observation can be reasonably correlated to the local effects of a nearby primary e^+ source [153, 154], maybe a pulsar [155], since its environment is generally characterized by high-energy outflows of electromagnetic radiation in a highly magnetized medium, leaving room for copious $e^\pm$ pair production in the Galaxy [156].

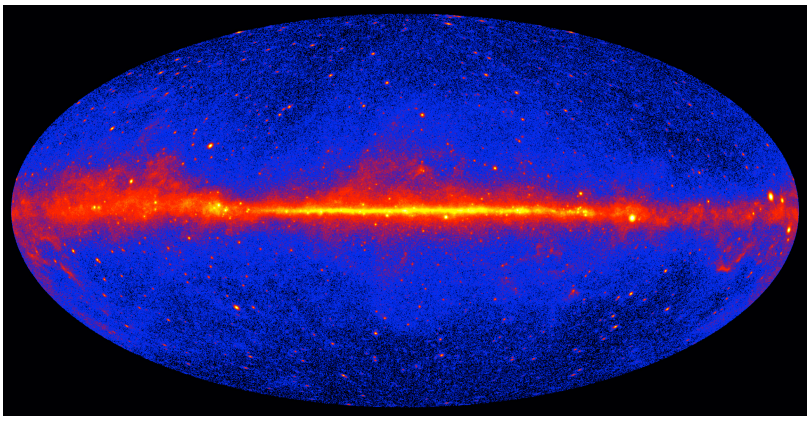

Figure 2.3: *Full-sky image at energies greater than 1 GeV based on five years of data from the LAT instrument on NASA's Fermi Gamma-ray Space Telescope. Brighter colors indicate brighter gamma-ray sources. Image Credit: NASA/DOE/Fermi-LAT collaboration.*

So far, we restricted our discussion of the physics encoded in Eq. (2.25) on the basis of local CR observables. As anticipated at the beginning of this section, today we can observe the Galaxy shining in the gamma-ray band, as displayed in the beautiful picture of Fig 2.3, thanks to the photon count mapping by the Fermi-LAT experiment. Since 2008 Fermi-LAT has been surveying the gamma-ray sky between about few hundred MeV and few hundred GeV with unprecedented sensitivity and resolution. The corresponding detailed picture of the Galaxy provided to us represents a unique opportunity to probe our current knowledge of CR propagation in the ISM. Indeed, the bulk of photons detected by Fermi-LAT is expected to be associated with diffuse emission from the MW, due to by Galactic CRs interacting with the ISM gas and the ISRF photons via production and decay of π^0s, inverse Compton, and bremsstrahlung. Consequently, the study of the gamma-ray sky offers a novel diagnostics of CR transport, allowing us to test what we have learnt so far from local CR measurements and eventually to go beyond: as we are going to discuss in detail in what follows, the global characterization of CR transport in the whole Galaxy may indeed differ from the one extrapolated from our local environment.

2.3 Gamma-ray diagnostics of cosmic-ray transport

As hinted by the large photon flux along the Galactic plane in Fig 2.3, there is a striking consistency between general features in the diffuse gamma-ray maps and the diffuse gamma-ray flux models. Predictions mainly rely, on the side concerning emitting targets, on (indirectly) measured gas column densities and ISRF models, while, on the side of incident particles, on propagation models tuned to reproduce locally measured fluxes.
When addressing at a quantitive level the quality of such match between predictions and data, most analyses have mainly developed optimized models looping over uncertainties on the emitting targets. In particular, in Ref. [157] the authors – besides allowing for a radially-dependent rescaling of the ISRF and different values of the spin temperature of the 21 cm transition (used to trace the atomic Hydrogen component in the ISM) – adopt a tuning of the poorly known conversion factor between the observed CO emissivities and the molecular hydrogen column densities, usually dubbed X_{CO}. In Ref. [157] it is shown that such approach is sufficient to generate models in agreement with the data within about 15% in most regions of the sky. A remarkable exception is the fact that this procedure tends to systematically underestimate the measured flux above few GeV in the Galactic plane region, most notably towards the inner Galaxy.

Fig. 2.4 shows the spectrum for the gamma-ray flux measured by the Fermi-LAT in the energy range between 300 MeV and 100 GeV and a large angular window encompassing the inner Galactic plane (5 years of data, within the event class `ULTRACLEAN` according to Fermi tools `v9r32p5`, as described in [158]). The yellow band corresponds to the point sources (PS) modeled using the 2-years Fermi-LAT Point Source Catalogue via a dedicated Monte Carlo (MC) code that looped over the uncertainties on the spectral energy characterization of each source. The brown line is the contribution of the extra-Galactic gamma-ray background (EGB) obtained by a full-sky fit of the data for $|b| > 20°$. The double dot-dashed line and gray triangles are, respectively, the prediction and residuals for the Fermi benchmark model, labelled ${}^{S}S^{Z}4^{R}20^{T}150^{C}5$ (FB hereafter), selected for Fig. 17 in Ref. [157], and reproduced here using the `GALPROP` WebRun [144, 145]: while the model is optimized at low energy, it gives a poorer description of the data at high energy, a feature that is generic for all models proposed in that analysis.

The selected angular window is interesting because the diffuse emission from the inner Galactic plane is potentially a precious source of information for CR transport modeling. Being the region with largest gas column densities, it is the brightest zone of the sky and, unlike other regions where the interplay among components allows

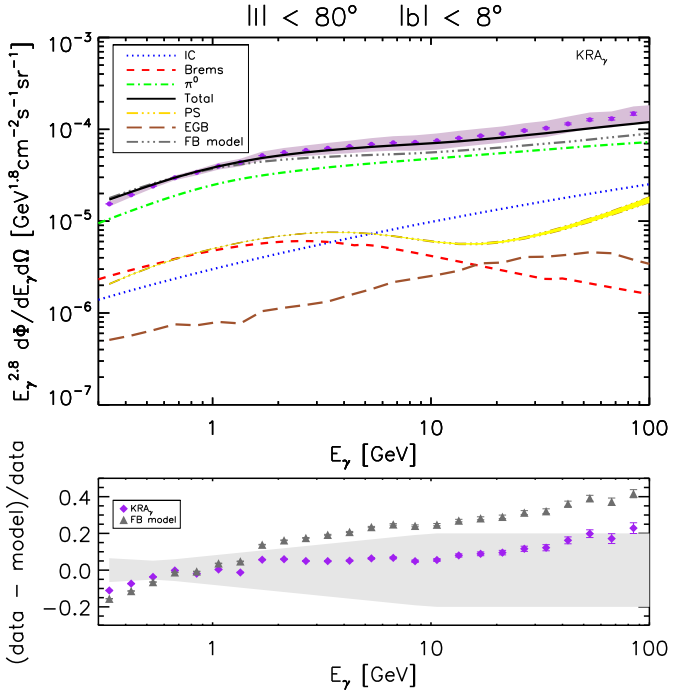

Figure 2.4: Upper Panel: *Comparison between the gamma-ray flux computed with the CR propagation model proposed (KRA_γ total flux: solid black line; individual components shown) and the Fermi-LAT data (purple dots, including both statistic and systematic errors) in the Galactic disk. For comparison, we also show the total flux for the FB model defined in Ref. [157] (double dot-dashed gray line).* Lower Panel: *Residuals computed for the KRA_γ and FB models.*

more modeling freedom, its flux is predominantly shaped by only one contribution, namely the π^0 decays of Eq. (2.1), especially when looking at intermediate energies. The π^0 emissivity spectral index is roughly equal to the incident proton one [159], hence the inner Galactic plane allows an indirect measurement of the CR proton slope towards the center of the Galaxy, far away from the region where direct measurements are available. This aspect is seldom emphasized, since the standard approach consists in solving the propagation equation for CR species under the assumption that diffusive properties of CRs are the same in the whole propagation volume. This implies reducing the spatial diffusion tensor in Eq. (2.25) to a single constant diffusion coefficient $D(R) = D_0(R/R_0)^\delta$, whose scaling δ on rigidity R and normalization D_0 are constrained by local CR data (a range between about $\delta = 0.3$ and about $\delta = 0.85$ is allowed [160–162]). Such hypothesis freezes the proton spectral index – and therefore the π^0 spectral index – to be very close to the local one everywhere in the CR propagation region. For this reason, in Fig. 2.4 and in the following, the gamma-ray flux is multiplied by $E_\gamma^{2.8}$, since

$\alpha = 2.820 \pm 0.003\,(\text{stat}) \pm 0.005\,(\text{sys})$ is the proton index measured by the PAMELA experiment in the range 30 GV–1.2 TV [163], in agreement with recent updates from AMS-02 [129]. The FB model gives a slightly rising curve since it assumes $\alpha = 2.72$.

These considerations motivate us to go beyond standard approaches to diffusion in CR transport, using as a guideline the Fermi-LAT gamma-ray data.

As previously derived, the diffusion term stems from a macroscopic effective description of the microscopic interplay between CRs and the magnetohydrodynamics turbulence. In the framework of quasi-linear theory (QLT), δ is related to the turbulence power spectrum introduced in Eq. (2.13) (well-studied regimes correspond to $\delta = 1/3$, i.e. Kolmogorov-like turbulence and $\delta = 1/2$, namely Kraichnan-like turbulence, see e.g. Ref. [137]). As we have seen, QLT is based on the assumption that the turbulent component of the magnetic field is subdominant compared to the regular one. Such hypothesis does not seem to be supported by most recent models for the Galactic magnetic field [134, 164]. Studies based on non-linear theory approaches, on the other hand, find more involved environmental dependencies, resulting in different scalings in different regions of the Galaxy, and deviations from a single power law in rigidity [165, 166]. Eventually, an additional element to take into account is the possibility that CRs themselves generate the turbulent spectrum responsible for their propagation [167], introducing local self-adjustments in propagation. Given this set of arguments, in the following we propose CR transport models phenomenologically based on Eq. (2.25) with a diffusion coefficient characterized by a spatially variable $\delta(r)$, highlighting how they naturally improve the description of gamma-ray data.

2.3.1 Gamma-ray-driven preliminaries

In order to follow a data-driven approach, we first of all quantify the change of the gamma-ray slope along the Galactic disk and estimate the resulting discrepancy between the FB model and the actual data. We report in Table A.1 the power-law index obtained by fitting the Fermi-LAT gamma-ray data in the energy window $E_\gamma = [5 - 50]$ GeV, and in the second row of Table 2.2 the χ^2 of the FB model.

Crucially, we observe the power-law index to range from $E_\gamma^{-2.47}$ to $E_\gamma^{-2.60}$, thus resulting in a gamma-ray flux much harder than the prediction of the FB model, especially in the central windows. We can conclude that these data, taken as a guideline, show a hint of a slope change with l. Note that while in the innermost windows one may be reasonably tempted to translate the measured spectral index as the one associated to π^0 emission only, in the outermost windows considered

in Table A.1 the gamma-ray emission has on top of the π^0 emission a sizable contribution from point sources and Inverse Compton emission.

sky window ($\|b\| < 5°$)	α ($\Phi \sim E_\gamma^{-\alpha}$)	sky window ($\|b\| < 5°$)	α ($\Phi \sim E_\gamma^{-\alpha}$)
$0° < \|l\| < 10°$	2.55 ± 0.09	$40° < \|l\| < 50°$	2.57 ± 0.09
$10° < \|l\| < 20°$	2.49 ± 0.09	$50° < \|l\| < 60°$	2.56 ± 0.09
$20° < \|l\| < 30°$	2.47 ± 0.08	$60° < \|l\| < 70°$	2.60 ± 0.09
$30° < \|l\| < 40°$	2.57 ± 0.08	$70° < \|l\| < 80°$	2.52 ± 0.09

Table 2.1: *Energy slope of Fermi-LAT gamma-ray data on the Galactic disk. The power-law index has been obtained by fitting the data in the energy window $E_\gamma = [5 - 50]$ GeV. We average in latitude over the angular interval $|b| < 5°$.*

Turning our attention to the quality of the fit, the FB model is worse in the innermost windows (e.g. $|l| < 10°$ and $20° < |l| < 30°$, with $|b| < 5°$), it improves going towards outer longitudinal values ($50° < |l| < 60°$, with $|b| < 5°$), but remains poor considering in average the whole Galactic disk ($|l| < 80°$, with $|b| < 5°$).

χ^2 values (25 data points)	$0° < \|l\| < 80°$ $0° < \|b\| < 8°$	$0° < \|l\| < 10°$ $0° < \|b\| < 5°$	$20° < \|l\| < 30°$ $0° < \|b\| < 5°$
χ^2 KRA$_\gamma$	11.30	3.79	12.27
χ^2 FB model	53.00	74.83	70.04
	$50° < \|l\| < 60°$ $0° < \|b\| < 5°$	$0° < \|l\| < 180°$ $10° < \|b\| < 20°$	- -
χ^2 KRA$_\gamma$	11.50	6.94	-
χ^2 FB model	24.85	17.60	-

Table 2.2: *Results of the χ^2 analysis for the fit of the Fermi-LAT gamma-ray data. For each angular window considered, we provide a comparison of the performance for the case of the Fermi-LAT benchmark and for the one of the novel model here proposed.*

In order to have a deeper understanding of the discrepancy, it is important to trace, for each line of sight (l.o.s.), which portion of the Galaxy the emission comes from. For this reason, in Fig. 2.5 we plot the relative contribution to the total π^0 emission for three reference l.o.s. as a function of the Galactocentric distance, r. At large values of the Galactic longitude l (where the FB model performs better in reproducing the gamma-ray data) the emission is dominated by the local environment; instead, the closer to the center we look, the wider the relevant region gets, with the central rings contributing as much as 20% for the Galactic center window (where the FB fit gets worse and data turn out to be significantly harder).

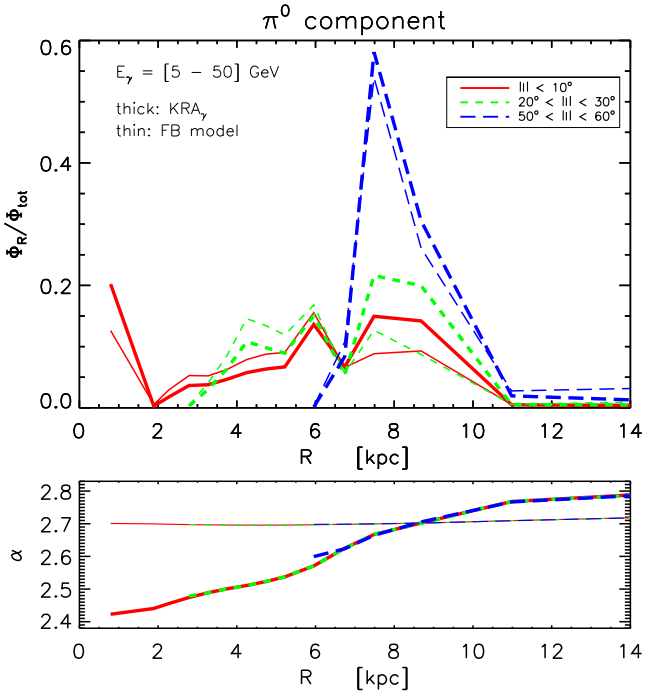

Figure 2.5: *Relative contribution (upper panel), and power-law spectral index of the π^0 emission (lower panel, with scaling $\sim E_\gamma^{-\alpha}$) for three reference l.o.s. as a function of the radial distance from the Galactic center. The FB (KRA$_\gamma$) model corresponds to thinner (thicker) lines. We average in latitude over the interval $|b| < 5°$.*

In the lower panel of Fig. 2.5, we show the power-law spectral index of the π^0 component as a function of r: as expected, for the FB model we find a constant value equal to the measured local proton spectral index.

Driven by these results, we argue that the FB model should be corrected in such a way to get a significantly harder propagated proton index for smaller values of r, while still matching local CR observations. We stress again that, in the sky windows where the emission is mostly local (at high longitude or high latitude), and the contribution of IC and point sources to total emission is relevant, we never observe a gamma-ray slope equal to the local π^0 slope.

2.3.2 A novel phenomenological model

We propose a propagation model based on the following three ingredients:

i) Bearing in mind the motivations outlined above, we drop the oversimplified assumption of constant diffusion, and we open up to the possibility that the slope of the diffusion coefficient δ is a function of the Galactocentric distance.

ii) We allow for position-dependent convective effects. The presence of a significant convective wind in an inner region of the Galaxy is indeed motivated by the X-ray observations by the ROSAT satellite [168], and may affect cosmic-ray propagation [169].

iii) We consider the X_{CO} profile, related to the conversion between measured CO emissivities and HII column densities, to get larger values in the outer part of the Galaxy. This hypothesis stems from the existence of a gradient in metallicity across the Milky Way [170]. The metallicity is a result of stellar and Galactic chemical evolution: it is higher towards the Galactic center, and decreases going outwards. Since lower metallicities imply less dust shielding [171], it is conceivable to expect larger values of X_{CO} in outer regions of the Galaxy.

For the purpose, we have solved E. (2.25) for each CR species phenomenologically relevant for our analysis, implementing the above listed ingredients in the numerical package `DRAGON` [141, 143]. Then, we have computed the diffuse gamma-ray maps through another dedicated code, `GammaSky`, used recently e.g. in [172–174], which exploits the gamma-ray emissivities reported in Ref. [174] and it is nicely interfaced with the output provided by `DRAGON`.

As a starting point, we consider the Kraichnan diffusion model defined in Ref. [175] (labeled KRA therein).[1] As a first step, we modify δ introducing a functional dependence on r: the simplest – a posteriori – sufficient guess, turns out to be

$$\delta(r) = A\, r + B \ , \tag{2.33}$$

with local normalization $\delta(r_\odot) = 0.5$, and – to avoid unrealistically large values – frozen at given radius $r_{\rm max}$, $\delta(r > r_{\rm max}) = \delta(r = r_{\rm max})$. For $r_{\rm max} > r_\odot$, the choice of $r_{\rm max}$ does not impact on the gamma-ray diffuse emission (the gas density drops off in the outermost regions of the MW), and CR local observables show also a weak dependence on it. Consequently, we safely set $r_{\rm max}$ to the nominal value of 11 kpc, The free parameter A is fixed by fitting the gamma-ray data in the energy range $E_\gamma = [5 - 50]$ GeV. To this purpose, we have analyzed the Galactic disk $|b| < 5°$, $|l| < 80°$ in eight longitudinal windows of 10° each.

The energy spectra we obtain from this procedure correctly reproduce the measured slope in all the studied sky windows but overshoot the data at low energies, in particular at small longitudes. To tame this problem, in the inner region with $r < r_{\rm w}$, we allow for a strong convective wind with uniform gradient in the z-

[1] We checked that the same conclusions can be reached starting from the Kolmogorov and thick-halo diffusion models also defined in [175].

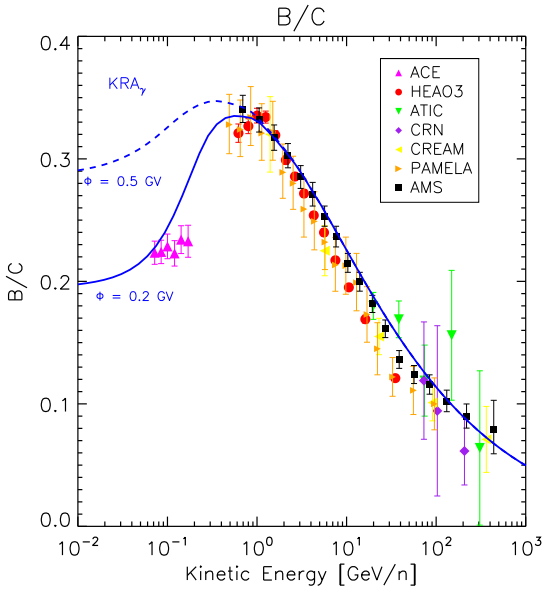

Figure 2.6: *Comparison between the local B/C ratio in the KRA$_\gamma$ model and the corresponding experimental data. We show two different values for the Solar modulation potential,* 500 *MV (dashed line) and* 200 *MV (solid line). Data points refer to different experiments: ACE [176], HEAO-3 [177], ATIC [178], CRN [179], CREAM [180], PAMELA [181] and AMS [182].*

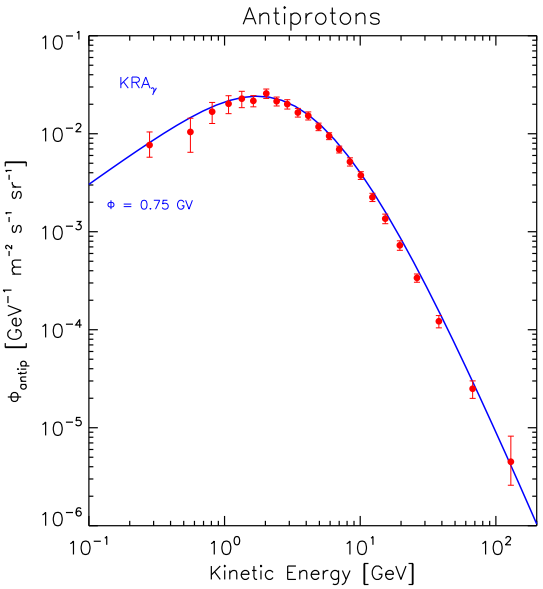

Figure 2.7: *Comparison between the local antiproton flux in the KRA$_\gamma$ model and the corresponding PAMELA data [183]. We use a fixed Solar modulation potential of* 750 *MV.*

direction. We extract r_w and the intensity of the convective gradient by fitting the low-energy data with $E_\gamma < 1$ GeV. Concerning the molecular hydrogen, we assume – in units of 10^{20} cm^{-2} K^{-1} km^{-1} s – $X_{CO} = 1.9$ at $r < 7.5$ kpc, and $X_{CO} = 5$ at $r > 7.5$ kpc, in order to correctly match the normalization of the observed flux for Galactic longitudes roughly greater than 50°.

The last step of our method consists in verifying a posteriori that the corrections described above do not spoil the prediction for local observables: we find that just a small tuning in the value of the normalization of the diffusion coefficient D_0 and in the source spectral index α_p are needed for the purpose. In Fig. 2.6 we show the model prediction against the data of the local diffusion indicator B/C, while in Fig. 2.7 it is displayed the comparison with data for the antiproton flux. More precisely, we compared against the measured fluxes of proton, Helium and heavier nuclei (up to Fe), leptons, and ^{10}Be/^{9}Be . Concerning the Beryllium ratio, the compatibility between the observational evidence of strong winds in the inner Galaxy and the constraints from the radioactive isotopes may be a problem (see e.g. [169]). Nevertheless, in our case the Galactic wind is not present locally and therefore we have a satisfactory agreement with data also for this CR observable.

All in all, we report the following nominal values for the parameters described above: $A = 0.035$ kpc^{-1}, $r_w = 6.5$ kpc, $du/dz = 100$ km s^{-1} kpc^{-1}, $D_0 = 2.24 \times 10^{28}$ cm^{2}s^{-1}, $\alpha = 2.35$. The model also features a vertical dependence of the diffusion coefficient, $D(z) \propto \exp(z/z_t)$, where the halo size z_t is conventionally set to be 4 kpc. We have labeled this model KRA$_\gamma$.

2.3.3 Looking at different patches of the sky

We show in Fig. 2.4, 2.8, and 2.9, the gamma-ray spectra for the KRA$_\gamma$ model in three relevant sky windows: the Galactic disk, a small window focused on the Galactic center, and the mid-latitude strip with $|l| < 180°$, $10° < |b| < 20°$.

In Fig. 2.10 we show the longitudinal profile. We remark that the model is not optimized for high longitudes ($|l| > 100°$), where the observed gamma-ray radial emissivity seems to fall less fast than the observed radial distribution of sources and gas, that hence lead to a much steeper prediction [185]. This is the so-called "gradient problem": this discrepancy can be reabsorbed either by a rescaling of the π^0 component, motivated by the possible presence of neutral gas not traced by HI and CO emission lines [186], or by a position-dependent normalization of the diffusion coefficient [173], or an altered source term [187] with respect to the one adopted in our study [133].

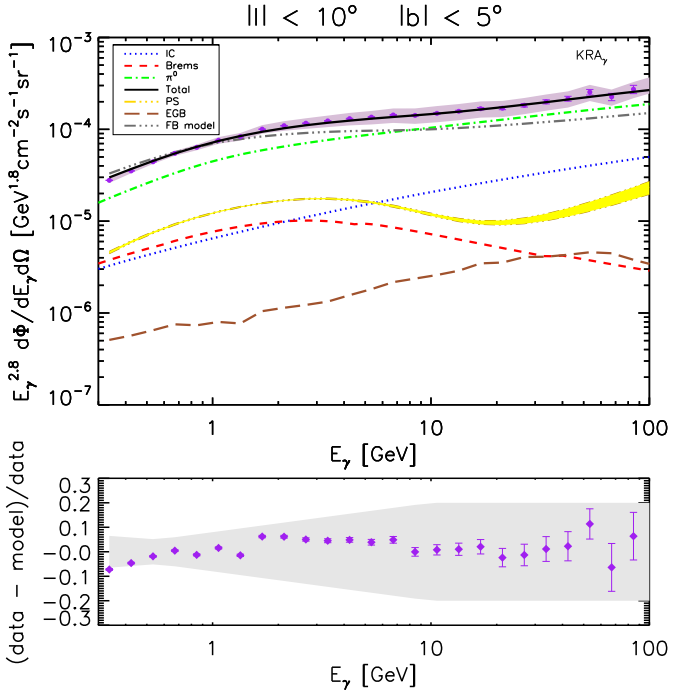

Figure 2.8: *The same as in Fig. 2.4 but considering the angular window $|l| < 10°$, $|b| < 5°$.*

In table 2.2 we list the χ^2 for our optimized model, showing a remarkable improvement with respect to the FB model.

There are alternative scenarios which have been proposed to account for tilted gamma-ray fluxes, see e.g. [157, 188–190]. Regarding some of these, however, we would like to remark here that:

- following Ref. [191], we find that a population of unresolved pulsars, with the same properties of e.g. the observed Fermi-LAT ones, gives an extra contribution to the total gamma-ray flux more than one order of magnitude smaller than needed;
- running a dedicated MC code where an analytical solution of the diffusion equation with proper boundary conditions is implemented, as described in [192], we simulate Supernova explosions with a reasonable rate $\simeq 3$/century distributed according to the source term presented in [133]. Fitting each realization with a power-law ansatz, we find that fluctuations in the proton spectrum due to the stochasticity of the sources never exceed – even in the inner Galactic region – the few percent level;
- testing the possibility of an enhanced IC emission, we find that a rescaling of the ISRF by one order of magnitude, together with a factor of 10 decrease

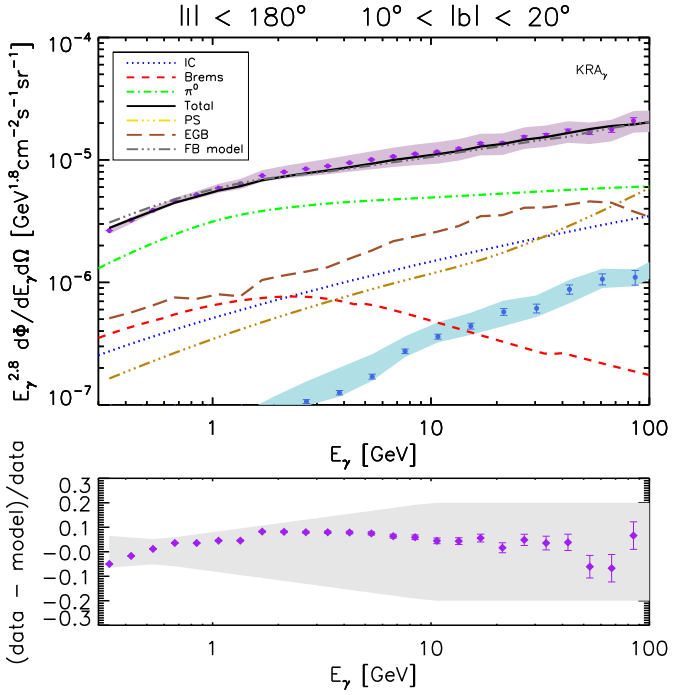

Figure 2.9: *The same as in Fig. 2.4 but considering the strip $|l| < 180°$, $10° < |b| < 20°$. The azure band represents the contribution of the Fermi bubbles according to Ref. [184].*

in the X_{CO}, may solve the discrepancy; however, in this case the bulk of the gamma-ray flux would have a leptonic origin, in contrast with the observed correlation with the gas distribution as shown in Fig. 2.10.

We can conclude this section remarking that a solution to the problem of modeling the gamma-ray emissivity in the Galaxy leads to a new perspective where properties of CR diffusion change through the Galaxy. While locally detected secondary species as the Boron, generally used to tune the relevant propagation parameters, are produced only within few kpc from the Earth and hence do not probe the conditions in the central region of the Galaxy, secondary gamma-rays, produced by the interaction of CR nuclei (electrons) with the interstellar gas (radiation), can actually offer a deeper insight of Galactic CR transport. Moreover, it is conceivable that CR diffusion – due to a stronger star forming activity and peculiar magnetic field strength/geometry – behaves differently in the inner Galactic region. For instance, the behavior of $\delta(r)$ envisaged in Eq. (2.33) may be connected to a smooth transition between a dominant parallel escape along the poloidal component of the regular Galactic magnetic field [134] present in the innermost part of the Galaxy (where δ is supposed to be smaller) and a perpendicular escape to the regular component in the outer regions of the MW (where the scaling of the diffusion

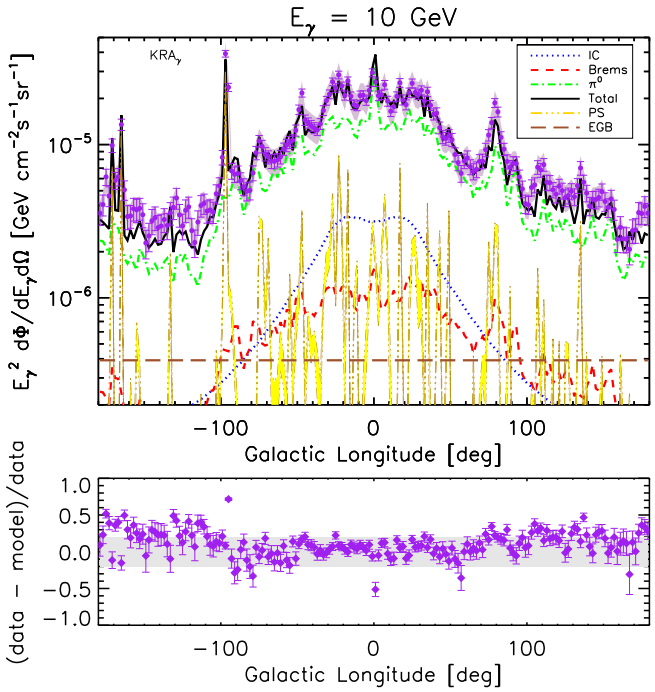

Figure 2.10: *KRA$_\gamma$ longitudinal profile at fixed energy $E_\gamma = 10$ GeV. We have averaged in latitude over the angular interval $|b| < 5°$.*

coefficient results to be steeper). The model introduced here – the KRA$_\gamma$ – is obtained without relying on tunings of astrophysical ingredients such as the ISM gas distribution, the X_{CO} conversion factor, the source distribution or the ISRF, in contrast to the set of models studied e.g. in [157]. At the same time, the KRA$_\gamma$ keeps track of the locally measured CR spectra, performing an overall good agreement with local CR data as well.

2.3.4 Predictions of the model at the TeV scale

The diffuse emission traced by Fermi-LAT along the Galactic plane is not the only puzzling observation in the gamma-ray band for standard propagation models. Interestingly, conventional CR models cannot explain the large gamma-ray flux measured by the Milagro observatory from the inner Galactic plane region ($|b| < 2°$, $30° < l < 65°$) at 15 TeV median energy [193, 194]. In particular, conventional models tuned to reproduce Fermi-LAT data [157] – such as the FB model previously introduced and conveniently re-labelled here KRA (it features a constant $\delta = 0.5$) – seem to fail in the match of the Milagro measurement, as displayed in Fig. 2.12.

The Milagro anomaly is an open issue also for the CR models that try to go beyond the standard lore. Optimized models in the inverse Compton component,

see Ref. [195], accounting for the EGRET GeV excess [185] and accounting also for reproducing the Milagro result as well, are now ruled out by Fermi-LAT [196]. The challenge of this observation still holds also for the recent CR models in [197], which consider the PAMELA hardening in CR proton and Helium fluxes [198] as a result of the Galactic CR acceleration mechanism.

In this respect, it is certainly interesting to see how non-standard diffusion models as the KRA$_\gamma$ behave in the angular window and energy bin of the Milagro excess.

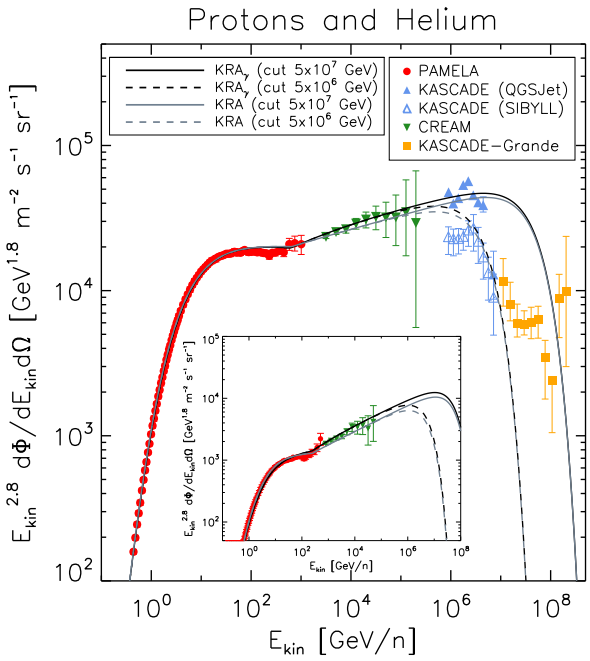

Figure 2.11: *The computed proton and Helium (in the insert) spectra at the Solar circle predicted by KRA and KRA$_\gamma$ models as described in the text. Predictions are compared against a representative set of experimental data [198–201]. All spectra account for Solar modulation with a potential of 0.5 GV.*

In order to do so, given the energy scale we are now considering, it is important to assess in the analysis the effect of p and He spectral hardening inferred from PAMELA [198] – recently confirmed by AMS-02 [206] – and CREAM [199] data above ∼250 GeV/n. We consider in the following the two possibilities:

1) a local hardening originating from nearby supernova remnants (see e.g. [207]), namely a stochastic effect that averages out on large scales and, hence, has no counterpart in the Galactic CR population used in this work;

2) a global hardening originating from a spectral feature in the rigidity dependence of either CR source spectra or the diffusion coefficient (here we only consider the former case, as both scenarios have the same effect on the

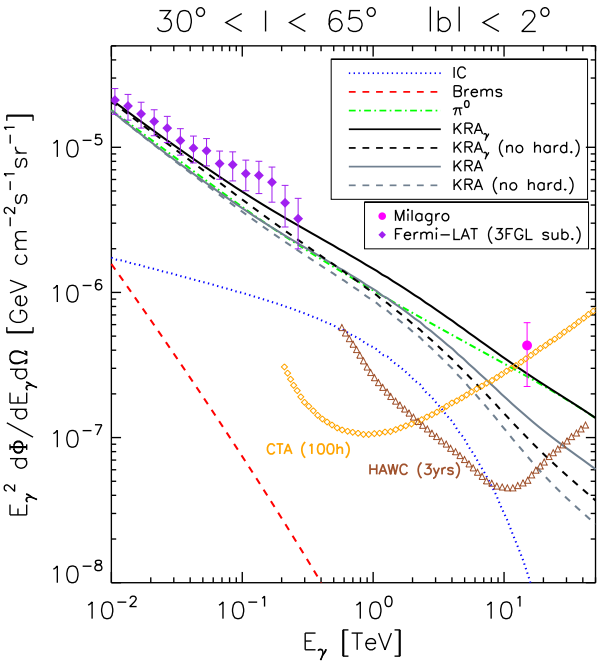

Figure 2.12: *Diffuse emission gamma-ray spectrum from the inner Galactic plane (|b|<2°, 30°< l <65°) computed for the reference models discussed in the text. Predictions are compared with Fermi-LAT and Milagro data. The Milagro differential flux reported here is 17% lower with respect to the flux reported in 2008 [194] due to the assumption of a spectral index of 2.4 instead of 2.7 [202]. The expected sensitivities of HAWC [203] and CTA [204] are reported. The spectral components are shown for the KRA$_\gamma$ model only. The Fermi-LAT data points refer to 5 years of data, within the event class ULTRACLEAN, according to Fermi tools* `v9r32p5`*, as described in [158]. Point sources taken from the 3FGL Point Source Catalogue were subtracted from the data [205].*

gamma-ray diffuse emission).

In both cases we assume that above 250 GeV/n the CR source spectra extend steadily up to an exponential cutoff at the energy E_{cut}/nucleon. As shown in Fig. 2.11, we have decided to consider two representative values of this quantity, namely E_{cut} = 5 and 50 PeV in order to match CREAM p and He data and to roughly bracket KASCADE [200] and KASCADE-Grande [201] high-energy proton data at the same time. Spectra of heavier nuclei in the PeV region are actually not very much informative given the large experimental uncertainties on their elemental spectral shapes and normalizations.

Exploiting once again the `DRAGON` and `GammaSky` packages, we compute the gamma-ray emissivities according to [174], taking also into account the energy dependence of the pp inelastic cross section, which is significant at the TeV scale [159]. We

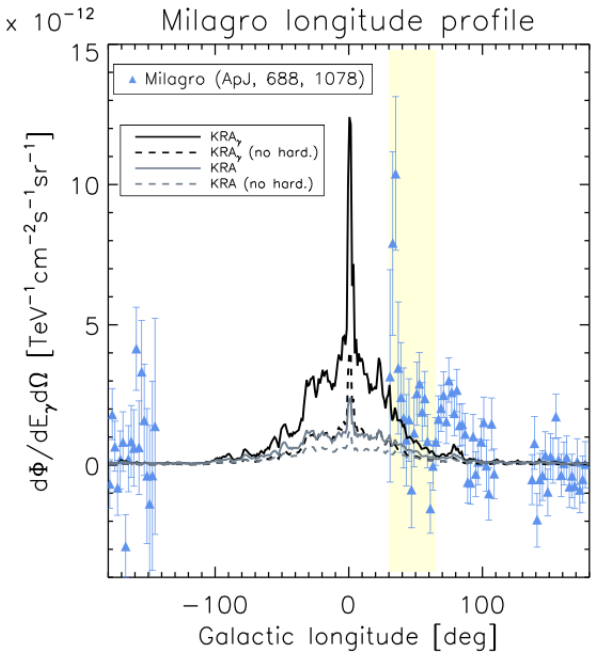

Figure 2.13: *Longitude profile at 15 TeV for the reference models discussed in the text compared with Milagro data. We have averaged in latitude over the angular interval of* $|b| < 2°$.

disregard in the computation the effect of gamma-ray opacity due to the ISRF, since it is supposed to be negligible up to a few tens of TeV [208].

Our results are shown in Fig. 2.12. As mentioned in the above, a representative conventional model, namely the KRA, cannot account for the flux measured by Milagro from the inner Galactic plane at 15 TeV even including the CR spectral hardening required to match the PAMELA and CREAM data. The KRA_γ setup, instead, is evidently successful, especially when a global hardening is assumed.

In Fig. 2.13 we also compare our results with the longitude profile at 15 TeV measured by Milagro. Although the data do not allow any strong claim, we can notice a mild better match of the KRA_γ model with data in the region highlighted by the light-yellow vertical band.
We can conclusively state that the prediction of the KRA_γ in the TeV region of Milagro is a remarkable result since:

- it supports the model in a higher-energy regime, providing the first consistent interpretation of Milagro and Fermi-LAT measurements;
- it reinforces the arguments in favor of a non-local origin of the hardening in the CR spectra above 250 GeV.

Another intriguing discrepancy present in the predictions of conventional CR models stems from the measurement performed by the H.E.S.S. collaboration in

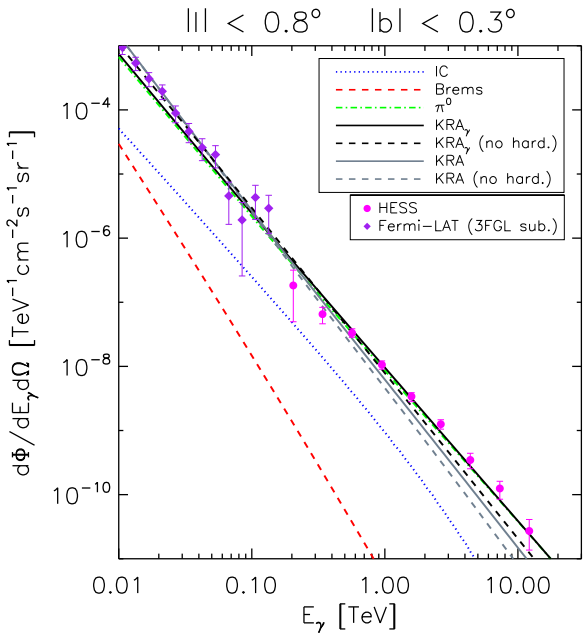

Figure 2.14: *The computed gamma-ray diffuse emission from the Galactic ridge region is compared with Fermi-LAT and H.E.S.S. data. For each model the spectrum normalization has been varied to minimize the residuals against the data. While the related reduced χ^2 for the KRA is 3.99 (2.92) with (without) hardening, the KRA$_\gamma$ with (without) hardening yields 1.79 (2.27). The spectral components are shown for the best-fit KRA$_\gamma$ model only.*

the innermost part of the Galactic ridge region ($|l| < 0.8°$, $|b| < 0.3°$) [209]. The diffuse spectrum measured by H.E.S.S. for $0.3 \lesssim E_\gamma \lesssim 10$ TeV in that region is well described by a power law $E_\gamma^{-\alpha}$ with index $\alpha = 2.29 \pm 0.07 \pm 0.20$. This is significantly harder than what expected from π^0 decays if a CR spectral shape identical to that found in the Solar neighborhood is assumed around the Galactic center. Since the emission is spatially correlated with a complex of giant molecular clouds in the central 200 pc of the MW, the authors in [209] suggest the hardness of the observed spectrum to be connected to freshly accelerated CRs from a local source in that region. Indeed, local CR accelerators are reasonably expected to be found in the rich environment around the Galactic center and the same past activity of Sagittarius A* may have played an important role, as recently noticed in [210]. However, if one can assume that the CR diffuse sea is smooth at scales of $\mathcal{O}(10^2)$ pc and that it does not exhibit strong fluctuations on such small scales, it is compelling to see if the H.E.S.S. hardening may be related instead to the transport properties of CRs in the steady state limit.

Interestingly, the predicted CR density and gamma-ray diffuse emission at 1 - 10 TeV is appreciably larger in the KRA$_\gamma$ scenarios than in conventional models,

especially in the inner few degree from the Galactic center, where the gas column density is larger. Adopting the detailed gas distribution of Ref [211] for the ISM in the inner Galaxy, we show in Fig. 2.14 the prediction of the KRA_γ compared to H.E.S.S. data on the Galactic ridge region. For the purpose we have rescaled the nominal prediction of the KRA_γ models by a factor of 0.3 in order to minimize the residuals against the H.E.S.S. data together with Fermi-LAT ones above 10 GeV. This factor can be actually justified by the smaller value of the conversion factor X_{CO} expected in the central region of the MW [211]. From the residuals reported in Fig. 2.14 we can conclude that the KRA_γ prediction offers an interesting alternative explanation of H.E.S.S. observation. This result supports again the hypothesis of global hardening in CR primary spectra, already envisaged by our study of the Milagro excess.

2.4 Picking up multi-messenger opportunities: predictions for the Galactic neutrinos

As we have already observed in Eq. (2.1), among the yields of the interaction of high-energy protons with the ISM there is a copious production of neutral and charged pions: as a result of their decays, we expect a relevant production of secondary high-energy photons as well as of neutrinos. Given their weak interaction with the environment, neutrinos are the ideal cosmic-ray species we may look for: as in the case of photons, their propagation keeps track of the directionality towards the origin of emission, but differently from gamma rays it is not affected by any absorption. Indeed, the interaction with the background light is negligible even for ultra-high-energy neutrinos. Clearly, a very small interaction cross-section, namely $\sigma(\text{TeV - PeV}) \sim$ pb - npb, has also the net drawback of a particularly challenging experimental detection.

In the most recent years, a tremendous effort on the experimental side allowed us to open the era of high-energy neutrino astronomy. Today, we have eventually at our disposal gigantic detectors like the IceCube experiment [212]: being currently the largest neutrino observatory in the world, placed at the South Pole, it deploys a set of photo-multiplier strings deep in the ice, forming a structure able to cover an effective volume of the size of a cubic kilometer. At the end of 2013, IceCube collaboration announced the detection of 28 neutrinos of extraterrestrial origin in the 30 TeV - 1 PeV energy range [213, 214]. An year after 9 more events were reported, with the highest energy event at $E_\nu \simeq 2$ PeV, reinforcing the evidence of an excess with respect to the expected atmospheric background (estimated by

experiment via dedicated Monte Carlo showering analyses) up to 5.7σ [215]. The inferred flavor composition, compatible with an equal mixture of electronic, muonic and tauonic neutrinos, is also expected if their origin were astrophysical [216, 217]. More recently, a preliminary analysis based on four years of data has risen the total number of high-energy starting events (HESE) to 54 [218], establishing at more than 6 σ of confidence level the extraterrestrial nature.

The astrophysical spectrum inferred by IceCube on the basis on the three-year data set is fitted by a power law with index $\alpha = -2.3 \pm 0.3$ above 60 TeV [215], while the preliminary four-year data analysis favors a slightly steeper spectrum, $\alpha = -2.58 \pm 0.25$ [218]. Although a statistically significant departure from isotropy cannot be claimed yet, the recent analysis in Ref. [219] shows that the angular distribution of HESE allows up to 50% of the full-sky astrophysical flux to have a Galactic origin (see Fig. 2.17 below). Moreover, a hint of a harder spectrum in the Northern Hemisphere may be found in the recent study of the collaboration on the muon neutrino events coming from the Northern sky [220].

Although the origin of this radiation is still unclear, the discovery has triggered many different studies proposing several types of extra-Galactic sources, see e.g. [221–223]. The possibility of a sizable contribution of Galactic origin is also compelling, within the uncertainties on the angular reconstruction of the HESE. However, freshly accelerated CRs from Galactic sources, undergoing hadronic scattering with gas clumps, cannot explain the steepness of the neutrino spectrum measured by IceCube and are in tension with Fermi-LAT upper limit on the correlated gamma-ray emission [224]. On the other hand, if the local CR spectrum is assumed to be representative of the entire Galactic population, the predicted neutrino spectrum [225, 226] derived from hadronic interactions between Galactic CR sea and ISM is significantly lower than the one measured by IceCube. Under the conventional assumption that the same CR transport properties hold throughout the whole Galaxy, only between 4% - 8% of the HESE can be typically accounted [197].

The results derived in the previous section showed that the hadronic emission computed with the KRA$_\gamma$ setup above the TeV is significantly enhanced with respect to the conventional model predictions. Then, it is certainly interesting to see how this reflects in the high-energy neutrino channel and how the corresponding prediction compares against the recent data from IceCube. To compute ν_e and ν_μ production spectra we use the emissivities provided in [174] for projectile energies below $\sim$ 500 TeV, while we adopt the emissivities provided in [159] when above that energy value. We account for neutrino oscillations considering the effect of an almost equally redistribution in the composition among the three flavors [227]. We only consider proton and Helium CRs/gas, since heavier nuclear species give a

negligible contribution in the energy range of interest [228].

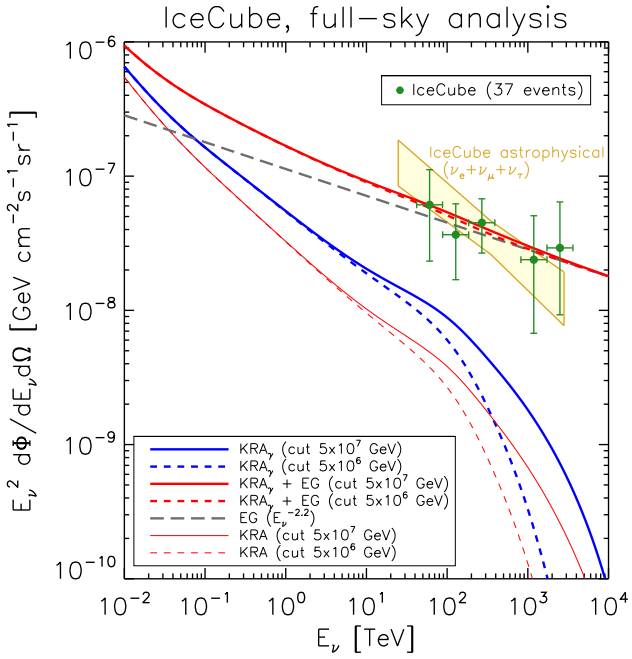

Figure 2.15: *Full-sky neutrino spectrum (all flavors, both neutrinos and antineutrinos) predicted by the KRA$_\gamma$ and KRA models (with global CR hardening), adopting two different choices for the CR high-energy cutoff. We also plot the combination of the Galactic (KRA$_\gamma$) and a benchmark extra-Galactic spectrum. The extra-Galactic flux is consistent with that inferred from IceCube collaboration in the northern hemisphere [220]. The models are compared with the 68% confidence region for IceCube astrophysical neutrino flux obtained with a maximum-likelihood (yellow region) [219] and the three years HESE (green points) [215].*

In Fig. 2.15 we present the full-sky total neutrino spectrum (all flavors, including antiparticles) computed for the KRA$_\gamma$ and KRA models with global CR hardening, and compare it to IceCube results. Our prediction for CR conventional setups (KRA model) is in good agreement with Ref. [197], where the benchmark Galactic model accounts for 8% of the flux measured by IceCube above 60 TeV, for a CR spectrum similar to the one used here above 50 PeV. On the other hand, the KRA$_\gamma$ predicts a neutrino full-sky spectrum two times larger above 10 TeV: the model prediction is consequently only 4 times smaller than the best-fit of the astrophysical flux measured by IceCube on the whole sky. We remark that another analysis [230], based on an extrapolation of Fermi-LAT data, points toward a non-negligible Galactic contribution to the full-sky neutrino flux due to a hard diffuse CR spectrum. In that study the authors address the (softer) locally observed

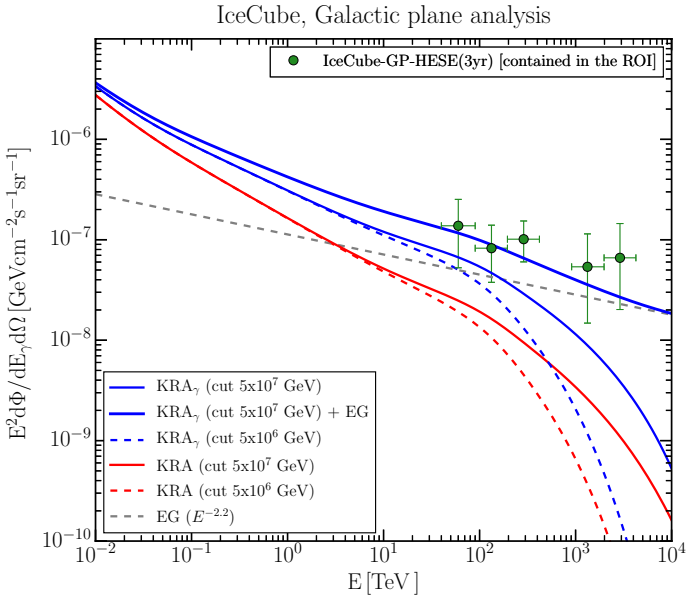

Figure 2.16: *Neutrino spectrum (all flavors, both neutrinos and antineutrinos) in the angular window $|l| < 180°$, $|b| < 7.5°$ predicted by the KRA$_\gamma$ and KRA models (with global CR hardening), adopting two different choices for the CR high-energy cutoff. We also plot the combination of the Galactic (KRA$_\gamma$) and the extra-Galactic spectrum inferred from [220]. The spectral data points are derived from IceCube spectral measurements reported in [215]. Following the guideline in Ref. [229], data points have been properly normalized in order to consider the neutrino events reconstructed inside the region of interest (ROI).*

CR spectrum to the effect of one or more local sources. Differently from our model, such a scenario still has to be validated against Fermi-LAT data. Setting a threshold energy at 60 TeV and convolving the KRA$_\gamma$ spectrum (with $E_{cut} = 50$ PeV) with IceCube HESE effective areas [214], the expected number of neutrino events in three years of IceCube observation represents roughly 15% of the published sample [215]. These rates are well above those expected due to atmospheric muons and atmospheric neutrinos at those energies and confirm the spectral comparison between KRA$_\gamma$ and IceCube data.

From Fig. 2.15 we can clearly see that another component – most likely of extra-Galactic origin – needs to be invoked in order to account for all of IceCube events. Here we assume this component to be isotropic and use the astrophysical muon neutrino IceCube measurements from the Northern Hemisphere [220] – where the Galactic emission should be roughly an order of magnitude smaller than the total flux – to probe its spectral properties. Although the Northern spectral slope is statistically compatible with the full-sky one, given the hint of a steeper spectrum

in the Southern Hemisphere, it is interesting to check if the combination of our Galactic prediction and the extra-Galactic flux inferred from the aforementioned muon neutrino measurement provide a better agreement with the data. For illustrative purposes, in Fig. 2.15 we show the effect of adding an isotropic extra-Galactic emission to the Galactic neutrino emission computed with the KRA_γ model, with a spectrum given by IceCube best-fit of $\Phi^{\mathrm{North}}_{\nu_\mu}$ [220] multiplied by three to account for all flavors. As already said, the nature of such emission is still under debate: as pointed out e.g. in [231] and [232], neither blazars nor star-forming galaxies can provide more than a subdominant contribution, given the constraints imposed by the gamma-ray extra-Galactic background inferred from Fermi-LAT data. The plot in Fig. 2.15 shows how the KRA_γ is contributing to the IceCube full-sky spectrum together with the assumed extra-Galactic component.

If we now focus the analysis on the Galactic plane region, we expect neutrinos in the Galactic emission to be maximal there, as also suggested by the brighter red strip in the right panel of Fig. 2.17 below. Interestingly, if we assume the same extra-Galactic flux inferred from Ref. [220], the neutrino spectrum measured by IceCube in the window of the Galactic plane can only be explained within the KRA_γ scenario, as displayed in Fig. 2.16. An enhanced extra-Galactic component is required instead when we consider the prediction of conventional models.

2.4.1 A smoking-gun region: the inner Galactic plane

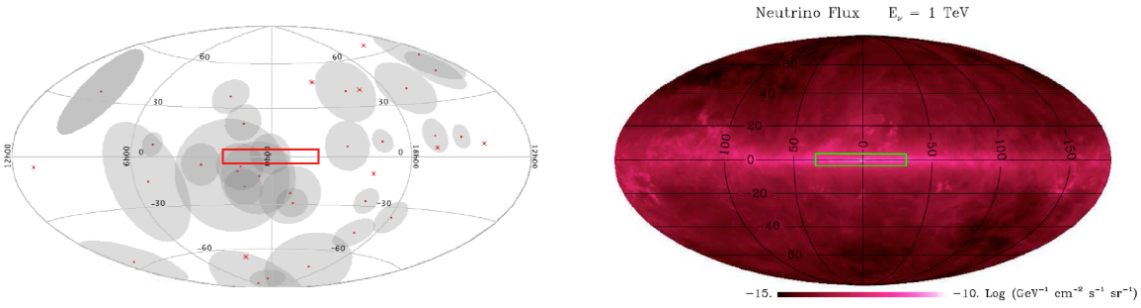

Figure 2.17: Left panel: *The cosmic neutrino sky-map obtained with 3 years of IceCube data. Red cross: Track- like events. Red dots: Shower-like events. The gray surfaces indicate the estimated angular uncertainties for each of these 37 events. Only 3 of these events can be associated to the region $|l| < 30^\circ$ and $|b| < 4^\circ$, highlighted in red.* Right panel: *The sky-map of neutrino events obtained with KRA_γ at 1 TeV (the shape does not change significantly at larger energies). The same inner region is highlighted by the green box.*

Given the interesting result we got for the prediction of the Galactic emission of neutrinos in Fig. 2.16, it is worth further exploring the inner Galactic plane region with the study of the Galactic "ridge", namely on the inner Galactic plane window defined by $|l| < 30°$ and $|b| < 4°$. Indeed, most of the events expected in this region of interest should likely correspond to Galactic secondary neutrinos. Remarkably, there is a set of three shower-like events in the IceCube HESE sample potentially correlated with this patch of the sky, as highlighted in the left panel of Fig. 2.17. Moreover, current and incoming Mediterranean telescopes, given their position, are particularly suitable for a dedicated study of the Galactic ridge. Recently, the ANTARES collaboration [233] has released an upper limit on the muon neutrino flux based on the result of an unblinding analysis regarding the events collected between 2007 and 2013 in the energy range 3 - 300 TeV [234].

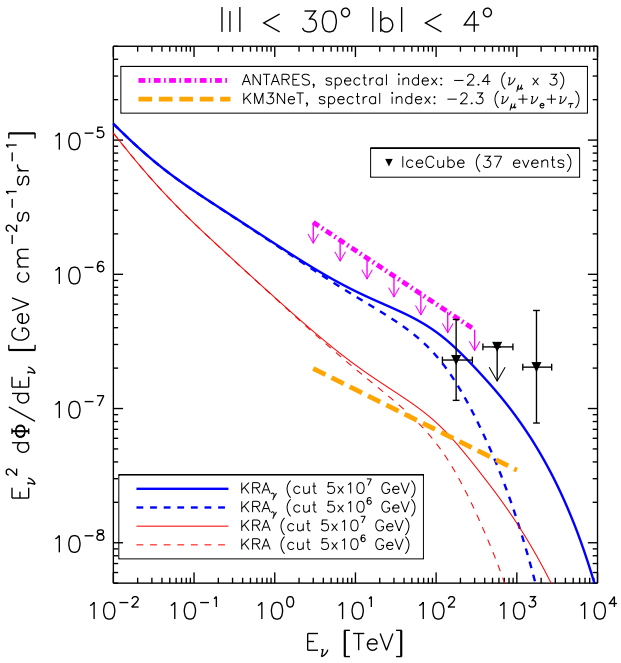

Figure 2.18: *Solid and dashed red (blue) lines: expected neutrino spectra (all flavors, both neutrinos and antineutrinos) in the inner Galactic plane region computed for the KRA (KRA$_\gamma$) models for two different cutoff values. We also show the maximal flux, estimated considering three years of IceCube HESE as described in [229], the constraint from the ANTARES experiment [234, 235] (1500 days of experiment livetime between 2007 and 2013) as well as the deduced sensitivity of the future Mediterranean observatory KM3NeT [236, 237] with four years (∼ 1500 days) of livetime.*

In Fig. 2.18 we compare the ν_μ flux computed in the KRA and KRA$_\gamma$ scenarios against a set of three distinct experimental informations. First, we can observe that

the prediction of KRA_γ is in good agreement with the maximal flux inferred from the fraction of IceCube HESE sample, whose angular reconstruction is compatible with the Galactic ridge. We can note that there is a large enhancement (almost a factor of 5 at 100 TeV) in the neutrino flux obtained with the KRA_γ model with respect to the one of a conventional scenario. This implies that the expected flux from conventional CR models may require very long times of observation even by future telescopes such as the KM3NeT observatory [237], while the prediction of the KRA_γ model is well above the sensitivity of four years of KM3NeT data taking. We wish to emphasize how the KRA_γ neutrino flux is already close to the recent upper limit set by ANTARES. Collecting more statistics, the experiment has room for further improvements in sensitivity before the end of the current year [234] and hence there may be good odds for an exciting detection.

2.5 Confirmations and perspectives

The existence of radial gradients in CR transport, supported by the interplay between what we can measure in the local neighborhood of the Solar system and what we can indirectly infer in the Galaxy with multi-messenger and multi-wavelength searches, triggered the interest of several recent studies in the community.

Most notably, a new characterization of the diffuse Galactic gamma-ray emissivity has been singled out by the Fermi-LAT collaboration in [238]. Exploiting the spatial correlation between the gamma-ray data and a linear combination of maps for the interstellar gas column density, organized in several Galactocentric annuli, and inverse Compton emission produced in the Galaxy, the Fermi-LAT collaboration has been able to estimate the intensity of the Galactic diffuse components with a direct fit to the gamma-ray data rather than through the computation of secondaries from an assumed set of CR densities and production cross-sections. A similar template-fitting methodology has been also applied in [239], yielding to analogous conclusions about the characterization of the diffuse components.

Remarkably, while the measured gas emissivity spectra confirmed that the cosmic-ray proton density decreases with Galactocentric distance beyond 5 kpc from the Galactic center, a softening of the proton spectrum with Galactocentric distance has also been found. As ultimately discussed in [240], these findings represent a challenge for standard calculations of CR propagation based on assuming a uniform diffusion coefficient within the Galactic volume. They may be also an indication for non-linear CR propagation, in which transport is due to particle scattering and advection off self-generated turbulence. Interestingly, the effects of self-generated

diffusion may be also at the basis of a viable explanation to the PAMELA hardening of CR proton and Helium spectra [167].

The evidence for a gradual spectral softening while moving outward from the center of the Galaxy to its outskirts is an important confirmation of the effect phenomenologically captured by us in Eq. (2.33), promoting the scaling of the diffusion coefficient with rigidity to be spatially dependent. The successful validation made by Fermi-LAT of our new proposal for CR transport is reported in Fig. 2.19.

Future measurements from next-generation gamma-ray surveys will be able to further probe our understanding of the intimate connection between CR transport and the observed gamma-ray sky. For instance, as displayed in Fig. 2.12, the future sensitivity of CTA [204] and HAWC [203] will definitely shed new lights on the impact of non-standard CR diffusion in the very high-energy gamma-ray band.

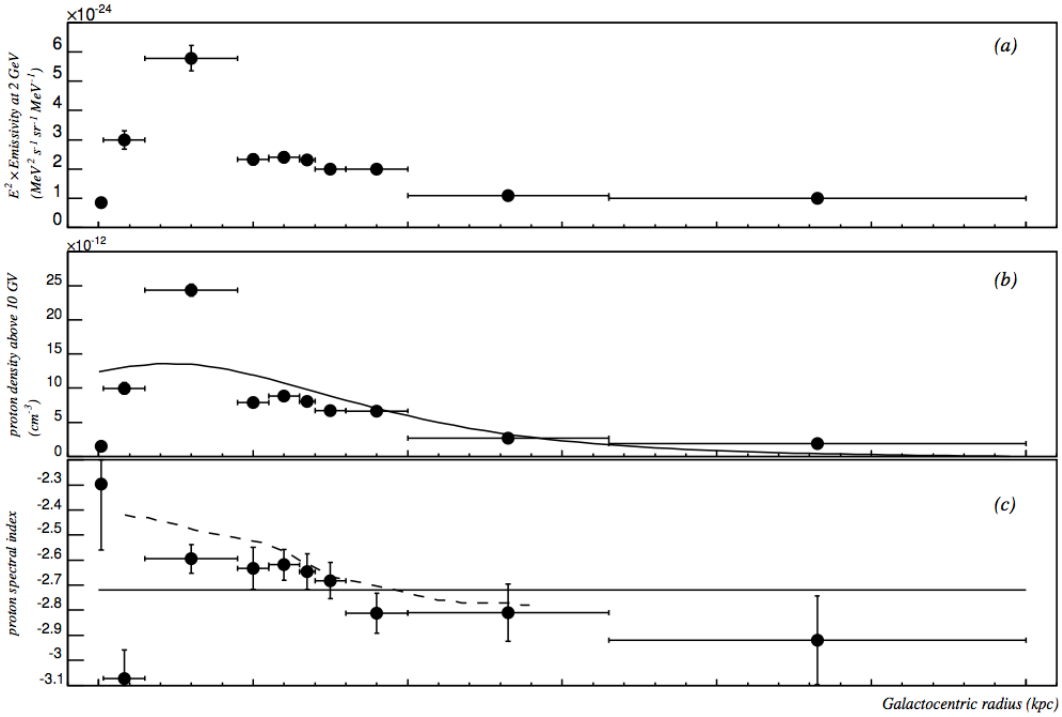

Figure 2.19: *Radial distributions across the Galaxy from Ref. [238] of (a) the gamma-ray emissivity per H atom measured at 2 GeV; (b) the proton flux integrated above 10 GV, with the prediction from CR conventional models [157]; (c) the proton spectral index with statistical error bars and the prediction for proton rigidities above 1 TV from the same conventional models (solid line) and from the KRA$_\gamma$ model (dashed line). In all plots, the horizontal bars span the radial widths of the gas annuli used for the measurements. The two data points with smallest Galactocentric radii have large systematic uncertainties [238].*

From this perspective, the recently opened era of neutrino astronomy we are now living in is even more precious. As highlighted by Fig. 2.18, the joint observational effort of experiments like IceCube and ANTARES, and of incoming ones like KM3NeT, may constitute a unique opportunity to push forward our knowledge about the essential ingredients on the Galactic CR diffusive motion. On more general grounds, the study of the neutrino sky certainly offers a complementary way to the picture of the Galaxy we are able to draw in detail with current observations in the gamma-ray band, and may represent at the same a new important particle discovery tool for the scientific community [241].

Chapter 3
3 The GC GeV gamma-ray excess

3.1 A gamma-ray excess around the Galactic center

As we have extensively discussed in Chapter 2, there is a quite remarkable agreement between models for the diffuse gamma-ray emission in the Galaxy and data from the all-sky survey from the Fermi Large Area Telescope (Fermi-LAT). A fairly good match [157] is obtained in most regions of the sky implementing only minor readjustments to a standard recipe [242] based on:

i) supernova remnants (SNRs) as cosmic-ray (CR) sources;

ii) the steady-state propagation of CRs in the Galaxy as tuned on local CR measurements;

iii) gamma-ray emitting targets, namely the gas of the interstellar medium (ISM) and the interstellar radiation field (ISRF), as indirectly derived from observations at other wavelengths.

According to what we have illustrated in the previous chapter, a notable exception to the successes of this framework is a systematic underestimate of the flux above the GeV in the inner Galactic plane [1]. As already mentioned, a discrepancy between the predicted CR spatial density profile and the one inferred from gamma-ray emissivity along the Galactic plane is also found [173]. Another example of interesting features present in the gamma-ray sky are the so-called Fermi bubbles [243], lobes with hard spectrum extending from the GC out to about 40° in longitude and 50° above and below the Galactic center (GC). They are most likely associated to the signal with similar morphology previously discovered at microwave frequencies and dubbed WMAP haze [244]. Finally, a roughly spherical excess in the inner few degrees from the GC and peaking at an energy of few GeV has been firstly noticed in Ref. [245] and its origin, as we are going to discuss in the present chapter, is still a matter of a fascinating debate in the community.

State-of-the-art N-body simulations [246,247] clearly show an extended Dark Matter (DM) halo embedding the Milky Way (MW), with a central density enhancement co-located with the GC. Hence, in case DM particles annihilate in pairs giving

rise to a gamma-ray yield, the DM gamma-ray flux would scale with the square of the DM density profile, the GC is expected to be the brightest DM source. In the latest years a growing number of studies have been dedicated to the search for DM signals in the gamma-ray emission from the innermost degrees around the GC. Along this direction, the first claim of a statistically significant excess in Fermi-LAT data around the GC region dates few years back: [248, 249] have identified a bump-like feature peaking at 2-5 GeV in the innermost two degrees of the inner Galaxy, on top of the estimated astrophysical background. Both the spectrum and spherical morphology of the signal could be easily accounted for by annihilating DM. A refinement of this conclusion has been successively done in Ref. [250], with the help of a slightly improved astrophysical background built upon analytical models for the gas distribution in the Galactic disk. The excess emission has been further characterized with a radial volume emissivity profile falling off as a power law in Galactocentric distance with scaling index that ranges from 2.2 [251] up to 2.4 [252]. While the spectrum peaked at few GeV is broadly demonstrated to be consistent with a signal from DM annihilation, power-law and log-parabola spectra of possible other sources have been also proposed in order to describe the spectral residuals featuring the excess [252, 253].

Despite the compelling features of the signal matching the predictions of annihilation of DM particles, the uncertainties on the modeling of the Galactic diffuse emission (GDE) within the inner few hundred pc from the GC and the limited knowledge of point sources (PSs) in the inner Galaxy have not allowed the alleged claim to be promoted into a genuine discovery [157, 254]. A crucial step forward in favor of the DM interpretation has been provided by the more recent studies on region of interests (ROIs) of tens of degrees around the GC: in the DM scenario, indeed, the spectral and morphological properties of the excess emission should not pertain only to the innermost few degrees from the GC [255, 256]. The first strong hint about this fact has come from Ref. [257] in the ROI correlated with the presence of the Fermi bubbles, i.e. up to tens of degrees in latitude: a detailed inspection of the gamma-ray emission in this region has allowed the authors to connect the spectral feature visible in the low-latitude bubbles to the extended counterpart of the inner GC excess. This study has been independently confirmed by [158] and has characterized the excess to be extended out to at least 2-3 kpc from the GC. Eventually, a more general scrutiny of the gamma-ray emission from the central regions of the MW has been carried out in [258], exploiting particular event cuts to Fermi-LAT data in order to optimize the resolution of the gamma-ray maps. This procedure has led the authors to single out a statistical preference of about 30σ for the inclusion of the dark matter template in the analysis, pointing to the

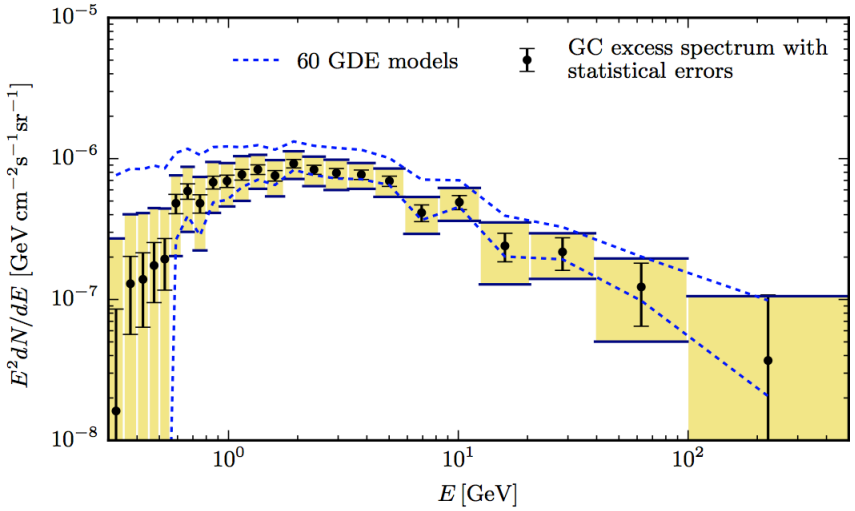

Figure 3.1: *From Ref. [292], the spectrum of the GCE emission for the best-fit model found in that analysis (black dots) together with statistical and systematical (yellow boxes) errors. The dashed blue lines delineate the envelope of the GCE spectrum for all the 60 GDE models considered in that work.*

very appealing scenario of Weakly Interacting Massive Particles (WIMPs) as early Universe thermal relics [258]. This result has resonated on the particle community triggering several theoretical embeddings of the picture from the DM model-building side [259–287]. At the same time, best-fit DM benchmarks compatible with the GeV excess have shown some tension when compared to null findings from other DM indirect searches [147, 148, 288–291].

In spite of the high statistical significance of this gamma-ray anomaly, it is important to stress that also in the context of an extended ROI of tens of degrees around the GC, it is extremely difficult to provide a solid evidence in favor of DM annihilation, mainly because of the dominant background represented by gamma rays originating from the interactions of CRs with the ISM and the photons of the ISRF. This has motivated a closer investigation of the impact of the Galactic diffuse emission (GDE) on the robustness of such claim [292, 293]. In particular, considering an extended ROI of $20° \times 20°$ around the GC and excluding the potentially problematic strip of the innermost two degrees in Galactic latitude, the authors of Ref. [292] have assessed in a comprehensive manner the systematic uncertainties related to the modeling of diffuse backgrounds, studying both theoretical model systematics, which are related to variations in the different possible models for the GDE, and empirical model systematics, namely data-driven uncertainties estimated by an analysis of residuals from a large number of test regions along the Galactic disk (see the discussion in **??** for further details). As it stands out in Fig. 3.1 taken from Ref. [292],

the empirical and theoretical systematics are roughly of the same order in the energy range and ROI considered. According to the correlated errors derived through a principal component analysis in [292], a critical reassessment of DM interpretations has recently enlarged the best-fit scenarios of WIMP candidates [275, 277] able to explain the GC excess. At the same time, a more complicated morphology like a spatial dependence of the energy spectrum, or simultaneous contributions from different physical mechanisms have been envisaged as a feasible fit of the excess within the uncertainties in Fig. 3.1. For instance, an inverse Compton (IC) emission from leptonic burst-like events has been recently studied in detail in Ref. [294], with the conclusion that a combination of two burst events may provide a good fit of the excess spectrum, although with quite unnatural values of the involved parameters (e.g. extremely hard source spectral indices).

In the end, the seminal study in [292] has highlighted to the community the interesting aspect that a spherical and spectrally uniform excess emission around the GC would not only be in very good agreement with data, but may seem remarkably stable against GDE variations in state-of-the-art gamma-ray analyses.

3.2 Towards an ordinary astrophysical explanation

The GC region, namely the inmost few hundred parsecs, is one of the most challenging from the point of view of the theoretical modeling for the diffuse gamma-ray emissivity. All the three ingredients we listed for the standard recipe at the beginning of the chapter show problematic aspects. First of all, catalogues used for CR source distributions, mainly the observed distributions of SNRs [295] and pulsars [296, 297], are not optimal for the inner Galaxy. The fitting functions extrapolated from such catalogues, and used for CR transport studies and to derive gamma-ray emissivities in numerical propagation codes such as `Galprop` [139, 144, 145, 242] and `DRAGON` [141, 143, 226], simply fall off close to zero at the GC. While this approximation has a negligible impact on a general analysis of the emissivity of secondaries in the Galaxy like the study illustrated in Chapter 2, it may become crucial when the analysis focuses exactly on the details of the GC region [298]. As we are going to analyze in what follows, it should be of primary importance to consider in this context the very active star forming region emerging from multi-wavelength surveys of the central Galaxy.

From the point of view of CR propagation, there are several features making it likely that transport properties in the GC region differ significantly from average properties in the Galaxy as fitted to local CR data. E.g., the GC region seems

to host strong magnetic fields, at the level of 50-100 μG [299], much above the estimated average value within the disk or the CR diffusive halo, probably impacting on the structure and effective values for the diffusion tensor appearing in Eq. (2.25). Also, very strong convective effects have been claimed in this region [300, 301], in analogy to outflows from external starburst systems, as well as from the fact that at the GC there is a violation of the correlation between far-infrared and radio continuum luminosities observed for systems with in-situ energy losses of CR electrons. Most importantly, the density distribution and dynamics of molecular gas at the GC is still actively investigated, see, e.g., [302].

The most robust analyses providing evidence in favor of a GeV excess in the inner Galaxy are based on the template-fitting method, see for instance [258, 292]. Extensively used for the analysis and subtraction of CMB radiation foregrounds, this technique has led, for example, first to the identification of the WMAP haze and then successfully applied to search for its (alleged) gamma-ray counterpart, the Fermi bubbles. The rationale of this procedure is to test whether, on top of small-scale discrepancies, the GDE model captures the correct intermediate-to-large scale morphologies, or data favor extra contributions with different angular imprint in the region under investigation. Morphological templates are assigned – based on theoretical modeling and/or observations – to components connected to different physical emission mechanisms, such as: the component taken as the sum of the term due to the production and decay of π^0 plus bremsstrahlung emission, both related to the gas distribution in the Galaxy; the IC term, as correlated to the ISRF model; and the isotropic template for the extra-Galactic background component. Each template is then let free to fluctuate, independently for each energy bin, to find the configuration providing the best fit to the data. In this way, one accounts for possible spectral distortions and normalization uncertainties of the different components within the theoretical model. Indications for an extra component can be claimed if a significant improvement of the overall fit is found when repeating the same exercise with an additional physically motivated template.

In the following, we concentrate on the choice of templates for the CR-induced components and on the impact of such choice on the evidence for the excess. As discussed above, none of the ingredients of the "standard" theoretical model setting those templates are actually optimized for the GC environment. At the level of proper statistical assessments of the goodness of the fit to the data, a comparison between alternative theoretical models is a very hard task due to small-scale discrepancies which have a significant impact on statistical estimators and prevent a reliable comparison with the data. In order to alleviate these problems, we have adopted therefore the template-fitting strategy, described in the next section.

As a preliminary step, we have tested a few hypotheses on whether significant changes in the CR transport equation would mimic the required morphological features characterizing the observed emission in the GC region. In our attempts we have included a sampling of radial dependences for the diffusion coefficient as in Eq. (2.33) and also anisotropic diffusion. At this level, in agreement with and as an extension of the results in [292, 293], we have not found suitable configurations.

We have turned then to considering an adjustment in the choice of the CR source function, introducing, as a new ingredient, a steady-state source located at the GC and with a narrow spatial extension – few hundred pc. As already mentioned above, the GC seems indeed to harbor significant star formation and a large rate of Supernova explosions compared to the average value in the Galaxy: according to [303], the star formation rate (SFR) in the inner few degrees away from the GC is of order 1% of the SFR in the Galaxy, making it roughly a factor of 250 higher than the mean rate in the Galaxy. This should be the consequence of two facts:

i) the presence of a large reservoir of molecular gas filling the inner part of the Galactic bulge (the Central Molecular Zone (CMZ) [211], extending up to $\sim$ 200 - 300 pc away from the GC);

ii) the very peculiar physical properties of this environment, where the ISM appears significantly hotter, more turbulent, and more magnetized.

Solid evidence for the high SFR level comes from infrared observations – performed with the Hubble Space Telescope – of some extremely dense stellar clusters in the inner 50 pc (the Central, Arches, and Quintuplet clusters). These structures are rich of young, very hot stars that are many times larger and more massive than the Sun, see, e.g., [304, 305]. Moreover, many isolated Wolf-Rayet Stars and O Supergiants were observed in the inner 100 pc [306]. The Supernova explosions connected with this relevant star formation activity are expected to accelerate a large amount of CRs. While this contribution has no impact on the local CR fluxes, it drives major consequences on gamma-ray emissivities in the GC region, as we shall see in a moment.

We take as reference case the fit of the data for "standard-lore" CR templates, re-derive the improvements in the fit obtained when including the DM template, and then compare such refinements to those we can obtain in the case when the new CR templates are adopted. From such a comparison we are going to show that the two scenarios are in most respects equivalent and hence that the "excess" can be almost entirely reabsorbed within a framework involving only a minimal picture of steady-state propagation of CRs. Note that the approach we follow is the appropriate one to realistically reproduce the energy dependence of the

diffuse emission template. Indeed, while the Dark Matter morphology is fixed at all energies, the IC, π_0 and bremsstrahlung ones change in energy as a result of CR transport. It is therefore extremely important to incorporate the contribution related to the new source directly into the original diffuse emission template rather than study an extra-component directly on the residuals of Fig. 3.1.

3.2.1 The template-fitting analysis

Let us describe in some detail the method that we use to compare our proposed astrophysical scenario with the DM interpretation of the GC excess.

The starting point of the analysis is to compute a physical model for the CR distribution in the Galaxy obtained solving Eq. 2.25 with the help of a numerical package like e.g. `DRAGON`.

We then perform a line-of-sight integral and obtain the gamma-ray sky-maps from $\simeq 0.3$ GeV to $\simeq 300$ GeV using `GammaSky`, taking into account the decay of neutral pions produced by collision of CRs with the interstellar gas, the IC scattering of CR leptons on the diffuse radiation field and the bremsstrahlung emission due to CR leptons interacting with the interstellar gas.

Exploiting such description of the diffusion emission induced by the CR interactions, we model the gamma-ray sky as a linear superposition of the following templates:

- π^0-decay + bremsstrahlung template, produced with `GammaSky` from the CR distributions computed with `DRAGON`, adopting the same gas model taken of the latest public version of `Galprop` CR package [144, 242];
- IC template (produced with `GammaSky`). Here we use the leptonic distributions calculated with `DRAGON` and the most recent ISRF model included in [144, 242];
- isotropic extra-Galactic background (EGB) template with a spectrum taken from a recent analysis of the Fermi collaboration [307];
- PS template, obtained from the 4-year Point Source Catalog (3FGL) provided by the Fermi collaboration [205]; the angular resolution of the Fermi-LAT instrument is taken into account smoothing the emission of each PS according to the Fermi-LAT point spread function (PSF), modeled using the Fermi tool `gtpsf`;
- Fermi bubbles template with morphology and spectrum as derived by the Fermi collaboration in [184];

- a DM template obtained integrating along the line of sight the square of a generalized NFW profile:

$$\rho(r) = \rho_0 \left(\frac{r}{r_s}\right)^{-\gamma} \left(1 + \frac{r}{r_s}\right)^{-3+\gamma} , \tag{3.1}$$

  where r corresponds is the Galactocentric distance and the scale radius r_s is fixed to $r_s = 20$ kpc, while the normalization ρ_0 is chosen in order to obtain a DM density at the Sun position $\rho(r_\odot) = 0.3$ GeV cm^{-3}, with $r_\odot = 8.5$ kpc, and the inner slope is set to $\gamma = 1.26$,[1] as in [258].

We consider 5 years of Fermi-LAT data, within the event class `ULTRACLEAN`. We use the Fermi tools `v9r32p5` to perform analysis cuts and to compute the exposure of the instrument. Events with zenith angles larger than 100° are rejected. We also apply the following selection cuts: `(DATA_QUAL==1) && (LAT_CONFIG==1) && (ABS(ROCK_ANGLE)<52) && (IN_SAA!=T)`. The exposure maps are computed using the response function `P7REP_ULTRACLEAN_V15`. The data are organized in 30 energy bins from 300 MeV to 300 GeV, equally spaced on a logarithmic scale.

We work with the `HEALPix` tessellation scheme for all our maps [308]. We choose a resolution $n_{side} = 256$, corresponding to a pixel size of $\sim 0.23°$. Finally, the templates and the Fermi-LAT data are smoothed to a common angular size using a gaussian kernel. In this way all the maps have the same angular resolution. For this purpose we use the `HEALPix` routine `smoothing`. We follow the method in [158] using $f_{target} = 3°$ for $E_\gamma < 0.6$ GeV and $f_{target} = 1°$ for greater energies. We checked that our results are insensitive to such smoothing choices, with the exception of the low-energy portion of the spectrum ($E_\gamma \lesssim 1$ GeV), where the recipe adopted for the smoothing of the templates has a non negligible impact on the result, see below for further details.

At the end of this process, we perform the template-fitting analysis. We focus on a region of interest (ROI) defined as:

$$|\mathrm{l}| < 20°; \quad 2° < |\mathrm{b}| < 20°,$$

with l and b the longitude and latitude Galactic coordinates. For each energy bin, we construct then the following Poisson likelihood function:

$$-2\ln(\mathcal{L}) = 2\sum_i [e_i - o_i \ln(e_i)] + 2\sum_i \ln(o_i!) + \chi^2_{\rm ext}\,, \tag{3.2}$$

[1] We have checked that different values of γ do not alter the conclusion of our analysis. In general, we have found that profiles with $\gamma \simeq 1 - 1.6$ are preferred by data.

where the index i labels each pixel inside the ROI, and we have introduced the following quantities:

- o_i is the number of *observed* events, i.e. the Fermi-LAT data;
- e_i is the number of *expected* events, that can be written as a linear combination of the events corresponding to the templates described above:

$$e_i = \sum_k \alpha_k \, e_i^{(k)} \, , \tag{3.3}$$

  where k runs over the different templates.

The counts are obtained multiplying the differential flux per unit of solid angle by the Fermi-LAT exposure map, the energy bin width and the solid angle per pixel. Eventually, the Fermi bubbles and the isotropic emissions are better determined with observations outside our ROI. For this reason, we have introduced in Eq. (3.2) a penalty factor $\chi^2_{\rm ext}$ for their coefficients:

$$\chi^2_{\rm ext} = \sum_h \frac{\phi_h^2 \, (1-\alpha_h)^2}{\epsilon_h^2}. \tag{3.4}$$

where h now only refers to the Fermi bubbles and isotropic emission templates. ϕ_h and ϵ_h are the nominal fluxes and uncertainties taken from the Fermi analysis mentioned above.

The minimization of the statistical estimator in Eq. (3.2) provides the best-fit values of the coefficients α_k in each energy bin.

Concerning the treatment of point-source emission, we have checked the possibility of introducing a masking procedure to mitigate their role in our analysis and/or account for reconstruction faults. Masks of two types have been considered: a sharp cut around each PS of all pixel within a 68% containment radius, depending on energy and sharply increasing at $E \lesssim 1$ GeV, as obtained from the PSF of the instrument Fermi tool `gtpsf`. We have also exploited the soft mask suggested in [292], according to which the contribution of each pixel to the likelihood is re-weigthed depending on the flux from the PSs expected in that pixel. Consequently, this mask lowers the impact on the likelihood of pixels whose counts are dominated by PSs. We have found, however, that our results are not severely affected by adopting any of these masks and hence we are going to disregard the masking procedure for simplicity in what follows.

3.2.2 A suitable benchmark model

Having set the framework, we are at the point of introducing a benchmark case to examine whether, within the template-fitting analysis, a properly modified CR emissivity model can be considered equivalent to introducing the DM template.

We have chosen as starting point for the CR propagation framework one of the reference cases in [292], labelled "Model A" in that analysis. This model has a standard scaling of the diffusion coefficient with rigidity (a Kolmogorov-type $\delta = 0.33$), and reasonable values for the normalization of the diffusion coefficient ($5{\cdot}10^{28}$ cm^2/s at 4 GV), the height of the diffusion halo (4 kpc), and the Alfvén speed (32.7 km/s); moreover, the model features a moderate convective wind gradient (50 km/s/kpc). The injection slope is a broken power law. For the hadrons the indexes are 1.89 (2.47) below (above) the reference rigidity of 11.3 GV, while for the electrons 1.6 (2.43) below (above) 2.18 GV. The model has a sharply enhanced IC component obtained by rescaling the normalization of the CR electrons by a factor $\simeq 2$ with respect to local measurements, as well as a $\simeq 40\%$ increase in the ISRF; the synchrotron energy losses are also enhanced, adjusting the overall normalization of a conventional large-scale magnetic field model for the Galaxy in such way that, after the rescaling, it matches the claimed value of about 50 μG at the GC. While the latter assumptions make the model not compatible with local CR measurements, we remind that the goal of the template-fitting analysis is not to find a model valid in the whole Galaxy, but rather to describe in detail the morphology of the GC region (i.e. reproducing at the same time the local measurements and other observables is well beyond the scope of this kind of analyses).

As also discussed in [292], the specific choice of propagation parameters is not crucial for the template-fitting analysis. The point is that the free floating of the individual templates in each energy bin always tends to readjust the input model towards a preferred output, carrying in the end common features, such as an enhancement in the IC component. Model A seems to be preferred in [292] since implies the smallest changes in normalization and spectral features between input and output model (namely the minimum of the likelihood function is reached for the smallest departure from 1 of the coefficients α_k introduced in Eq. (3.3)). It is also one of the cases in which the template fitting gives a very clean indication, over a large span of energy bins, for a sharp improvement in the data fit when including the DM template: we take the challenge to focus on this sort of "worst-case scenario" to test whether our alternative picture can perform equally well. On the other hand, we stress again that, as tested on a few sample cases, changing the propagation setup would only impact on minor details of the fit, leaving the overall picture

substantially unchanged.

Model A adopts as CR source function a smooth interpolation from a SNR catalogue [295]. As already mentioned in Section 3.2, this term clearly does not satisfactorily describe of the Galactic bulge region. We consider then an extra steady-state source term, which we model as a Gaussian (hereafter "spike"):

$$\mathcal{Q}_{\rm spike} = \mathcal{Q}_0 \, e^{-(r/\sigma)^2} \, . \tag{3.5}$$

In the following, we are going to express the normalization $\mathcal{Q}_0$ of this source in terms of $\mathcal{N}$, i.e. the ratio (in percentage) between the volume integral of the spike and the volume integral of the conventional source term, namely

$$\mathcal{N} \equiv \mathcal{Q}_0 \int d^3x \, e^{-|\vec{x}|^2/\sigma^2} \Big/ \int d^3x \, \mathcal{Q}_{\rm conv.}(\vec{x}) \, . \tag{3.6}$$

The definition of $\mathcal{N}$ provides a simple way to compare against observational constraints, since the novel CR injection term in Eq. (3.5) should be correlated to the Supernova explosion rate in the central region of the Galaxy and, hence, on the SFR rate as well. Therefore, according to Eq. (3.5) and Eq. (3.6), the relevant parameters describing the new ingredient under consideration are the spatial extension σ and the normalization $\mathcal{N}$ of the spike.

In our ROI the spike mainly affects the IC template, since the region containing most of the π^0 and bremsstrahlung emission is masked out[2]. The additional contribution due to the spike impacts on the IC template as shown in the upper panel of Fig. 3.2 where we plot the total IC longitudinal profile for different spike widths. On the lower panel, we show instead the contribution to the IC emission from the spike only and compare it to the DM template. The plots are produced for sample gamma-ray energy values.

It is important to notice that, while on the morphological side the two scenarios are similar, in the spike case we are not treating the extra ingredient as an independent term, rather we are correlating its spectrum to the overall IC emission.

[2]We remark that the reference model considered here is not tuned for the Galactic plane, within 2° in latitude. In this region, a much more detailed treatment of the astrophysical ingredients (concerning both the emitting targets and the CR transport properties) would be in order.

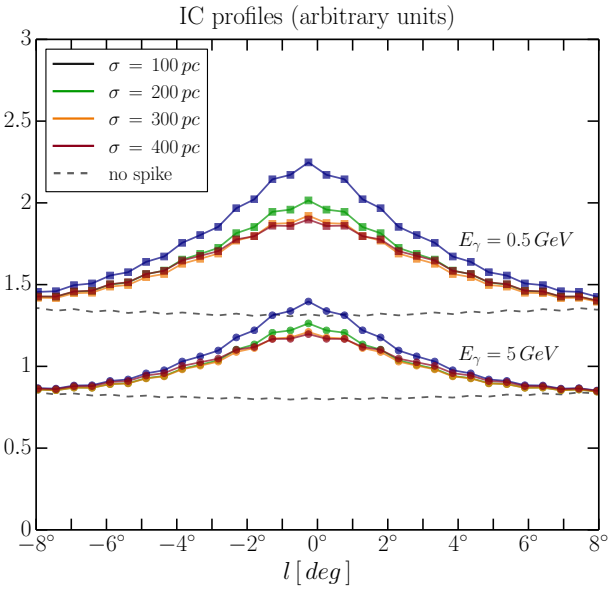

Figure 3.2: Upper panel: *The IC longitudinal profiles integrated in the range* $2° < |b| < 5°$ *for two reference values of* E_γ *and for spikes with different widths* ($\sigma = 200 - 400$ pc). *We remind that the normalization of the spike is set in such a way to absorb most of the GC excess. We checked a posteriori that the chosen value is compatible with astrophysical estimates regarding the SFR in the GC region.*
Lower panel: *The IC profiles at* 0.5 *GeV for the spike terms with different values of the width* σ *in Eq. (3.5) compared against the corresponding profile from a DM-like template.*

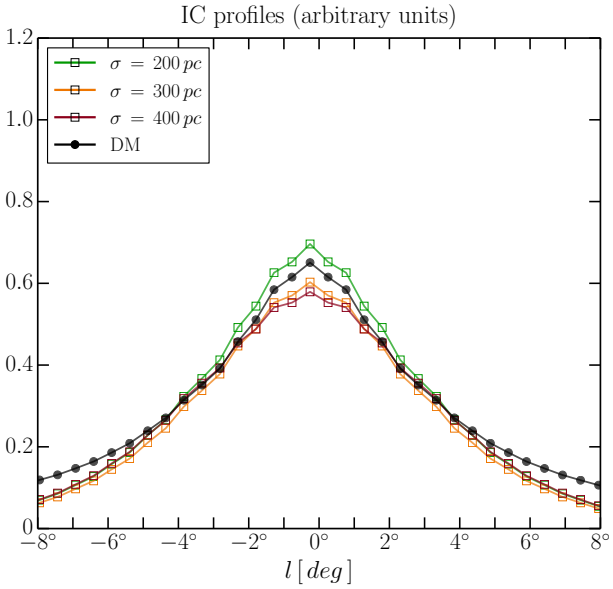

3.2.3 Results: energy spectrum and test statistics

We have chosen $\sigma = 300$ pc as a sample value for the spike width, roughly matching the size of the CMZ. The choice of $\mathcal{N}$ is based on two objective requirements[3]: the value cannot be too large, since the SFR in the GC cannot exceed few percent of the total rate in the Galaxy; moreover, we verify *a posteriori* that the spike emission absorbs the majority of the GC excess (to put it another way, it means that if we include in the fit of the reference model the DM template as well, the latter should be used only marginally).

Our analysis is based on the comparison between the reference model described above, and the case in which we add to Model A a DM template, the latter modeled according to the modified NFW distribution in Eq. (3.1). The inclusion of a DM template in the fitting procedure in addition to standard astrophysical background models – like the Model A considered in this analysis – provided the most striking evidence supporting the DM interpretation of the GC excess. As already noted at the beginning of the chapter, in Ref. [258] the addition of the DM template dramatically improved the fit up to an overwhelming high level of statistical significance. For this reason, it is mandatory to compare the performances of the spike model with those of the DM template. In what follows, we present the results of our analysis in three subsequent steps: we first analyze the result of the template fit in terms of energy spectra, then we provide a more quantitative discussion based on the likelihood analysis, and finally we offer a more direct comparison with data based on the analysis of gamma-ray profiles along three complementary directions.

As far as the energy spectra are concerned, Fig. 3.3 encodes the results of our template-fitting analysis. In the upper panel, the best fit obtained for the Model A including the DM template is displayed. As described in the caption of Fig. 3.3, we explicitly show for all components both pre- and post-template fitting values. As expected, the fit heavily uses the DM template, and the corresponding energy spectrum (magenta diamonds in Fig. 3.3) clearly shows the familiar bump-shaped form peaked at few GeV, in good agreement with that predicted from a WIMP with ~ 45 GeV mass annihilating, among other possibilities, into $b\bar{b}$ [115]. For illustrative purposes, it is also instructive to look at the residual map – i.e. the difference in counts between data and model evaluated at the best-fit point – obtained without the inclusion of the DM template. We show this residual map in the upper left panel of Fig. 3.4 for the energy window $E_\gamma = 1$ - 10 GeV, where the presence of an excess distributed around the GC stands out in full glory. This excess is fully absorbed by the DM template in the fit, as shown in the upper right panel of

[3] We refer the reader to Section 3.2.4 for a more complete discussion about the impact of different values of σ and $\mathcal{N}$.

Fig. 3.4, where we present the residuals after template fitting including the DM template.

Let us now turn the attention to our reference model. In the central lower panel of Fig. 3.4 we show the pattern of residuals replacing the DM template with the spike ($\mathcal{N} = 2.2\%$). The resulting pattern looks pretty much similar to the one exhibited by the DM case. In the lower panel of Fig. 3.3, instead, we consider the possibility of having at the same time the spike and the DM component. The contribution of the DM template is now significantly reduced, is consistent with zero (within the statistical error bars obtained from the fit) in a large energy range, and – most importantly – gives rise to a roughly featureless spectrum.

Precisely in this energy range, 1 - 10 GeV, our model (without DM) gives a description of the gamma-ray emission quantitatively similar to that of the Model A+DM. In other words, most of the GC excess is absorbed by the spike, and the presence of an extra DM template only gives a slight improvement in the fit. In order to support this statement and to further scrutiny the performance of our model, we can consider now the upper left panel of Fig. 3.5 where we compare, for each energy bin, the test statistic (TS) of the models we are studying. The TS is defined by $\mathrm{TS} = -2\Delta \log \mathcal{L}$, where $\mathcal{L}$ is the likelihood defined in Eq. (3.2).

First, we show the improvement in the TS obtained adding the DM template to the Model A. More precisely, the yellow dashed line with open circles in Fig. 3.5 represents the square root of the difference $-2 \log \mathcal{L}_{\text{Model A}} + 2 \log \mathcal{L}_{\text{Model A+DM}}$ (hereafter, ΔTS). In terms of energy spectra, the case Model A+DM corresponds to the one displayed in the upper panel of Fig. 3.3. The plot clearly shows the improvement in the fit due to the presence of the DM template. If taken at face value, it corresponds to a statistical preference of about 15σ at the position of the peak. Of course, we remark that this value should be taken *cum grano salis*, since – in addition to the extremely small statistical errors – Fermi-LAT photon counts are plagued by unavoidable systematic errors difficult to assess and hence not taken into account in the likelihood fit [292]. However, it is indisputable that including the DM template greatly improves the fit; therefore, it is crucial to compare this result with the performance of our spike.

The green solid line with filled circles represents the improvement in the fit (quantified by ΔTS) obtained considering our reference spike model with respect to the Model A. The plot highlights that our scenario – without any DM contribution – performs better than the starting Model A, and gives a result comparable (even at the level of statistical preference) with the DM case. For completeness, we also show the TS for the combination of the spike and the DM template. The green solid line with open circles represents the corresponding ΔTS, so that negative

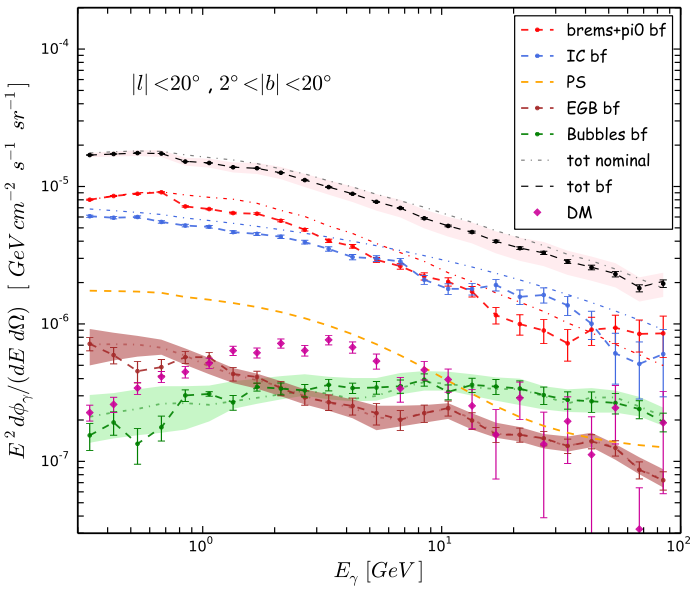

Figure 3.3: Upper panel: *Model A+DM.* Lower panel: *Model A+spike+DM. Spectrum of the various contributions to the total gamma-ray flux (light and dark grey dashed lines) compared to Fermi-LAT data. The violet band represents the systematic uncertainty on the spectrum [157]. For IC (light blue), π^0+Bremsstrahlung (red), EGB emission (brown) and Fermi bubbles (green) dot-dashed lines show the nominal spectrum (pre-fitting) while points and dashed lines are the post-fitting values. Uncertainties bands and central values for bubbles and EGB are taken respectively from [184] and [307]. Magenta diamonds: DM contribution. PS template (orange dashed line) is not touched by the fit. The error bars on the templates are obtained from the fitting procedure.*

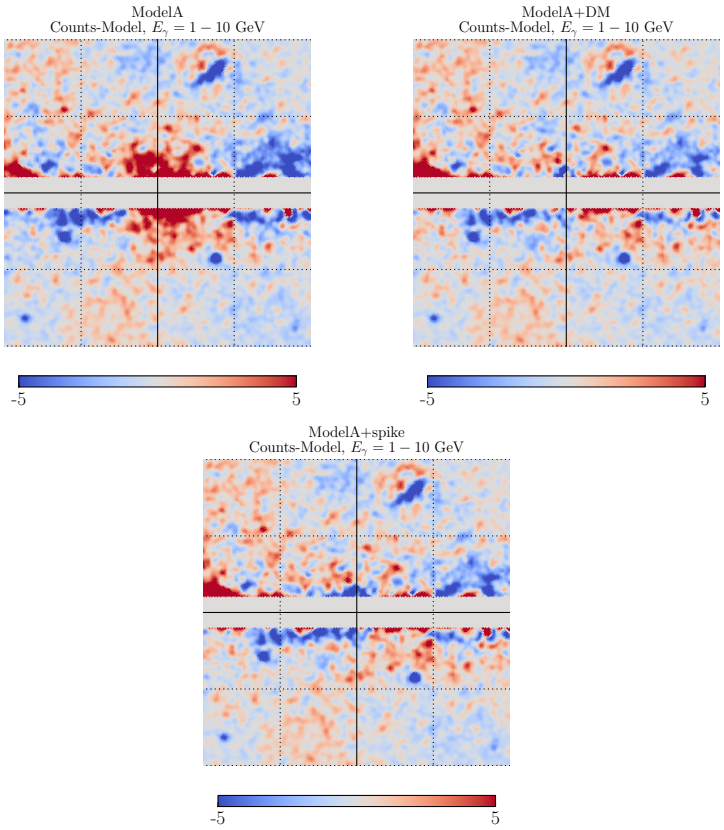

Figure 3.4: *Residual counts obtained for the Model A (left upper panel, without the inclusion of DM template), for the Model A + DM (right upper panel), and for the reference model described in Section 3.2.2 (lower central panel, without the inclusion of DM template). See text for a detailed discussion.*

values indicate a statistical preference for the addition of the DM template. In terms of energy spectra, this situation corresponds to the upper panel of Fig. 3.3. The TS plot shows that the addition of the DM template slightly improves the fit in the energy window $E_\gamma = 1\text{-}10$ GeV. However – as already noticed discussing the energy spectrum in Fig. 3.3 and the residual map in the right panel of Fig. 3.4 – this improvement is mild given that the majority of the excess has been absorbed by the presence of the spike. Moreover, the residual spectrum absorbed now by the template in Eq. (3.1) is not resembling anymore – neither in spectral emissivity nor in normalization – possible distinct features of WIMP pair annihilation.

Let us now pause a moment to summarize what we have found.

Looking at spectra and ΔTS, we have clarified that the presence of the spike – even in the simple realization provided by Eq. (3.5) and discussed here – provides a viable astrophysical alternative to the DM interpretation of the GC excess.

In the following, on top of the information carried by the energy spectra in Fig. 3.3

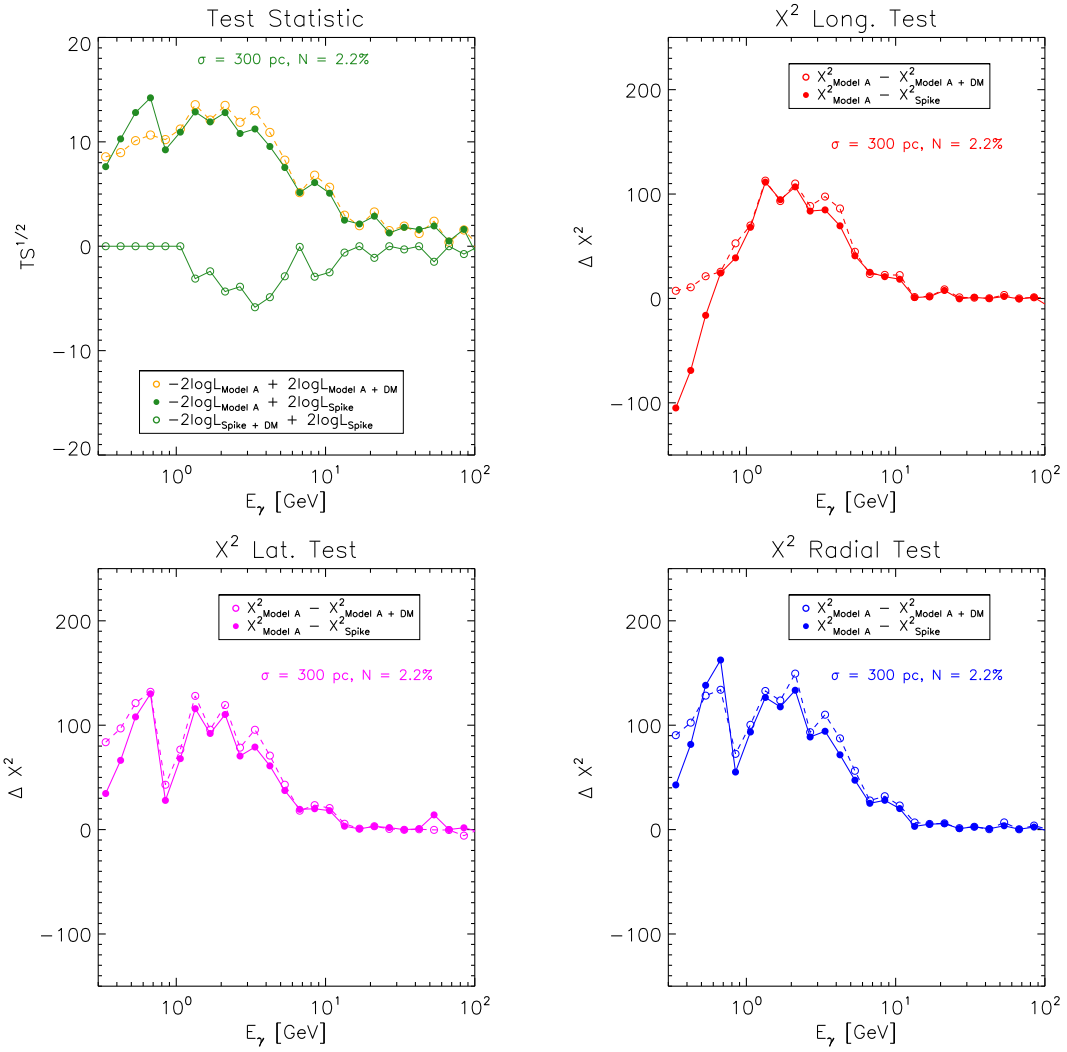

Figure 3.5: Top left panel: *we compare the test statistic (*$\mathrm{TS} = -2\Delta \log \mathcal{L}$*, we show the square-root of TS) of the models we consider; a positive difference between two models means that the second model performs better. Yellow filled circles:* $-2 \log \mathcal{L}_{\mathrm{Model\,A}} + 2 \log \mathcal{L}_{\mathrm{Model\,A+DM}}$. *Green filled circles:* $-2 \log \mathcal{L}_{\mathrm{Model\,A}} + 2 \log \mathcal{L}_{\mathrm{Spike}}$. *Green empty circles:* $-2 \log \mathcal{L}_{\mathrm{Spike+DM}} + 2 \log \mathcal{L}_{\mathrm{Spike}}$.
Top right panel: *we compare the* χ^2 *of the longitude profiles for the same models. Filled circles:* $\chi^2_{\mathrm{Model\,A}} - \chi^2_{\mathrm{Spike}}$. *Empty circles:* $\chi^2_{\mathrm{Model\,A}} - \chi^2_{\mathrm{Model\,A+DM}}$.
Bottom panels. *the same as the top right panel, for latitude and radial profiles.*

and the TS in the upper left panel of Fig. 3.5, we would like to get more deeply into the details of the ROI by analyzing latitude, longitude and radial profiles. As we are going to see, this may offer to us a more transparent picture of the performance of our spike in reproducing the gamma-ray data throughout the ROI.

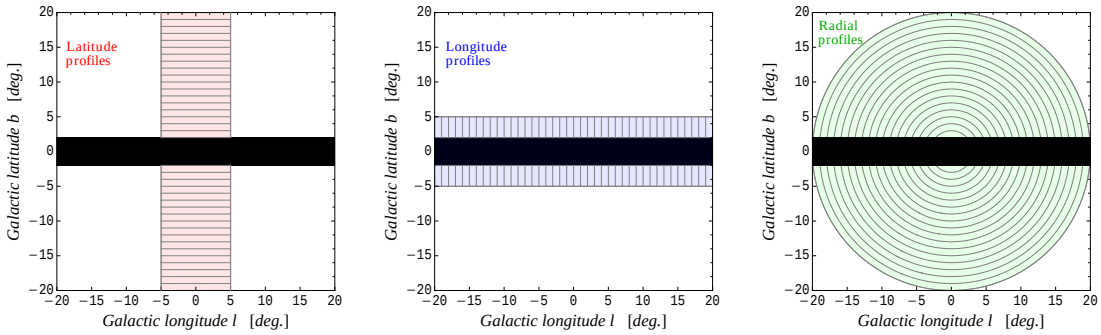

Figure 3.6: *Control regions used for the computation of the gamma-ray latitude, longitude and radial profiles. See the text for details.*

- *Latitude profiles.* These profiles most closely reflect the morphology of the excess. The GC excess extends far away from the GC itself, out to at least 10° in latitude [158, 257, 258]. This is clear from the latitude profile shown in the central and lower panels of the right column in Fig. 3.7 where, at the reference energies $E_\gamma = 2.12$ GeV and $E_\gamma = 10.64$ GeV, the DM template gives a sizable contribution to the total count density up to $|b| \sim 10°$. From the central and lower panels of the left column in the same figure, we see that the spike gives a comparably good fit, since the role of the DM contribution is essentially played by the enhanced IC emission due to the extra electrons emitted in the spike, and radiating on the ISRF up to fairly large latitudes. This effect is confirmed by the lower-left panel of Fig. 3.5 where it is shown that, in the mid-energy region, the spike provides a fit of the latitude profiles remarkably close to the one obtained by using the DM template. As far as the low-energy region is concerned, in the lower-left panel of Fig. 3.5 we observe that, in the first two energy bins, the DM template produces a slightly better fit if compared to the spike. We investigate this point in the upper panel of both left and right column in Fig. 3.7, where we zoom the latitude profiles in the data bin with central energy $E_\gamma = 0.424$ GeV. While the DM contribution is suppressed at low energy (see also Fig. 3.3, upper panel), the steady-state emission of the spike, being correlated to the overall IC component, cannot be equally suppressed (at least in the simplified model studied in this paper), and therefore leads to a slight overshooting in the region $3° \lesssim |b| \lesssim 5°$. We would like to remark however that the apparently large difference ($\chi^2_{\rm Spike} - \chi^2_{\rm Model\,A+DM} \sim 50$) reported in Fig. 3.7 for this low-energy bin is likely affected by the fact that we included in the computation of the χ^2s only statistical errors. Indeed, the systematic errors are estimated for the integrated spectra only ($\simeq 5\%$ at $E_\gamma = 562$ MeV [157]) and a better understanding of this uncertainty would presumably change the rules of the

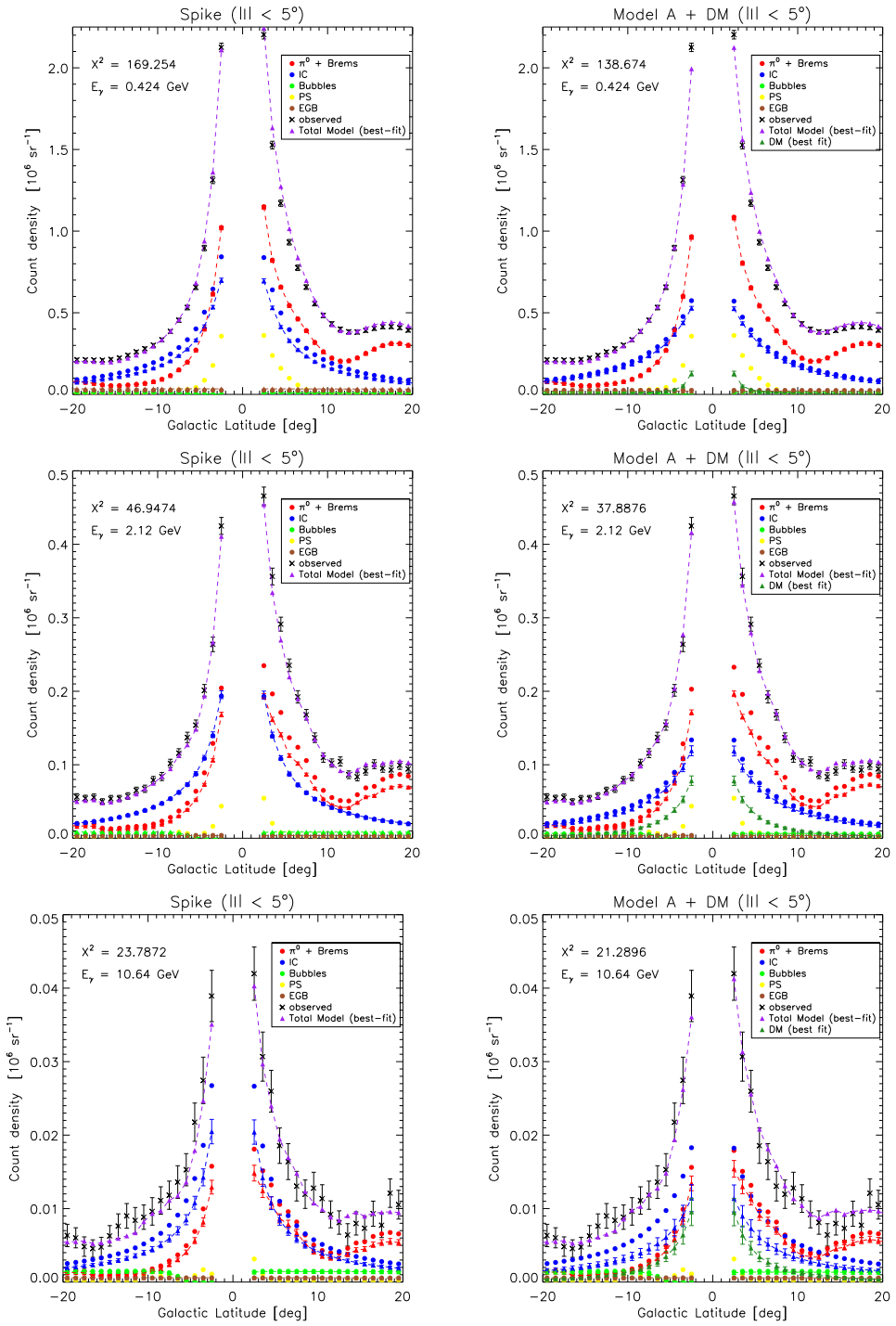

Figure 3.7: Left column: *the latitudinal profiles for our best case at several energies. From left to right,* 400 *MeV,* 2 *GeV,* 10 *GeV. Red circles (triangles):* π^0*+Bremsstrahlung contribution, pre- and post-fitting. Blue circles (triangles): IC contribution, pre- and post-fitting. Magenta triangles: total model, to be compared with Fermi-LATdata.* Right column: *the same plots for Model A+DM (DM contribution in forest green triangles).*

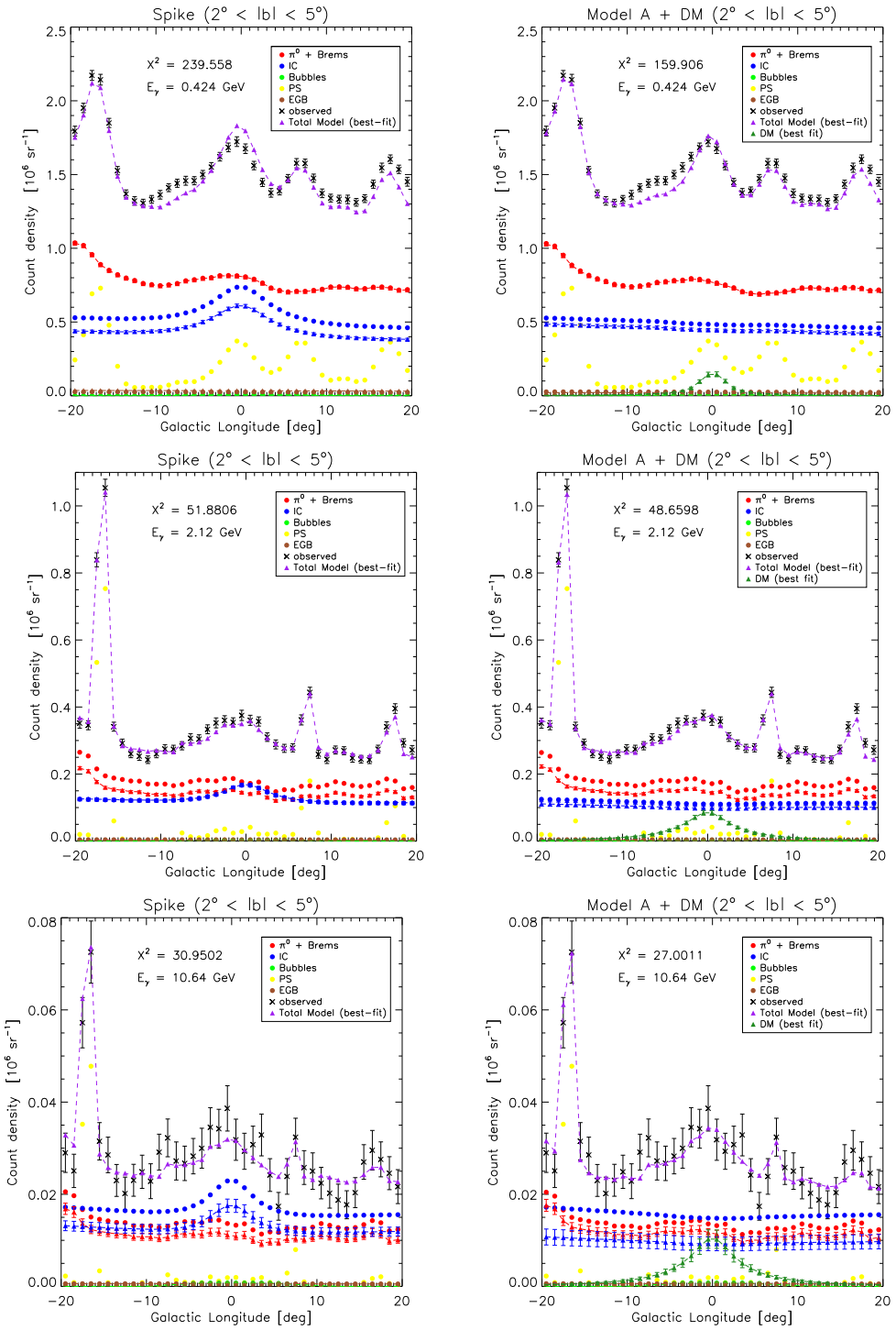

Figure 3.8: *The same as Fig. 3.7 for the longitudinal profiles.*

comparison, ameliorating the discrepancy.

On the basis of these considerations, we can therefore conclude that the spike provides a fit of the latitude profiles comparable in quality with the one obtained using the DM template.

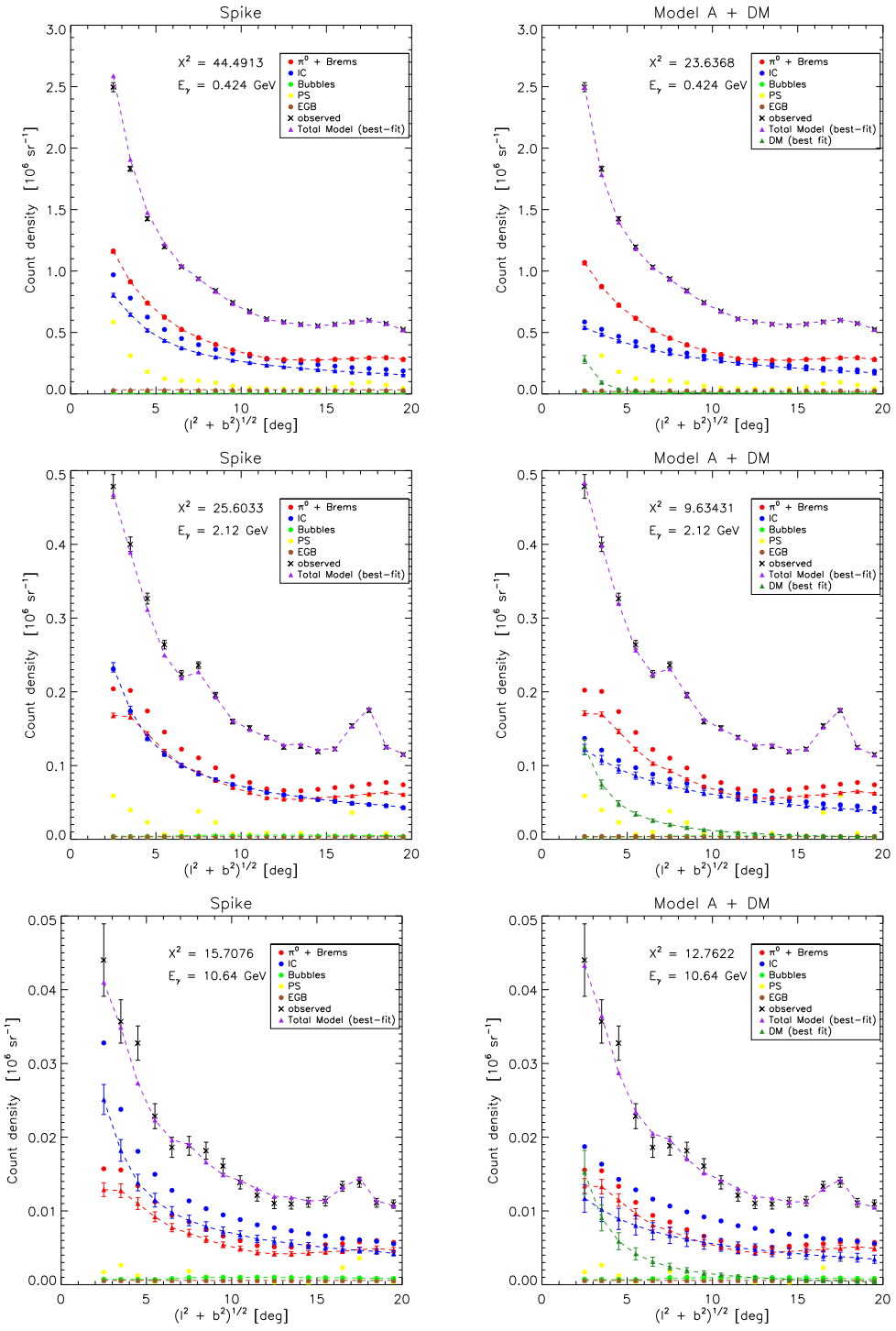

Figure 3.9: *The same as Fig. 3.7 for the radial profiles.*

- *Longitude profiles.* We can start again our discussion from the mid-energy region, focussing our attention on the central and lower panels of the right column in Fig. 3.8. For these energy bins the bump-shaped form of the GC excess distinctly stands out. Even in this case, we notice that the spike provides an excellent fit to data, comparable in quality to the DM template.

This is confirmed by the central left panel of Fig. 3.5, where we show the comparison between $\Delta\chi^2_{\rm DM}$ and $\Delta\chi^2_{\rm Spike}$: no significant discrepancy is reported, and in the mid-energy region the spike perfectly substitutes the DM template. In the low-energy region, while the spike seems to improve the fit if compared with the Model A as suggested from the upper-left panel of Fig. 3.5, we find in the first three bins a net preference (up to $\chi^2_{\rm Spike} - \chi^2_{\rm Model\,A+DM} \sim 100$) for the DM template. Moreover, differently from what we have observed for latitude profiles, in the low-energy range the agreement with data worsens when we introduce the spike. Indeed, from Fig. 3.8, taking the bin with central energy $E_\gamma = 0.424$ GeV, it seems quite clear that the presence of the spike is disfavored since it produces a visible overshoot of low-energy longitude profiles in $|l| \lesssim 4°$. This is what happens in the first three energy bins from the upper-left panel in Fig. 3.5 and seems to be in contrast with the information carried out by the TS. The simplistic assumptions on the CR modeling from one side, and the unknown systematics on Fermi-LAT counts from the other one, may provide arguments in favor of alleviating the discrepancy at low-energy between the TS and longitude profile in Fig. 3.5 for the case of the spike. Actually, exploring better the impact of our smoothing procedure in the analysis, we have found that the low-energy tail of the spectrum (below 1 GeV) is very sensitive to the results of the adopted smoothing algorithm. In particular, if we choose the alternative strategy of smoothing only the GDE templates, applying a convolution with the Fermi-LAT PSF, and leaving the PSs, exposure, and count maps untouched, in the case of the spike we find for $E_\gamma < 1$ GeV a worsening of the TS (in the first two energy bins $\sqrt{\text{-TS}} \simeq 10$, then it rapidly improves).

We can conclude that while our spike scenario is very competitive in the mid-energy region with the DM one, it fails to account for low-energy gamma-ray data along the Galactic longitude direction. Given its successful prediction in the mid-energy region – where the evidence of the GC excess is most robust – the simple proposed adjustment given by Eq. (3.5) may be too simplified to work fine on the whole spectrum of energies measured by Fermi-LAT. For instance, the associated CR injection spectrum may be not the same as the ordinary source term, and it may possibly feature a spectral break at low energies. However, the non-standard acceleration mechanism behind such ad hoc injection spectral break may be hard to foresee. Low-energy effects on CR modeling like convection or re-acceleration may also turn out to be very important in this context: unfortunately, an analysis with more physical insights – i.e. truly based on the propagation properties of CR primaries

rather than on a free-floating of templates performed independently on each energy bin – is extremely challenging, since the GC "excess" arises only as an effect at the level of few % in Fermi-LAT data.

- *Radial profiles.* at last, we discuss radial profiles. From the right panel in Fig. 3.6 we first notice that the adopted binning spans a wider region of the ROI compared to the previously discussed profiles. Indeed, the comparison between $\Delta\chi^2_{\rm DM}$ and $\Delta\chi^2_{\rm Spike}$ in the lower-right panel of Fig. 3.5 closely resembles the TS. The spike provides a very good fit, comparable in quality with the DM template both in mid- and low-energy regions. The only exception is represented by the first energy bins, but the same arguments outlined for latitude profiles hold true. The radial profiles in the top and bottom rows in Fig. 3.9 show in detail – considering the usual benchmark bins at $E_\gamma = 0.424,\, 2.12\,,10.64$ GeV – the performance of the spike with respect to the DM template. It is clear as the modified IC emission, altered by the presence of the spike, mimics the DM contribution up to $\sqrt{l^2+b^2} \sim 10^\circ$.

To summarize, if we focus on energies greater than 1 GeV, namely the energies on which the GeV excess at the GC is mostly based, the analysis of latitude, longitude and radial profiles enforces what already found in the study of the TS. Motivated by the high star formation expected in the region around the GC, we can confirm that the presence of the spike in our reference model depicts a viable astrophysical scenario, potentially able to address most of the putative excess at the GC.

3.2.4 Discussion

Although we have presented in detail a viable working scenario, for the sake of completeness it is worth mentioning that several variations are possible.

- First of all, we show that the nice agreement with the data obtained for the reference case, can be extended to different values of σ (see Fig. 3.10).

  In particular we verified that, going down to $\sigma = 200$ pc and up to $\sigma = 400$ pc (with a proper rescaling of $\mathcal{Q}_0$ in Eq. 3.5), all the results of the previous section are almost unchanged. Interestingly, in all cases the optimal value of $\mathcal{N}$ does not change much.

  We remark that spikes more extended than those considered here are in tension with astrophysical observations, since the evidence for a significant star-forming activity is confined in the inner part of the Galactic bulge, and the SFR is expected to steeply decrease at $r \simeq 0.5$ kpc.

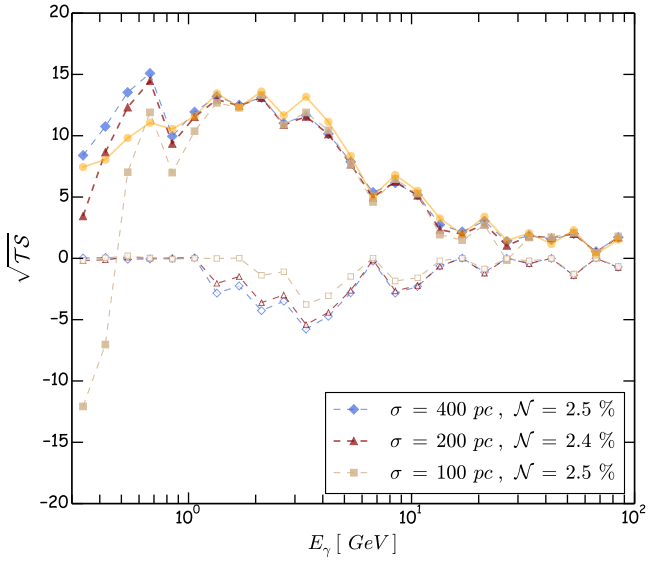

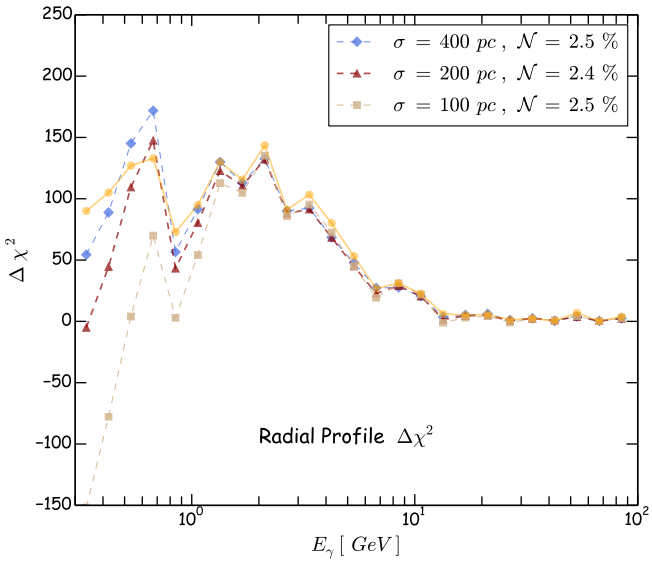

Figure 3.10: Upper panel: *TS, as shown in the upper-left panel of Fig. 3.5, for different values of the spike width, namely* $\sigma = 100 - 400$ *pc.* Lower panel: *Radial* χ^2*, as shown in the lower-right panel of Fig. 3.5, for different values of the spike width, namely* $\sigma = 100 - 400$ *pc.*

On the other hand, for small values of σ, below 200 pc, the fit of gamma-ray data with the spike significantly worsens for mid and lower energies , indicating an unsatisfactory description of the gamma-ray emission: in particular, a narrow spike exacerbates the problems highlighted in the previous section with longitude profiles. The origin of the problem is twofold: on one side, to roughly match the SFR in the CMZ, the normalization of the spike source term is relatively enhanced with respect to the choice of spike with greater

width σ, which implies a more pronounced central bump in the best-fit IC longitude profile; moreover, the shape of the IC emission for a narrow spike is significantly steeper than larger values of σ, as shown in Fig. 3.2. The resulting morphology is not only greatly disfavored by the low-energy tail of the spectrum, but it starts to be problematic also above the GeV.

- In order to provide a more realistic description of the inner Galaxy, one should take into account how the complex interplays in the GC environment impact on CR transport properties.

  In particular, we know that the regular Galactic magnetic field has a complex structure: besides a well-known pattern lying on the Galactic plane, in the detailed analysis of Ref. [134] the authors point out the existence of a X-shaped magnetic field component extending from the GC up to a Galactocentric radius $r \simeq 4$ - 5 kpc and to $z \simeq 2$ - 3 kpc. CR diffusion is expected to be anisotropic: according to the quasi-linear theory, valid in the low-turbulence limit, parallel diffusion should dominate over the perpendicular one, leading to an efficient CR escape due to parallel diffusion in the vertical direction. We checked several values of the ratio between the perpendicular and parallel diffusion components of the diffusion tensor (D_{zz}/D_{rr}) for each value of σ, but we did not find any relevant and solid improvement in the quality of the fit valid in the whole energy range.

- Although we chose Model A as a reference case, we verified that our results are not strongly dependent on the CR transport model. The same trends we discussed in detail in the previous section emerge if other CR propagation models are adopted. In particular, we have considered the conventional KRA model described in [175], and Model F in [292]. In both cases, we find that the spike plays a crucial role when the template-fitting algorithm is applied, and all the results presented in the previous section still hold.

The latter two points likely stem from the limitations that a standard template-fitting analysis implies in this context. Indeed, we wish to stress once again that although the template-fitting method is very powerful in addressing morphological agreements or flaws of a given theoretical model, there are some clear drawbacks on the information we can extract out of it. Since the free-floating of the templates is realized in each energy bin independently, the gamma-ray spectral features corresponding to the different components can be seriously altered, loosing their original spectral correlation in energy, and resulting in little control on the way the physical properties of the CR transport model are in general modified.

Eventually, we wish to remark that the additional source term proposed here provides extra gamma-ray emissivity also at energies larger than the GeV range analyzed in this work, with a progressively smaller angular extent in the leptonic channel, given that, due to the increase in the energy loss efficiency, electron diffusion is reduced on a shorter scale. This prediction may be tested in the near future, in the perspective of comparing low- and high-energy measurements by experiments such as ASTROGAM [309] and GAMMA-400 [310].

3.3 A confirmation of our findings

The inadequacy of the standard GDE models used for the analysis of the gamma-ray emission from the GC region has been more recently addressed in [311, 312]. Also in the case of Ref. [311, 312], the main motivation at the basis of the work comes from the expectation for a significant production of Galactic CRs in observed star-forming regions like the CMZ, along the lines of what already discussed at the beginning of Section 3.2.

In their study, the authors have first of all hypothesized that a fraction f_{H_2} of CRs has been injected with a spatial distribution tracing the density of collapsed H_2 in molecular clouds, with the remaining fraction $1 - f_{H_2}$ reflecting instead the injection of CRs due to the traditionally used distribution of SNRs [295–297]. They have consequently employed new high-resolution three-dimensional H_2 density maps that utilize gas flow simulations to resolve non-circular velocities in the inner Galaxy [313]. Moreover, they have assumed a simple power-law model for the star-formation rate [314] triggered in molecular clouds, characterized by a

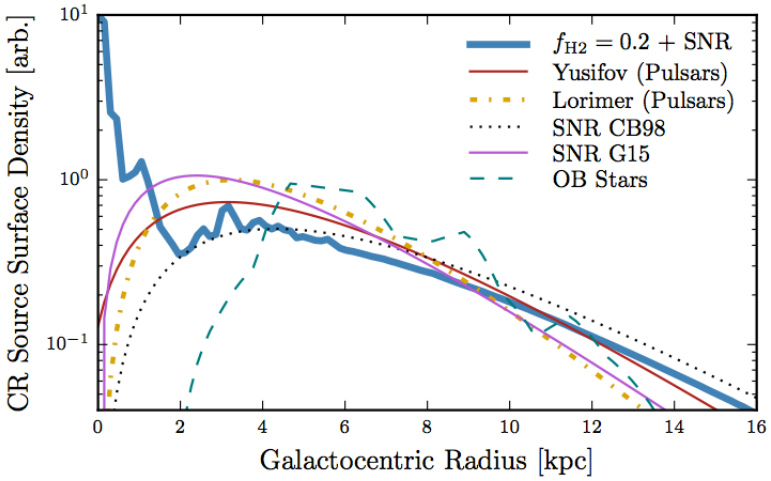

Figure 3.11: *The azimuthally averaged surface density of CR source distributions. For more details, see the caption of Fig. 1 in Ref. [312].*

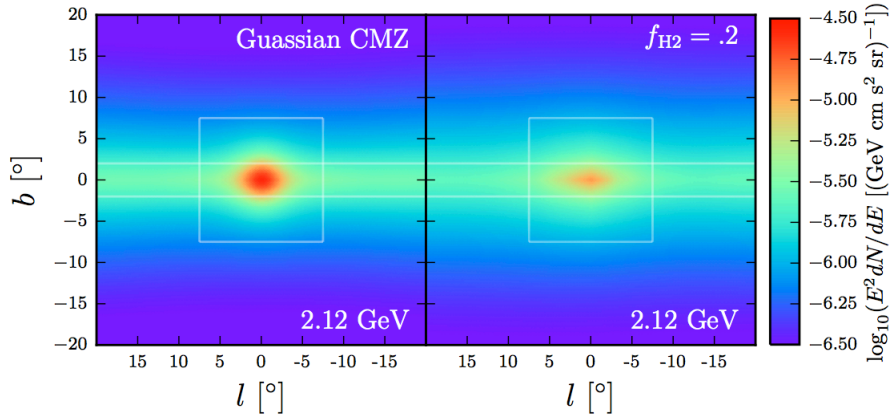

Figure 3.12: *From Ref. [312], the IC emission over the inner Galaxy at the fixed energy $E_\gamma = 2.12$ GeV when adding a Gaussian CR spike of width $\sigma = 200$ pc and proper normalization to fit the GeV excess versus the canonical model of [311, 312].*

spectral index n_s and a critical density ρ_c under which such star formation is frozen. Eventually, they have corrected the traditionally used source term through an additional CR injection contribution that traces the novel 3D H_2 gas distribution derived by them:

$$\mathcal{Q}(\vec{r}) \propto \begin{cases} 0 & \text{if } \rho_{H_2} < \rho_c \\ \rho_{H_2}^{n_s} & \text{if } \rho_{H_2} \geq \rho_c \end{cases} . \tag{3.7}$$

Such a source term reflects non-axisymmetric features like the bar and the spiral arms of the MW disk, that can be imprinted in the details of a 3D template for ρ_{H_2}. Beyond such refinements, the radial profile of this source term looks most importantly peaked towards the GC: as displayed in Fig. 3.11, the resulting total CR source term closely resembles the effect of the spike introduced by us in Eq. (3.5) on top of the standard source term. We can conclude that the main picture provided by our Gaussian ansatz for the radial profile of the new source term in the central region can be further supported and validated by a better physical modeling of the source distribution, exploiting the correlation with the gas density as in Eq. (3.7).

In the top-left panel of Fig. 3.12 we show the IC emission for the spike scenario with width $\sigma = 200$ pc and proper normalization to fit the GeV excess and the canonical star-formation based model of [311, 312] over the inner Galaxy ROI at the peak GC emission energy. While the morphology associated to the inverse Compton emission from our Gaussian spike is completely spherically symmetric (at least in the case of an isotropic diffusion tensor), the one of the $f_{H_2} = 0.2$ model is elongated along the plane. Note that the latter is more realistic, since in reality, the height of the CMZ is quite small, with $\sigma_z \simeq 45$ pc [211] rather than the few hundred pc implemented in our model. Making it more realistic would imply to

differentiate between the size of the radial width of the Gaussian source profile and the one related to its axial extension, namely $\sigma_r \sim \mathcal{O}(100)$ pc, while $\sigma_z \sim \mathcal{O}(10)$ pc. Notice also that the $f_{\rm H_2} = 0.2$ model in Fig. 3.12 features an axisymmetric structure from the MW bar which extends toward positive longitudes.

Despite some difference at the quantitative level, the overall picture of the study described above is qualitative the same provided by us in the previous section and the results in [311,312] fully support our conclusions. Performing a template-fitting analysis focussed on three distinct ROIs – the full sky, the inner Galaxy and the inner $15^\circ \times 15^\circ$ around the GC – and studying the impact of the main parameters characterizing the H_2 gas model, namely $f_{\rm H_2}$, n_s and ρ_c, the authors in [311,312] reach the following main conclusions:

- GDE models of the full sky strongly favor a CR injection distribution that includes a counterpart to star-forming regions;
- the features of the GC excess are significantly affected by the choice of the CR source distribution: postulating 20 - 25% of the cosmic-ray injection to trace the distribution of H_2 regions improves the global fit to the observed gamma-ray data, while it also decreases the intensity and significance of the GC excess;
- while n_s and ρ_c do not play a fundamental role in the final outcome of the analysis, a typical value of $f_{\rm H_2} \sim 0.2$ - 0.25 supported by the multi-wavelength analysis of the CMZ implies that the original roughly spherical morphology of the GC excess can get distorted at the level of being not compatible anymore with a DM interpretation.

In addition to the above results, the same authors have notably found a substantial improvement of the description of low-energy gamma-ray data (i.e. $E_\gamma \lesssim 1$ GeV) by implementing a radially outflowing wind at the Galactic Center, again supported by multi-wavelength evidence in favor of large wind speeds (i.e. $\gtrsim 500$ km/s) in the region (see, e.g., the detailed discussion in Ref. [315]). In the end, both our findings and the ones successively obtained in [311,312] point to the existence of a degeneracy between the intensity spectrum, and morphology of the GC emission and an enhanced IC emission near the GC, possibly connected to (physically motivated) CR injection sources in the environment.

A similar result has been recently claimed by the Fermi-LAT collaboration as well [316]. The collaboration has analyzed the $15^\circ \times 15^\circ$ region around the GC with specialized GDE models tuned on the gamma-ray sky out of this ROI. Finding point-source seeds for the same region using a method that does not rely on details of the GDE, the corresponding PS and GDE templates have been combined in

a maximum-likelihood fit to determine the interstellar emission across the inner $\sim$ 1 kpc around the GC and PSs over the region. The outcome of the analysis indicates that the inferred PS contribution can account only for the 15% of the emission, showing at the same time good correlation with the already known 3FGL catalogue [205], while best-fit GDE models in the ROI are characterized by a $\sim$ 20% component mainly due to IC from the inner region. In doing so, weakly asymmetric residual counts around the GC have been also found – but with large noise – for energies greater than 2 GeV. The collaboration has then studied the impact of a model for these residuals with a spatial distribution that peaks near the GC. While no explicit interpretation of the residuals has been provided, the Fermi-LAT analysis shows that the range of spectral parameters defining a model for the positive residual strongly depends on the assumed GDE. Moreover, despite the additional parameters introduced by the template for the residuals, the post-fitting IC flux still remains the dominant interstellar emission component over the inner region around the GC. According to Ref. [316], such finding suggests that CR electron and/or ISRF intensities in the ROI are likely higher than those usually implemented in baseline GDE modeling [157, 195]. Therefore, this result stands out along the lines of our refinement of GDE templates in virtue of the expected environmental complexity in the GC region.

3.4 Alternative scenarios and general outlook

The fact that CRs are injected in the central regions of the MW offers a valuable astrophysical explanation at the basis of the high statistical significance of the GeV excess. Besides this compelling possibility, a few competing scenarios accounting for an "extra component" have been suggested as well.

Among the proposed explanations, a non-thermal bremsstrahlung emission from a population of electrons scattering off neutral molecular clouds has been considered in [317, 318], while in [319] the authors have studied the interactions between the gas and protons accelerated by the super-massive black hole sitting at the GC. While those mechanisms may contribute to the excess emission in the innermost GC region, where the gas distribution is pretty uncertain, an extended signal up to a few kpc is very unlikely for these cases. Burst-like events connected to an active past of our Galaxy have also been investigated with interest [298, 320]. As already mentioned at the beginning of this chapter, the typical scenario arising from these cases is not very good at reproducing both the observed energy spectrum and the spatial morphology of the excess and – as a standalone solution to the problem – it is probably already disfavored [294].

A much more vivid debate in the community instead pertains to the role of unresolved PSs. In fact, whether or not there may be a plausible correlation between a yet-undetected PS population around the GC and the GeV excess signal is still a matter of ongoing investigation.

In this respect, as originally noted in Ref. [321, 322], promising candidates are millisecond pulsars (MSPs), i.e. pulsars with a rotational period of about few milliseconds, originating from old neutron stars that spun up through accretion of matter. The expected prompt gamma-ray emission from MSPs has soon appeared to be compatible with the excess spectrum peaked at few GeV [252, 253, 322, 323]. Moreover, the MSP distribution is expected to correlate with the star distribution, and therefore, in the bulge region of the Galaxy it may extend far enough from the Galactic plane so that the spatial morphology of the GC excess can also be addressed [251, 324].

On the other hand, stringent constraints on the MSP hypothesis, coming from our current observational knowledge about these astrophysical objects, must be taken into account. Exploiting the limits from the observed distribution of Fermi sources – including both sources known to be MSPs, and unidentified sources which could be associated to pulsars – in [325] it has been claimed that MSPs cannot account for more than $\sim$10% of the GeV excess in the inner Galaxy. In Ref. [191] the observational information on MSPs coming from the Australia Telescope National Facility has been collected together with the Fermi-LAT pulsar catalog in order to model the spatial distribution and gamma-ray emission of MSPs in the Galaxy. Through a dedicated Monte Carlo simulation, the authors have also obtained that the prompt emission from the population of predicted pulsars in the GC region (within the 1σ statistical uncertainty band) is roughly an order of magnitude smaller than the excess spectrum. Using the observed population of bright low-mass X-ray binaries (progenitor systems of MSPs) to estimate the number of MSPs in the inner Galaxy, in Ref. [326] the estimated contribution to the excess from these PSs has resulted being even smaller, around 1 - 5%. Moreover, stemming from measurements in the local Galactic environment, the modeling of the MSP luminosity function, along with the number of PSs resolved by Fermi allowed the authors to derive an upper limit on the MSP diffuse emission in strong tension with the hypothesis that most of the GC excess is originating from these objects.

On the basis of such findings, the viability of MSPs as an explanation to the GC excess should be considered as severely challenged. However, in Ref. [327] a parametric approach aimed at minimizing underlying theoretical priors involved in the estimate of the MSP gamma-ray luminosity function, together with the systematics associated to the Fermi PS catalogue, has shown that an unresolved

bulge population of MSPs is still a viable candidate for most or all of the GC excess within current observational and theoretical uncertainties.

Triggering renewed interest in the community, the MSP interpretation of the GC excess has received recent support by the results of two studies dedicated to an improved targeting of PSs [328, 329]. Implementing different statistical techniques, these two analyses obtain a very similar conclusion: studying the statistics of clustering in the photon measured count maps, there is a very high evidence in favor of a hitherto undetected population of (MSP-like) PSs, able to fully absorb the GeV gamma-ray excess. While the agreement between the two independent works is remarkable, both analyses are not free from certain limitations. First of all, the results of both studies are based on the analysis of one single energy bin – in correspondence to the inferred peak of the GC excess. This is demanded by the particular statistical methods implemented, which require a very large collection of photons in order to provide an informative statistical estimator. However, as a consequence of that, no spectral information imprinted in the observed counts can be either extracted from or exploited in these studies. Second, the impact of GDE models in this kind of analyses may be much more dramatic than what has been suggested in Ref. [328,329]. Both studies have considered only few simple variations of conventional diffuse emission templates, already finding a non-negligible impact of this ingredient in the final outcome. Most importantly, GDE models optimized for the inner Galaxy, i.e. with non-vanishing CR injection profile at the GC, have not been considered yet and therefore, their (likely relevant) impact on these analyses remains to be addressed. Eventually, as already envisaged in [328] and very recently investigated in Ref. [330], this kind of analyses may be potentially affected by relevant systematics. Indeed, the map of photon count residuals can possibly contain small-scale spatial structures due to the mis-modeling of backgrounds and foregrounds. Through the application of the statistical techniques in Ref. [328,329], these spurious features may be erroneously interpreted as sub-threshold PSs, as explicitly highlighted in [330].

To conclude, we wish to stress once again that the detailed features of the gamma-ray emission at the GC are prone to large systematic uncertainties stemming from bright astrophysical diffuse emission which must be removed in order to infer a putative "excess". As a result of that, it is probably very difficult to pin down a reliable estimate of the emission from dim PSs in the GC region [316]. From this perspective, it is even harder to claim any detection of some more exotic component – as it may be represented by Dark Matter particle annihilation – with any statistical confidence level. At the qualitative level, it is probably fair to say that a more convincing and complete picture of the gamma-ray emission at the

GC will be involving both a more realistic treatment of CRs in the region as well as a refined estimate of the emission from faint sub-threshold PSs.

Note that all the inconsistencies discussed so far may strongly point to such a combined scenario. On one side, as it stands out e.g. from Fig. 3.5, the original GC excess does not seem to be completely addressed by improved GDE models in the region. As already mentioned, the same conclusion has also been corroborated by [311, 312] and by the Fermi-LAT collaboration [316] as well. On the other hand, a standalone explanation with a MSP-like population in the bulge region of the Galaxy still looks very contrive. Most recent investigations on the characterization of such population [331] and its correlation with globular clusters in the region [332] keep pointing to a strong incompatibility with the standard properties expected from already known pulsars. Of course, one may still remain completely agnostic about the nature of the members of this undetected population and assume that no obvious counterpart of them shows up in the local Galactic environment. Leaving aside this rather conservative perspective, very recent studies [330, 333, 334] have focussed on the potentially informative high-energy tail of the excess spectrum in the inner Galaxy. For instance, in the context of pulsar interpretations, a high-energy tail could be naturally accommodated through the secondary gamma-ray emission of high-energy electrons accelerated in the pulsar magnetosphere and then interacting with both the ISM gas and the photons of the ISRF. Depending on the annihilation channel and the particle mass, also a DM interpretation of the excess could leave an important imprint at high energies via secondary emission, and a distinction between the two scenarios may be ideally possible [333]. While at present there is no definite clue for such a kind of "high-energy excess", a mild hint in favor of a radially spatial variation in the high-energy part of the excess spectrum has been recently noticed in [330, 334] and it certainly offers another compelling aspect to be further investigated in future analyses.

Chapter 4

4 Dwarf spheroidal Galaxies and Dark Matter limits

4.1 The satellites of the Milky Way

In Chapter 3 we have analyzed in detail the region around the Galactic Center (GC), highlighting on one side the appealing role it is playing in indirect detection searches for Dark Matter (DM), but also stressing the difficulties one inevitably encounters in the interpretation of a signal coming from such a rich and complex astrophysical environment.

The dwarf spheroidal satellites (dSphs) of the Milky Way can be certainly considered a prime target for Dark Matter indirect detection searches as well [335, 336]. First of all, they are relatively close to us and have fairly large DM densities [337–341], and hence are expected to have among the brightest DM-induced emissivities. Differently from the GC region, dSphs seem to be really ideal "DM laboratories": intrinsic emission from standard astrophysical sources can generally be neglected (they host old low-luminosity stellar populations and tiny – most often below detection sensitivities – amounts of gas [342, 343]); at the same time, most dwarfs are located at intermediate or high galactic latitudes where Galactic foregrounds are suppressed.

Multi-wavelength campaigns have therefore been promoted to search for DM signals, with some of the most impressive results obtained with γ-ray telescopes: e.g., the Fermi collaboration has recently published updated limits on weakly interacting massive particles (WIMPs), excluding pair annihilating cross sections at the level of WIMP thermal relic cross sections for DM masses lighter than about 100 GeV [291, 344]. Limits from these searches may be meaningfully translated into Particle Physics constraints (see e.g. [345–347]) and, as already mentioned at the end of Chapter 1, they seem to be in tension with the most popular DM interpretations of the GC excess [275, 277].

A few of the proposed signals (including the γ-ray flux from WIMP pair annihilations just mentioned or, e.g., the X-ray signal from sterile neutrino decays [41]) are

connected to prompt emission from DM particles [115]. As we have described in Chapter 1, in these cases the flux predictions can be conveniently factorized into a term depending on the DM particle physics embedding (specifying, e.g., for a WIMP: the mass, the annihilation cross section and the emission yields), and a term depending on the distribution of DM in the dwarf. For reader's convenience, we recall here the definition of the J-factor for DM pair annihilation signals, namely an angular and line-of-sight (l.o.s.) integral of the square of the DM density profile:

$$J \equiv \int_{\Delta\Omega} d\Omega \int_{\text{l.o.s.}} d\ell \, \rho^2(\vec{x}) \, . \tag{4.1}$$

The tight constraints on particle DM properties claimed from dwarf surveys reflect the assumption that fairly small observational and theoretical uncertainties affect these astrophysical factors: e.g. in the analysis of [291] mentioned above, limits are derived exploiting the full ensemble of known dwarfs and introducing a likelihood in which the J-factor dependence for each dwarf i follows a log-normal distribution of given central value $\overline{\log_{10}(J_i)}$ and width σ_i. For most of the so-called classical dwarfs – namely the only 8 dwarfs known before the first discoveries of ultra-faint ones as a byproduct in large scale structure surveys [348] – the assumed values of σ_i are of the order of 0.2 [291, 349, 350]. This translates into an uncertainty on J of about a factor of 1.5. At a superficial level, looking at Eq. (4.1) and assuming as known the distance of the object as well as – most crucially – the shape of the DM density profile, one would deduce that the normalization of the density profile can be inferred from observations with an uncertainty at the 20-25% level.

Indeed, once a specific approach has been adopted in determining such normalization, it is in general true that, in case of the classical dwarfs, the quality of kinematical data is adequate to provide fairly small statistical errors [351]. On the other hand, it is a much more delicate issue to address intrinsic systematic errors of the theoretical models and their impact on parameter determinations, including the normalization and more critically the J-factor itself.

Analyses in the literature give contradictory results: e.g. [352] presents a comprehensive discussion of the impact of different theoretical assumptions on interpreting kinematical data within the framework of the Jeans equation (a moment projection of the collision-less Boltzmann equation) in the spherical symmetric limit; they conclude that systematic biases and uncertainties on the J-factor for classical dwarfs are up to a factor of 3 to 4, including a rather mild impact of a factor of 2.5 from the effect of the dwarf being a triaxial system rather than a spherical one. On the other hand, the authors in [353] (see also Ref. [354]) show that the impact of axisymmetric models for non-spherical DM structures can be much more dramatic

on the mass at a reference radius, and hence the normalization of the profile, pointing to uncertainties of factors as large as 10 even for the classical dwarfs. However, a recent update along these lines [355], targeted on assessing J-factor uncertainties using non-spherical Jeans equations, finds quite milder differences in the comparison with up-to-date analogous studies treating MW satellites as spherical systems [291, 356, 357].

In the following, while still assuming as theoretical playground the Jeans equation for a spherically symmetric system, we aim to discuss the impact of the method that has been adopted in its solution by the vast majority of recent analyses. This goes into two steps:

1) to introduce parametric forms for the quantities appearing in the equation, namely the DM mass profile and the number density and velocity anisotropy profiles of the stellar populations used as dynamical tracers;

2) to sample the relative parameter space via Monte Carlo techniques in order to perform Bayesian inference, despite some loose theoretical and observational guidance.

In particular, it is well known that the stellar anisotropy profile introduces patterns of degeneracies in the result and is unfortunately scarcely constrained by observations. Several recent studies seem to indicate a minor impact on the J-factor estimates [351, 356–362], however they mostly refer to "blind analyses" involving a marginalization over a parameter space and integration measure which, not being driven by observations or by theory, are essentially an arbitrary choice.

Here, instead, we are going to examine the problem under a different perspective, exploiting an approach in which the Jeans equation is so-to-speak "inverted", rewriting the DM mass profile in a form in which its dependence on the stellar anisotropy profile becomes explicit. This method was originally outlined in two parallel analyses, see [363, 364]. We re-derive in full detail the inversion formula in Appendix B.2, providing a new compact form of it, suitable for numerical analyses. We then use it for the first time to discuss J-factor estimates: our efforts, indeed, go in the direction of providing a systematic study of dSph J-factors without the need to marginalize over unknown parameters.

4.2 The spherical Jeans analysis

Mass models for dwarf satellites of the Milky Way are most commonly derived exploiting a stellar population as a dynamical tracer of the underlying gravitational

potential well (and hence of the dominant mass component, namely the DM mass profile). Supposing that the tracers belong to a non-rotating pressure-supported population in dynamical equilibrium, one can assume that the stellar density function obeys a time-independent collision-less Boltzmann equation, to be solved projecting out velocity moments. Going to the limit in which the stellar and DM components are spherically symmetric, the second moment projection reduces to a single Jeans equation [365, 366], usually recast in the form:

$$\frac{dp}{dr} + \frac{2\,\beta(r)}{r} p(r) = -\nu(r)\,\frac{G_N \mathcal{M}(r)}{r^2}\,, \quad \text{with} \quad p(r) \equiv \nu(r)\sigma_r^2(r)\,. \tag{4.2}$$

This equation shows that the radial dynamical pressure $p(r)$, the product of the tracer number density profile $\nu(r)$ and the radial component of the velocity dispersion tensor $\sigma_r^2(r)$, can be expressed in function of $\nu(r)$ itself, as well as of the total mass profile $\mathcal{M}(r)$ and the orbital velocity dispersion anisotropy $\beta(r)$. The latter involves also the other two diagonal components of the velocity dispersion tensor σ_θ^2 and σ_ϕ^2, being defined as:

$$\beta(r) \equiv 1 - \frac{\sigma_\theta^2(r) + \sigma_\varphi^2(r)}{2\,\sigma_r^2(r)}\,. \tag{4.3}$$

$\beta(r)$ parametrizes the deviation of the velocity ellipsoid from a sphere of radius squared $\sigma_r^2 = \sigma_\theta^2 = \sigma_\varphi^2$ [366, 367]. By definition, $\beta(r)$ can cover the range $(-\infty, 1]$, where the lower (upper) extreme corresponds to tracers moving on purely circular (radial) orbits. The formal solution of Eq. (4.2) is:

$$p(r) = G_N \int_r^\infty dr' \frac{\nu(r')\mathcal{M}(r')}{r'^2} \exp\left[2\int_r^{r'} dr'' \frac{\beta(r'')}{r''}\right]\,. \tag{4.4}$$

The difficulty in fully exploiting this approach is that, despite the assumption of dynamical equilibrium and spherical symmetry at the bases of Eq. (4.2), the problem still involves three unknown functions: $\mathcal{M}(r)$, $\nu(r)$ and $\beta(r)$, to be inferred from only two quantities connected to observations:

1) the stellar surface density, namely:

$$I(R) = \int_R^\infty dr \frac{2r}{\sqrt{r^2 - R^2}}\,\nu(r)\,, \tag{4.5}$$

(here and everywhere in the following "R" refers to the l.o.s. projected radius, while "r" is the radius in the spherical coordinate system centered on the dwarf) which, assuming constant stellar luminosity over the whole system, is proportional to the surface brightness as mapped in photometric surveys

(see, e.g., [368]);

2) the l.o.s. velocity dispersion $\sigma_{los}(R)$, which traces the only velocity component accessible to spectroscopic measurements [340, 341]; the l.o.s. velocity dispersion profile can be expressed in terms of the radial dynamical pressure [369]:

$$\sigma^2_{los}(R) = \frac{1}{I(R)} \int_R^\infty dr \frac{2r}{\sqrt{r^2 - R^2}} \left[1 - \beta(r)\frac{R^2}{r^2}\right] p(r)\,. \tag{4.6}$$

The mapping of the three unknowns into two observables is usually done by introducing parametric forms for the three unknowns: the template for $\nu(r)$ is typically related to a $I(R)$ supported in stellar photometric studies, such as the Plummer [370], the King [371] and the Sersic [372] profiles. The mass profile $\mathcal{M}(r)$ originates from DM density profiles $\rho(r)$ usually motivated by:

- numerical N-body simulations of hierarchical clustering in cold DM cosmologies [373], such as, e.g., the Navarro-Frenk-White (NFW) profile [374] (with a $1/r$ singularity towards the center of the system and a scale radius r_n to set the transition into the $1/r^3$ scaling at large radii);
- phenomenological studies [375, 376] on the distribution of DM in galaxies, such as, e.g., the Burkert profile [377] (in this case the characteristic scale r_b sets the size of the inner constant density core, before the transition again into the $1/r^3$ regime at large radii).

Finally for what regards the stellar anisotropy profile $\beta(r)$, templates assumed in the literature (see e.g. [378–380]) reflect more simplicity arguments rather than profound physical motivations, ranging from some constant value to functions connecting two asymptotic values at large and small radii, eventually with some parameter setting the sharpness of the transition.

Attempts to break the degeneracy in Eq. (4.2) between $\mathcal{M}(r)$ and $\beta(r)$ using higher velocity moments [339, 381–385] or the determination of multiple tracer populations [386–388], together with the progress of N-body simulations [389–391], may represent a promising future opportunity to fully overcome current study limitations due to l.o.s. measurements available for these systems [392].

Given the large parameter space at hand, one needs an efficient scanning technique and careful addressing of error propagation: for $\nu(r)$ (or directly for $I(R)$) a frequentist fit of data is usually implemented, in case of the classical dwarfs most often referring to the data compilation in [368]. On the other hand, all recent analyses explore the parameter space connected to $\mathcal{M}(r)$ and $\beta(r)$ introducing a likelihood addressing the matching of the theoretical model for $\sigma_{los}(R)$ with data, and employ a Markov Chain Monte Carlo (MCMC) sampling in the context of

Bayesian inference. After a choice of priors and integration measures – which in case of the anisotropy function, as for the choice of the functional form, seem essentially arbitrary – one derives posteriors for the parameters defining $\mathcal{M}(r)$ or $\rho(r)$, as well as for derived quantities such as the J-factor introduced in Eq. (4.1) above. While this procedure gives for the classical dwarfs posteriors on J with small error bars, it is not transparent what is the impact of having selected given parametric forms, priors and integration measures, especially in the case of $\beta(r)$ for which a robust physical guidance is still missing.

4.3 General trends from an inversion formula

As mentioned before, the method we build on here has been already outlined in two parallel analyses, see [363, 364]. The starting point relies on the observation that the two available observables, namely Eqs. (4.5) and (4.6) above, correspond to the Abel transform f of a function $\widehat{f}$:

$$f(x) = \mathbf{A}[\widehat{f}(y)] = \int_x^\infty \frac{dy}{\sqrt{y-x}}\,\widehat{f}(y) \;\Leftrightarrow\; \widehat{f}(y) = \mathbf{A}^{-1}[f(x)] = -\frac{1}{\pi}\int_y^\infty \frac{dx}{\sqrt{x-y}}\,\frac{df}{dx}\,. \tag{4.7}$$

In fact, looking back at Eq. (4.5) the surface density $I(R^2)$ is the Abel transform of the number density profile $\nu(r)$ (everywhere in the following we will use $\widehat{I}(r^2)$ to indicate the number density profile instead of $\nu(r)$). In a similar fashion, introducing the projected dynamical pressure, $P(R) \equiv \sigma_{los}^2(R)\, I(R)$, this expression can be manipulated (see Appendix B.2 for a detailed derivation) inverting it into a formula for the radial dynamical pressure:

$$p(r) = [a_\beta(r) - 1]\int_r^\infty dr' \mathcal{H}_\beta(r,r')\,\frac{d\widehat{P}}{dr'} \tag{4.8}$$

where $\widehat{P}(r^2)$ is the inverse Abel transform of $P(R^2)$ and we defined:

$$a_\beta(r) \equiv -\frac{\beta(r)}{1-\beta(r)}\,, \quad \text{and} \quad \mathcal{H}_\beta(r,r') \equiv \exp\left(\int_r^{r'} dr'' \frac{a_\beta(r'')}{r''}\right)\,. \tag{4.9}$$

Inserting this result into the Jeans equation [366], Eq. (4.2), one can find the mass profile of the system:

$$\mathcal{M}(r) = \frac{r^2}{G_N\,\widehat{I}(r)}\left\{-\frac{d\widehat{P}}{dr}[1-a_\beta(r)] - \frac{a_\beta(r)\,b_\beta(r)}{r}\int_r^\infty dr' \mathcal{H}_\beta(r,r')\,\frac{d\widehat{P}}{dr'}\right\}\,, \tag{4.10}$$

with

$$b_\beta(r) \equiv 3 - a_\beta(r) + \frac{d\log a_\beta}{d\log r}\,. \tag{4.11}$$

An expression equivalent to Eq. (4.10) can be extracted from Ref. [364], while Ref. [363] gives explicit formulas for several simple anisotropy models; it is however the first time such a compact form in terms of observables is given, showing that the mass profile depends on the anisotropy profile only through the function $a_\beta(r)$ as defined above. The expression in Eq.(4.11) shows that, at given $a_\beta(r)$, the mass profile can be properly reconstructed if the projected dynamical pressure can be efficiently constrained from data. From the expression just derived one can read out the behaviour of the mass function in some special limits that will be useful in the discussion below. First of all, in case of isotropic stellar orbits, namely $\beta(r) \to 0$ for any r (and hence $a_\beta(r) \to 0$):

$$\mathcal{M}_{\beta=0}(r) = -\frac{r^2}{G_N\,\widehat{I}(r)}\frac{d\widehat{P}}{dr}\,. \tag{4.12}$$

For circular orbits instead, i.e. $\beta(r) \to -\infty$ for any r (and hence $a_\beta(r) \to 1$, $b_\beta(r) \to 2$):

$$\mathcal{M}_{\beta\to-\infty}(r) = -\frac{2}{G_N\,\widehat{I}(r)}\int_r^\infty dr' r'\frac{d\widehat{P}}{dr'}\,. \tag{4.13}$$

Eq. (4.10) is derived under the hypothesis $\beta \neq 1$. To take the exact radial orbit limit it is simpler to notice that the radial pressure for $\beta = 1$ (i.e. $a_\beta \to -\infty$) takes the form:

$$p_{\beta=1}(r) = -r\frac{d\widehat{P}}{dr}\,, \tag{4.14}$$

and replacing this into the Jeans equation, Eq. (4.2), one finds:

$$\mathcal{M}_{\beta=1}(r) = \frac{1}{G_N\,\widehat{I}(r)}\frac{d}{dr}\left(r^3\frac{d\widehat{P}}{dr}\right)\,. \tag{4.15}$$

4.3.1 A mass estimator for dwarf galaxies?

As first noticed in MCMC analyses, regardless of what is assumed for the stellar velocity anisotropy $\beta(r)$, all models fitting the l.o.s. velocity dispersion profile tend to have approximately the same mass at a scale corresponding to about the surface brightness half-light radius [393–400]. In Ref. [364] a rationale for the existence of such a mass estimator is provided through an analytic manipulation of the solution of the Jeans equation. Briefly recapping their argument, it is useful to consider the difference between the mass profile $\mathcal{M}(r)$ for a generic anisotropy profile and

$\mathcal{M}_{\beta=0}(r)$; after some algebra one finds:

$$\mathcal{M}(r) - \mathcal{M}_{\beta=0}(r) = -\frac{\beta(r)\, r\, \sigma_r^2}{G_N} \left(\frac{d\log \widehat{I}}{d\log r} + \frac{d\log \sigma_r^2}{d\log r} + \frac{d\log \beta}{d\log r} + 3 \right) . \tag{4.16}$$

Among the terms within brackets on the r.h.s., towards the outskirts of the dwarf, the logarithmic derivative of the stellar number density $\widehat{I}(r)$ rapidly varies from close to zero to a negative number. In the same region, the l.o.s. velocity dispersion is generally close to being flat and also σ_r^2 is arguably not too rapidly varying. If one now assumes that also $\beta(r)$ does not have a sharp change in that region, the difference in Eq. (4.16) is approximately zero at the radius r_* defined as:

$$-\left.\frac{d\log \widehat{I}}{d\log r}\right|_{r=r_*} = 3\,. \tag{4.17}$$

Since this condition does not depend on β, $\mathcal{M}$ almost matches $\mathcal{M}_{\beta=0}$ at r_* regardless of the stellar anisotropy:

$$\mathcal{M}(r_*) \simeq \mathcal{M}_{\beta=0}(r_*) \simeq \frac{3}{G_N} \langle \sigma_{los}^2 \rangle\, r_* \equiv \mathcal{M}_*\,, \tag{4.18}$$

where in the second step the symbol $\langle\ \rangle$ stands for a weighted average on the stellar number density, and $\langle \sigma_{los}^2 \rangle$ has been factorized out in computing $\widehat{P}(r)$ and implementing it in Eq. (4.12).

We can check here this result with the formulas derived at the beginning of this section. We start from a simple model where $\sigma_{los}^2(R)$ is assumed to be just a constant σ_{los}^2, and the stellar profile is described by a Plummer model [370], a case in which the Abel transform can be performed analytically:

$$I(R^2) = \frac{I_0}{\pi R_{1/2}^2} \frac{1}{(1 + R^2/R_{1/2}^2)^2} \;\Leftrightarrow\; \widehat{I}(r^2) = \frac{3 I_0}{4\pi R_{1/2}^3} \frac{1}{(1 + r^2/R_{1/2}^2)^{\frac{5}{2}}}\,. \tag{4.19}$$

Under these two working hypotheses, the mass profile in the isotropic case has also a simple analytical form:

$$\mathcal{M}_{\beta=0}(r) = \frac{r\, \sigma_{los}^2}{G_N} \frac{5\, r^2/R_{1/2}^2}{1 + r^2/R_{1/2}^2}\,, \tag{4.20}$$

while Eq. (4.17) gives $r_* = \sqrt{3/2}\, R_{1/2}$. Assuming also a constant anisotropy profile, $\beta(r) = \beta_c$, in the upper panel of Fig. 4.1 we show the relative difference in mass $|\Delta\mathcal{M}(r)|/\mathcal{M}_{\beta=0}(r) \equiv |\mathcal{M}_{\beta=\beta_c}(r) - \mathcal{M}_{\beta=0}(r)|/\mathcal{M}_{\beta=0}(r)$ versus the quantity $2^{a_{\beta_c}}$, useful to have circular and radial stellar anisotropies equally spaced in the segment

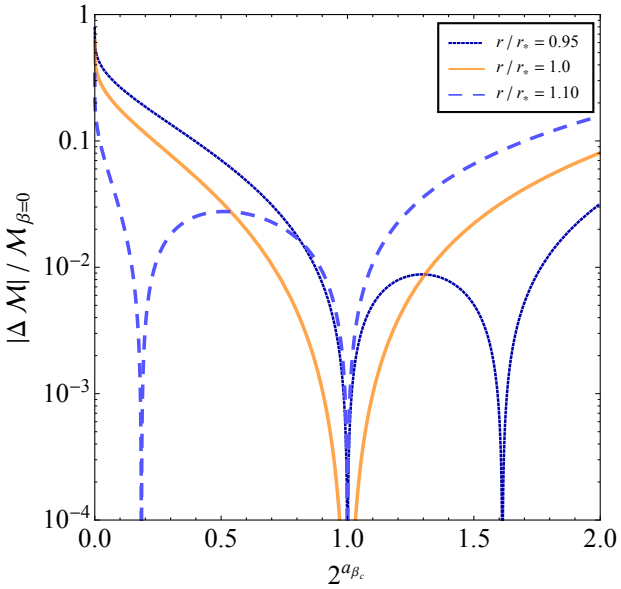

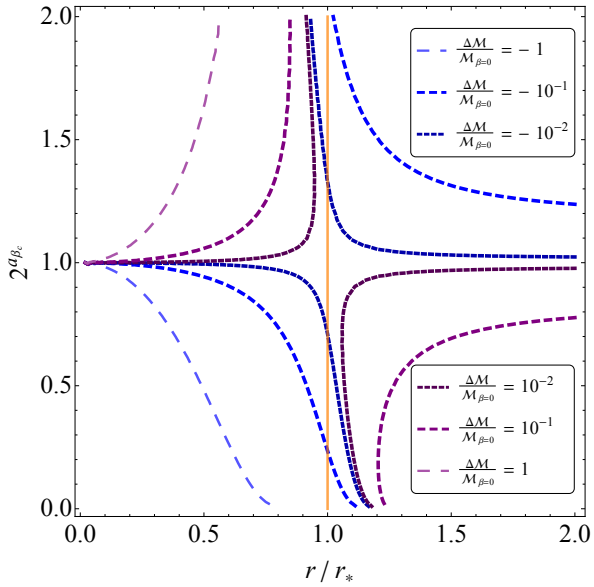

Figure 4.1: Upper panel: *Difference in mass profiles,* $\Delta\mathcal{M}(r) \equiv \mathcal{M}_{\beta=\beta_c}(r) - \mathcal{M}_{\beta=0}(r)$*, relative to the isotropic case,* $\mathcal{M}_{\beta=0}(r)$*, for the model with constant* σ_{los}*, Plummer stellar profile and constant orbital anisotropy, as a function of* $2^{a_{\beta_c}}$*. The orange, light blue and dark blue curves correspond, respectively, to a radius equal to* $r_* = \sqrt{3/2}\, R_{1/2}$*, 5% lower, 10% larger.* Lower panel: *Isolevels for fixed relative mass difference in the plane* $2^{a_{\beta_c}}$ *versus* r/r_* *within the same set of assumptions. The vertical orange line indicates* r_* *as expected mass estimator.*

$[0, 2]$ (i.e. 0 corresponds to radial, 1 to isotropic and 2 to circular orbits). The solid orange line corresponds to $r = r_*$ and shows that in the specific simple model under consideration the goodness of r_* and $\mathcal{M}_*$ as mass estimator is within a level of about 8% going to circular orbits, while it degrades to 10% and larger towards radial

orbits (in the purely radial limit derived in Eq. (4.15) the discrepancy reaches the value of 75%). Also shown in the plot is the relative mass difference at $r = 0.95\, r_*$ and $r = 1.1\, r_*$ for which there is a better match, respectively, in the radial and circular regimes, as well as a larger discrepancy in the opposite regimes. In the lower panel of Fig. 4.1 we show the isolevels for fixed relative mass difference in the plane $2^{a_{\beta_c}}$ versus r/r_*; one can see that – still in the same model introduced above – the mass difference is minimized along a curve that is slightly tilted with respect to the estimator proposed in Eq. (4.18), $r = r_*$. On the other hand moving away from r_* the match rapidly diminishes in one of the two regimes; for example, taking $r = R_{1/2} \simeq 0.82\, r_*$ as estimator radius is in our example a significantly worse choice, with relative mass differences at the level of 15% for purely circular orbits and raising up to the level of 150% in the radial regime. The 3D half-light radius proposed in [364], namely $r_{1/2} \simeq 1.3\, R_{1/2} \simeq 1.06\, r_*$ for the Plummer case, actually provides a better choice.

The failure of $\mathcal{M}_*$ as an exact estimator stems from the fact that even assuming that σ_{los} is constant, for $\beta \neq 0$ there is still a non-negligible radial dependence in σ_r (for $\beta = 0$ one trivially gets $\sigma_r(r) = \sigma_{los}$). This is shown in Fig. 4.2 where we plot the logarithmic derivative of the radial dynamical pressure versus r/r_*. This quantity is related to $\sigma_r(r)$ via:

$$\frac{d\log p}{d\log r} = \frac{d\log \sigma_r^2}{d\log r} + \frac{d\log \widehat{I}}{d\log r}\,, \tag{4.21}$$

and hence, for $\beta = 0$ and constant σ_{los}, it coincides with the logarithmic derivative of the stellar number density $\widehat{I}$. In Fig. 4.2 $-d\log\widehat{I}/d\log r$ is plotted with a dashed line; by definition it crosses the value of 3 at r_*. The blue band on the upper panel shows the span in the logarithmic derivative for $p(r)$ when varying β_c in the whole range of $(-\infty, 1]$ (respectively, upper and lower boundary of the band). The intersection of the band with the horizontal line at the value of 3 gives the shift on r needed to get $\Delta\mathcal{M} = 0$; the one with the vertical line at $r = r_*$ gives instead the magnitude of the departure of $\mathcal{M}_*$ from being an exact mass estimator.

Although the assumptions in the model we considered may appear rather drastic, the trends displayed are actually general. First, the hypothesis of constant σ_{los} is not critical. Taking into account that available kinematical informations (see, for example, the binned data in [397]) suggest l.o.s. velocity dispersions to be nearly flat in the region around r_*, we can parametrize $\sigma_{los}(R)$ via the linear expression $c_0 + c_1\, R/R_{1/2}$ and vary the slope c_1/c_0 in a generous range encompassing trends usually reported in literature, as e.g. those in [397] (note however that the error associated to an overall normalization, while propagating on $\mathcal{M}_*$, does not enter in

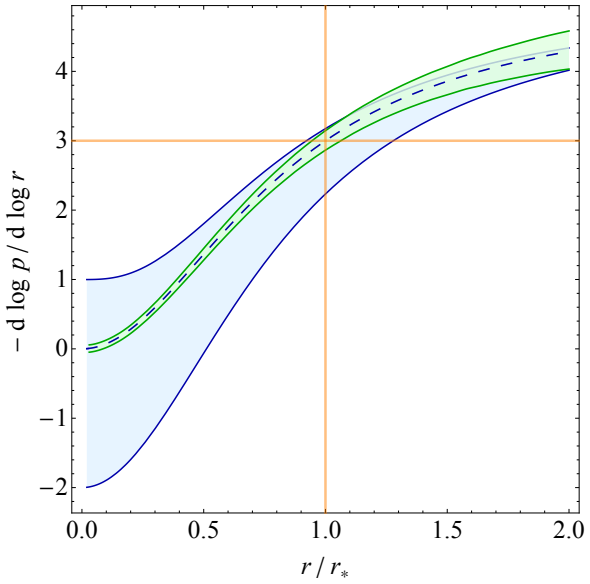

Figure 4.2: Upper panel: *Logarithmic derivative of the dynamical pressure for a simple model with constant orbital anisotropy and Plummer stellar profile versus* r/r_*. *The blue band is relative to the case of constant l.o.s. velocity dispersion and* β_c *varied in* $(-\infty, 1]$, *while the green one is obtained assuming a linear form in* $R/R_{1/2}$ *with slope* $\pm 6\%$ *and* $\beta = 0$. Lower panel: *Same quantity assuming constant* σ_{los} *and* $\beta = 0$, *but for the stellar profiles introduced in Eq. (4.19), Eq. (4.22)-(4.23). The bands reflect typical uncertainty on the characteristic scale parameter of the stellar template.*

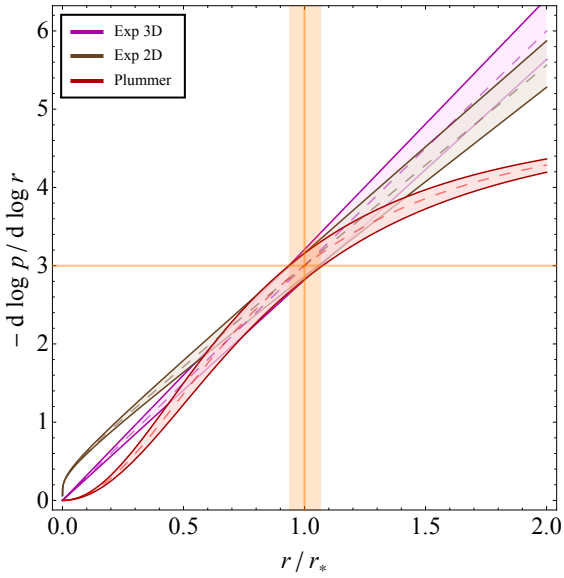

relative mass differences). As can be seen in the upper panel of Fig. 4.2 the impact of this uncertainty is marginal with respect to the one due to the orbital anisotropy. The same conclusion holds when considering also the second ingredient at hand, the modeling of the stellar distribution. As alternatives to the Plummer model, we

introduce the two following exponential templates:

$$I(R^2) = \frac{I_0}{2\pi R_e^2} \exp\left(-\frac{R}{R_e}\right) \;\Leftrightarrow\; \widehat{I}(r^2) = \frac{I_0}{2\pi^2 R_e^2} K_0\left(\frac{r}{R_e}\right) , \tag{4.22}$$

for which $r_* \simeq 2.54\, R_e \simeq 1.51\, R_{1/2}$, and:

$$I(R^2) = \frac{I_0}{4\pi r_e^2} \frac{R}{r_e} K_1\left(\frac{R}{r_e}\right) \;\Leftrightarrow\; \widehat{I}(r^2) = \frac{I_0}{8\pi r_e^3} \exp\left(-\frac{r}{r_e}\right) , \tag{4.23}$$

for which $r_* = 3\, r_e \simeq 1.48\, R_{1/2}$ ($K_n(x)$ is the modified Bessel function of the second kind). The functions above qualitatively reproduce typical realizations of a multi-parameter template like the Sersic profile, while differing substantially in the inner region from the Plummer model (the King model is instead qualitatively equivalent to the Plummer). Back to the working hypothesis of constant σ_{los} and $\beta = 0$, we plot in the lower panel of Fig. 4.2 the logarithmic derivative of $p(r)$ as a function of r/r_* for the three stellar profiles. The uncertainty bands displayed are obtained by the generation of a set of surface brightness mock data with binning and associated errors matching typical photometric maps of the 8 classical dSphs as in [368]. Although within a given stellar profile the impact on $\mathcal{M}_*$ from our estimated uncertainty on r_* is negligible as shown in Fig. 4.2, a higher impact derives from the mis-reconstruction of the stellar profile within a wrongly assumed parametric form, see the shift in r_* with respect to the observable radius $R_{1/2}$ between the Plummer model and the two exponential profiles.

To summarize this part of the discussion, we find that the uncertainty on the dwarf mass estimator is dominated by the kinematical determination of the normalization on σ_{los} as long as models with radial-like tracer orbits are not included in the analysis. While general criteria hinting for unphysical phase-space densities in connection to radial-like tracer orbits are present in literature (see e.g. [401, 402]), a rigorous theorem for the exclusion of these scenarios holds only at the center of the system [403].

4.3.2 Extrapolating to inner radii: density profiles

While in the standard approach to solve the Jeans equation, Eq. (4.2), physical mass profiles are automatically obtained imposing a "physical" parametric ansatz, there is no a priori guarantee that the procedure proposed here gives physical outputs. A first basic check is on the positivity of the solution of Eq. (4.10) at any radius. E.g. in the simplified model introduced above one finds a non-trivial constraint on the allowed range of orbital anisotropies. This is shown in Fig. 4.3

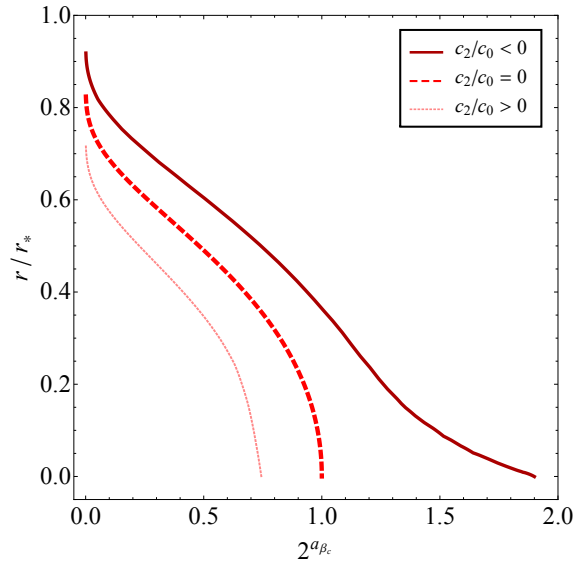

Figure 4.3: *Isolevel for $\mathcal{M} = 0$ in the plane β_c - r/r_* assuming a Plummer stellar template: The red dashed line corresponds to the case of constant σ_{los} and delimits the region above the curve where $\mathcal{M} > 0$ from the one where the mass becomes negative. Exploiting a quadratic expression in R for $\sigma_{los}(R)$, we plot also a dark red (light red dashed) line that corresponds to a convex (concave) tilt in the extrapolation of the constant σ_{los} value towards inner radii, using as a reference $c_2/c_0 = 0.5$ and $c_1/c_0 = -0.8$, ($c_2/c_0 = -1.4$ and $c_1/c_0 = 2.3$).*

in the plane $2^{a_{\beta_c}}$ - r/r_*, where isolevels for $\mathcal{M} = 0$ are displaced in the limit of constant orbital anisotropy, marking the minimum radius at which a solution of Eq. (4.10) is positive. In particular, the red dashed line corresponds to the case of constant σ_{los} and Plummer surface brightness. One can see that, within this setup, positive mass solutions can be extrapolated down to $r = 0$ only when $\beta_c \leq 0$. On the other hand, the extrapolation to $r \to 0$ critically depends on what is assumed for the extrapolation of $\sigma_{los}(R)$ for $R \to 0$. To sketch this effect we introduce as sample parametrization for the l.o.s. velocity dispersion the form:

$$\sigma_{los}(R) = \begin{cases} c_0 + c_1(R/R_{1/2}) + c_2(R/R_{1/2})^2 & \text{iff } R/R_{1/2} \leq 1/2 \ , \\ \text{constant} & \text{iff } R/R_{1/2} > 1/2 \ . \end{cases} \tag{4.24}$$

Fig. 4.3 shows that an inner concave tilt of $\sigma_{los}(R)$ forces to restrain to progressively more negative values of β_c (with a_β approaching 1), while a concave one allows for radially anisotropic stellar velocity profiles.

In general, the positivity of the mass is not the only condition we would like to supplement the Jeans inversion with: e.g. the mass profile should not decrease going to larger radii (i.e., up to the cutoff of the profile). In the following, we will

be actually more restrictive and define as a physical outcome of our inversion the model satisfying the following requirements:

$$\mathcal{M}(r) > 0 \ , \ \rho(r) = \frac{1}{4\pi r^2}\frac{d\mathcal{M}}{dr} > 0 \ , \ \frac{d\rho}{dr} \leq 0 \quad \forall \ r > 0 \ . \tag{4.25}$$

Assuming that the density of the DM profile $\rho(r)$ provides the dominant component to the dSph potential well, the third condition ensures the potential well to be monotonic and hence provides a necessary condition of stability for the model. Checking a posteriori these conditions, $\rho(r)$ is simply obtained taking the derivative of the mass function, Eq. (4.10):

$$\begin{aligned} 4\pi G_N \, r^2 \, \rho(r) \quad = \quad & - a_\beta \, b_\beta \left[1 - a_\beta - \frac{d\log \widehat{I}}{d\log r} + \frac{d\log a_\beta b_\beta}{d\log r}\right] \left(\frac{1}{\widehat{I}} \int_r^\infty dr' \mathcal{H}_\beta(r,r') \, \frac{d\widehat{P}}{dr'}\right) \\ & - [1 - a_\beta] \, \frac{d}{dr}\left(\frac{r^2}{\widehat{I}}\frac{d\widehat{P}}{dr}\right) + a_\beta \left[\frac{d\log a_\beta}{d\log r} + b_\beta\right] \left(\frac{r}{\widehat{I}}\frac{d\widehat{P}}{dr}\right) \ . \end{aligned} \tag{4.26}$$

Among the three terms on the r.h.s., only the first contributes in the limit of isotropic motion of the tracers ($\beta \to 0$ or equivalently $a_\beta \to 0$); assuming also that the l.o.s. velocity dispersion is constant, one simply finds:

$$\rho_{\beta=0}(r) = \frac{\sigma_{los}^2}{4\pi G_N \, r^2} \frac{d}{dr}\left(-r \frac{d\log \widehat{I}}{d\log r}\right) \ . \tag{4.27}$$

For such profile to have a core (namely: $d\log\rho_{\beta=0}/d\log r \to 0$ for $r \to 0$), the logarithmic slope of the stellar density profile needs to scale as r^2 towards the center of the system. E.g., considering a multi-parameter stellar template like the Zhao profile [404]:

$$\widehat{I}(r) = \frac{\widehat{I}_0}{\left(\frac{r}{r_s}\right)^\gamma \left[1 + \left(\frac{r}{r_s}\right)^\alpha\right]^{\frac{\delta-\gamma}{\alpha}}} \ , \tag{4.28}$$

where γ and δ represent the inner and outer slope of the profile, and r_s and α the scale radius and the smoothness of the transition between the inner and outer scaling, the logarithmic slope is:

$$\frac{d\log \widehat{I}}{d\log r} = -\gamma - (\delta - \gamma)\frac{\left(\frac{r}{r_s}\right)^\alpha}{1 + \left(\frac{r}{r_s}\right)^\alpha} \ , \tag{4.29}$$

and a cored profile is obtained only in case $\gamma = 0$ and $\alpha = 2$. For any $\gamma > 0$ the scaling of the DM profiles jumps to $1/r^2$, as in the isothermal sphere model.

Looking back at Eq. (4.19), one sees that the Plummer model belongs exactly to the class of the Zhao profiles providing a core in $\rho_{\beta=0}(r)$ if σ_{los} is constant. This is

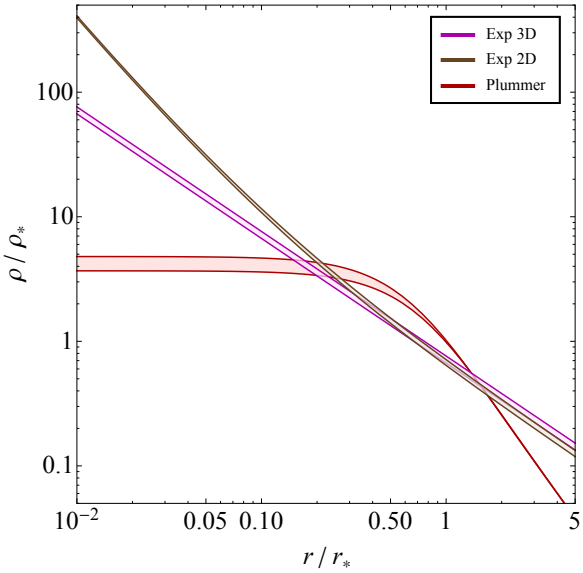

Figure 4.4: Upper panel: *Density profile of the system in the model with constant σ_{los} and isotropic tracer orbits, for the choices of stellar template: a Plummer model, an exponential profile for the stellar density and for the surface brightness. The error bands reflect the uncertainty on the stellar model assumed as in Fig. 4.2. Each profile is normalized to $\rho_* = \rho(r_*)$ in the Plummer case.* Lower panel: *Density profile assuming the Plummer surface brightness and $\beta = 0$, parametrizing $\sigma_{los}(R)$ with a linear expression in R (green band) and angular coefficient varied as in Fig. 4.2. In the same plot, the effect on $\rho(r)$ due to a departure from a constant σ_{los} for radii $R \leq R_{1/2}/2$, slightly tilting its constant profile according to a convex (concave) quadratic ansatz in R, i.e. using $c_2/c_0 = 0.1$ and $c_1/c_0 = -0.3$ ($c_2/c_0 = -0.1$ and $c_1/c_0 = 0.3$).*

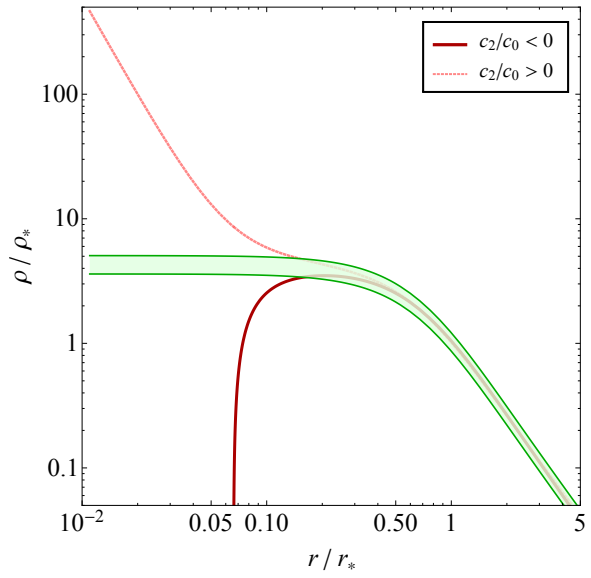

also shown in the upper panel of Fig. 4.4, where we plot the result for the inversion within the assumptions of constant σ_{los} and $\beta = 0$. In the same plot we show also the resulting case of the two exponential stellar templates introduced in Eq.(4.22)-(4.23). Note that an exponential surface brightness implies a logarithmically divergent stellar number density and hence a scaling of the inner density of $(r \log r)^{-2}$, while the (cored) exponential stellar density gives a $1/r$ inner density scaling, standing in between the cored case and singular isothermal sphere. Indeed, the Plummer model is the simplest stellar template we can consider which provides a core in the density profile. Since cored profiles are of particular importance when estimating minimal values for the l.o.s. integral of squared densities, it is the case we will concentrate on in the following.

Before discussing the case of $\beta \neq 0$, it is interesting to assess how the density profile is affected by a mild departure from the approximation of constant σ_{los}. The green band in the lower panel of Fig. 4.4 shows the very mild impact on $\rho(r)$ when we implement the linear scaling of the l.o.s. velocity dispersion already introduced in Fig. 4.2. For the quadratic scalings already implemented in Fig. 4.4 – even using much milder concave and convex tilts for $\sigma_{los}(R)$ – one sees instead a rather drastic change in $\rho(r)$, with a sharp enhancement of the inner density for a convex perturbation and an unphysical solution induced by the concave tilt. Associating the trends seen in both panels of the figure, one can deduce that a cored profile, standing also at the border with unphysical solutions, is obtained in the inversion procedure only via a fine adjustment between the trend imposed by the choice of stellar number density profile and that from the $R \to 0$ scaling of $\sigma_{los}(R)$.

We are now in the position to address the implications on $\rho(r)$ of a non-vanishing orbital anisotropy, considering first of all the case in which it does not depend on the radial coordinate, i.e. $\beta(r) = \beta_c$. Looking back at Eq. (4.26), also the second and the third term on the r.h.s. give a contribution to $\rho(r)$; the second term however has the same $r \to 0$ scaling as the first, hence does not alter the discussion just presented for $\rho_{\beta=0}(r)$. The third term instead introduces a non-trivial dependence on a_{β_c} of the inner radial slope. Assuming $a_{\beta_c} \neq 1$, the scaling can be read out from the corresponding logarithmic derivative diminished by 2 (taking into account the r^2 factorized on the l.h.s. of Eq. (4.26)):

$$\frac{d}{d\log r}\left[\log\left(\frac{1}{\widehat{I}}\int_r^\infty dr' \mathcal{H}_\beta(r,r')\,\frac{d\widehat{P}}{dr'}\right)\right] - 2 = -2 - a_{\beta_c} - \frac{r^{a_{\beta_c}}\frac{d\widehat{P}}{dr}}{\int_r^\infty dr' r'^{a_{\beta_c}}\frac{d\widehat{P}}{dr'}} - \frac{d\log\widehat{I}}{d\log r}. \tag{4.30}$$

In general the term $-2 - a_{\beta_c}$ is the most relevant, driving $\rho(r)$ to a scaling that is even more singular than the singular isothermal sphere in case of circularly

anisotropic profiles; the term in the logarithmic derivative of $\widehat{I}$ can at most mitigate the singularity in case $\widehat{I}$ itself is singular. The third term on the r.h.s. of Eq. (4.30) is in general less relevant; for constant σ_{los} and a Plummer $\widehat{I}$, in the limit $r \to 0$ it is equal to 0 if $a_{\beta_c} \geq -2$, and to $a_{\beta_c} + 2$ for $a_{\beta_c} < -2$. In this last case, one would apparently get a cored profile; note however that $\rho(r)$ is obtained by summing this contribution to the first two terms in Eq. (4.26), and, in the same limit, these drive $\rho(r)$ to an unphysical result, with the negative mass solution already discussed above. Analogously to what is shown in Fig. 4.4, a proper readjustment of the inner radial scaling of $\sigma_{los}(R)$ would be needed, requiring however a even more severe tuning to get physical solutions with a core [405], since $\sigma_{los}(R)$ impacts also on the scaling in Eq. (4.30).

A further subtle point regards the limit of $a_{\beta_c} \to 1$. When β_c approaches extreme negative values, the logarithmic derivative of $\widehat{I}$ appears as an extra multiplicative factor in the third term on the r.h.s. of Eq. (4.26) and hence its radial scaling (the logarithmic derivative of the logarithmic derivative of $\widehat{I}$) should be added to Eq. (4.30). Referring again to the Zhao profile in Eq. (4.29), this contribution is 0 if $\gamma \neq 0$, it is equal to $+\alpha$ if $\gamma = 0$. Back to the Plummer model and constant σ_{los} one would then find a scaling of the density profile that goes like $r^{-2-a_{\beta_c}+\alpha} \to 1/r$, as opposed to $r^{-2+a_{\beta_c}}$ valid for $0 < a_{\beta_c} < 1$.

In the upper panel of Fig. 4.5 we show the slope of the density at the fixed value $r = 0.05\, r_*$ as a function of all the set of a_{β_c} that provide a physical solution (see Eq. (4.25)) in our Jeans inversion approach. The resulting blue band in the plot highlights qualitatively the trend analyzed so far: exploring even smaller ratios of r/r_*, one would retrieve the linear $-2 - a_{\beta_c}$ scaling with sudden transition of $d\log\rho/d\log r$ to 0 at $a_{\beta_c} = 0$ and to -1 at $a_{\beta_c} = 1$. Once we leave the center of the dSph to move towards its outskirts, such a behaviour related to the allowed physical solutions gets relaxed: e.g. at $r = r_*/2$, within the uncertainty of the Plummer profile, physical densities are allowed up to $\beta_c = 1/2$, scaling with a power law index between -1.5 and 0, as represented by the blue band in the lower panel of Fig. 4.5. Also shown in the same figure is the value of the profile at the two chosen radii normalized to $\rho_* = \rho_{\beta=0}(r_*)$. In the central region of the system there is a smooth, but sharp, variation of the density varying a_{β_c}, spanning roughly two orders of magnitude. On the other hand, at large radii the variation in $\rho(r)$ is within 50%.

The subtle limit $a_{\beta_c} \to 1$ could have been inferred also looking at the behaviour of the mass profile in the case of purely circular stellar motion. In fact, for the model

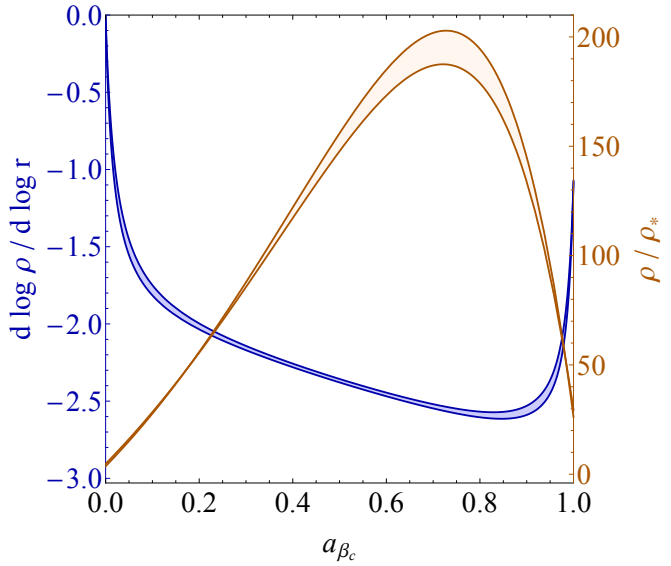

Figure 4.5: Upper panel: *Logarithmic slope (blue colour) and density profile normalized at* $\rho_* = \rho_{\beta=0}(r_*)$ *(yellow colour) for a physical model implemented with Plummer stellar density and constant* σ_{los} *as a function of the allowed values of* a_{β_c} *and at the fixed ratio* r/r_* *of* 5%*. The bands are related to the error on the characteristic scale radius of the Plummer profile.* Lower panel: *Same kind of plot produced at the fixed ratio* r/r_* *of* 50%*. Note that the values of* a_{β_c} *for which the model is physical span in this case the whole possible range,* $\beta_c \in (-\infty, 1]$.

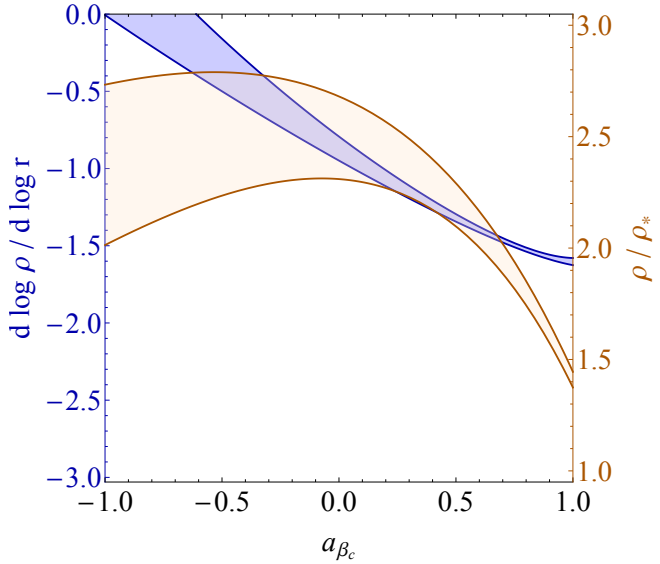

implementing a constant σ_{los} and Plummer surface brightness Eq. (4.13) goes as:

$$\mathcal{M}_{\beta\to-\infty}(r) = \frac{2\,R_{1/2}\,\sigma_{los}^2}{3\,G_N}\left[2\left(1+\frac{r^2}{R_{1/2}^2}\right)^{5/2} - \frac{r^3}{R_{1/2}^3}\left(5+2\frac{r^2}{R_{1/2}^2}\right)\right] \tag{4.31}$$

and in the limit of r going to 0 becomes

$$\lim_{r\to 0}\mathcal{M}_{\beta\to-\infty}(r) = \frac{4R_{1/2}\,\sigma_{los}^2}{3\,G_N}\ . \tag{4.32}$$

We observe that the case of constant orbital anisotropy going to $-\infty$ is the only case when the condition of $\mathcal{M}(0)=0$ is not met in this model, mimicking the scenario of a black hole at the center of the dwarf supporting the velocity dispersion. With the logarithmic slope of $\rho(r)$ approaching -3, the mass profile gets a larger and larger contribution close to $r=0$. The log divergence is avoided via the appearance of the black hole-like feature and hence a discontinuity in the density profile:

$$\rho(r)_{\beta\to-\infty} = \frac{5\,\sigma_{los}^2}{6\pi\,R_{1/2}^2 G_N}\left(\frac{R_{1/2}}{r}\right)\left[2\left(1+\frac{r^2}{R_{1/2}^2}\right)^{3/2} - 3\frac{r}{R_{1/2}} - 2\frac{r^3}{R_{1/2}^3}\right]\ , \tag{4.33}$$

holding a logarithmic slope equal to -1 at the center, as anticipated.

We summarize the results of this section, briefly recapping what we have achieved so far with our method. First, we have highlighted the existence of possible unphysical solutions encoded in the general master formula, Eq. (4.10), derived by inverting Eq. (4.2). Physical solution within this approach require the following two conditions:

$$\begin{aligned} &i)\ \ \mathcal{M}(r) > 0 && \forall\ \ r>0 \\ &ii)\ \ \mathcal{M}(r') \geq \mathcal{M}(r) && \forall\ \ r'\geq r \end{aligned}$$

Then, we have made a step forward deriving Eq. (4.26) to study the density of non-rotating pressure-supported systems like dSphs. In order to deal with a physical density, we have supplemented the latter with the following third condition:

$$iii)\ \ \rho(r') \leq \rho(r) \qquad \forall\ \ r'\geq r$$

We have primarily focussed our attention on the trends of the inner density profile of the system for several tracer density templates and l.o.s. velocity dispersion profiles, see Fig. 4.4, under the assumption of an isotropic tracer motion. Eventually, we have analyzed in details the benchmark scenario of σ_{los} and stellar Plummer model, varying the orbital anisotropy β_c, as reported in Fig. 4.5.

4.3.3 J-factor scalings

The simple form of $\rho(r)$ derived in the circular anisotropy limit may be taken as a good starting point to discuss J-factor trends in the inversion approach considered here. Indeed, integrating the square of the profile in Eq. (4.33) following the definition in Eq. (4.1), we can get an analytic form for J. In Appendix B.1 we provide an expression for the J-factor, see Eq. (B.11), which is valid in the limit of distance $\mathcal{D}$ of the dwarf much larger with respect to the typical transverse size of these galaxies (note that the "optimal" angular aperture $\psi \sim 0.5°$ is usually considered in literature, see e.g. [349, 352, 358]). In the case at hand it gives:

$$J_{\beta\to-\infty} = \frac{1}{\pi\mathcal{D}^2}\frac{\sigma_{los}^4}{R_{1/2}G_N^2}\frac{5}{63}\Big[68+140\,\mathcal{Z}+245\,\mathcal{Z}^3+168\,\mathcal{Z}^5+40\mathcal{Z}^7 - (68+40\mathcal{Z}^2)\,(1+\mathcal{Z}^2)^{5/2}\Big] \xrightarrow[\mathcal{Z}\to\infty]{} \frac{340}{63\pi}\frac{R_{1/2}^3}{\mathcal{D}^2}\left(\frac{\sigma_{los}^2}{R_{1/2}^2G_N}\right)^2 \quad (4.34)$$

where the quantity in the last brackets is an energy density and the dimensionless ratio $\mathcal{Z} = \mathcal{R}/R_{1/2}$ is introduced to take into account a possible finite size $\mathcal{R}$ of the spherical halo density $\rho(r)$.

Plugging in Eq. (4.34) typical values for dSphs, namely $\sigma_{los} \sim 10$ km s^{-1}, $R_{1/2} \sim 0.3$ kpc and $\mathcal{D} \sim 100$ kpc, one gets a J-factor of about 10^{18} GeV^2 cm^{-5}. Notice that this is not a totally realistic case since the black hole mass one would infer from Eq. (4.32) would be $\sim 10^7\ M_\odot$, possibly consistent with kinematical observables, but likely too large to be found at the center of these galaxies [406, 407].
Even in case of perfect isotropic motion of the stellar tracers an analytic expression for the density profile, Eq. (4.27), and the J-factor can be provided:

$$J_{\beta=0} = \frac{25}{4\pi\mathcal{D}^2}\frac{\sigma_{los}^4}{R_{1/2}G_N^2}\left[\frac{\mathcal{Z}\,(-3+\mathcal{Z}^2)\,(5+3\mathcal{Z}^2)}{12\,(1+\mathcal{Z}^2)^3}+\frac{5}{4}\arctan\mathcal{Z}\right] \xrightarrow[\mathcal{Z}\to\infty]{} \frac{125}{32}\frac{R_{1/2}^3}{\mathcal{D}^2}\left(\frac{\sigma_{los}^2}{R_{1/2}^2G_N}\right)^2, \quad (4.35)$$

that is about a factor of 2 larger than the $\beta \to -\infty$ case. The picture for constant orbital anisotropies related to physical solutions (still taking σ_{los} constant and Plummer profile) is shown in Fig. 4.6: we plot a function $\widetilde{J}(r)$ appearing as a linear measure in the J-factor computation (the area under each curve represents the J-factor, up to the normalization factor $\widetilde{J}_{\beta=0}(r_*)$), see Eq. (B.10). Therefore, the general trend for the J-factor at constant σ_{los} can be drawn: starting from the J-value corresponding to the case of $\beta = 0$, the J-factor increases going to smaller values of β_c, with an inner cusp appearing and at the same time a reduction of the

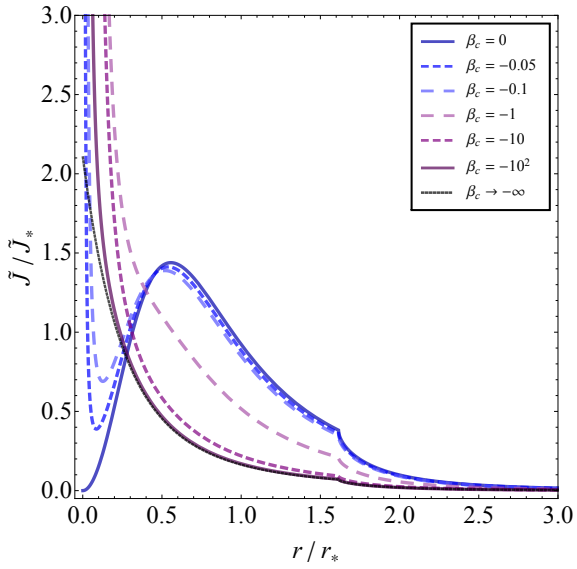

Figure 4.6: *Integrand of the J-factor in radial coordinates according to Eq. (B.10) for different realizations of constant orbital anisotropies in a model with constant σ_{los} and with a Plummer stellar template. We assumed a distance $\mathcal{D} = 10^2$ kpc and an angular aperture $\psi_{max} \simeq 0.5°$, normalizing $\widetilde{J}(r)$ at the reference value $\widetilde{J}_* = \widetilde{J}_{\beta=0}(r_*)$.*

contribution at larger radii, up to the exact circular limit, when the central cusp is suddenly reduced in correspondence to the discontinuity of $\rho(r)$.

As anticipated, the picture above is expected to provide a rather conservative estimate of the J-factor: leaving a cored stellar template in favor of a more general Zhao profile, Eq. (4.28), with $\gamma > 0$, or an exponential template, like the Sersic one, would enhance the inner density profile and hence the J-value; moreover, an inner convex tilt in the profile of the l.o.s. velocity dispersion would go in the same direction. A concave perturbation to a flat σ_{los} would offer a way out to lower the J-value, but would apply only to the cases of circular-like stellar orbits, where the density is relatively cuspy, to not generate unphysical outputs like the one previously encountered in Fig. 4.4. Therefore, discarding the "extreme" solution of the Jeans inversion at $\beta \to -\infty$, the lowest J-factor emerging from a physical model in Fig. 4.6 corresponds to the case of perfectly isotropic stellar motion, given by Eq. (4.35).

Within the same framework, this conclusion can be modified once we follow a more conservative approach in extrapolating the inner density of $\rho(r)$. Indeed, one may question whether the basic assumptions involved in the derivation of Eq. (4.2) itself, most importantly the spherical symmetry of the system, should be trusted down to exceedingly small radii, imposing by construction a choice of coordinates which are singular in the origin and also extrapolating σ_{los} in a

region which is simply not accessible to data. An alternative is to introduce a saturation scale r_c so that $\rho(r \leq r_c) = \rho(r_c)$; in Fig. 4.6 one sees that a relatively small inner cutoff, i.e. $r_c/r_* \simeq 0.1$, has an important impact on the inner density profiles with $-\infty < \beta_c < 0$ and hence on the corresponding J-factors. Focussing on the area below each curve of Fig. 4.6 one can easily visualize that in the case of $\beta_c \simeq 0$, the J-factor is almost insensitive to an inner cutoff, while for a negative orbital anisotropy, a very small r_c can significantly enhance the J-value with respect to what can be obtained with a more conservative cut on the inner density. In the exact circular orbit limit the J-factor is again quite insensitive to the choice of r_c. Note that with the implementation of $r_c \neq 0$, the density $\rho(r)$ related to very negative orbital anisotropies is now smoothly tracking the – previously discontinuous – case of circular orbits. Therefore, the flattening of the density due to the a non-vanishing inner cut allows for lower J-factors than the one obtained at $\beta = 0$. At the same time, one should not forget that lower orbital anisotropies in this context would imply growing black-hole-like features up to the questionable point that an important contribution to the total mass of the system comes from the center of the system. Note also that – in contrast to the approach followed in this work – a physical black hole at the center of the dSph may be instead modeled so to strengthen the DM annihilation signal from the galaxy. This possibility has been explored in, e.g., [408, 409].

Focussing on the minimum J-value one can obtain, we can now address the impact of a radial dependence in the orbital anisotropy function. In what follows we will assume the orbital anisotropy profile to be well described by the rather general form provided in [380]:

$$\beta(r) = \frac{\beta_0 + \beta_\infty \left(\frac{r}{r_\beta}\right)^{\eta_\beta}}{1 + \left(\frac{r}{r_\beta}\right)^{\eta_\beta}} \,, \tag{4.36}$$

offering an interpolation between the tracer behaviour at the center of the system, set by β_0, and the one towards the outer part, set by β_∞, with characteristic scale and sharpness between the two regimes respectively determined by r_β and η_β.
Note that, on general grounds, for solution to be physical satisfying the conditions in Eq. (4.25), a sharp radial dependence in $\beta(r)$ (such that its derivatives would even impact on the scalings discussed looking at Eq. (4.30)) can be implemented only together equally sharp variations of $\sigma_{los}(R)$ in R; we will provide an explicit example in the next section, enlightening also the level of tuning involved.
Here we will consider instead smoother behaviour for $\beta(r)$, assuming then, without loss of generality, a constant σ_{los} and referring to the trends illustrated in Fig. 4.4 for its extensions.

We have seen in Section 4.3.1 that a notion of a mass estimator for the system is

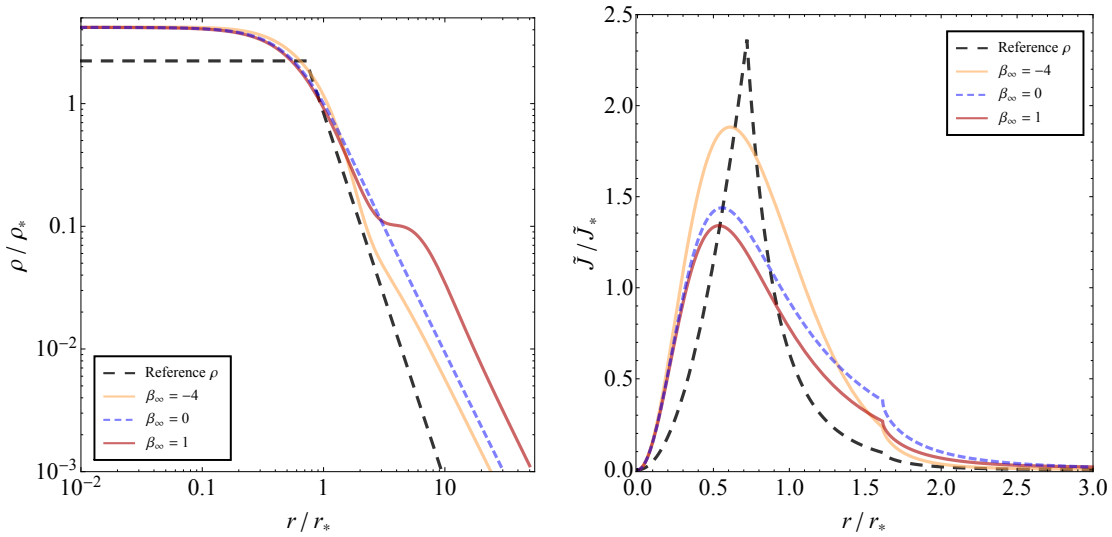

Figure 4.7: Left Panel: *Reference density profile obtained by minimizing the J-factor at given* $\mathcal{M}_*$*. In the same panel, three solutions of Eq. (4.26) matching the reference* $\rho(r)$ *in the simple model of constant* σ_{los} *and with Plummer stellar profile and with orbital anisotropy profile* $\beta(r)$ *given in Eq. (4.36), defined by the set* $r_\beta/r_* = 3, \eta_\beta = 3, \beta_0 = 0$ *and* $\beta_\infty = -4, 0, 1$*, light orange, dashed blue and dark red line respectively. All the profiles are normalized to* $\rho_* = \rho_{\beta=0}(r_*)$*.* Right Panel: *Corresponding* $\widetilde{J}(r)$ *function, Eq. (B.10), whose integral yields the J-factor, for the same set of density profiles. We assumed a distance* $\mathcal{D} = 10^2$ *kpc and an angular aperture* $\psi_{max} \simeq 0.5°$*, normalizing* $\widetilde{J}(r)$ *at the reference value* $\widetilde{J}_* = \widetilde{J}_{\beta=0}(r_*)$*.*

to some extent available thorough the mass enclosed in r_*. We can exploit this information to find the density profile that minimizes the J-factor. This can be done introducing a simple broken power-law ansatz for $\rho(r)$:

$$\rho(r) = \rho_0 \left[\left(\frac{r_1}{r}\right)^{\alpha_1} \theta_H\left(r_1 - r\right) + \sum_{i=2}^{n} \prod_{j=2}^{i-1} \left(\frac{r_{j-1}}{r_j}\right)^{\alpha_j} \left(\frac{r_{i-1}}{r}\right)^{\alpha_i} \theta_H\left(-\Delta r_i\right) \theta_H(\Delta r_{i-1}) \right] \tag{4.37}$$

with $\Delta r_i \equiv r - r_i$, α_i being the logarithmic derivative of the profile within the radial interval $[r_{i-1}, r_i]$, $\theta_H(r)$ the Heaviside step function, and the normalization ρ_0 derived from the condition $\mathcal{M}(r_*) = \mathcal{M}_*$. For a given $\mathcal{M}_*$ (as following from the approximate relation in Eq. (4.18)), the J-factor can be minimized as a function of the α_i and r_i. In Fig. 4.7 we show the outcome of this procedure in the sample case of 4 power-law indices; we imposed as constraints -3[1] $\leq \alpha_i \leq 0$ and $r_2 \leq r_* < r_3$: not too surprisingly the result is that the profile minimizing the J-factor at given

[1]Here we are also assuming the mass profile to grow at least logarithmically with the radius, as e.g. for a NFW profile.

$\mathcal{M}_*$, drawn with a black dashed line, is cored for $r \lesssim r_*$ and it drops to 0 as fast as possible for larger r. We checked explicitly that such result is independent of number of power laws assumed to model $\rho(r)$.
This result provides an independent check about our findings at constant orbital anisotropy: as long as the volume integral of the density profile at r_* encloses the whole mass in r_*, i.e. no black-hole-like feature is present, the physical configuration that has the minimum J-factor happens to be at $\beta = 0$, namely when $\rho(r)$ features an inner core.

In Fig. 4.7 we report with a dashed blue curve the density profile obtained from the Jeans inversion procedure with $\beta = 0$, constant σ_{los}, Plummer stellar profile and same $\mathcal{M}_*$ of the reference density. The good agreement with the latter in the innermost part of the profile does not leave so much room for improvements. Indeed, exploiting the orbital anisotropy form of Eq. (4.36), a good match to the black dashed line requires $\beta_0 = 0$ to generate an inner core. Moreover, one needs $r_\beta \gtrsim r_*$ to have such a core as extended as in the reference case. Consequently, one ends up to require $\eta_\beta \gtrsim 1$ (but not too large in order to not invalidate conditions in Eq. (4.25)) to get an appreciable departure from isotropy with $\beta_\infty \neq 0$. We display this set of results in the left and right panel of Fig. 4.7:

- in the left panel we show two different configurations of the density profile with $\beta(r) \neq 0$ in the outskirts of the dSph, through a mildly circular-like or a purely radial value assigned to β_∞; both profiles do not provide a dramatic improvement in matching the reference density;
- in the right panel we see that the J-value corresponding to the case of $\beta_\infty < 0$ has slightly increased, while the radial case gives slightly lower values of J (an effect anyhow at the per mille level). Note however that in the limit of $\beta_\infty = 1$ the density is almost turning to an unphysical profile, since an unphysical ripple is starting to appear.

We can then conclude this section stating that in the search for density profiles that minimize the J-factor – within a given mass $\mathcal{M}_*$ at the radius r_*, as constrained by kinematical data – a radial dependence in the unknown orbital anisotropy profile does not significantly alter the picture previously outlined assuming constant β_c.

4.4 Ursa Minor as a study case

4.4.1 A few generalities on the dwarf

Ursa Minor is most often referred to as the target for which both signal and background are most reliably estimated, providing a very competitive limit on annihilating DM models. As discussed in the first analysis on Milky Way satellites by the Fermi collaboration [349] (assuming NFW DM profiles and a fixed angular acceptance of solid angle $\Delta\Omega = 2.4 \times 10^{-4}$ sr), and in agreement with previous analyses [335], Draco and Ursa Minor are the prime targets among the classical dSphs. Ref. [410], assuming instead a Burkert profile and performing an optimization of the angular acceptance, has discussed uncertainties in the gamma-ray background determination, concluding that Ursa Minor is the favorite target from this point of view, followed by Sextans which however provides less stringent constraints, while large uncertainties lie in Draco and Sculptor. All this motivated us to consider Ursa Minor as a suitable sample object for the purpose of our study.

We briefly summarize here the main characteristics of this satellite, specifying some of the choices for the data set considered in the phenomenological analysis that follows. The wide field photometry study in [411] finds that Ursa Minor hosts a predominantly old stellar population, with virtually all the stars formed before 10 Gyr ago, and 90% of them formed before 13 Gyr ago, making it the only dSph Milky Way satellite hosting a pure old stellar population. Using the magnitude of the horizontal branch stars and comparing with Hipparcos data on globular clusters the authors determined the distance of Ursa Minor from the Sun to be $\mathcal{D} = 76 \pm 4$ kpc, in agreement with the determination from [412], but larger than the mid 1980's value of 66 ± 3 kpc quoted in [413, 414]. As pointed out in [415], the difference is mainly due to the absolute magnitude calibration of the horizontal branch; standing in between are the values of 70 ± 9 kpc [416] and 69 ± 4 kpc [417]. Here we choose to adopt the mean value $\mathcal{D} = 66$ kpc from the old determination of [413, 414], since most often the same has been done in the most recent literature discussing J-factor uncertainties, see, e.g., [357]. Note that, while we will be mostly concerned about relative shifts on J-factor determinations connected to the solution of the Jeans equation, switching from 66 kpc to 76 kpc would imply an overall decrease in values quoted below of about 25%.

Regarding the stellar surface brightness, the one of Ursa Minor shows the largest ellipticity among all classical dwarfs (excluding Sagittarius that is suffering heavy tidal disruption), with mean value of $\epsilon \equiv 1 - b/a$ (where b/a is the minor over major axis ratio) estimated in [368] to be 0.56 ± 0.05. Nevertheless, most analyses

treat Ursa Minor as a spherically symmetric system, with stellar surface brightness to be fitted with a template, most often via the Plummer, the King or the Sersic model. We will follow [397, 398] which suggest to adopt the Plummer model, also in view of the discussion on stellar number density profiles in the previous section. While the value of the normalization parameter I_0 in Eq. (4.19) does not need to be specified in the Jeans analysis as well as in its inversion, as projected half-light radius we assume $R_{1/2} = 0.30 \pm 0.02$ kpc, estimate originally obtained in [368] from a geometric average of the corresponding half-brightness radii along the semi-major and semi-minor axis of the projected stellar profile.

In what follows, the computation of the l.o.s. integral of $\rho^2(r)$ of Ursa Minor will always refers to pointing to the center of the system with the optimal angular aperture $\psi_{max} = \arctan(2\, R_{1/2}/\mathcal{D}) \simeq 0.5°$, as most often adopted in literature (see e.g. [291, 357]). J-factors will be computed according to Eq. (B.9), integrating up to an estimated outer radius $\mathcal{R} = 1$ kpc (changing this to an arbitrarily larger value, as a negligible numerical impact, generally at the per mille level).

4.4.2 Jeans inversion with Ursa Minor data

The starting point of our phenomenological analysis on Ursa Minor is a χ^2 fit of the binned l.o.s. velocity dispersion data from [397]. We consider two possibilities for the fit:

i) the standard approach in which $\sigma_{los}(R)$ is computed solving the Jeans equation, see Eq. (4.4)-(4.6), for given parametric forms of the DM density $\rho(r)$ and of the orbital anisotropy $\beta(r)$ (in the following we will refer to this procedure as *parametric fit*);

ii) a direct fit of the data within a given functional form for $\sigma_{los}(R)$ (in the following: σ_{los} *-driven fit*).

The result of the fit according to four different benchmark cases is shown in Fig. 4.8. The two parametric fits correspond to a cuspy and a cored $\rho(r)$, namely a NFW and Burkert halo density together with the assumption of constant orbital anisotropy. The other two cases considered are of the two simplest σ_{los} -driven kind, namely constant $\sigma_{los}(R)$ and a linear regression in R. The best-fit parameters and the corresponding $\chi^2_{\rm red} \equiv \chi^2/{\rm n.d.f.}$ are given in Table 4.1; as it can be seen all the four benchmarks provide fairly good fits and comparable $\chi^2_{\rm red}$.

Fits of the l.o.s. velocity dispersion data are taken as an input for the procedure of inversion of the Jeans equation, to reconstruct – at given $\beta(r)$ – the DM mass and density profiles, and hence study how the minimal J-factor of Ursa Minor, i.e.

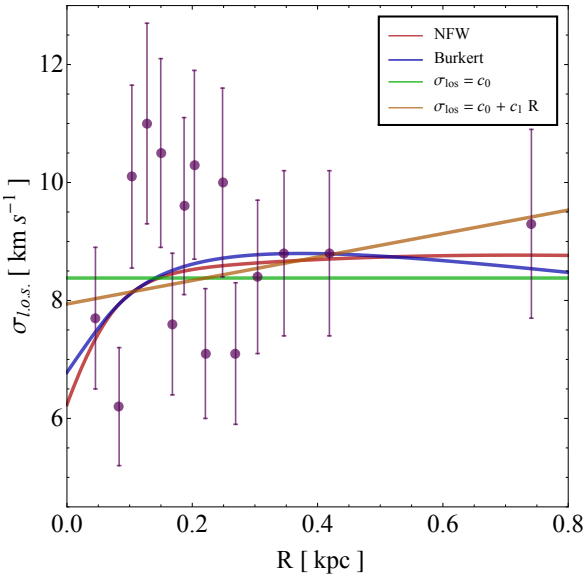

Figure 4.8: *Binned l.o.s. velocity dispersion data for Ursa Minor dwarf galaxy from [397]. Best-fit curves are also shown according to four benchmark cases: a parametric fit with a NFW or Burkert density profile together with the assumption of constant orbital anisotropy, and a σ_{los} -driven fit assuming $\sigma_{los}(R)$ to be a constant or a linear function in R.*

Table 4.1: *Best-fit values for the parameters involved in the fit of Ursa Minor data from [397] for the four reference cases under scrutiny. We minimize a χ^2 estimator under the assumption of Gaussian distributed data, using MINUIT package [418] and estimating the confidence level (C.L.) intervals for the fitted parameters with the MINOS algorithm.*

Benchmark	Parameters	Mean value	68% C.L.	$\chi^2_{\rm red}$
NFW	r_n [kpc]	0.61	[0.14 , 2.94]	1.41
	ρ_n [GeV]	2.59	[0.30 , 35.68]	
	β_c	-0.83	[−3.02 , −0.19]	
Burkert	r_b [kpc]	0.28	[0.12 , 0.54]	1.44
	ρ_b [GeV]	12.77	[5.59 , 55.13]	
	β_c	-0.36	[−1.63 , 0.10]	
$\sigma_{los} = c_0$	c_0 [km s^{-1}]	8.38	[8.03 , 8.73]	1.32
$\sigma_{los} = c_0 + c_1 \frac{R}{\mathcal{R}}$	c_0 [km s^{-1}]	7.94	[7.32 , 8.56]	1.35
	c_1 [km s^{-1}]	1.99	[−0.29 , 4.27]	

the 2σ lower limit of the probability distribution of J, depends on the assumed $\beta(r)$. The different choices of $\sigma_{los}(R)$ have been considered to check whether the parametric fit from an a priori physical model and/or the σ_{los} -driven fit (agnostic, but non-necessarily corresponding to a physical model) may be introducing a bias in the analysis. Incidentally, the parametric fits also allow for a cross-check on the

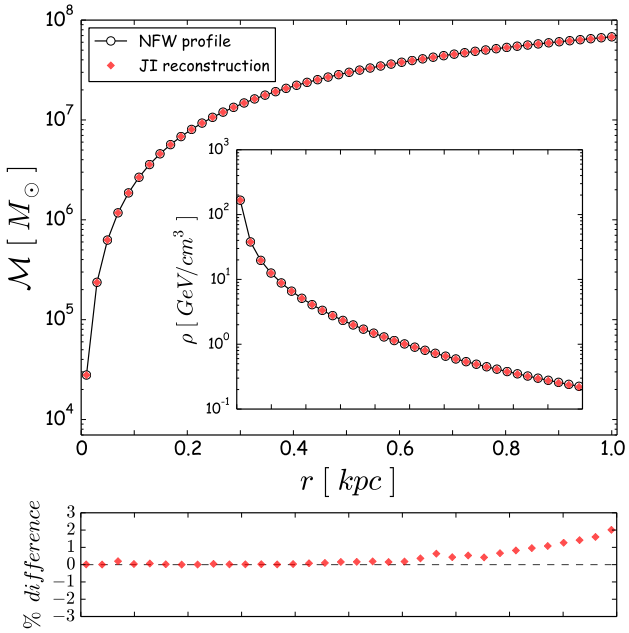

Figure 4.9: *Mass and the density profiles reconstructed via the Jeans inversion (JI) algorithm taking as input the parametric fit of $\sigma_{los}(R)$, in case of the NFW (upper panel) and Burkert (lower panel) best-fit values reported in Table 4.1.*

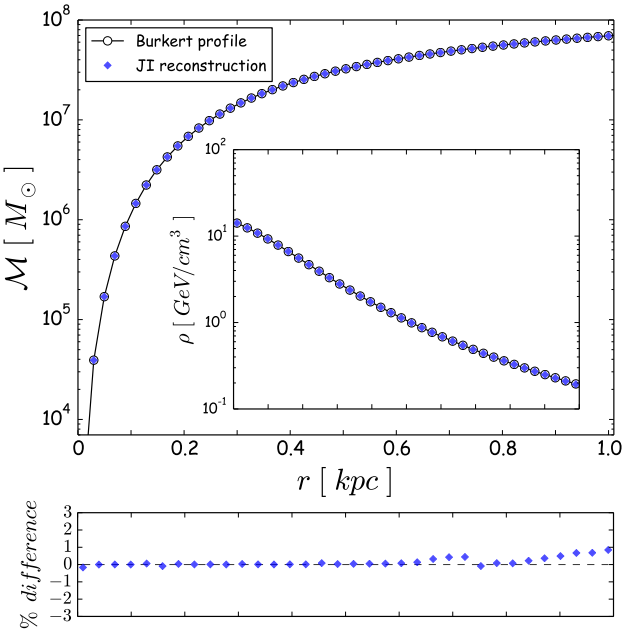

accuracy of our numerical implementation of the inversion procedure. In Fig. 4.9 we show profiles reconstructed via Eq. (4.10) compared against the initial NFW and Burkert parametric forms. The latter are given as an input to derive the parametric fits for $\sigma_{los}(R)$, which are displayed in Fig. 4.8. To perform this exercise we used the best-fit values specified in Table 4.1. The displayed reconstruction of the mass

profile for both cuspy and cored cases comes with a level of accuracy better than the per mille in the whole range of the binned dispersion data of Ursa Minor, i.e. $40 - 750$ pc; relative differences above few percent arise only at inner radii much smaller than 10 pc. A similar level of accuracy is found for the reconstruction of the inner density profile, for which we also show the relative percentage difference in the insets below the two plots. The density $\rho(r)$ of parametric fits can be conveniently evaluated via an iterative difference quotient algorithm [419] applied to $\mathcal{M}(r)$.

4.4.3 Inversion and MCMC with constant anisotropies

When investigating the impact of orbital anisotropy on density profiles and J-factors the emphasis will be on discussing minimum values consistent with kinematical observables. In fact, since the DM velocity averaged pair annihilation cross section $\langle\sigma v\rangle$ accessible to gamma-ray observations scales with the measured flux ϕ_γ as $\langle\sigma v\rangle \propto \phi_\gamma/J$, the lowest J-value allowed by Ursa Minor data can be directly linked to how much the upper bound on $\langle\sigma v\rangle$, reported e.g. in [350] for this galaxy, can be relaxed. As shown in Section 4.3, the minimum J-value turns out to be weakly affected by a radial dependence of the anisotropy profile as long as $\sigma_{los}(R)$ is mildly varying in R as well. Thus, we can restrict our phenomenological analysis to the simple case of $\beta(r) = \beta_c$ without loss of generality in the conclusions.

Starting with the four benchmark cases for $\sigma_{los}(R)$ shown in Fig. 4.8, in the upper panel of Fig. 4.10 we show results for $\log_{10} J$ as a function of the value assumed for β_c and in the range corresponding to models satisfying the set of conditions for a physical model, see Eq. (4.25): for the parametric fits only values of β_c lower or equal than the one assumed for computing $\sigma_{los}(R)$ are allowed; for the σ_{los} -driven fits, the Jeans inversion procedure gives physical models up to $\beta_c = 0$. Note, in particular, that for all the four benchmarks considered, radial-like anisotropy profiles provide unphysical solutions. This finding is actually in agreement with the requirement of a positive stellar phase-space density at the center of the system as studied in Ref. [403]. The behavior of $\log_{10} J$ as a function of β_c is qualitatively the same for all the four scenarios: for a given stellar surface density and $\sigma_{los}(R)$ when starting from β_c close to 0 and going to progressively larger circular anisotropy the density profiles becomes progressively more concentrated and hence the J-factor grows. This growth proceeds up to the level one starts to see the turnaround in logarithmic slope already appreciated in the upper panel of Fig. 4.5 when getting close to the pure circular orbit limit. The decrease in J-factor at this turning point becomes even more pronounced since we are taking here the conservative view of not extrapolating the profile obtained from the inversion procedure all the way

to $r \to 0$. We rather introduce an inner density cutoff $\rho(r < r_c) = \rho(r_c)$, with $r_c = 10$ pc as sample value avoiding an extrapolation to radii smaller than the order of magnitude of the radius in the innermost bin of σ_{los} data. The two benchmark $\sigma_{los}(R)$ obtained from parametric fits are both characterized by a concave inner tilt; this makes the density profile shallower than those for the σ_{los}-driven cases at small negative values of β_c and hence we find lower J-factors. On the other hand, the same concave tilt partially washes out the cancellation we discussed for purely circular orbits, as well as makes the effect of the internal cutoff less severe, and hence drives a less pronounced decrease of the J-factor at very large negative β_c. In the upper panel of Fig. 4.10 we show also the 1σ band for the Ursa Minor J-factor adopted in the Fermi-LAT analysis of Ref. [291] (scaled to the same dwarf distance $\mathcal{D}$ adopted here): the minimum J-values for the parametric fit cases are obtained for the same β_c implemented to generate the $\sigma_{los}(R)$ profiles and are within 2σ with respect to Fermi quoted values (we take the Fermi band as visual guide only and do not intend to make any statistical statement at this point). For the case of σ_{los}-driven fits, i.e. when assuming a constant $\sigma_{los}(R)$ or a linear regression, the minimum J turns out to correspond to the circular orbit limit; in particular to the sample benchmark with constant $\sigma_{los}(R)$ the minimum J is roughly 4σ away from the nominal value in [291] for Ursa Minor, driving – as naive estimate – a relaxation of the extrapolated limit on $\langle\sigma v\rangle$ of a factor of few. On the other hand, these correspond to rather extreme configurations, with, as explained in the previous section, extreme cusps which would be developing in the very inner region of the system (even below the cutoff radius we are considering), finally shrinking to a $1/r$ profile and a central "black hole". The mass at the center of the system for $\beta_c \lesssim -100$ would be of the order of 10^6 $M_\odot$ or larger: while physical black holes could be motivated in connection to flat inner densities, see, e.g., scenarios in Ref. [420], such black-hole masses seem to be at the edge of current observational limits available for Ursa Minor [421, 422].

In order to provide a more robust statistical assessment of these findings, we also present here the results of a Bayesian fit of Ursa Minor σ_{los} binned data, computing the J-factor through the inversion formula for a finite grid of constant orbital anisotropies. We have exploited for the purpose two different parameterizations of $\sigma_{los}(R)$, namely the same linear expression in R already introduced, and the following polynomial form (recall that $\mathcal{R}$ is the outer radius and we picked as reference value 1 kpc):

$$\sigma_{los}(R) = c_0 + c_{1/2}\sqrt{\frac{R}{\mathcal{R}}} + c_1\frac{R}{\mathcal{R}} + c_{3/2}\frac{R}{\mathcal{R}}\sqrt{\frac{R}{\mathcal{R}}}\ . \tag{4.38}$$

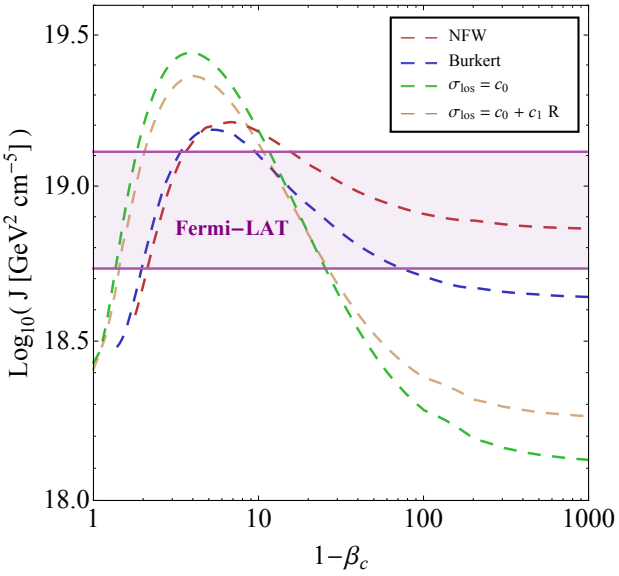

Figure 4.10: Upper panel: *J-factor as a function of constant orbital anisotropy β_c for the four benchmark cases at hand. An inner cut of* 10 *pc is applied to all the physical densities as described in text. In the plot also the representative* 1σ *band for the J-factor of Ursa Minor assumed by Fermi-LAT in the most recent analysis on DM limits from dSphs [291].* Lower panel: 68% *and* 95% *probability region associated to the J-factor as a function of* β_c *from the MCMC we performed – in the context of the Jeans inversion approach proposed – with the BAT library [423]. We considered two different parameterizations of* $\sigma_{los}(R)$*, as reported in the legend.*

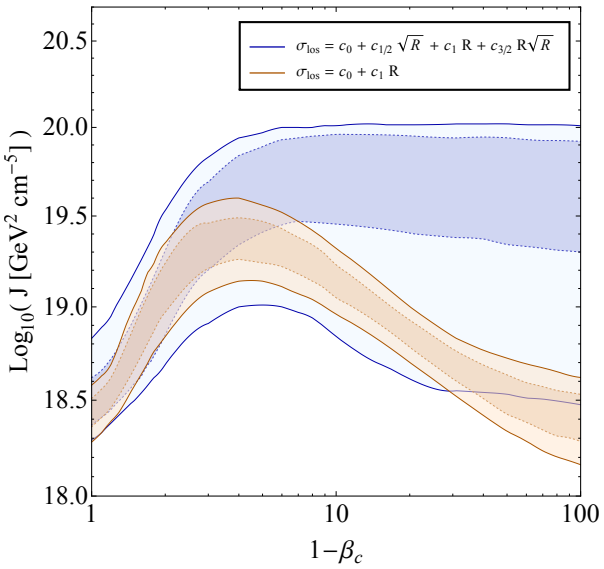

This form can nicely interpolate among the four benchmarks in Fig. 4.8 within a broader set of behaviours, including eventually convex and concave tilts at small R. To perform our MCMC analysis we use the Bayesian Analysis Toolkit library

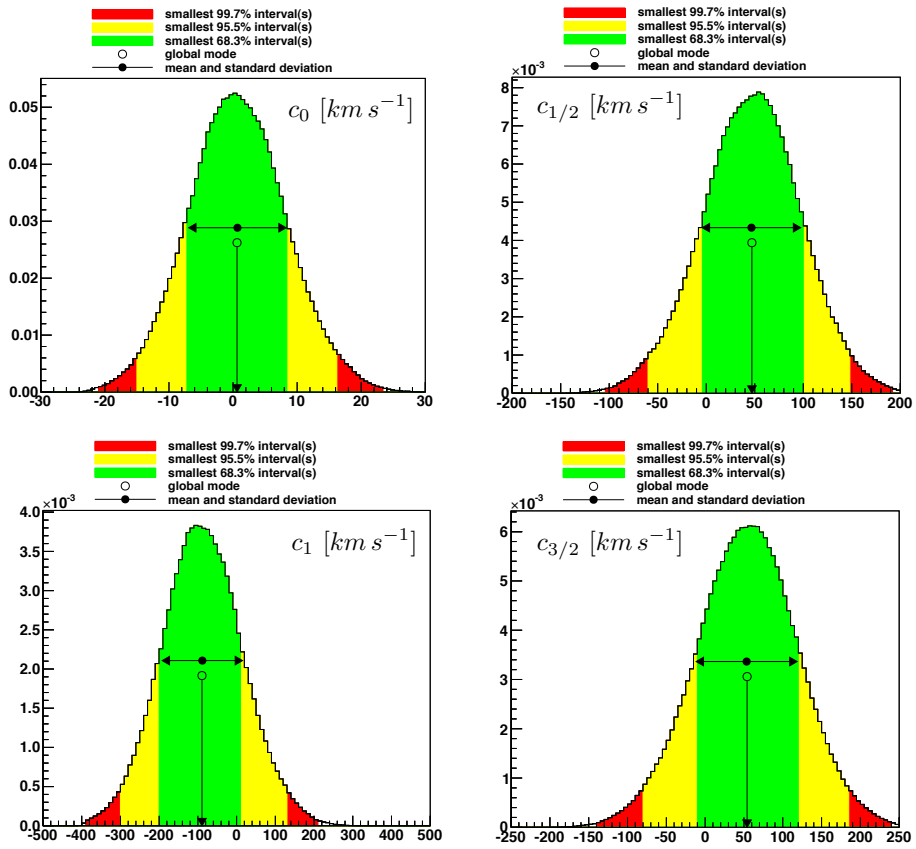

Figure 4.11: *P.d.f. posteriors of the parameters which define the polynomial form for the l.o.s. velocity dispersion profile according to Eq. (4.38).*

[423], assigning generous flat priors to the coefficients defining $\sigma_{los}(R)$ – namely $c_0 \in [-30, 30]$, $c_{1/2} \in [-200, 200]$, $c_{1/2} \in [-250, 250]$ and $c_{3/2} \in [-500, 500]$ – and performing a total of 10^8 iterations distributed in 20 chains. In each iteration of the MCMC we invert the Jeans equation for all the set of β_c considered, computing the density profiles via Eq. (4.26) and the J-factor when the physical conditions in Eq. (4.25) are met. As a result of this involved procedure, we are eventually able to compute the posterior probability density function (p.d.f.) of $\log_{10} J$ for each of the selected constant anisotropies, i.e. without any marginalization over unknown parameters unrelated to observable quantities. Indeed, in contrast to other approaches, we wish to note that the MCMC we have performed here actually aims at sampling the parameter space related to a simple phenomenological expression for $\sigma_{los}(R)$, without any further theoretical or experimental input. As shown in Fig. 4.11, the posterior distribution of the parameters defined in Eq. (4.38) are very well constrained despite the initially assigned large flat priors.

In the lower panel of Fig. 4.10, we plot the 68% and 95% probability region of $\log_{10} J$ for orbital anisotropies in the range $-100 \lesssim \beta_c \leq 0$, finding again for the linear parametrization of $\sigma_{los}(R)$ that the minimum value of J happens in the

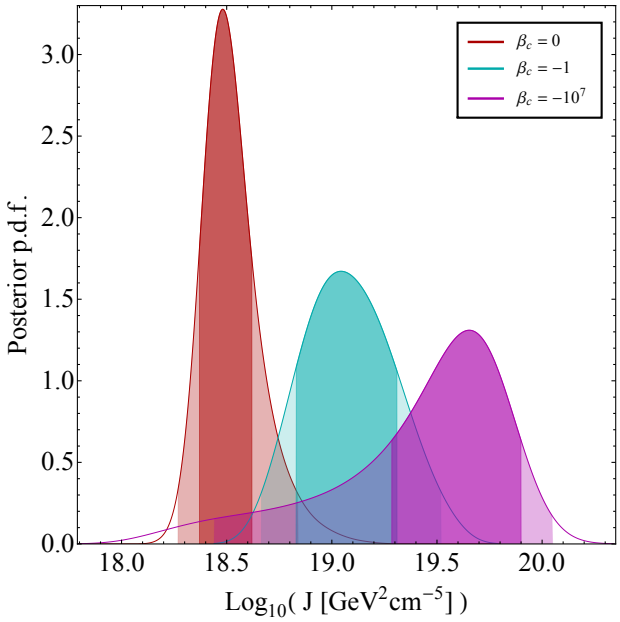

Figure 4.12: *Posterior probability density function of* $\log_{10}(J)$ *for a constant orbital anisotropy* $\beta_c = 0, -1, -10^7$ *obtained through our inversion of the spherical Jeans equation. The darker colored area in each distribution corresponds to the* 68% *probability region, the shader one accounts for the* 95%*.*

circular orbit limit, with precise value sensitive to the choice of inner cutoff radius at 10 pc. While the more general parametrization in Eq. (4.38) encodes the linear behaviour as well, the latter becomes now only a special realization of it, and consequently populate the tail of the distribution in $\log_{10} J$ when one probes lower ad lower stellar anisotropies. This trend of the posteriors of $\log_{10} J$ is summerized in Fig. 4.12, where we show three illustrative cases, highlighting with the color code their 68% and 95% probability area (defined from the local mode of the p.d.f.).

Eventually, we can conclude that the lowest J-value is again found in correspondence

Table 4.2: 68% *and* 95% *minimum* J *for the two different parameterizations of* $\sigma_{los}(R)$ *used in our MCMC and related to our Jeans inversion approach. In the last column we report the relaxing factor one can naively derive for the constraints of DM particle properties comparing our* J*-value at* 95% *probability with the* $2\,\sigma$ *Fermi-LAT minimum value for Ursa Minor in [291], namely* $\min J^{Fermi}_{@\,2\,\sigma} = 3.5 \times 10^{18}$ GeV^2 cm^{-5} *after the appropriate rescaling to the distance of the dSph used in our analysis.*

$\sigma_{los}(R)$	$\min J_{@68\%(95\%)}$ [GeV^2 cm^{-5}]	$\min J^{\rm Fermi}_{@\,2\,\sigma}$ / $\min J_{@95\%}$
$c_0 + c_1 R/\mathcal{R}$	1.09×10^{18} (9.12×10^{17})	3.83
Eq. (4.38)	2.34×10^{18} $(1.86 \times 10^{18}$)	1.88

to the isotropic stellar motion when considering the case of Eq. (4.38), while it is provided by the limit of circular-like orbits in case a linear form for $\sigma_{los}(R)$ is implemented (together with the caveats of the related black-hole feature discussed above). For what concerns the bounds on the cross section of a DM annihilating pair, in Table 4.2 we report the naive maximum relaxation one can apply to these limits for the study case of Ursa Minor: at $2\,\sigma$ upper bound on $\langle\sigma v\rangle$ should be relaxed by a factor roughly ranging from 2 to 4.

4.4.4 Minimal J-factors for NFW and Burkert profiles

While the general impact on J for spatially dependent orbital anisotropies has been qualitatively discussed in Section 4.3, we try to address here a slightly different, though related issue: within a physically motivated ansatz for the DM density profile of the system, what is the orbital anisotropy profile compatible with the velocity dispersion data that, at the same time, provides the smallest J-factor possible for the galaxy?
Assuming a rather general form for the profile of $\beta(r)$, we can answer this question quantitatively taking again Ursa Minor as our study case.

Using as reference parametric forms the NFW and Burkert DM density profiles, these are completely determined by only two parameters, namely a characteristic scale radius r_s and a normalization ρ_0. As discussed in Section 4.3.1, in case of nearly flat projected l.o.s. velocity dispersion profile in the outskirts of galaxy – as, for instance, shown by Ursa Minor kinematical data in Fig. 4.8 – the mass $\mathcal{M}_*$ enclosed within the radius r_* (close to the half-light radius of the stellar profile and defined as the radius at which its logarithmic slope is equal to -3, see Eq. (4.17)) is nearly independent of the assumed orbital anisotropy profile. So, to a good approximation, we can trade the normalization of the DM profile ρ_0 by $\mathcal{M}_*$:

$$\mathcal{M}_* = 4\pi \int_0^{r_*} d\tilde{r}\,\tilde{r}^2\,\rho(\tilde{r};\rho_0,r_s) \;\Rightarrow\; \rho_0 = \rho_0(\mathcal{M}_*,r_s)\;. \tag{4.39}$$

This expression then sets the normalization of ρ to be a function of r_s and $\mathcal{M}_*$, with in turn the latter being set in terms of the normalization of σ_{los}. At fixed $\mathcal{M}_*$, the J-factor for the profile becomes only a function of r_s and selecting the minimum J fixes this parameter as well, fully determining the density profile. Eventually, assuming a definite form for the stellar anisotropy, one is able to read the profile from a fit of the dispersion data.

In Fig. 4.13 we show the logarithm of J as a function of the scale radius r_s for both the NFW and Burkert cases fixing $\mathcal{M}_* = 1.82\cdot 10^7\,M_\odot$, as follows from

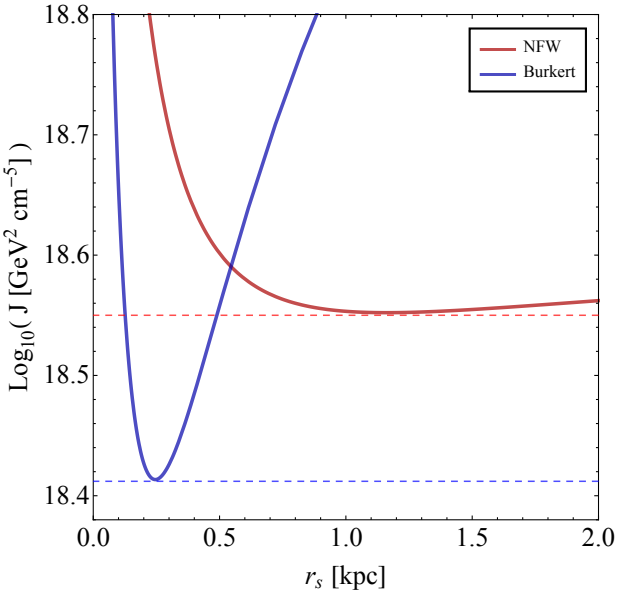

Figure 4.13: Upper panel: *J-factor for the NFW and Burkert profiles as a function of the scale radius r_s, after fixing the density normalization assuming $\mathcal{M}_* = 1.82 \cdot 10^7\, M_\odot$. The dashed horizontal lines highlight the minimum J-value compatible with such constraint.* Lower panel: *The fit of the l.o.s. velocity dispersion data of Ursa Minor considered in our analysis using NFW and Burkert profiles that minimize the J-factor according to the constraint $\mathcal{M}_* = 1.82 \cdot 10^7\, M_\odot$.*

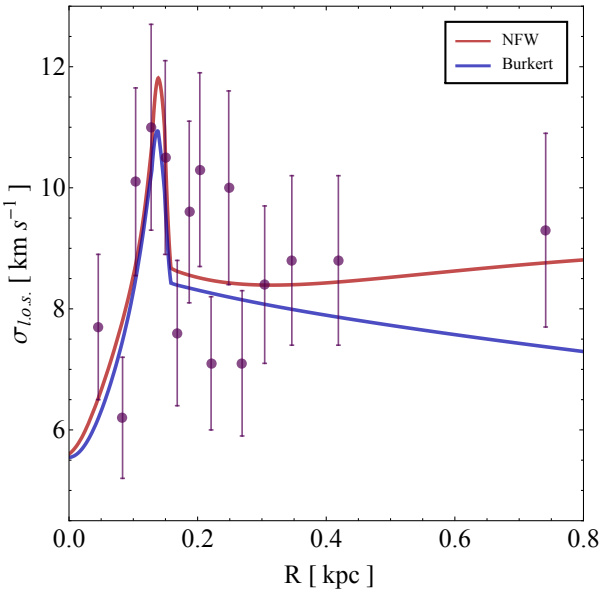

applying Eq. (4.18) to the Ursa Minor σ_{los} binned data. Analogously to the results in Section 4.3, for both the NFW and Burkert profiles, the minimum of J corresponds to an intermediate value for the scale radius r_s such that the density profile flattens as much as possible in the inner part, and falls off rapidly in the outskirts. Comparing the two cases, the lowest J-value corresponds once again to

Table 4.3: *Nominal best-fit values of the orbital anisotropy parameters ($\eta_\beta \gtrsim 10^3$) fitted using NFW and Burkert profiles that minimize the J-factor according to the constraint $\mathcal{M}_* = 1.82 \times 10^7\, M_\odot$.*

$\rho(r)$	r_s [kpc]	$\log_{10}(J\,[GeV^2cm^{-5}])$	β_0	β_∞	r_β [kpc]	χ^2_{red}
NFW	1.16	18.55	-8.0	0	0.15	0.98
Burkert	0.25	18.41	-5.0	0	0.15	1.17

the most cored of the two density profiles. The radius r_s that minimizes J at fixed $\mathcal{M}_*$ is reported in Table 4.4.

Having selected within this approach one NFW and one Burkert profile, we search for a compatible orbital anisotropy profile through Eq. (4.4)-(4.6), using Ursa Minor velocity dispersions data and the 4 parameter function in Eq. (4.36) for $\beta(r)$. The corresponding best-fit $\sigma_{los}(R)$ are plotted in the upper panel of Fig. 4.13 and are generated in both cases by a $\beta(r)$ making, in correspondence to the deep in $\sigma_{los}(R)$, a violent transition between a mild circular orbit regime to a purely isotropic tracer motion. The nominal best-fit values of the anisotropy parameters are collected in Table 4.4, together with the χ^2_{red} of the fit related only to the stellar anisotropy degrees of freedom.

Since the value of $\log_{10}(J\ [\mathrm{GeV}^2\ \mathrm{cm}^{-5}])$ for Ursa Minor reported by the Fermi collaboration in [350] is respectively 18.92 ± 0.19 and 18.82 ± 0.20 for an assumed NFW and Burkert density (considering a distance $\mathcal{D}$ of 66 kpc), according to our findings in Table 4.4, the minimum possible J compatible with a mass estimator of $1.82 \times 10^7\, M_\odot$ and a NFW or Burkert profile is essentially within the $2\,\sigma$ range of the corresponding Fermi-LAT quoted value. An uncertainty to $\mathcal{M}_*$ can be naively associated from a simple constant fit of the dispersion data, namely $\sigma_{\mathcal{M}_*}/\mathcal{M}_* = 2\,\sigma_{\sigma_{los}}/\sigma_{los}$. Then, at $2\,\sigma$ we find that the minimum mass estimator is $\mathcal{M}_* = 1.52 \times 10^7\, M_\odot$ and the corresponding J-factor in Table 4.4 shifts to the value of 2.49×10^{18} GeV^2 cm^{-5} for the NFW profile, 1.8×10^{18} GeV^2 cm^{-5} for the Burkert case. It follows that relaxation of the DM particle physics limits for the cuspy or cored case results only in a factor of 1.39 or 1.46, respectively.

Hence, we conclude that, when assuming standard functional forms for the DM density profile, such as NFW and Burkert ones, as long as there is a good notion for the mass estimator of the dwarf, we do expect Fermi-LAT bounds on DM pair annihilation to be generally robust, even against the extreme case of a dramatic radial dependence in the profile of the tracer orbital anisotropy.

4.5 New J-factor estimate for the eight Classicals

On the basis of the general trends derived in Section 4.3 with the inversion method implemented for the spherical Jeans equation, a data-driven analysis concerning a conservative estimate of the J-factor can be applied to any dwarf of adequate kinematical data, along the lines of the detailed study carried out for Ursa Minor. The requirement is certainly fulfilled for all the classical satellites of the MW [340–343].

Table 4.4: *Structural parameters (distance taken from [342], half-light projected radius from [368]), and best-fit value a constant l.o.s. velocity dispersion reported for all the classical satellites of the MW. The kinematical data for the dSphs are taken from [397].*

Classical dSph	$\mathcal{D}$ [kpc]	$R_{1/2}$ [kpc]	$\sigma_{los} = c_0 \pm \sigma_{c_0}$ [km/s]	$\chi^2_{\rm red}$
Ursa Minor	66	0.30	8.38 ± 0.34	1.32
Sculptor	79	0.26	8.32 ± 0.18	1.40
Draco	82	0.20	8.62 ± 0.40	0.77
Sextans	86	0.68	5.99 ± 0.27	1.00
Carina	101	0.24	5.76 ± 0.21	1.40
Fornax	138	0.67	9.57 ± 0.14	1.21
Leo II	205	0.15	7.04 ± 0.45	0.44
Leo I	250	0.25	9.17 ± 0.41	0.47

In Table 4.4 we report distances from the Sun [342] and projected half-light radii inferred from photometric measurements [368]. Using the set of l.o.s. velocity dispersion data available in [397] for all the eight galaxies, we also report the best-fit value to the binned kinematical data points of each object assuming a spatially constant l.o.s. velocity dispersion profile, together with its standard deviation and the reduced χ^2. From the latter we can see that kinematical data of all the classical dwarfs adequately support the simple ansatz of constant l.o.s. velocity dispersion. A pretty low reduced chi-squared, $\chi^2_{\rm red} \sim 0.45$, is obtained for Leo I and Leo II dwarf galaxies. This is not really due to the inadequacy of the ansatz of a constant dispersion profile, but mostly because of the modest number of stellar members lying in these two objects, and because of the relatively large errors attached to the measured velocity dispersions, probably related to distance that separates them from us.

Using as a fiducial model for each object a constant $\sigma_{los} = c_0$ and a Plummer surface brightness with characteristic radius $R_{1/2}$, Eq. (4.26), supplemented also by

Table 4.5: *Minimum J-factor at 1σ and 2σ obtained for all the classical dSphs using the informations in Table 4.4. All the J-factors have been computed using an internal cut for each dwarf of 10 pc and the outer radius $\mathcal{R}$ reported below. The comparison with the corresponding value quoted by the Fermi-LAT collaboration is carried out taking into account the appropriate rescaling to the distance of the dSph used in our analysis.*

Classical dSph	$\mathcal{R}$ [kpc]	$\min J_{@\,1\sigma(@\,2\sigma)}$ [GeV^2 cm^{-5}]	$\min J^{\rm Fermi}_{@\,2\sigma} / \min J_{@\,2\sigma}$
Ursa Minor	1.0	1.10×10^{18} (9.18×10^{17})	3.80
Sculptor	1.25	9.56×10^{17} (8.74×10^{17})	2.36
Draco	2.0	1.22×10^{18} $(1.0 \times 10^{18}$)	2.59
Sextans	1.25	6.83×10^{16} $(5.63 \times 10^{16}$)	12.88
Carina	1.0	1.40×10^{17} $(1.20 \times 10^{17}$)	3.94
Fornax	2.0	2.18×10^{17} $(2.05 \times 10^{17}$)	3.34
Leo II	2.0	1.09×10^{17} $(8.28 \times 10^{16}$)	2.70
Leo I	2.2	1.42×10^{17} $(1.18 \times 10^{17}$)	1.91

the assumption of constant orbital anisotropy, reduces to:

$$\rho_{\beta_c}(z) = \frac{5\,c_0^2}{4\pi G_N R_{1/2}^2}\left\{(1-a_{\beta_c})\frac{3+z^2}{(1+z^2)^2} + a_{\beta_c}(3-a_{\beta_c})\left[-\frac{1}{1+z^2}\right.\right.$$
$$\left.\left. + \left(6-a_{\beta_c}-\frac{5}{1+z^2}\right) z^{-a_{\beta_c}-2}(1+z^2)^{5/2}\int_z^\infty d\tilde{z}\frac{\tilde{z}^{1+a_{\beta_c}}}{(1+\tilde{z}^2)^{7/2}}\right]\right\}, \quad (4.40)$$

where we have set by convenience $z \equiv r/R_{1/2}$. From Eq. (4.40) we can easily compute for the fiducial model of each dwarf the corresponding J-factor as a function of the constant orbital anisotropy, $J_{\beta_c}[c_0]$. In this framework, the comparison with Fermi-LAT bounds can now be easily obtained by defining that the N σ lower bound on J corresponds simply to:

$$\min J_{@\,N\sigma} \equiv \min_{\beta_c\in(-\infty,1\,]} J_{\beta_c}[c_0 - N\sigma_{c_0}] = \left(\frac{c_0 - N\sigma_{c_0}}{c_0}\right)^4 \min_{\beta_c\in(-\infty,1\,]} J_{\beta_c}[c_0]\ . \quad (4.41)$$

The above definition is statistically meaningful as long as the probability distribution of J at given β_c is Gaussian. In the MCMC analysis of the previous section this has turned out to be true for the case of the linear parametrization of $\sigma_{los}(R)$. Consequently, the assumption of Gaussianity underlying Eq. (4.41) is well justified.

In Table 4.5 we have collected our main results. All the J-values have been computed assuming $\psi_{max} = 0.5°$, since this is most often quoted in literature as the optimal angular acceptance [291, 357]. Moreover, in integrating Eq. (4.40) along the l.o.s., we have implemented an inner cut of 10 pc and an outer cut $\mathcal{R}$ on the

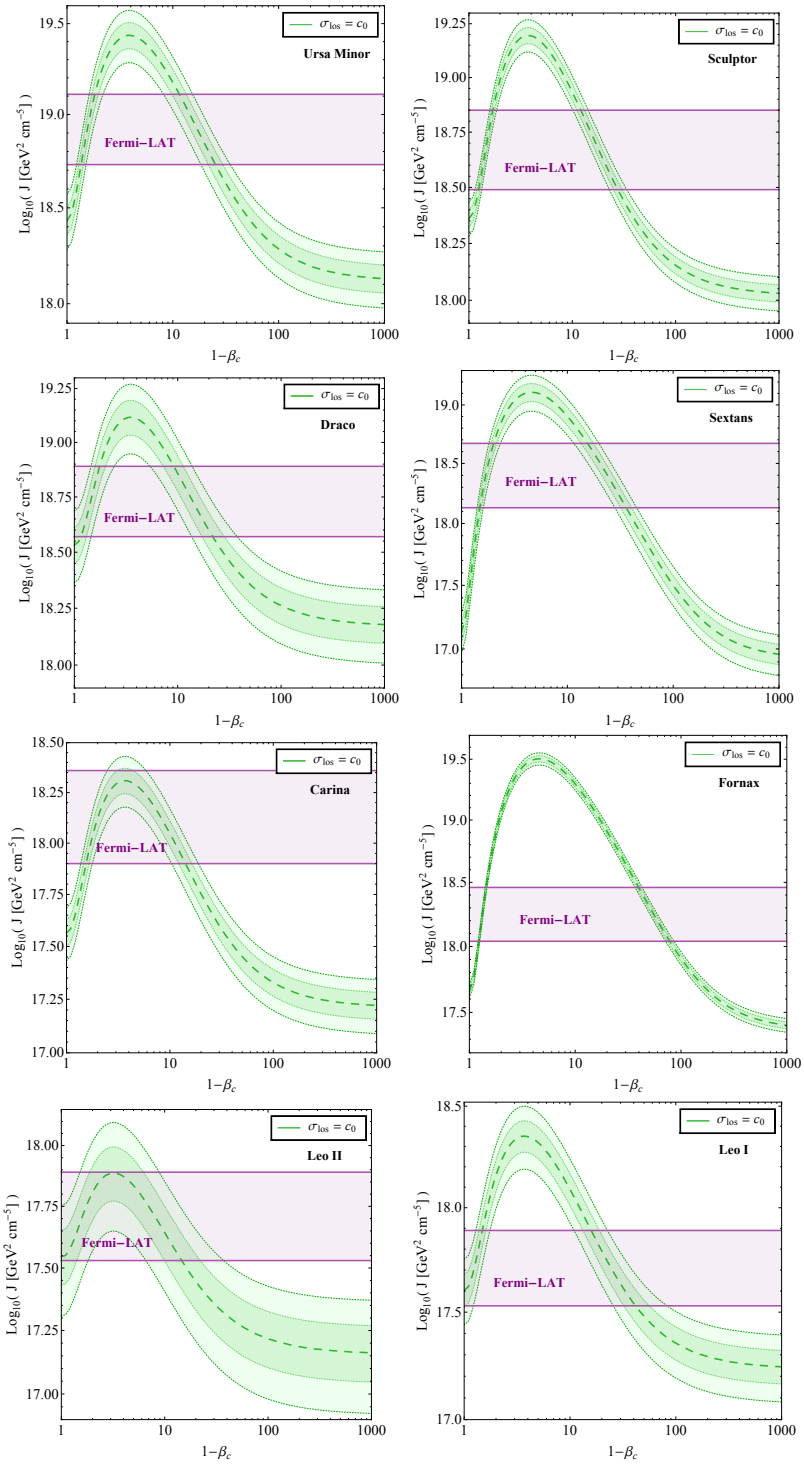

Figure 4.14: *J-factor as a function of constant orbital anisotropy β_c for all the classical satellites of the MW. The dashed green line represents the J-value corresponding to the best-fit constant l.o.s. velocity dispersion reported in Table 4.4, while the darker (lighter) green band encapsulates the 1σ (2σ) statistical uncertainty associated to σ_{los}. Also reported the 1σ band of the J-factor used in Ref. [291].*

density profile, as reported in Table 4.5. As for Ursa Minor, the choice of these values are again related to the order of magnitude of the first and last projected binned radius of the kinematical data set of each dSph in Ref. [397]. Finally, we show in Fig. 4.14 the J-factor for all the Classicals as a function of the constant anisotropy parameter β_c up to $\beta_c \simeq -10^3$. We remind that, within the chosen working setup, physical profiles are obtained from Eq. (4.40) only for $\beta_c \leq 0$.

As it stands out from Table 4.5 and Fig. 4.14, the economical method presented here yields for Ursa Minor results affine to the ones obtained in the previous section with the more involved MCMC analysis. Indeed, the integration for the J-factor is dominated by the inner part of the density profile, where the linear term in $\sigma_{los}(R) = c_0 + c_1 R/\mathcal{R}$ is suppressed both by $R/\mathcal{R} \ll 1$ and $c_1/c_0 \ll 1$. In Fig. 4.14 we find also the same behavior of J as a function of β_c for all the Classicals, given the same underlying fiducial model. From Fig. 4.14 we can clearly see that the dwarfs that present the largest span in J – more than two order of magnitudes for Sextans and Fornax – are also the ones characterized by the larger half-light radius. This trend is also confirmed by the fact that the dashed green line of the best-fit for Leo II covers less than one order of magnitude in J.

In Table 4.5 we report $\min J_{@\,1,2\sigma}$ of each of the analyzed objects. We can observe from Table 4.5 that each of the Classicals cannot relax the corresponding Fermi-LAT upper bound at 2σ on s-wave DM thermal relics by more than a factor of ~ 4, with the notable exception of Sextans, in which case the 2σ Fermi upper limit on $\langle \sigma v \rangle$ gets relaxed according to our conservative estimate of the J-factor by more than one order of magnitude. The J-factor of Sextans adopted by the Fermi collaboration seems to be quite large also if compared with other recent estimates in literature, see, e.g., Ref. [357]. In particular, comparing our results about $\min J_{@\,1,2\sigma}$ with those reported in Ref. [357] for the MW satellites, we never find differences with factors greater than ~ 5.

4.6 Open problems and opportunities

While sensitivity projections for DM limits/detection in the analysis of dwarf spheroidals remain particularly promising [424–426], pinning down a definite form for the DM profile of the MW satellites may be definitely of much broader relevance. As briefly mentioned in Chapter 1, within a cosmological context, dwarf spheroidal galaxies play today a central role in the understanding of possible controversies related to the small-scale predictions of the standard cold DM (CDM) paradigm.

CDM high-resolution N-body simulations typically predict subhalo mass functions

of MW-sized main halos scaling like $dN/dM \propto M^{-1.9}$ [427], with about 20% of the mass in subhalos, and a large number of not-yet-observed satellites in the MW. However, the "missing satellite" problem [428] has potentially been ameliorated with the advent of new surveys sensitive to extremely low-luminosity dwarf galaxies such as the recently discovered ultra-faint dSphs [348].

On the other hand, issues about the inner shape of the density profiles of the DM halos hosting galaxies – the "core-cusp" problem [429] – and the phenomenological inadequacy of NFW-inner cusps arising in CDM simulations [374], are still very debated subjects in literature, not only connected to the physics of baryonic feedback and star formation, but possibly also related to the fundamental properties of DM particles [430, 431]. For what concerns dwarf spheroidal galaxies, this issue is still very open since – as we have explicitly seen in our study case of Ursa Minor – kinematical data can support fairly well both cusps and cores in virtue of the mass-anisotropy degeneracy. From this point of view, it would be very interesting to investigate the "core-cusp" problem in MW satellites putting our inversion method in the context of a mass-anisotropy breaking pattern. While attempts to break the mass-anisotropy degeneracy based on the identification of different chemo-dynamical stellar components provides possible evidence of a core in Fornax and Sculptor [386, 387], opposite conclusions can be reached as well [388]. On top of the multi-component stellar populations, another possibility to attack the mass-anisotropy degeneracy may be offered by higher moments of the Boltzmann equation for the tracers of the system. For instance, its fourth moment yields a set of differential equations connected to the (potentially) observable kurtosis [384,385]. An inversion method for higher moment equations is still missing.

Finally, risen only few years back, we have to face today the so-called "too big to fail" problem [36]. Indeed, the existence of a good mass estimator at the half-light radius according to Eq. (4.18) allows one to have a reliable measurement of the subhalo mass function in the MW, to be compared with the expected population of subhalos found in numerical simulations of MW-size halos. It turns out that CDM-predicted subhalos are usually too massive and too numerous to be easily identified with the typical internal kinematics from known MW dSphs. At the same time, quite intriguingly, such predicted very massive subhalos should have triggered star formation much more efficiently than in MW satellites. While our study confirms the goodness of the MW satellite mass estimator at the basis of the "too big to fail", the very recent CDM N-body simulation in Ref. [432] seems to suggest that (possibly fine-tuned) mechanisms of baryonic physics may have played a quite relevant role in the evolution history of the predicted, but not detected, massive subhalos, in contrast to the original expectations from Ref. [36].

Closing remarks

A striking set of evidences is presently supporting the existence of Dark Matter (DM), i.e. the main constituent of the matter density in our observable Universe: making up roughly 26% of the total energy budget present in the Universe, they span an impressive range of scales in orders of magnitude, bracketed from below by the kpc size of the smallest observed galaxies, and from above by the tens of Mpc of the large-scale structures in the local Universe, aiming to a comprehensive picture about Nature itself. As of now, we know that DM has been playing the role of main character in accounting for the formation and evolution of structures, at the origin of life itself. However, after more than 80 years from the first indirect gravitational evidence, we still have very few informations about the fundamental building blocks of this dominant matter component. Addressing the "DM problem" is one of the most compelling challenges to undertake in Science today.

Thanks to the experimental sensitivity reached by a multitude of astrophysical and cosmological surveys in the last few decades, the set of different measurements we have nowadays at our disposal for the study of DM constitutes the pieces of an intricate puzzle. Once we have joined them all together, we get an informative identikit of some new degrees of freedom pertaining to the world of Particle Physics, rather than pointing to a modification of the laws of gravity or to the presence of a large amount of very faint massive compact objects. The resulting picture cannot single out an exact profile about the particle DM nature. However, a very simple paradigm like the freeze-out of a cold thermal relic in the early stages of the primordial Universe fits particularly well with deeply motivated theories beyond the Standard Model such as, e.g., Supersymmetry, projecting us onto the phenomenological window of the weak interactions of a weak-scale massive particle.

On the basis of these general considerations, illustrated in more detail in Chapter 1, the work of this thesis has been devoted to the study of the imprints in the gamma-ray sky coming from the annihilation of DM thermal relics, possibly occurring still today in galactic halos. This scientific investigation is generally demanding, but certainly urgent in these times, given the golden era we are living in with very precise measurements in the gamma-ray band, that stem from the realm of ground-based Cherenkov telescopes and, most importantly, from the continuous monitoring of the sky performed on-flight by the Fermi-LAT experiment.

In particular, in Chapter 2 we have set up the stages for the study of the gamma-ray sky, scrutinizing its main component coming from the interaction of cosmic-ray

particles with the interstellar medium. We have shown how gamma rays represent a complementary tool to learn about the propagation properties of charged particles out of the context of the set of cosmic-ray measurements available in our local environment. We have presented a phenomenological cosmic-ray propagation model characterized, in particular, by a radial dependence on the spectral index of the diffusion coefficient, reproducing state-of-the-art high-energy gamma-ray data, and, moreover, making distinctive predictions for the flux of Galactic neutrinos, with a detailed comparison with current and future neutrino observatory sensitivities.

We have scrutinized in Chapter 3 the claim of a clean gamma-ray signal from DM particles annihilating in the innermost central part of our Galaxy, analyzing the current gamma-ray data from the Galactic center region with the attempt of providing a careful interpretation of them. We have shown that, indeed, a net extended spherical excess – compatible with DM annihilation – stands out in the data as long as we completely ignore the effect of the high star-formation rate present in the region, that reasonably turns out into an injecting source of cosmic-ray particles previously missed in the literature. As highlighted in the final part of the chapter, further independent investigation of this effect by other groups, including the Fermi-LAT collaboration itself, leads to conclusions similar to those obtained in our study. This confirms the important role played by the physically expected injecting source of cosmic rays at the center of our Galaxy in relation to the interpretation of the so-called "GeV excess" at the Galactic center.

Finally, in Chapter 4, in opposition to the case of the Galactic center, we have analyzed the DM content of some of the most compelling targets for a DM particle indirect detection, the dwarf spheroidal galaxies of the Milky Way, characterized by large mass-to-light ratios, low backgrounds/foregrounds, and being relatively close to us. We have critically refined the estimate of astrophysical boost factors for a gamma-ray signal from DM annihilation in these objects. We have developed for the purpose a novel approach based on a direct link with the available kinematical and photometric informations for these galaxies. We have carried out in detail the study case of Ursa Minor and – as last original contribution in the thesis – we have extended the analysis to the whole set of classical satellites of the Milky Way. In light of the comparison of our findings with the literature, we can conclude that the classical dwarf spheroidals stand out as remarkable "DM laboratories", offering to us quite robust constraints from null findings in indirect DM searches and possibly offering new insights to go beyond the standard lore of the cold DM paradigm.

Appendix A

A spiky investigation on subregions around the GC

In Chapter 3, the predictions of the benchmark model introduced in Section 3.2.2 have been compared against the case of Dark Matter (DM) within the region of interest (ROI) defined by Galactic longitudes $|l| < 20°$ and Galactic latitudes $2° < |b| < 20°$. The results of the template fitting in the ROI show that the model proposed provides an overall good description of data, competitive with the one hold by DM. Using the best-fit components of our study in the full ROI, we can further investigate the comparison between the spike scenario and the DM one in a set of subregions of the ROI. In literature, the analysis of slices of the ROI has been indeed relevant to establish the morphological characterization of the excess emission, turned out to be almost spherical around the GC [292].

We report below the performance of our reference case against the DM one looking at the residuals with data in the predicted spectrum for each of the subregions defined in Table A.1 and illustrated in Fig. A.1. As displayed in Fig. A.2 - A.9, the reference case provides a good description of data in each of the subregions within systematic uncertainties. While the DM offers a slightly better agreement with data, the spike scenario can reproduce the morphology of the observed emission from the ROI with comparable accuracy.

ROI	**Definition**	$\Omega_{\mathbf{ROI}}$ [sr]
Region I, II	$\sqrt{l^2 + b^2} < 5°\,,\ \pm b > \lvert l\rvert$	$6.0 \cdot 10^{-3}$
Region III, IV	$5° < \sqrt{l^2 + b^2} < 10°\,,\ \pm b > \lvert l\rvert$	$1.78 \cdot 10^{-2}$
Region V, VI	$10° < \sqrt{l^2 + b^2} < 15°\,,\ \pm b > \lvert l\rvert$	$2.93 \cdot 10^{-2}$
Region VII, VIII	$5° < \sqrt{l^2 + b^2} < 15°\,,\ \pm l > \lvert b\rvert$	$3.54 \cdot 10^{-2}$

Table A.1: *Definition of the subregions for the morphological characterization of the GC excess emission. We remark also that every ROI has $|b| > 2°$.*

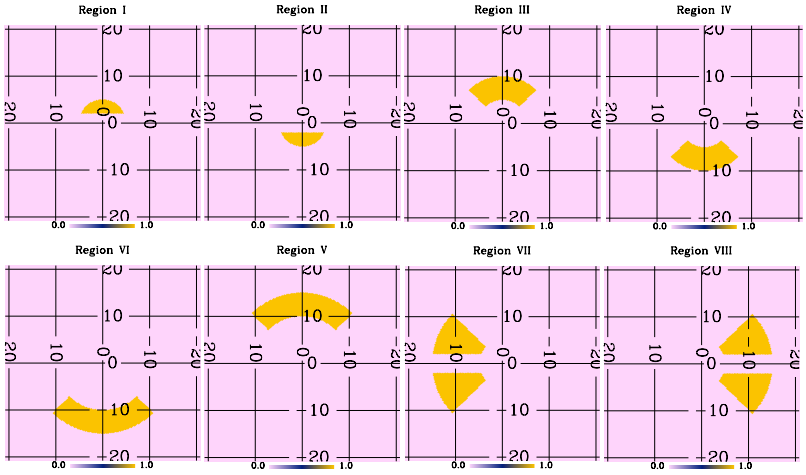

Figure A.1: *Subregions of the full ROI, namely $|l| < 20°$ and $2° < |b| < 20°$.*

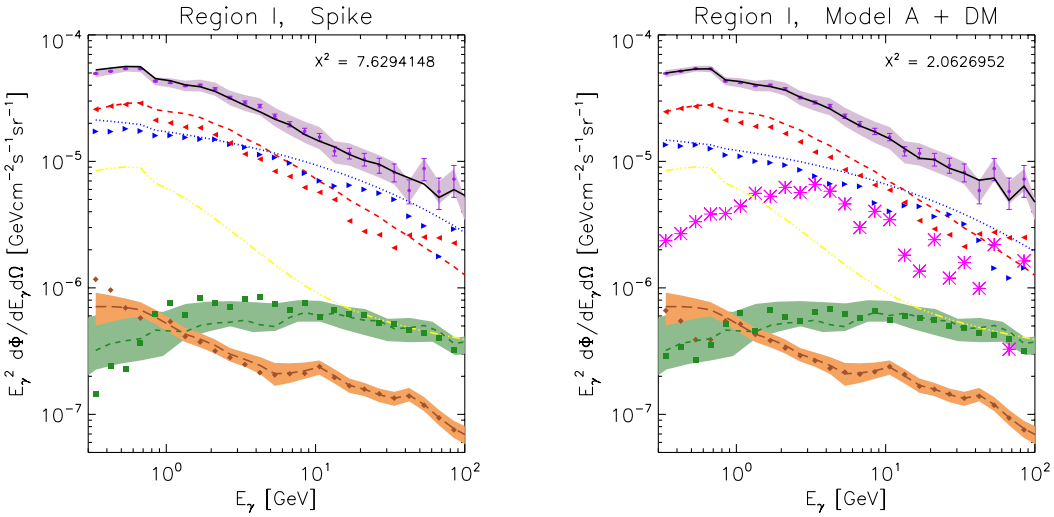

Figure A.2: *Predicted spectrum for the spike and DM scenario in Region I.*

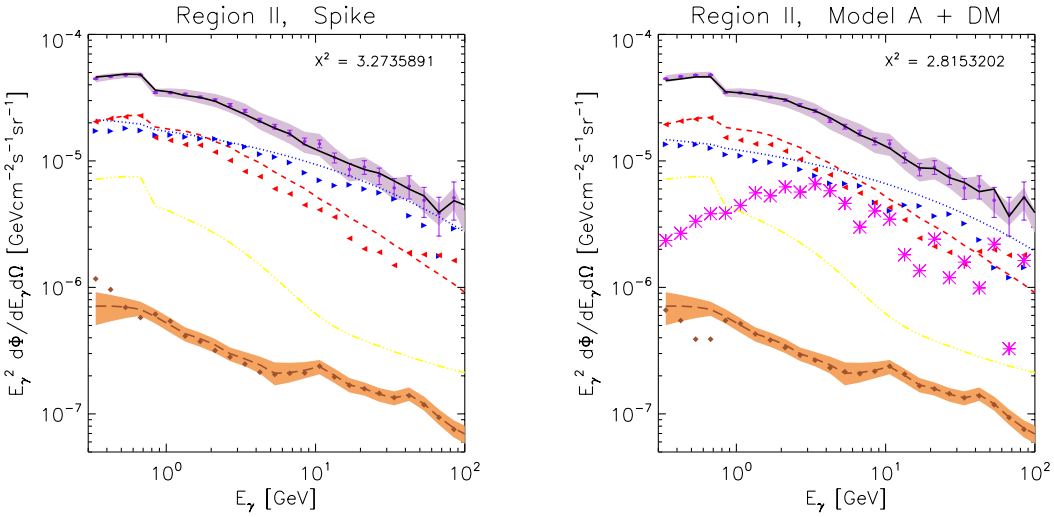

Figure A.3: *Predicted spectrum for the spike and DM scenario in Region II.*

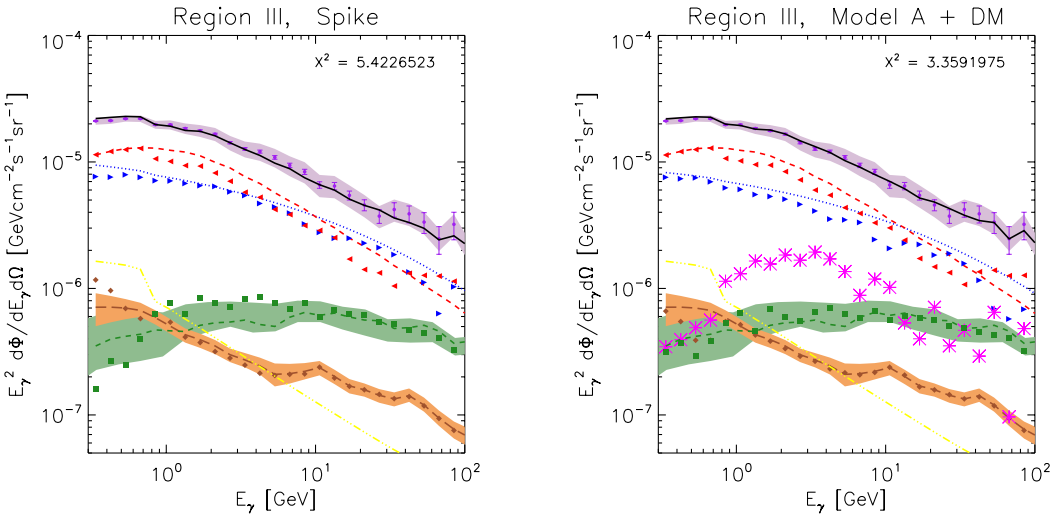

Figure A.4: *Predicted spectrum for the spike and DM scenario in Region III.*

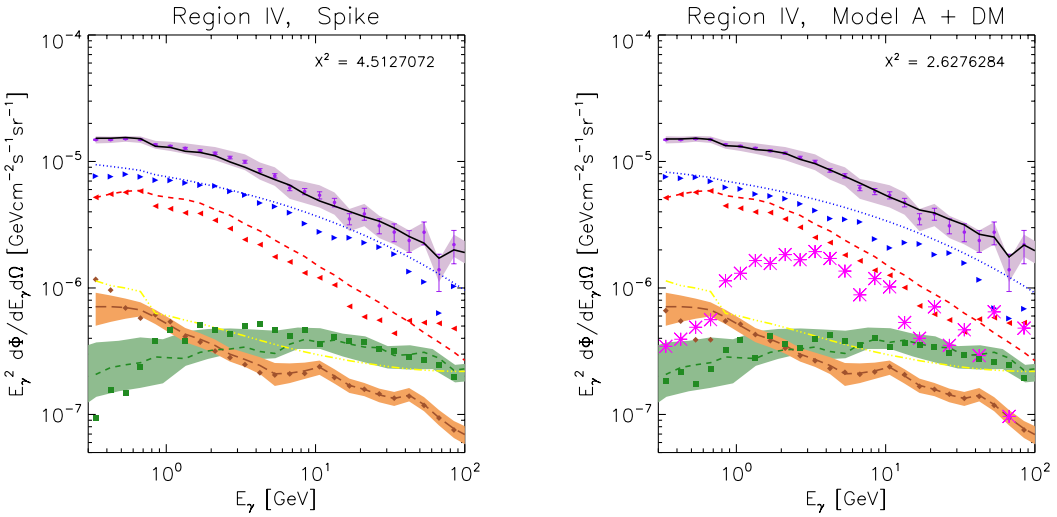

Figure A.5: *Predicted spectrum for the spike and DM scenario in Region IV.*

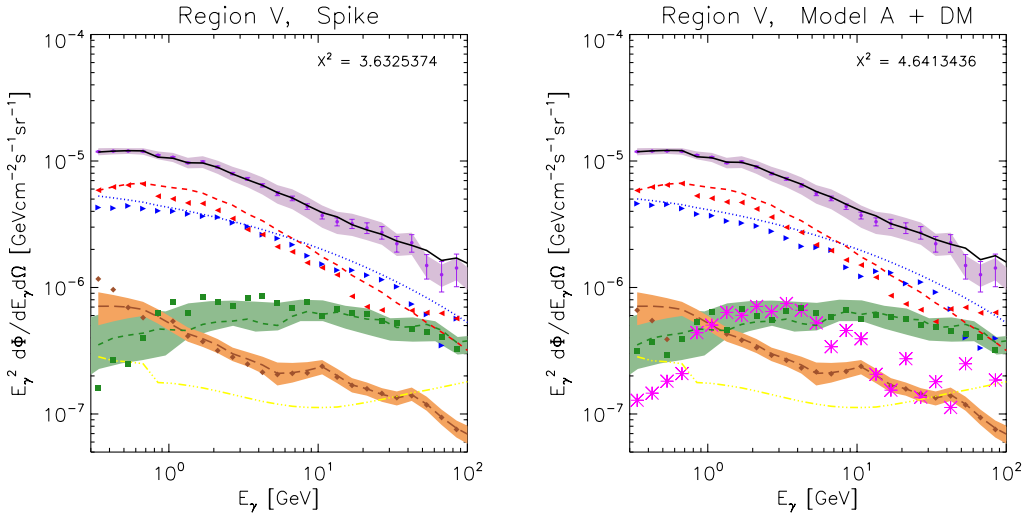

Figure A.6: *Predicted spectrum for the spike and DM scenario in Region V.*

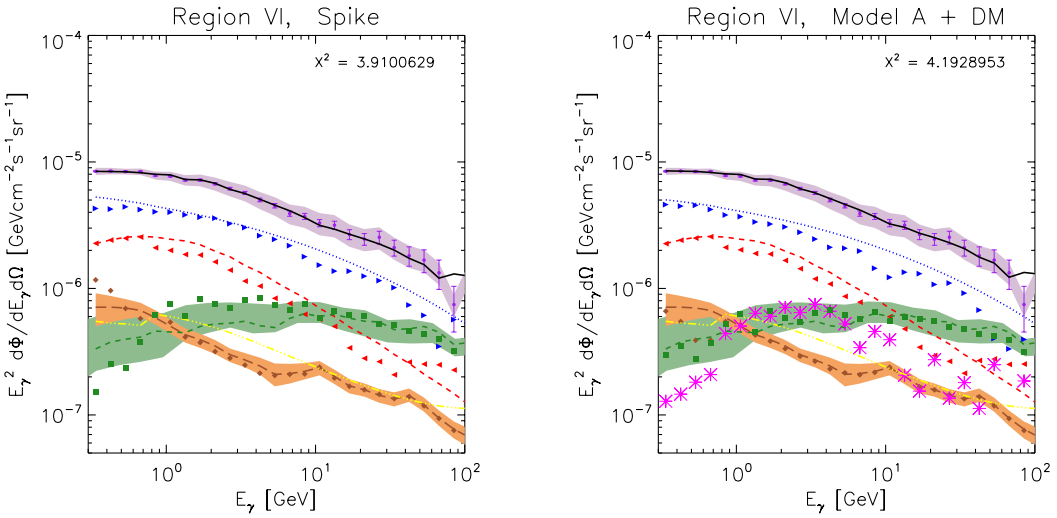

Figure A.7: *Predicted spectrum for the spike and DM scenario in Region VI.*

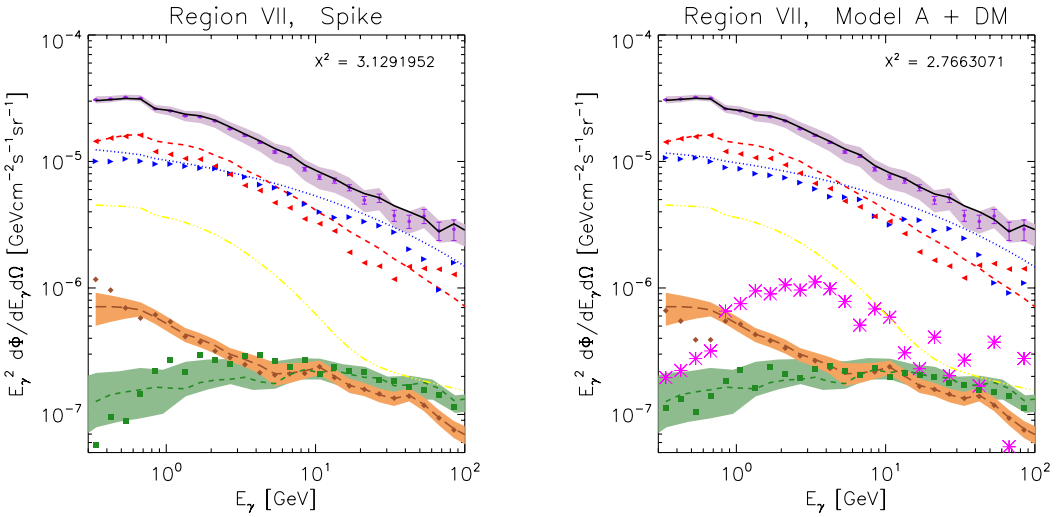

Figure A.8: *Predicted spectrum for the spike and DM scenario in Region VII.*

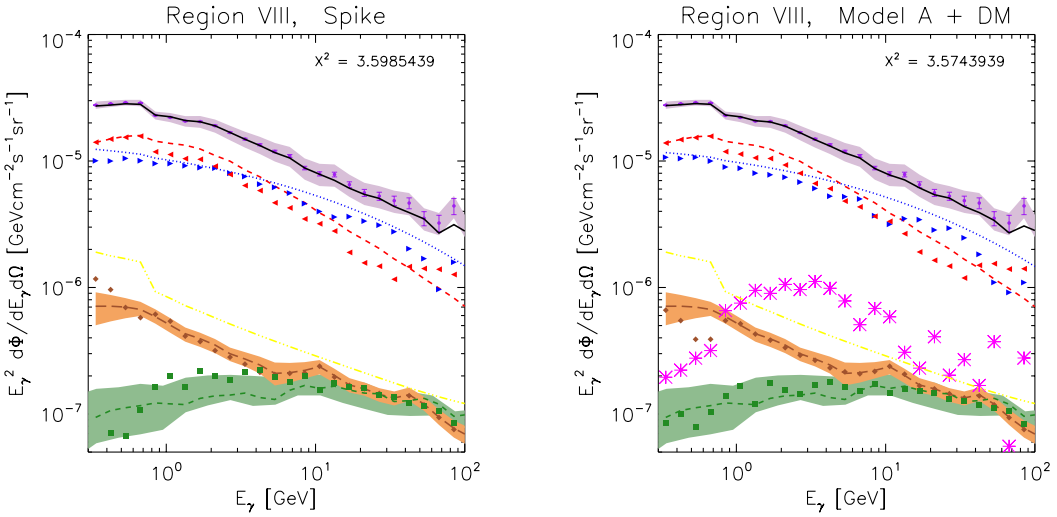

Figure A.9: *Predicted spectrum for the spike and DM scenario in Region VIII.*

B Appendix B

J-factors and Jeans inversion in spherical systems

B.1 Computing J-factors: the easy-peasy pieces

The angular + line-of-sight integral of a spherically symmetric source takes a simple form when the observer looks at the center of the source. In such case, introducing a change of coordinates that fully exploits the symmetry of the problem, the J-factor computations reduces to a single radial integration over the DM density squared times an appropriate radial window function. We briefly resume here the steps to perform this convenient mapping.
Consider an observer $\mathcal{O}$ pointing towards the center of the astrophysical system under study, located at the distance $\mathcal{D}$, with an angular acceptance $\Delta\Omega$. In the coordinate system centered on $\mathcal{O}$ – see Fig. B.1 – Eq. (4.1) can be written as:

$$J = 2\pi \int_0^{\cos\psi_{\rm max}} d\cos\psi \int_{\ell_-(\psi,\mathcal{R})}^{\ell_+(\psi,\mathcal{R})} d\ell \; \rho^2\left[r(\psi,\ell)\right] \;, \tag{B.1}$$

where $\psi_{\rm max}$ is obtained from $\Delta\Omega = 2\pi\Big(1-\cos\psi_{\rm max}\Big)$ and $\mathcal{R}$ is the radial boundary for the spherical system. In Eq. (B.1) the explicit expression for $r(\psi,\ell)$ is given by the geometrical relation:

$$r^2 = \ell^2 + \mathcal{D}^2 - 2\,\ell\,\mathcal{D}\cos\psi \;, \tag{B.2}$$

and the extremes of integration ℓ_+ and ℓ_- are the solutions of the equation above:

$$\ell_\pm(\psi, r) = \mathcal{D}\cos\psi \pm \sqrt{r^2 - \mathcal{D}^2\sin^2\psi} \;. \tag{B.3}$$

The values of $\psi_{\rm max}$, $\mathcal{R}$ and $\mathcal{D}$ correspond to the set of data needed to determine the J-factor. Note that one can also trade line-of-sight angles for line-of-sight projected radii, replacing $\psi_{\rm max}$ with $R_{\rm max}$ as given by $\tan\psi_{\rm max} = R_{\rm max}/\sqrt{\mathcal{D}^2 - R_{\rm max}^2}$. In light of the axial symmetry along the line of sight of $\mathcal{O}$, it is sufficient to perform a two-dimensional mapping in order to move to the coordinate system centered on

the halo density. Following Fig. B.1, the new set of coordinates (R, r) we want to introduce is related to the starting pair (ℓ, ψ) by:

$$d\Big(\cos\psi\Big) = dR\frac{\partial}{\partial R}\sqrt{1-\frac{R^2}{\mathcal{D}^2}} \qquad \text{and} \qquad \pm\, d\ell = dr\frac{\partial}{\partial r}\Big(\sqrt{\mathcal{D}^2-R^2} \pm \sqrt{r^2-R^2}\Big)\,. \tag{B.4}$$

Thus, we can easily rewrite Eq. (B.1) in the new coordinate system as:

$$J = \frac{4\pi}{\mathcal{D}^2}\int_0^{R_{\rm max}} \frac{dR\,R}{\sqrt{1-\frac{R^2}{\mathcal{D}^2}}}\int_R^{\mathcal{R}} \frac{dr}{\sqrt{1-\frac{R^2}{r^2}}}\rho^2(r)\;, \tag{B.5}$$

and exchanging the order of integration we get:

$$J = \frac{4\pi}{\mathcal{D}^2}\;\Bigg[\;\int_0^{R_{\rm max}} dr\rho^2(r)\int_0^{r}\frac{dR\,R}{\sqrt{\Big(1-\frac{R^2}{\mathcal{D}^2}\Big)\Big(1-\frac{R^2}{r^2}\Big)}} \tag{B.6}$$

$$+\;\int_{R_{\rm max}}^{\mathcal{R}} dr\rho^2(r)\int_0^{R_{\rm max}}\frac{dR\,R}{\sqrt{\Big(1-\frac{R^2}{\mathcal{D}^2}\Big)\Big(1-\frac{R^2}{r^2}\Big)}}\;\Bigg]\,, \tag{B.7}$$

where now the R integral can be performed analytically in both terms. Introducing the dimensionless radial function:

$$\mathcal{W}(r;s,t) \equiv \frac{1}{\mathcal{D}^2}\int_{s^2}^{t^2}\frac{dR^2}{2\sqrt{\Big(1-\frac{R^2}{\mathcal{D}^2}\Big)\Big(1-\frac{R^2}{r^2}\Big)}} = \frac{r}{\mathcal{D}}\,\log\left(\frac{\sqrt{\mathcal{D}^2-t^2}-\sqrt{r^2-t^2}}{\sqrt{\mathcal{D}^2-s^2}-\sqrt{r^2-s^2}}\right)\,, \tag{B.8}$$

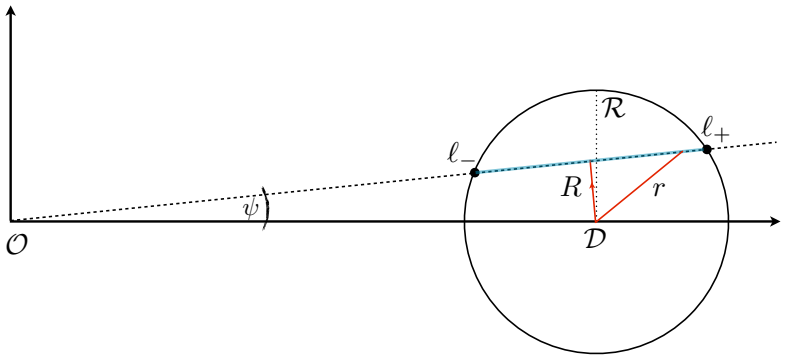

Figure B.1: *L.o.s. integration (light blue segment) in (R, r) coordinates (in red) of an observer $\mathcal{O}$ with angular aperture ψ, placed at a distance $\mathcal{D}$ from a spherical system of finite size $\mathcal{R}$.*

we obtain then that the J-factor can be evaluated by a single integral formula:

$$J = 4\pi \int_0^{\mathcal{R}} dr\, \widetilde{J}(r)\,, \tag{B.9}$$

where the integrand $\widetilde{J}$ is a function of the radial coordinate r and carries the dimension of $\rho^2(r)$:

$$\widetilde{J}(r) = \rho^2(r)\,[\,\mathcal{W}(r;0,r)\,\theta_H(R_{\rm max}-r) + \mathcal{W}(r;0,R_{\rm max})\,\theta_H(r-R_{\rm max})\,]\,, \tag{B.10}$$

with $\theta_H(r)$ being the Heaviside step function.
In case of $r \leq R_{\rm max}$ and $R_{\rm max} \ll \mathcal{D}$, the function $\mathcal{W}(r;0,r)$ is very well approximated by $r^2/\mathcal{D}^2$, while for greater radii $\mathcal{W}(r;0,R_{\rm max})$ rapidly decreases towards the limit $1-\sqrt{1-R_{\rm max}^2/\mathcal{D}^2}$.
Thus, choosing an angular aperture $\psi_{\rm max}$ so that $R_{\rm max}/\mathcal{D} \ll 1$, since usually $\rho(r)$ rapidly approaches 0 with increasing radius, Eq. (B.9) can be numerically approximated as:

$$J \simeq \frac{4\pi}{\mathcal{D}^2} \int_0^{\mathcal{R}} dr\, r^2\, \rho^2(r)\,. \tag{B.11}$$

In Section 4.4 we presented all the results for the computation of the J-factor making use of the full expression in Eq. (B.9)-(B.10). However, the approximation above performs better than the per mille level already for $\mathcal{D} \sim \mathcal{O}(10^2)$ kpc, $\psi_{\rm max} \lesssim 1^\circ$. Note that if we would have studied the case of decaying DM particles (see e.g. [433]) rather than DM pair annihilation, the analogous of Eq. (B.11) would have allowed us to focus directly on the mass profile, Eq. (4.10), without the need to compute the density profile and to argue the validity of its extrapolation to inner radii.

B.2 Jeans inversion in spherical systems: the details

In this appendix we review the "inversion" of the Jeans equation for spherical systems. We start following the procedure outlined in [364], and we end with a general expression for the inverted mass profile $\mathcal{M}$ that holds for any generic l.o.s. velocity dispersion and surface brightness profile. Our derivation is valid for a generic orbital velocity anisotropy, requiring only $\beta(r) \neq 1\ \forall\, r$. Inversion formulas for specific anisotropy models can be also found in [363].

A good starting point to derive the inversion formula is the definition of the projected dynamical pressure, $P(R) \equiv \sigma_{los}^2(R)\, I(R)$, see Eq. (4.6), split into two integrals

with integrand modified by adding and subtracting the term $p(r)\,\beta(r)/\sqrt{r^2-R^2}$:

$$P(R) = \int_{R^2}^{\infty} \frac{dr^2}{\sqrt{r^2-R^2}} p(r)\,[1-\beta(r)] + \int_{R^2}^{\infty} \frac{dr^2}{\sqrt{r^2-R^2}} \left(r^2-R^2\right) \frac{p(r)\beta(r)}{r^2} \;; \tag{B.12}$$

the second contribution on the r.h.s. can be rewritten as:

$$\int_{R^2}^{\infty} dr^2 \sqrt{r^2-R^2} \frac{d}{dr^2} \left[-\int_{r^2}^{\infty} d\tilde{r}^2 \, \frac{p(\tilde{r})\beta(\tilde{r})}{\tilde{r}^2} \right] \;, \tag{B.13}$$

and integrated by parts obtaining:

$$\frac{1}{2} \int_{R^2}^{\infty} \frac{dr^2}{\sqrt{r^2-R^2}} \int_{r^2}^{\infty} d\tilde{r}^2 \, \frac{p(\tilde{r})\beta(\tilde{r})}{\tilde{r}^2} \;, \tag{B.14}$$

with the boundary term at $r^2 \to \infty$ in the integration by parts vanishing under the assumption that $p(r)\beta(r)$ drops to 0 faster than $1/r$, i.e. the same assumption which had already to be valid for Eq. (4.6). Then, the projected dynamical pressure reads:

$$P(R) = \int_{R^2}^{\infty} \frac{dr^2}{\sqrt{r^2-R^2}} \left\{ p(r)\,[1-\beta(r)] + \frac{1}{2} \int_{r^2}^{\infty} d\tilde{r}^2 \, \frac{p(\tilde{r})\beta(\tilde{r})}{\tilde{r}^2} \right\} \;; \tag{B.15}$$

making it explicit that the quantity in the curly brackets is the inverse Abel transform of $P(R)$. Indeed, assuming that $P(R)$ vanishes at large R faster than $1/R$, one is formally allowed to invert this expression to find:

$$p(r)\,[1-\beta(r)] + \frac{1}{2} \int_{r^2}^{\infty} d\tilde{r}^2 \, \frac{p(\tilde{r})\beta(\tilde{r})}{\tilde{r}^2} = -\frac{1}{\pi} \int_{r^2}^{\infty} \frac{dR^2}{\sqrt{R^2-r^2}} \frac{dP}{dR^2} \;, \tag{B.16}$$

and performing another integration by parts,

$$p(r)\,[1-\beta(r)] + \frac{1}{2} \int_{r^2}^{\infty} d\tilde{r}^2 \, \frac{p(\tilde{r})\beta(\tilde{r})}{\tilde{r}^2} = \frac{2}{\pi} \int_{r^2}^{\infty} dR^2 \sqrt{R^2-r^2} \frac{d^2P}{(dR^2)^2} \;. \tag{B.17}$$

We can now differentiate the equation above in the log measure dr/r to get:

$$[1-\beta(r)]\; r\frac{dp}{dr} - \left[\beta(r) + r\frac{d\beta}{dr}\right] p(r) = -\frac{2r^2}{\pi} \int_{r^2}^{\infty} \frac{dR^2}{\sqrt{R^2-r^2}} \frac{d^2P}{(dR^2)^2} \;, \tag{B.18}$$

i.e. a first order differential equation for $p(r)$ analogous to Eq. (4.2), where the substantial difference lies on the presence of the second derivative of $P(R)$ in place of the first derivative of the gravitational potential. The formal solution for a

physical radial pressure vanishing at infinity is:

$$p(r) = \int_r^\infty d\tilde{r} \frac{2\tilde{r}}{\pi\,[1-\beta(\tilde{r})]}\,\exp\left\{-\int_r^{\tilde{r}} dr' \frac{\beta(r') + r'\frac{d\beta}{dr'}}{r'\,[1-\beta(r')]}\right\} \int_{\tilde{r}^2}^\infty \frac{dR^2}{\sqrt{R^2-\tilde{r}^2}} \frac{d^2P}{(dR^2)^2} \tag{B.19}$$

and, exchanging the order of integration, it can be rewritten as:

$$p(r) = \frac{1}{\pi\,[1-\beta(r)]} \int_{r^2}^\infty dR^2 \frac{d^2P}{(dR^2)^2} \int_{r^2}^{R^2} \frac{d\tilde{r}^2}{\sqrt{R^2-\tilde{r}^2}} \mathcal{H}_\beta(r,\tilde{r})\ , \tag{B.20}$$

where $\mathcal{H}_\beta(r,\tilde{r})$ was defined in Eq. (4.9). Finally, plugging this result in Eq. (4.2) we get:

$$\mathcal{M}(r) = \frac{r^2}{G_N \nu(r)} \left\{ \frac{2\,r}{\pi\,[1-\beta(r)]} \int_{r^2}^\infty \frac{dR^2}{\sqrt{R^2-r^2}} \frac{d^2P}{(dR^2)^2} - \left[\frac{\frac{\beta(r)}{r} + \frac{d\beta}{dr}}{1-\beta(r)} + 2\frac{\beta(r)}{r}\right] p(r) \right\}\ . \tag{B.21}$$

Taking into account that:

i) $\nu(r)$ is the inverse Abel transform $\widehat{I}(r^2)$ of the surface brightness $I(R^2)$;

ii) the Abel integral transform satisfy the property that, if $f(x) = \mathbf{A}[\widehat{f}(y)]$, then $df/dx = \mathbf{A}[d\widehat{f}/dy]$;

iii) it is convenient to introduce $a_\beta(r)$ using the definition given in Eq. (4.9);

it is then easy to rewrite the above inversion formula for the mass in the compact form given in Eq. (4.10).
In case the computation of the inverse Abel transform and its derivative becomes numerically challenging, alternatively the mass profile can be calculated as a single integral of the second derivative in R^2 of the projected dynamical pressure over a kernel depending on r. In this form Eq. (B.21) just reads:

$$\mathcal{M}(r) = \frac{r}{G_N\,\pi\,\nu(r)\,[1-\beta(r)]} \int_{r^2}^\infty dR^2 \frac{d^2\,P}{(dR^2)^2} \widetilde{W}_\beta(r,R)\,, \tag{B.22}$$

with the kernel being:

$$\widetilde{W}_\beta(r,R) = \frac{2r^2}{\sqrt{R^2-r^2}} - \frac{\beta(r)}{1-\beta(r)}\left(3 + \frac{d\log\beta}{d\log r} - 2\,\beta(r)\right) \int_{r^2}^{R^2} \frac{d\tilde{r}^2}{\sqrt{R^2-\tilde{r}^2}} \mathcal{H}_\beta(r,\tilde{r})\,. \tag{B.23}$$

Eq. (B.22) is the form which has been used to compute mass profiles corresponding to projected line-of-sight velocity dispersions derived from a trial parametric form of the DM density profiles, the "parametric fit" cases we introduced at the beginning of Section 4.4.2. To reach the exquisite precision level displayed in Fig. 4.9, rather

than computing $\sigma_{los}(R)$ alone, it was actually useful to implement the analytic expression for $d^2P/(dR^2)^2$ one finds taking the definition Eq. (4.6), supplemented by Eq. (4.4), and performing a few manipulations:

$$\begin{aligned}\frac{d^2\,P}{(dR^2)^2} \quad = \quad & \frac{G_N}{2}\int_R^\infty \frac{dr}{\sqrt{r^2-R^2}}\left[\frac{\mathcal{M}_i(r)\nu(r)}{r^2}\right]\Bigg\{\left(1-\frac{R^2}{r^2}\right)\frac{1}{R}\left(\frac{\partial K_1}{\partial R}+\frac{\partial K_2}{\partial R}\right) \\ & -\frac{K_1(r,R)+K_2(r,R)-2\,K_3(r,R)}{r^2} \\ & -2\sqrt{r^2-R^2}\int_R^r \frac{d\tilde{r}}{\sqrt{\tilde{r}^2-R^2}}\left[\left(1-\frac{R^2}{\tilde{r}^2}\right)\frac{1}{\tilde{r}\,R}\left(\frac{\partial K_4}{\partial R}-\frac{\partial K_5}{\partial R}\right)\right. \\ & \left.-\frac{K_4(\tilde{r},R)-K_5(\tilde{r},R)}{\tilde{r}^3}\right]\exp\left[2\int_{\tilde{r}}^r ds\frac{\beta_i(s)}{s}\right]\Bigg\}\,; \end{aligned} \tag{B.24}$$

where $\mathcal{M}_i(r)$ and $\beta_i(r)$ label, respectively, the mass and orbital anisotropy profiles taken as trial initial step, while the five integral kernels just introduced are the following dimensionless functions:

$$\begin{aligned} K_1(r,R) &= \left[1+\beta_i(r)\left(2-3\frac{R^2}{r^2}\right)\right]\left(\frac{d\log\mathcal{M}_i}{d\log r}+\frac{d\log\nu}{d\log r}-3\right)\,, \\ K_2(r,R) &= \beta_i(r)\left[6\frac{R^2}{r^2}+\frac{d\log\beta_i}{d\log r}\left(2-3\frac{R^2}{r^2}\right)\right]\,, \\ K_3(r,R) &= \beta_i(r)+\bar{\beta}_i(r)\left(8-9\frac{R^2}{r^2}\right)\,, \\ K_4(r,R) &= 2\left[1+\beta_i(r)\right]\left[\beta_i(r)+\bar{\beta}_i(r)\left(2-3\frac{R^2}{r^2}\right)\right]\,, \\ K_5(r,R) &= \beta_i(r)\frac{d\log\beta_i}{d\log r}+\bar{\beta}_i(r)\left[\frac{d\log\bar{\beta}_i}{d\log r}\left(2-3\frac{R^2}{r^2}\right)+6\,\frac{R^2}{r^2}\right]\,, \end{aligned} \tag{B.25}$$

with the auxiliary function $\bar{\beta}_i(r)$ given by:

$$\bar{\beta}_i(r)=\beta_i(r)\left[1+\beta_i(r)-\frac{1}{2}\frac{d\log\beta_i}{d\log r}\right]\,. \tag{B.26}$$

Acknowledgements

The first acknowledgements go to my family. The way they have educated me is the reason why I got so interested and curious about Nature. I will be always infinitely grateful to them for everything they have done. This last effort of mine is firstly dedicated to them.

The second special acknowledgement goes to Serena. She looks pretty tiny, and she is, but she is also the strongest person I have ever met in my whole life. I have been 4π-impressed by her, but she still keeps surprising me every day. I triggered her interest somehow – how? – ... well, I don't really know how, but what happened is definitely the best thing that could happen to me in this Ph.D. .

I had the privilege to be supervised by a person that has a true horizontal knowledge about Physics, as very few scientists I met, I would say. Also, despite the cultural gap, I have never felt uncomfortable in making mistakes or supporting wrong statements in front of him. He has been always open-minded to me, the reason why I have been able to make some progress in different areas of research at the same time. I wish to acknowledge Piero for all that. For all his invaluable teaching. The critical way he approaches to a Physics problem is for me a reference case for the researcher I would like to be one day.

During my Ph.D. in SISSA, I have also accepted the challenge to do a sort of "Ph.D. in the Ph.D.". I am "in debt" with Luca Silvestrini for this extra source of stress and painful difficulty. Luca is probably the academic that knows me the best. Despite this, he still keeps believing in me like few ones. I really had the pleasure to work with a "rising Italian star", see [434] for details, since I were an undergrad, that is to say, I have been tremendously lucky from the beginning. I wish to thank him for the endless patience and support, for all the time and resources he saved for me in these years. Of course, I am extremely grateful also to Enrico Franco and Marco Ciuchini. Discussing about Physics with them has been another great advantage of mine in my young career as a researcher. I wish also to thank Ayan and Marco for the "flavorful" gratifying collaboration we have been sharing so far.

I wish to thank very much Dario Grasso to have involved me in his original project, at the basis of some of the material presented in Chapter 2. I want to thank a lot Antonio Marinelli as well for the important contribution he has been giving to that. I am certainly thankful to Marco Taoso for his fundamental contribution to the study carried out in Chapter 3. I wish to thank also Carmelo Evoli and Gabrijela Zaharijas for several delightful discussions on cosmic-ray physics and gamma rays.

I am in debt (this time I am serious) with all the staff of the AstroParticle Physics and Theoretical Particle Physics group for the high quality of teaching in the classes attended in these years, and for the discussions I have enjoyed with many of the members of these two groups. I wish also to thank explicitly Andrea Romanino and Stefano Liberati for valuable extra-curricula advices.

I have several friends from SISSA I would like to thank today for collaborations and/or discussions: Alejandro, Alessio, Federico, Bruno, Marco, Giovanni, Ivan, Alex, Emanuele, Gabriele, David and Marko. I hope I did not forget anybody else.

Eventually, I wish to deeply thank Andrea and Stefano, since 23 years of true friendship do not grow on trees.

The last acknowledgements I want to make are again very special. All the material presented in Chapter 2 and Chapter 3 of this thesis is strongly correlated to the patience, the endless discussions, and the hours of day&night work experienced together with two amazing researchers, that turned out to be also very good friends: Alfredo Urbano and Daniele Gaggero. The intense collaboration I had with them has signed the most crucial and important steps of my Ph.D., and of myself, as a researcher. This thesis is certainly dedicated to them as well.

I am finally grateful to Nicolao Fornengo and Subir Sarkar for a careful reading of this thesis and for the improvements that have lead to the current revised version.

Bibliography

[1] D. Gaggero, A. Urbano, M. Valli and P. Ullio, Gamma-ray sky points to radial gradients in cosmic-ray transport, *Phys. Rev.* **D91** (2015) 083012, [1411.7623].

[2] D. Gaggero, D. Grasso, A. Marinelli, A. Urbano and M. Valli, The gamma-ray and neutrino sky: A consistent picture of Fermi-LAT, Milagro, and IceCube results, *Astrophys. J.* **815** (2015) L25, [1504.00227].

[3] D. Gaggero, M. Taoso, A. Urbano, M. Valli and P. Ullio, Towards a realistic astrophysical interpretation of the gamma-ray Galactic center excess, *JCAP* **1512** (2015) 056, [1507.06129].

[4] P. Ullio and M. Valli, A critical reassessment of particle Dark Matter limits from dwarf satellites, *JCAP* **1607** (2016) 025, [1603.07721].

[5] D. Gaggero, D. Gaggero, D. Grasso, A. Marinelli, A. Urbano and M. Valli, Gamma-ray and neutrino diffuse emissions of the Galaxy above the TeV, 1507.07796.

[6] D. Gaggero, D. Grasso, A. Marinelli, A. Urbano and M. Valli, A Hadronic Scenario for the Galactic Ridge, 2015. 1508.03681.

[7] A. Marinelli, D. Gaggero, D. Grasso, A. Urbano and M. Valli, Interpretation of astrophysical neutrinos observed by IceCube experiment by setting Galactic and extra-Galactic spectral components, *EPJ Web Conf.* **116** (2016) 04009, [1604.05776].

[8] "HEPfit, a tool to combine indirect and direct constraints on high energy physics." http://hepfit.roma1.infn.it/.

[9] M. Ciuchini, M. Fedele, E. Franco, S. Mishima, A. Paul, L. Silvestrini and M. Valli, $B \to K^* \ell^+ \ell^-$ decays at large recoil in the Standard Model: a theoretical reappraisal, *JHEP* **06** (2016) 116, [1512.07157].

[10] G. Bertone and D. Hooper, A History of Dark Matter, 1605.04909.

[11] F. Zwicky, Die Rotverschiebung von extragalaktischen Nebeln, *Helvetica Physica Acta* **6** (1933) 110–127.

[12] A. D. Lewis, D. A. Buote and J. T. Stocke, Chandra observations of Abell 2029: The Dark matter profile at < 0.01 R(VIR) in an unusually relaxed cluster, *Astrophys. J.* **586** (2003) 135–142, [astro-ph/0209205].

[13] R. Massey, T. Kitching and J. Richard, The dark matter of gravitational lensing, *Rept. Prog. Phys.* **73** (2010) 086901, [1001.1739].

[14] D. Paraficz, J.-P. Kneib, J. Richard, A. Morandi, M. Limousin and E. Jullo, The Bullet Cluster revisited: New results from new constraints and improved strong lensing modeling technique, *ArXiv e-prints* (Sept., 2012) , [1209.0384].

[15] V. C. Rubin and W. K. Ford, Jr., Rotation of the Andromeda Nebula from a Spectroscopic Survey of Emission Regions, *The Astrophysical Journal* **159** (Feb., 1970) 379.

[16] M. Milgrom, A modification of the Newtonian dynamics as a possible alternative to the hidden mass hypothesis, *The Astrophysical Journal* **270** (July, 1983) 365–370.

[17] J. D. Bekenstein, Relativistic gravitation theory for the MOND paradigm, *Phys. Rev.* **D70** (2004) 083509, [astro-ph/0403694].

[18] Planck collaboration, P. A. R. Ade et al., Planck 2015 results. XIII. Cosmological parameters, 1502.01589.

[19] A. Joyce, B. Jain, J. Khoury and M. Trodden, Beyond the Cosmological Standard Model, *Phys. Rept.* **568** (2015) 1–98, [1407.0059].

[20] D. S. Gorbunov and V. A. Rubakov, *Introduction to the theory of the early universe: Cosmological perturbations and inflationary theory.* 2011, 10.1142/7874.

[21] B. D. Fields, P. Molaro and S. Sarkar, Big-Bang Nucleosynthesis, *Chin. Phys.* **C38** (2014) , [1412.1408].

[22] S. Dodelson and M. Liguori, Can Cosmic Structure form without Dark Matter?, *Phys. Rev. Lett.* **97** (2006) 231301, [astro-ph/0608602].

[23] S. Dodelson, The Real Problem with MOND, *Int. J. Mod. Phys.* **D20** (2011) 2749–2753, [1112.1320].

[24] M. Yu. Khlopov, Primordial Black Holes, *Res. Astron. Astrophys.* **10** (2010) 495–528, [0801.0116].

[25] D. R. Law, S. R. Majewski and K. V. Johnston, Evidence for a Triaxial Milky Way Dark Matter Halo from the Sagittarius Stellar Tidal Stream, *The Astrophysical Journal Letters* **703** (Sept., 2009) L67–L71, [0908.3187].

[26] J. Miralda-Escudé, A test of the collisional dark matter hypothesis from cluster lensing, *The Astrophysical Journal* **564** (2002) 60.

[27] D. Harvey, R. Massey, T. Kitching, A. Taylor and E. Tittley, The non-gravitational interactions of dark matter in colliding galaxy clusters, *Science* **347** (2015) 1462–1465, [1503.07675].

[28] J. L. Feng, M. Kaplinghat and H.-B. Yu, Halo Shape and Relic Density Exclusions of Sommerfeld-Enhanced Dark Matter Explanations of Cosmic Ray Excesses, *Phys. Rev. Lett.* **104** (2010) 151301, [0911.0422].

[29] M. R. Buckley and P. J. Fox, Dark Matter Self-Interactions and Light Force Carriers, *Phys. Rev.* **D81** (2010) 083522, [0911.3898].

[30] S. Tulin, H.-B. Yu and K. M. Zurek, Beyond Collisionless Dark Matter: Particle Physics Dynamics for Dark Matter Halo Structure, *Phys. Rev.* **D87** (2013) 115007, [1302.3898].

[31] M. J. Jee, H. Hoekstra, A. Mahdavi and A. Babul, Hubble Space Telescope/Advanced Camera for Surveys Confirmation of the Dark Substructure in A520, *Astrophys. J.* **783** (2014) 78, [1401.3356].

[32] L. Berezhiani and J. Khoury, Theory of dark matter superfluidity, *Phys. Rev.* **D92** (2015) 103510, [1507.01019].

[33] L. Wyrzykowski, J. Skowron, S. Kozłowski, A. Udalski, M. K. Szymański, M. Kubiak, G. Pietrzyński et al., The OGLE view of microlensing towards the Magellanic Clouds - IV. OGLE-III SMC data and final conclusions on MACHOs, *MNRAS* **416** (Oct., 2011) 2949–2961, [1106.2925].

[34] J. Yoo, J. Chaname and A. Gould, The end of the MACHO era: limits on halo dark matter from stellar halo wide binaries, *Astrophys. J.* **601** (2004) 311–318, [astro-ph/0307437].

[35] W. Hu, R. Barkana and A. Gruzinov, Cold and fuzzy dark matter, *Phys. Rev. Lett.* **85** (2000) 1158–1161, [astro-ph/0003365].

[36] M. Boylan-Kolchin, J. S. Bullock and M. Kaplinghat, Too big to fail? The puzzling darkness of massive Milky Way subhaloes, *Mon. Not. Roy. Astron. Soc.* **415** (2011) L40, [1103.0007].

[37] M. Boylan-Kolchin, J. S. Bullock and M. Kaplinghat, The Milky Way's bright satellites as an apparent failure of LCDM, *Mon. Not. Roy. Astron. Soc.* **422** (2012) 1203–1218, [1111.2048].

[38] S. Tremaine and J. E. Gunn, Dynamical role of light neutral leptons in cosmology, *Physical Review Letters* **42** (Feb., 1979) 407–410.

[39] A. Boyarsky, O. Ruchayskiy and D. Iakubovskyi, A Lower bound on the mass of Dark Matter particles, *JCAP* **0903** (2009) 005, [0808.3902].

[40] E. W. Kolb and M. S. Turner, The Early Universe, *Front. Phys.* **69** (1990) 1–547.

[41] R. Adhikari et al., A White Paper on keV Sterile Neutrino Dark Matter, *Submitted to: White paper* (2016) , [1602.04816].

[42] D. H. Weinberg, J. S. Bullock, F. Governato, R. Kuzio de Naray and A. H. G. Peter, Cold dark matter: controversies on small scales, in *Sackler Colloquium: Dark Matter Universe: On the Threshhold of Discovery Irvine, USA, October 18-20, 2012*, 2013. 1306.0913.

[43] M. Viel, G. D. Becker, J. S. Bolton and M. G. Haehnelt, Warm dark matter as a solution to the small scale crisis: New constraints from high redshift Lyman-α forest data, *Phys. Rev.* **D88** (2013) 043502, [1306.2314].

[44] A. Brooks, Re-Examining Astrophysical Constraints on the Dark Matter Model, *Annalen Phys.* **526** (2014) 294–308, [1407.7544].

[45] E. Witten, Cosmic Separation of Phases, *Phys. Rev.* **D30** (1984) 272–285.

[46] P. Gondolo and G. Gelmini, Cosmic abundances of stable particles: Improved analysis, *Nucl. Phys.* **B360** (1991) 145–179.

[47] G. Steigman, B. Dasgupta and J. F. Beacom, Precise Relic WIMP Abundance and its Impact on Searches for Dark Matter Annihilation, *Phys. Rev.* **D86** (2012) 023506, [1204.3622].

[48] B. W. Lee and S. Weinberg, Cosmological lower bound on heavy-neutrino masses, *Phys. Rev. Lett.* **39** (Jul, 1977) 165–168.

[49] M. I. Vysotsky, A. D. Dolgov and Ya. B. Zeldovich, Cosmological Restriction on Neutral Lepton Masses, *JETP Lett.* **26** (1977) 188–190.

[50] K. Griest and M. Kamionkowski, Unitarity limits on the mass and radius of dark-matter particles, *Phys. Rev. Lett.* **64** (Feb, 1990) 615–618.

[51] K. Harigaya, M. Ibe, K. Kaneta, W. Nakano and M. Suzuki, Thermal Relic Dark Matter Beyond the Unitarity Limit, 1606.00159.

[52] J. L. Feng and J. Kumar, The WIMPless Miracle: Dark-Matter Particles without Weak-Scale Masses or Weak Interactions, *Phys. Rev. Lett.* **101** (2008) 231301, [0803.4196].

[53] P. A. M. Dirac, The Cosmological constants, *Nature* **139** (1937) 323.

[54] K. G. Wilson and J. B. Kogut, The Renormalization group and the epsilon expansion, *Phys. Rept.* **12** (1974) 75–200.

[55] G. 't Hooft, Naturalness, chiral symmetry, and spontaneous chiral symmetry breaking, *NATO Sci. Ser. B* **59** (1980) 135.

[56] W. Skiba, Effective Field Theory and Precision Electroweak Measurements, in *Physics of the large and the small, TASI 09, proceedings of the Theoretical Advanced Study Institute in Elementary Particle Physics, Boulder, Colorado, USA, 1-26 June 2009*, pp. 5–70, 2011. 1006.2142. DOI.

[57] P. Langacker, Grand Unified Theories and Proton Decay, *Phys. Rept.* **72** (1981) 185.

[58] J. Wess and J. Bagger, *Supersymmetry and supergravity*. 1992.

[59] R. Barbieri and A. Strumia, The 'LEP paradox', in *4th Rencontres du Vietnam: Physics at Extreme Energies (Particle Physics and Astrophysics) Hanoi, Vietnam, July 19-25, 2000*, 2000. hep-ph/0007265.

[60] N. Craig, The State of Supersymmetry after Run I of the LHC, in *Beyond the Standard Model after the first run of the LHC Arcetri, Florence, Italy, May 20-July 12, 2013*, 2013. 1309.0528.

[61] G. F. Giudice and A. Romanino, Split supersymmetry, *Nucl. Phys.* **B699** (2004) 65–89, [hep-ph/0406088].

[62] N. Arkani-Hamed, S. Dimopoulos, G. F. Giudice and A. Romanino, Aspects of split supersymmetry, *Nucl. Phys.* **B709** (2005) 3–46, [hep-ph/0409232].

[63] S. P. Martin, A Supersymmetry primer, hep-ph/9709356.

[64] G. Jungman, M. Kamionkowski and K. Griest, Supersymmetric dark matter, *Phys. Rept.* **267** (1996) 195–373, [hep-ph/9506380].

[65] J. Ellis and K. A. Olive, Revisiting the Higgs Mass and Dark Matter in the CMSSM, *Eur. Phys. J.* **C72** (2012) 2005, [1202.3262].

[66] H. Baer, V. Barger and A. Mustafayev, Neutralino dark matter in mSUGRA/CMSSM with a 125 GeV light Higgs scalar, *JHEP* **05** (2012) 091, [1202.4038].

[67] T. Cohen, M. Lisanti, A. Pierce and T. R. Slatyer, Wino Dark Matter Under Siege, *JCAP* **1310** (2013) 061, [1307.4082].

[68] J. Fan and M. Reece, In Wino Veritas? Indirect Searches Shed Light on Neutralino Dark Matter, *JHEP* **10** (2013) 124, [1307.4400].

[69] A. Hryczuk, I. Cholis, R. Iengo, M. Tavakoli and P. Ullio, Indirect Detection Analysis: Wino Dark Matter Case Study, *JCAP* **1407** (2014) 031, [1401.6212].

[70] K. Griest and D. Seckel, Three exceptions in the calculation of relic abundances, *Phys. Rev.* **D43** (1991) 3191–3203.

[71] N. Arkani-Hamed, A. Delgado and G. F. Giudice, The Well-tempered neutralino, *Nucl. Phys.* **B741** (2006) 108–130, [hep-ph/0601041].

[72] G. Bertone, D. Hooper and J. Silk, Particle dark matter: Evidence, candidates and constraints, *Phys. Rept.* **405** (2005) 279–390, [hep-ph/0404175].

[73] T. Moroi, H. Murayama and M. Yamaguchi, Cosmological constraints on the light stable gravitino, *Phys. Lett.* **B303** (1993) 289–294.

[74] A. de Gouvea, T. Moroi and H. Murayama, Cosmology of supersymmetric models with low-energy gauge mediation, *Phys. Rev.* **D56** (1997) 1281–1299, [hep-ph/9701244].

[75] M. Frigerio, A. Pomarol, F. Riva and A. Urbano, Composite Scalar Dark Matter, *JHEP* **07** (2012) 015, [1204.2808].

[76] D. Marzocca and A. Urbano, Composite Dark Matter and LHC Interplay, *JHEP* **07** (2014) 107, [1404.7419].

[77] K. Agashe, R. Contino and A. Pomarol, The Minimal composite Higgs model, *Nucl. Phys.* **B719** (2005) 165–187, [hep-ph/0412089].

[78] T. Asaka, S. Blanchet and M. Shaposhnikov, The nuMSM, dark matter and neutrino masses, *Phys. Lett.* **B631** (2005) 151–156, [hep-ph/0503065].

[79] T. Asaka and M. Shaposhnikov, The nuMSM, dark matter and baryon asymmetry of the universe, *Phys. Lett.* **B620** (2005) 17–26, [hep-ph/0505013].

[80] R. D. Peccei and H. R. Quinn, CP Conservation in the Presence of Instantons, *Phys. Rev. Lett.* **38** (1977) 1440–1443.

[81] R. D. Peccei and H. R. Quinn, Constraints Imposed by CP Conservation in the Presence of Instantons, *Phys. Rev.* **D16** (1977) 1791–1797.

[82] S. Weinberg, A New Light Boson?, *Phys. Rev. Lett.* **40** (1978) 223–226.

[83] F. Wilczek, Problem of Strong p and t Invariance in the Presence of Instantons, *Phys. Rev. Lett.* **40** (1978) 279–282.

[84] J. Preskill, M. B. Wise and F. Wilczek, Cosmology of the Invisible Axion, *Phys. Lett.* **B120** (1983) 127–132.

[85] D. Abercrombie et al., Dark Matter Benchmark Models for Early LHC Run-2 Searches: Report of the ATLAS/CMS Dark Matter Forum, 1507.00966.

[86] M. W. Goodman and E. Witten, Detectability of Certain Dark Matter Candidates, *Phys. Rev.* **D31** (1985) 3059.

[87] SuperCDMS collaboration, R. Agnese et al., Search for Low-Mass Weakly Interacting Massive Particles with SuperCDMS, *Phys. Rev. Lett.* **112** (2014) 241302, [1402.7137].

[88] LUX collaboration, D. S. Akerib et al., The Large Underground Xenon (LUX) Experiment, *Nucl. Instrum. Meth.* **A704** (2013) 111–126, [1211.3788].

[89] T. Asaka, K. Ishiwata and T. Moroi, Right-handed sneutrino as cold dark matter, *Phys. Rev.* **D73** (2006) 051301, [hep-ph/0512118].

[90] C. Arina, M. E. C. Catalan, S. Kraml, S. Kulkarni and U. Laa, Constraints on sneutrino dark matter from LHC Run 1, *JHEP* **05** (2015) 142, [1503.02960].

[91] DAMA, LIBRA collaboration, R. Bernabei et al., New results from DAMA/LIBRA, *Eur. Phys. J.* **C67** (2010) 39–49, [1002.1028].

[92] "SABRE: WIMP Modulation Detection in the Northern and Southern Hemisphere." https://idm2016.shef.ac.uk/indico/event/0/session/11/contribution/94/material/slides/0.pdf.

[93] LUX collaboration, D. S. Akerib et al., Improved Limits on Scattering of Weakly Interacting Massive Particles from Reanalysis of 2013 LUX Data, *Phys. Rev. Lett.* **116** (2016) 161301, [1512.03506].

[94] R. Iengo, Sommerfeld enhancement: General results from field theory diagrams, *JHEP* **05** (2009) 024, [0902.0688].

[95] A. Hryczuk, R. Iengo and P. Ullio, Relic densities including Sommerfeld enhancements in the MSSM, *JHEP* **03** (2011) 069, [1010.2172].

[96] S. Profumo and P. Ullio, Multi-Wavelength Searches for Particle Dark Matter, 1001.4086.

[97] L. Bergstrom, P. Ullio and J. H. Buckley, Observability of gamma-rays from dark matter neutralino annihilations in the Milky Way halo, *Astropart. Phys.* **9** (1998) 137–162, [astro-ph/9712318].

[98] T. Bringmann and C. Weniger, Gamma Ray Signals from Dark Matter: Concepts, Status and Prospects, *Phys. Dark Univ.* **1** (2012) 194–217, [1208.5481].

[99] T. Bringmann, X. Huang, A. Ibarra, S. Vogl and C. Weniger, Fermi LAT Search for Internal Bremsstrahlung Signatures from Dark Matter Annihilation, *JCAP* **1207** (2012) 054, [1203.1312].

[100] C. Weniger, A Tentative Gamma-Ray Line from Dark Matter Annihilation at the Fermi Large Area Telescope, *JCAP* **1208** (2012) 007, [1204.2797].

[101] Fermi-LAT collaboration, M. Ackermann et al., Updated search for spectral lines from Galactic dark matter interactions with pass 8 data from the Fermi Large Area Telescope, *Phys. Rev.* **D91** (2015) 122002, [1506.00013].

[102] M. Backović, A Theory of Ambulance Chasing, 1603.01204.

[103] A. Strumia, Interpreting the 750 GeV digamma excess: a review, 2016. 1605.09401.

[104] L. Bergstrom and P. Ullio, Full one loop calculation of neutralino annihilation into two photons, *Nucl. Phys.* **B504** (1997) 27–44, [hep-ph/9706232].

[105] E. Bulbul, M. Markevitch, A. Foster, R. K. Smith, M. Loewenstein and S. W. Randall, Detection of An Unidentified Emission Line in the Stacked X-ray spectrum of Galaxy Clusters, *Astrophys. J.* **789** (2014) 13, [1402.2301].

[106] A. Boyarsky, O. Ruchayskiy, D. Iakubovskyi and J. Franse, Unidentified Line in X-Ray Spectra of the Andromeda Galaxy and Perseus Galaxy Cluster, *Phys. Rev. Lett.* **113** (2014) 251301, [1402.4119].

[107] T. E. Jeltema and S. Profumo, Discovery of a 3.5 keV line in the Galactic Centre and a critical look at the origin of the line across astronomical targets, *Mon. Not. Roy. Astron. Soc.* **450** (2015) 2143–2152, [1408.1699].

[108] E. Carlson, T. Jeltema and S. Profumo, Where do the 3.5 keV photons come from? A morphological study of the Galactic Center and of Perseus, *JCAP* **1502** (2015) 009, [1411.1758].

[109] T. E. Jeltema and S. Profumo, Deep XMM Observations of Draco rule out at the 99% Confidence Level a Dark Matter Decay Origin for the 3.5 keV Line, *Mon. Not. Roy. Astron. Soc.* **458** (2016) 3592–3596, [1512.01239].

[110] O. Ruchayskiy, A. Boyarsky, D. Iakubovskyi, E. Bulbul, D. Eckert, J. Franse, D. Malyshev et al., Searching for decaying dark matter in deep XMM-Newton observation of the Draco dwarf spheroidal, *Mon. Not. Roy. Astron. Soc.* **460** (2016) 1390–1398, [1512.07217].

[111] A. Ibarra, S. Lopez Gehler and M. Pato, Dark matter constraints from box-shaped gamma-ray features, *JCAP* **1207** (2012) 043, [1205.0007].

[112] A. Ibarra, S. Lopez-Gehler, E. Molinaro and M. Pato, Gamma-ray triangles: a possible signature of asymmetric dark matter in indirect searches, 1604.01899.

[113] P. Ciafaloni, D. Comelli, A. Riotto, F. Sala, A. Strumia and A. Urbano, Weak Corrections are Relevant for Dark Matter Indirect Detection, *JCAP* **1103** (2011) 019, [1009.0224].

[114] G. Bertone, M. Cirelli, A. Strumia and M. Taoso, Gamma-ray and radio tests of the e+e- excess from DM annihilations, *JCAP* **0903** (2009) 009, [0811.3744].

[115] M. Cirelli, G. Corcella, A. Hektor, G. Hutsi, M. Kadastik, P. Panci, M. Raidal et al., PPPC 4 DM ID: A Poor Particle Physicist Cookbook for Dark Matter Indirect Detection, *JCAP* **1103** (2011) 051, [1012.4515].

[116] ANTARES collaboration, S. Adrian-Martinez et al., Search of Dark Matter Annihilation in the Galactic Centre using the

ANTARES Neutrino Telescope, *JCAP* **1510** (2015) 068, [1505.04866].

[117] IceCube collaboration, M. G. Aartsen et al., All-flavour Search for Neutrinos from Dark Matter Annihilations in the Milky Way with IceCube/DeepCore, 1606.00209.

[118] J. Silk, K. A. Olive and M. Srednicki, The Photino, the Sun and High-Energy Neutrinos, *Phys. Rev. Lett.* **55** (1985) 257–259.

[119] W. H. Press and D. N. Spergel, Capture by the sun of a galactic population of weakly interacting massive particles, *Astrophys. J.* **296** (1985) 679–684.

[120] K. Freese, Can Scalar Neutrinos Or Massive Dirac Neutrinos Be the Missing Mass?, *Phys. Lett.* **B167** (1986) 295–300.

[121] L. M. Krauss, M. Srednicki and F. Wilczek, Solar System Constraints and Signatures for Dark Matter Candidates, *Phys. Rev.* **D33** (1986) 2079–2083.

[122] IceCube collaboration, M. G. Aartsen et al., Search for dark matter annihilations in the Sun with the 79-string IceCube detector, *Phys. Rev. Lett.* **110** (2013) 131302, [1212.4097].

[123] J. Silk and M. Srednicki, Cosmic Ray anti-Protons as a Probe of a Photino Dominated Universe, *Phys. Rev. Lett.* **53** (1984) 624.

[124] F. Donato, N. Fornengo, D. Maurin and P. Salati, Antiprotons in cosmic rays from neutralino annihilation, *Phys. Rev.* **D69** (2004) 063501, [astro-ph/0306207].

[125] T. Delahaye, R. Lineros, F. Donato, N. Fornengo and P. Salati, Positrons from dark matter annihilation in the galactic halo: Theoretical uncertainties, *Phys. Rev.* **D77** (2008) 063527, [0712.2312].

[126] J. Lavalle and P. Salati, Dark Matter Indirect Signatures, *Comptes Rendus Physique* **13** (2012) 740–782, [1205.1004].

[127] PAMELA collaboration, O. Adriani et al., An anomalous positron abundance in cosmic rays with energies 1.5-100 GeV, *Nature* **458** (2009) 607–609, [0810.4995].

[128] PAMELA collaboration, O. Adriani et al., Cosmic-Ray Positron Energy Spectrum Measured by PAMELA, *Phys. Rev. Lett.* **111** (2013) 081102, [1308.0133].

[129] "AMS-02 Collaboration, talks at "AMS Days at CERN", 15-17 April 2015." http://indico.cern.ch/event/381134/.

[130] K. Greisen, End to the Cosmic-Ray Spectrum?, *Physical Review Letters* **16** (Apr., 1966) 748–750.

[131] G. T. Zatsepin and V. A. Kuz'min, Upper Limit of the Spectrum of Cosmic Rays, *Soviet Journal of Experimental and Theoretical Physics Letters* **4** (Aug., 1966) 78.

[132] Pierre Auger collaboration, J. Abraham et al., Observation of the suppression of the flux of cosmic rays above 4×10^{19}eV, *Phys. Rev. Lett.* **101** (2008) 061101, [0806.4302].

[133] K. M. Ferriere, The interstellar environment of our galaxy, *Rev. Mod. Phys.* **73** (2001) 1031–1066, [astro-ph/0106359].

[134] R. Jansson and G. R. Farrar, A New Model of the Galactic Magnetic Field, *The Astrophysical Journal* **757** (Sept., 2012) 14, [1204.3662].

[135] T. K. Gaisser, *Cosmic rays and particle physics*. 1990.

[136] V. S. Berezinskii, S. V. Bulanov, V. A. Dogiel and V. S. Ptuskin, *Astrophysics of cosmic rays*. 1990.

[137] R. Schlickeiser, *Cosmic Ray Astrophysics*. 2002.

[138] J. Skilling, Cosmic ray streaming. I - Effect of Alfven waves on particles, *MNRAS* **172** (Sept., 1975) 557–566.

[139] A. W. Strong and I. V. Moskalenko, Propagation of cosmic-ray nucleons in the galaxy, *Astrophys. J.* **509** (1998) 212–228, [astro-ph/9807150].

[140] A. W. Strong, I. V. Moskalenko and V. S. Ptuskin, Cosmic-ray propagation and interactions in the Galaxy, *Ann. Rev. Nucl. Part. Sci.* **57** (2007) 285–327, [astro-ph/0701517].

[141] "The DRAGON code: Diffusion of cosmic rays in galaxy modelization." https://github.com/grapes-dev/DRAGON/wiki.

[142] C. Evoli, D. Gaggero, A. Vittino, G. Di Bernardo, M. Di Mauro, A. Ligorini, P. Ullio et al., Cosmic-ray propagation with DRAGON2: I. numerical solver and astrophysical ingredients, 1607.07886.

[143] C. Evoli, D. Gaggero, D. Grasso and L. Maccione, Cosmic-Ray Nuclei, Antiprotons and Gamma-rays in the Galaxy: a New Diffusion Model, *JCAP* **0810** (2008) 018, [0807.4730].

[144] "The GALPROP code for cosmic-ray transport and diffuse emission production." http://galprop.stanford.edu/.

[145] A. E. Vladimirov, S. W. Digel, G. Jóhannesson, P. F. Michelson, I. V. Moskalenko, P. L. Nolan, E. Orlando et al., GALPROP WebRun: An internet-based service for calculating galactic cosmic ray propagation and associated photon emissions, *Computer Physics Communications* **182** (May, 2011) 1156–1161, [1008.3642].

[146] R. Kissmann, PICARD: A novel code for the Galactic Cosmic Ray propagation problem, *Astropart. Phys.* **55** (2014) 37–50, [1401.4035].

[147] G. Giesen, M. Boudaud, Y. Génolini, V. Poulin, M. Cirelli, P. Salati and P. D. Serpico, AMS-02 antiprotons, at last! Secondary astrophysical component and immediate implications for Dark Matter, *JCAP* **1509** (2015) 023, [1504.04276].

[148] C. Evoli, D. Gaggero and D. Grasso, Secondary antiprotons as a Galactic Dark Matter probe, *JCAP* **1512** (2015) 039, [1504.05175].

[149] M. Ackermann, M. Ajello, A. Allafort, W. B. Atwood, L. Baldini, G. Barbiellini, D. Bastieri et al., Measurement of Separate Cosmic-Ray Electron and Positron Spectra with the Fermi Large Area Telescope, *Physical Review Letters* **108** (Jan., 2012) 011103, [1109.0521].

[150] AMS Collaboration collaboration, L. Accardo, M. Aguilar, D. Aisa, B. Alpat, A. Alvino, G. Ambrosi, K. Andeen et al., High statistics measurement of the positron fraction in primary cosmic rays of 0.5–500 gev with the alpha magnetic spectrometer on the international space station, *Phys. Rev. Lett.* **113** (Sep, 2014) 121101.

[151] N. Arkani-Hamed, D. P. Finkbeiner, T. R. Slatyer and N. Weiner, A Theory of Dark Matter, *Phys. Rev.* **D79** (2009) 015014, [0810.0713].

[152] P. Meade, M. Papucci, A. Strumia and T. Volansky, Dark Matter Interpretations of the e+- Excesses after FERMI, *Nucl. Phys.* **B831** (2010) 178–203, [0905.0480].

[153] P. Mertsch and S. Sarkar, Testing astrophysical models for the PAMELA positron excess with cosmic ray nuclei, *Phys. Rev. Lett.* **103** (2009) 081104, [0905.3152].

[154] P. D. Serpico, Astrophysical models for the origin of the positron 'excess', *Astropart. Phys.* **39-40** (2012) 2–11, [1108.4827].

[155] S. Profumo, Dissecting cosmic-ray electron-positron data with Occam's Razor: the role of known Pulsars, *Central Eur. J. Phys.* **10** (2011) 1–31, [0812.4457].

[156] P. Blasi and E. Amato, Positrons from pulsar winds, *Astrophysics and Space Science Proceedings* **21** (2011) 624, [1007.4745].

[157] M. Ackermann, M. Ajello, W. B. Atwood, L. Baldini, J. Ballet, G. Barbiellini, D. Bastieri et al., Fermi-LAT Observations of the Diffuse γ-Ray Emission: Implications for Cosmic Rays and the Interstellar Medium, *The Astrophysical Journal* **750** (May, 2012) 3, [1202.4039].

[158] W.-C. Huang, A. Urbano and W. Xue, Fermi Bubbles under Dark Matter Scrutiny. Part I: Astrophysical Analysis, 1307.6862.

[159] S. R. Kelner, F. A. Aharonian and V. V. Bugayov, Energy spectra of gamma-rays, electrons and neutrinos produced at proton-proton interactions in the very high energy regime, *Phys. Rev.* **D74** (2006) 034018, [astro-ph/0606058].

[160] D. Maurin, F. Donato, R. Taillet and P. Salati, Cosmic rays below z=30 in a diffusion model: new constraints on propagation parameters, *Astrophys. J.* **555** (2001) 585–596, [astro-ph/0101231].

[161] G. Di Bernardo, C. Evoli, D. Gaggero, D. Grasso and L. Maccione, Unified interpretation of cosmic ray nuclei and antiproton recent measurements, *Astroparticle Physics* **34** (Dec., 2010) 274–283, [0909.4548].

[162] R. Trotta, G. Johannesson, I. V. Moskalenko, T. A. Porter, R. R. de Austri and A. W. Strong, Constraints on cosmic-ray propagation models from a global Bayesian analysis, *Astrophys. J.* **729** (2011) 106, [1011.0037].

[163] O. Adriani, G. C. Barbarino, G. A. Bazilevskaya, R. Bellotti, M. Boezio, E. A. Bogomolov, L. Bonechi et al., PAMELA Measurements of Cosmic-Ray Proton and Helium Spectra, *Science* **332** (Apr., 2011) 69, [1103.4055].

[164] T. R. Jaffe, A. J. Banday, J. P. Leahy, S. Leach and A. W. Strong, Connecting synchrotron, cosmic rays and magnetic fields in the plane of the Galaxy, *MNRAS* **416** (Sept., 2011) 1152–1162, [1105.5885].

[165] H. Yan and A. Lazarian, Cosmic Ray Propagation: Nonlinear Diffusion Parallel and Perpendicular to Mean Magnetic Field, *Astrophys. J.* **673** (2008) 942, [0710.2617].

[166] C. Evoli and H. Yan, Cosmic ray propagation in galactic turbulence, *Astrophys. J.* **782** (2014) 36, [1310.5732].

[167] P. Blasi, E. Amato and P. D. Serpico, Spectral breaks as a signature of cosmic ray induced turbulence in the Galaxy, *Phys. Rev. Lett.* **109** (2012) 061101, [1207.3706].

[168] S. L. Snowden, R. Egger, M. J. Freyberg, D. McCammon, P. P. Plucinsky, W. T. Sanders, J. H. M. M. Schmitt et al., Rosat survey diffuse x-ray background maps. ii., *The Astrophysical Journal* **485** (1997) 125.

[169] I. Gebauer and W. de Boer, An Anisotropic Propagation Model for Galactic Cosmic Rays, *ArXiv e-prints* (Oct., 2009) , [0910.2027].

[170] J. Y. Cheng, C. M. Rockosi, H. L. Morrison, R. A. Schönrich, Y. S. Lee, T. C. Beers, D. Bizyaev et al., Metallicity Gradients in the Milky Way Disk as Observed by the SEGUE Survey, *The Astrophysical Journal* **746** (Feb., 2012) 149, [1110.5933].

[171] F. P. Israel, H2 and its relation to co in the lmc and other magellanic irregulars, *Astron. Astrophys.* **328** (1997) 471–482, [astro-ph/9709194].

[172] M. Tavakoli, I. Cholis, C. Evoli and P. Ullio, Diffuse Galactic Gamma Rays at Intermediate and High Latitudes, Constraints on ISM Properties, *ArXiv e-prints* (Oct., 2011) , [1110.5922].

[173] C. Evoli, D. Gaggero, D. Grasso and L. Maccione, A common solution to the cosmic ray anisotropy and gradient problems, *Phys. Rev. Lett.* **108** (2012) 211102, [1203.0570].

[174] T. Kamae, N. Karlsson, T. Mizuno, T. Abe and T. Koi, Parameterization of γ, $e^{+/-}$, and Neutrino Spectra Produced by p-p Interaction in Astronomical Environments, *The Astrophysical Journal* **647** (Aug., 2006) 692–708, [astro-ph/0605581].

[175] C. Evoli, I. Cholis, D. Grasso, L. Maccione and P. Ullio, Antiprotons from dark matter annihilation in the Galaxy: astrophysical uncertainties, *Phys. Rev.* **D85** (2012) 123511, [1108.0664].

[176] N. E. Yanasak, M. E. Wiedenbeck, R. A. Mewaldt, A. J. Davis, A. C. Cummings, J. S. George, R. A. Leske et al., Measurement of the

SECONDARY RADIONUCLIDES 10BE, 26AL, 36CL, 54MN, AND 14C AND IMPLICATIONS FOR THE GALACTIC COSMIC-RAY AGE, *The Astrophysical Journal* **563** (2001) 768.

[177] J. J. Engelmann, P. Ferrando, A. Soutoul, P. Goret and E. Juliusson, CHARGE COMPOSITION AND ENERGY SPECTRA OF COSMIC-RAY NUCLEI FOR ELEMENTS FROM BE TO NI - RESULTS FROM HEAO-3-C2, *Astron. Astrophys.* **233** (July, 1990) 96–111.

[178] A. D. Panov et al., RELATIVE ABUNDANCES OF COSMIC RAY NUCLEI B-C-N-O IN THE ENERGY REGION FROM 10 GEV/N TO 300 GEV/N. RESULTS FROM ATIC-2 (THE SCIENCE FLIGHT OF ATIC), in *Proceedings, 30th International Cosmic Ray Conference (ICRC 2007)*, vol. 2, pp. 3–6, 2007. 0707.4415.

[179] D. Mueller, S. P. Swordy, P. Meyer, J. L'Heureux and J. M. Grunsfeld, ENERGY SPECTRA AND COMPOSITION OF PRIMARY COSMIC RAYS, *The Astrophysical Journal* **374** (June, 1991) 356–365.

[180] H. S. Ahn et al., MEASUREMENTS OF COSMIC-RAY SECONDARY NUCLEI AT HIGH ENERGIES WITH THE FIRST FLIGHT OF THE CREAM BALLOON-BORNE EXPERIMENT, *Astropart. Phys.* **30** (2008) 133–141, [0808.1718].

[181] O. Adriani et al., MEASUREMENT OF BORON AND CARBON FLUXES IN COSMIC RAYS WITH THE PAMELA EXPERIMENT, *Astrophys. J.* **791** (2014) 93, [1407.1657].

[182] "Preliminary B/C data from the AMS Collaboration." http://laspace.lsu.edu/ISCRA/ISCRA2014/Presentations/rclavero.pdf.

[183] A. G. Mayorov, O. Adriani, G. C. Barbarino, G. A. Bazilevskaya, R. Bellotti, M. Boezio, E. A. Bogomolov et al., MEASUREMENT OF ANTIPROTON FLUX IN PRIMARY COSMIC RADIATION WITH PAMELA EXPERIMENT, *Journal of Physics: Conference Series* **409** (2013) 012056.

[184] FERMI-LAT collaboration, M. Ackermann et al., THE SPECTRUM AND MORPHOLOGY OF THE *Fermi* BUBBLES, *Astrophys. J.* **793** (2014) 64, [1407.7905].

[185] S. D. Hunter, D. L. Bertsch, J. R. Catelli, T. M. Dame, S. W. Digel, B. L. Dingus, J. A. Esposito et al., EGRET OBSERVATIONS OF THE DIFFUSE GAMMA-RAY EMISSION FROM THE GALACTIC PLANE, *The Astrophysical Journal* **481** (May, 1997) 205–240.

[186] A. W. Strong, I. V. Moskalenko, O. Reimer, S. Digel and R. Diehl, The distribution of cosmic-ray sources in the galaxy, gamma-rays, and the gradient in the co-to-h2 relation, *Astron. Astrophys.* **422** (2004) L47–L50, [astro-ph/0405275].

[187] M. Ackermann, M. Ajello, L. Baldini, J. Ballet, G. Barbiellini, D. Bastieri, K. Bechtol et al., Constraints on the Cosmic-ray Density Gradient Beyond the Solar Circle from Fermi γ-ray Observations of the Third Galactic Quadrant, *The Astrophysical Journal* **726** (Jan., 2011) 81, [1011.0816].

[188] E. G. Berezhko and H. J. Volk, The Contribution of different supernova populations to the Galactic gamma-ray background, *Astrophys. J.* **611** (2004) 12–19, [astro-ph/0404307].

[189] A. D. Erlykin and A. W. Wolfendale, Cosmic rays in the inner galaxy and the diffusion properties of the interstellar medium, *Astroparticle Physics* **42** (Feb., 2013) 70–75, [1212.2760].

[190] W. de Boer and M. Weber, Fermi Bubbles and Bubble-like emission from the Galactic Plane, *Astrophys. J.* **794** (2014) L17, [1407.4114].

[191] F. Calore, M. Di Mauro, F. Donato and F. Donato, Diffuse gamma-ray emission from galactic pulsars, *Astrophys. J.* **796** (2014) 1, [1406.2706].

[192] P. Blasi and E. Amato, Diffusive propagation of cosmic rays from supernova remnants in the Galaxy. I: spectrum and chemical composition, *JCAP* **1** (Jan., 2012) 010, [1105.4521].

[193] T. Prodanovic, B. D. Fields and J. F. Beacom, Diffuse gamma rays from the galactic plane: probing the gev excess and identifying the TeV excess, *Astropart. Phys.* **27** (2007) 10–20, [astro-ph/0603618].

[194] A. A. Abdo et al., A Measurement of the Spatial Distribution of Diffuse TeV Gamma Ray Emission from the Galactic Plane with Milagro, *Astrophys. J.* **688** (2008) 1078–1083, [0805.0417].

[195] A. W. Strong, I. V. Moskalenko and O. Reimer, Diffuse galactic continuum gamma rays. A Model compatible with EGRET data and cosmic-ray measurements, *Astrophys. J.* **613** (2004) 962–976, [astro-ph/0406254].

[196] A. A. Abdo, M. Ackermann, M. Ajello, B. Anderson, W. B. Atwood, M. Axelsson, L. Baldini et al., Fermi Large Area Telescope

Measurements of the Diffuse Gamma-Ray Emission at Intermediate Galactic Latitudes, *Physical Review Letters* **103** (Dec., 2009) 251101, [0912.0973].

[197] M. Ahlers, Y. Bai, V. Barger and R. Lu, Galactic neutrinos in the TeV to PeV range, *Phys. Rev.* **D93** (2016) 013009, [1505.03156].

[198] O. Adriani, G. A. Bazilevskaya, G. C. Barbarino, R. Bellotti, M. Boezio, E. A. Bogomolov, V. Bonvicini et al., Measurement of the flux of primary cosmic ray antiprotons with energies of 60 mev to 350 gev in the pamela experiment, *JETP Letters* **96** (2013) 621–627.

[199] H. S. Ahn, P. Allison, M. G. Bagliesi, J. J. Beatty, G. Bigongiari, J. T. Childers, N. B. Conklin et al., Discrepant Hardening Observed in Cosmic-ray Elemental Spectra, *The Astrophysical Journal Letters* **714** (May, 2010) L89–L93, [1004.1123].

[200] KASCADE collaboration, T. Antoni et al., KASCADE measurements of energy spectra for elemental groups of cosmic rays: Results and open problems, *Astropart. Phys.* **24** (2005) 1–25, [astro-ph/0505413].

[201] W. D. Apel et al., KASCADE-Grande measurements of energy spectra for elemental groups of cosmic rays, *Astropart. Phys.* **47** (2013) 54–66, [1306.6283].

[202] P. Huentemeyer, private communication (2015).

[203] A. U. Abeysekara et al., Sensitivity of the High Altitude Water Cherenkov Detector to Sources of Multi-TeV Gamma Rays, *Astropart. Phys.* **50-52** (2013) 26–32, [1306.5800].

[204] M. Actis, G. Agnetta, F. Aharonian, A. Akhperjanian, J. Aleksić, E. Aliu, D. Allan et al., Design concepts for the Cherenkov Telescope Array CTA: an advanced facility for ground-based high-energy gamma-ray astronomy, *Experimental Astronomy* **32** (Dec., 2011) 193–316, [1008.3703].

[205] Fermi-LAT collaboration, F. Acero et al., Fermi Large Area Telescope Third Source Catalog, *Astrophys. J. Suppl.* **218** (2015) 23, [1501.02003].

[206] AMS Collaboration collaboration, M. Aguilar, D. Aisa, B. Alpat, A. Alvino, G. Ambrosi, K. Andeen, L. Arruda et al., Precision measurement of the proton flux in primary cosmic rays from rigidity 1 gv to 1.8 tv with the alpha magnetic spectrometer

on the international space station, *Phys. Rev. Lett.* **114** (Apr, 2015) 171103.

[207] S. Thoudam and J. R. Hörandel, Revisiting the hardening of the cosmic-ray energy spectrum at TeV energies, *Mon. Not. Roy. Astron. Soc.* **435** (2013) 2532, [1304.1400].

[208] M. Ahlers and K. Murase, Probing the Galactic Origin of the IceCube Excess with Gamma-Rays, *Phys. Rev.* **D90** (2014) 023010, [1309.4077].

[209] HESS collaboration, F. Aharonian et al., Discovery of very-high-energy gamma-rays from the galactic centre ridge, *Nature* **439** (2006) 695–698, [astro-ph/0603021].

[210] HESS collaboration, : et al., Acceleration of petaelectronvolt protons in the Galactic Centre, *Nature* **531** (2016) 476, [1603.07730].

[211] K. Ferriere, W. Gillard and P. Jean, Spatial distribution of interstellar gas in the innermost 3 kpc of our Galaxy, *Astron. Astrophys.* **467** (2007) 611–627, [astro-ph/0702532].

[212] IceCube collaboration, A. Achterberg et al., First Year Performance of The IceCube Neutrino Telescope, *Astropart. Phys.* **26** (2006) 155–173, [astro-ph/0604450].

[213] IceCube collaboration, M. G. Aartsen et al., First observation of PeV-energy neutrinos with IceCube, *Phys. Rev. Lett.* **111** (2013) 021103, [1304.5356].

[214] IceCube collaboration, M. G. Aartsen et al., Evidence for High-Energy Extraterrestrial Neutrinos at the IceCube Detector, *Science* **342** (2013) 1242856, [1311.5238].

[215] IceCube collaboration, M. G. Aartsen et al., Observation of High-Energy Astrophysical Neutrinos in Three Years of IceCube Data, *Phys. Rev. Lett.* **113** (2014) 101101, [1405.5303].

[216] IceCube collaboration, M. G. Aartsen et al., Flavor Ratio of Astrophysical Neutrinos above 35 TeV in IceCube, *Phys. Rev. Lett.* **114** (2015) 171102, [1502.03376].

[217] A. Palladino, G. Pagliaroli, F. L. Villante and F. Vissani, What is the Flavor of the Cosmic Neutrinos Seen by IceCube?, *Phys. Rev. Lett.* **114** (2015) 171101, [1502.02923].

[218] IceCube collaboration, M. G. Aartsen et al., The IceCube Neutrino Observatory - Contributions to ICRC 2015 Part II: Atmospheric and Astrophysical Diffuse Neutrino Searches of All Flavors, in *Proceedings, 34th International Cosmic Ray Conference (ICRC 2015)*, 2015. 1510.05223.

[219] IceCube collaboration, M. G. Aartsen et al., A combined maximum-likelihood analysis of the high-energy astrophysical neutrino flux measured with IceCube, *Astrophys. J.* **809** (2015) 98, [1507.03991].

[220] IceCube Collaboration collaboration, M. G. Aartsen, K. Abraham, M. Ackermann, J. Adams, J. A. Aguilar, M. Ahlers, M. Ahrens et al., Evidence for astrophysical muon neutrinos from the northern sky with icecube, *Phys. Rev. Lett.* **115** (Aug, 2015) 081102.

[221] R. Laha, J. F. Beacom, B. Dasgupta, S. Horiuchi and K. Murase, Demystifying the PeV Cascades in IceCube: Less (Energy) is More (Events), *Phys. Rev.* **D88** (2013) 043009, [1306.2309].

[222] L. A. Anchordoqui et al., Cosmic Neutrino Pevatrons: A Brand New Pathway to Astronomy, Astrophysics, and Particle Physics, *JHEAp* **1-2** (2014) 1–30, [1312.6587].

[223] K. Murase, On the Origin of High-Energy Cosmic Neutrinos, *AIP Conf. Proc.* **1666** (2015) 040006, [1410.3680].

[224] C. Tchernin, J. A. Aguilar, A. Neronov and T. Montaruli, Neutrino signal from extended Galactic sources in IceCube, *Astron. Astrophys.* **560** (2013) A67, [1305.4113].

[225] F. W. Stecker, Diffuse fluxes of cosmic high-energy neutrinos, *The Astrophysical Journal* **228** (Mar., 1979) 919–927.

[226] C. Evoli, D. Grasso and L. Maccione, Diffuse Neutrino and Gamma-ray Emissions of the Galaxy above the TeV, *JCAP* **0706** (2007) 003, [astro-ph/0701856].

[227] V. Cavasinni, D. Grasso and L. Maccione, TeV Neutrinos from SuperNova Remnants embedded in Giant Molecular Clouds, *Astropart. Phys.* **26** (2006) 41–49, [astro-ph/0604004].

[228] M. Kachelriess and S. Ostapchenko, Neutrino yield from Galactic cosmic rays, *Phys. Rev.* **D90** (2014) 083002, [1405.3797].

[229] M. Spurio, Constraints to a Galactic Component of the Ice

Cube cosmic neutrino flux from ANTARES, *Phys. Rev.* **D90** (2014) 103004, [1409.4552].

[230] A. Neronov and D. V. Semikoz, Evidence the Galactic contribution to the IceCube astrophysical neutrino flux, *Astropart. Phys.* **75** (2016) 60–63, [1509.03522].

[231] IceCube collaboration, T. Glüsenkamp, Analysis of the cumulative neutrino flux from Fermi-LAT blazar populations using 3 years of IceCube data, in *5th Roma International Conference on Astro-Particle physics (RICAP 14) Noto, Sicily, Italy, September 30-October 3, 2014*, 2015. 1502.03104.

[232] K. Bechtol, M. Ahlers, M. Di Mauro, M. Ajello and J. Vandenbroucke, Evidence against star-forming galaxies as the dominant source of IceCube neutrinos, 1511.00688.

[233] J. A. Aguilar, I. A. Samarai, A. Albert, M. André, M. Anghinolfi, G. Anton, S. Anvar et al., Search for a diffuse flux of high-energy ν with the ANTARES neutrino telescope, *Physics Letters B* **696** (Jan., 2011) 16–22, [1011.3772].

[234] ANTARES collaboration, S. Adrian-Martinez et al., Constraints on the neutrino emission from the Galactic Ridge with the ANTARES telescope, *Phys. Lett.* **B760** (2016) 143–148, [1602.03036].

[235] ANTARES collaboration, L. A. Fusco, Neutrino fluxes from the Galactic plane and the ANTARES limit, *EPJ Web Conf.* **116** (2016) 04007.

[236] KM3NeT collaboration, R. Coniglione, L. A. Fusco and D. Stransky, Predicted sensitivity of the KM3NeT/ARCA detector to a diffuse flux of cosmic neutrinos, *EPJ Web Conf.* **116** (2016) 04008.

[237] KM3NeT collaboration, S. Adrian-Martinez et al., Letter of intent for KM3NeT 2.0, *J. Phys.* **G43** (2016) 084001, [1601.07459].

[238] Fermi-LAT collaboration, F. Acero et al., Development of the Model of Galactic Interstellar Emission for Standard Point-Source Analysis of Fermi Large Area Telescope Data, *Astrophys. J. Suppl.* **223** (2016) 26, [1602.07246].

[239] R. Yang, F. Aharonian and C. Evoli, Radial distribution of the diffuse γ-ray emissivity in the Galactic disk, *Phys. Rev.* **D93** (2016) 123007, [1602.04710].

[240] S. Recchia, P. Blasi and G. Morlino, On the radial distribution of Galactic cosmic rays, *ArXiv e-prints* (Apr., 2016) , [1604.07682].

[241] IceCube Gen2 collaboration, PINGU: A Vision for Neutrino and Particle Physics at the South Pole, 1607.02671.

[242] A. W. Strong, I. V. Moskalenko and O. Reimer, Diffuse continuum gamma-rays from the galaxy, *Astrophys. J.* **537** (2000) 763–784, [astro-ph/9811296].

[243] M. Su, T. R. Slatyer and D. P. Finkbeiner, Giant Gamma-ray Bubbles from Fermi-LAT: Active Galactic Nucleus Activity or Bipolar Galactic Wind?, *The Astrophysical Journal* **724** (Dec., 2010) 1044–1082, [1005.5480].

[244] D. P. Finkbeiner, Microwave ism emission observed by wmap, *Astrophys. J.* **614** (2004) 186–193, [astro-ph/0311547].

[245] V. Vitale, A. Morselli and for the Fermi/LAT Collaboration, Indirect Search for Dark Matter from the center of the Milky Way with the Fermi-Large Area Telescope, *ArXiv e-prints* (Dec., 2009) , [0912.3828].

[246] V. Springel, S. D. M. White, C. S. Frenk, J. F. Navarro, A. Jenkins, M. Vogelsberger, J. Wang et al., A blueprint for detecting supersymmetric dark matter in the Galactic halo, 0809.0894.

[247] M. Schaller et al., Dark matter annihilation radiation in hydrodynamic simulations of Milky Way haloes, *Mon. Not. Roy. Astron. Soc.* **455** (2016) 4442–4451, [1509.02166].

[248] L. Goodenough and D. Hooper, Possible Evidence For Dark Matter Annihilation In The Inner Milky Way From The Fermi Gamma Ray Space Telescope, 0910.2998.

[249] D. Hooper and L. Goodenough, Dark Matter Annihilation in The Galactic Center As Seen by the Fermi Gamma Ray Space Telescope, *Phys. Lett.* **B697** (2011) 412–428, [1010.2752].

[250] D. Hooper and T. Linden, On The Origin Of The Gamma Rays From The Galactic Center, *Phys. Rev.* **D84** (2011) 123005, [1110.0006].

[251] K. N. Abazajian and M. Kaplinghat, Detection of a Gamma-Ray Source in the Galactic Center Consistent with Extended Emission from Dark Matter Annihilation and Concentrated Astrophysical Emission, *Phys. Rev.* **D86** (2012) 083511, [1207.6047].

[252] C. Gordon and O. Macias, Dark Matter and Pulsar Model Constraints from Galactic Center Fermi-LAT Gamma Ray Observations, *Phys. Rev.* **D88** (2013) 083521, [1306.5725].

[253] K. N. Abazajian, N. Canac, S. Horiuchi and M. Kaplinghat, Astrophysical and Dark Matter Interpretations of Extended Gamma-Ray Emission from the Galactic Center, *Phys. Rev.* **D90** (2014) 023526, [1402.4090].

[254] A. Boyarsky, D. Malyshev and O. Ruchayskiy, A comment on the emission from the Galactic Center as seen by the Fermi telescope, *Phys. Lett.* **B705** (2011) 165–169, [1012.5839].

[255] P. D. Serpico and G. Zaharijas, Optimal angular window for observing Dark Matter annihilation from the Galactic Center region: the case of γ^- ray lines, *Astropart. Phys.* **29** (2008) 380–385, [0802.3245].

[256] E. Nezri, J. Lavalle and R. Teyssier, Indirect dark matter searches: towards a consistent top-bottom approach for studying the gamma-ray signals and associated backgrounds, *Phys. Rev.* **D86** (2012) 063524, [1204.4121].

[257] D. Hooper and T. R. Slatyer, Two Emission Mechanisms in the Fermi Bubbles: A Possible Signal of Annihilating Dark Matter, *Phys. Dark Univ.* **2** (2013) 118–138, [1302.6589].

[258] T. Daylan, D. P. Finkbeiner, D. Hooper, T. Linden, S. K. N. Portillo, N. L. Rodd and T. R. Slatyer, The characterization of the gamma-ray signal from the central Milky Way: A case for annihilating dark matter, *Phys. Dark Univ.* **12** (2016) 1–23, [1402.6703].

[259] W.-C. Huang, A. Urbano and W. Xue, Fermi Bubbles under Dark Matter Scrutiny Part II: Particle Physics Analysis, *JCAP* **1404** (2014) 020, [1310.7609].

[260] C. Boehm, M. J. Dolan, C. McCabe, M. Spannowsky and C. J. Wallace, Extended gamma-ray emission from Coy Dark Matter, *JCAP* **1405** (2014) 009, [1401.6458].

[261] A. Hektor and L. Marzola, Coy Dark Matter and the anomalous magnetic moment, *Phys. Rev.* **D90** (2014) 053007, [1403.3401].

[262] A. Alves, S. Profumo, F. S. Queiroz and W. Shepherd, Effective field theory approach to the Galactic Center gamma-ray excess, *Phys. Rev.* **D90** (2014) 115003, [1403.5027].

[263] A. Berlin, D. Hooper and S. D. McDermott, Simplified Dark Matter Models for the Galactic Center Gamma-Ray Excess, *Phys. Rev.* **D89** (2014) 115022, [1404.0022].

[264] A. Berlin, P. Gratia, D. Hooper and S. D. McDermott, Hidden Sector Dark Matter Models for the Galactic Center Gamma-Ray Excess, *Phys. Rev.* **D90** (2014) 015032, [1405.5204].

[265] P. Agrawal, B. Batell, D. Hooper and T. Lin, Flavored Dark Matter and the Galactic Center Gamma-Ray Excess, *Phys. Rev.* **D90** (2014) 063512, [1404.1373].

[266] E. Izaguirre, G. Krnjaic and B. Shuve, The Galactic Center Excess from the Bottom Up, *Phys. Rev.* **D90** (2014) 055002, [1404.2018].

[267] S. Ipek, D. McKeen and A. E. Nelson, A Renormalizable Model for the Galactic Center Gamma Ray Excess from Dark Matter Annihilation, *Phys. Rev.* **D90** (2014) 055021, [1404.3716].

[268] C. Boehm, M. J. Dolan and C. McCabe, A weighty interpretation of the Galactic Centre excess, *Phys. Rev.* **D90** (2014) 023531, [1404.4977].

[269] P. Ko, W.-I. Park and Y. Tang, Higgs portal vector dark matter for GeV scale γ-ray excess from galactic center, *JCAP* **1409** (2014) 013, [1404.5257].

[270] M. Abdullah, A. DiFranzo, A. Rajaraman, T. M. P. Tait, P. Tanedo and A. M. Wijangco, Hidden on-shell mediators for the Galactic Center γ-ray excess, *Phys. Rev.* **D90** (2014) 035004, [1404.6528].

[271] A. Martin, J. Shelton and J. Unwin, Fitting the Galactic Center Gamma-Ray Excess with Cascade Annihilations, *Phys. Rev.* **D90** (2014) 103513, [1405.0272].

[272] T. Mondal and T. Basak, Class of Higgs-portal Dark Matter models in the light of gamma-ray excess from Galactic center, *Phys. Lett.* **B744** (2015) 208–212, [1405.4877].

[273] C. Cheung, M. Papucci, D. Sanford, N. R. Shah and K. M. Zurek, NMSSM Interpretation of the Galactic Center Excess, *Phys. Rev.* **D90** (2014) 075011, [1406.6372].

[274] C. Arina, E. Del Nobile and P. Panci, Dark Matter with Pseudoscalar-Mediated Interactions Explains the DAMA Signal and the Galactic Center Excess, *Phys. Rev. Lett.* **114** (2015) 011301, [1406.5542].

[275] P. Agrawal, B. Batell, P. J. Fox and R. Harnik, WIMPs at the Galactic Center, *JCAP* **1505** (2015) 011, [1411.2592].

[276] D. Hooper, Z' mediated dark matter models for the Galactic Center gamma-ray excess, *Phys. Rev.* **D91** (2015) 035025, [1411.4079].

[277] F. Calore, I. Cholis, C. McCabe and C. Weniger, A Tale of Tails: Dark Matter Interpretations of the Fermi GeV Excess in Light of Background Model Systematics, *Phys. Rev.* **D91** (2015) 063003, [1411.4647].

[278] K. Ghorbani and H. Ghorbani, Scalar split WIMPs in future direct detection experiments, *Phys. Rev.* **D93** (2016) 055012, [1501.00206].

[279] A. Alves, A. Berlin, S. Profumo and F. S. Queiroz, Dark Matter Complementarity and the Z′ Portal, *Phys. Rev.* **D92** (2015) 083004, [1501.03490].

[280] M. Kaplinghat, T. Linden and H.-B. Yu, Galactic Center Excess in γ Rays from Annihilation of Self-Interacting Dark Matter, *Phys. Rev. Lett.* **114** (2015) 211303, [1501.03507].

[281] A. Berlin, S. Gori, T. Lin and L.-T. Wang, Pseudoscalar Portal Dark Matter, *Phys. Rev.* **D92** (2015) 015005, [1502.06000].

[282] T. Gherghetta, B. von Harling, A. D. Medina, M. A. Schmidt and T. Trott, SUSY implications from WIMP annihilation into scalars at the Galactic Center, *Phys. Rev.* **D91** (2015) 105004, [1502.07173].

[283] A. Rajaraman, J. Smolinsky and P. Tanedo, On-Shell Mediators and Top-Charm Dark Matter Models for the Fermi-LAT Galactic Center Excess, 1503.05919.

[284] D. Borah, A. Dasgupta and R. Adhikari, Common origin of the 3.55 keV x-ray line and the Galactic Center gamma-ray excess in a radiative neutrino mass model, *Phys. Rev.* **D92** (2015) 075005, [1503.06130].

[285] E. C. F. S. Fortes, V. Pleitez and F. W. Stecker, Secluded WIMPs, dark QED with massive photons, and the galactic center gamma-ray excess, *Astropart. Phys.* **74** (2016) 87–95, [1503.08220].

[286] P. Ko and Y. Tang, Dark Higgs Channel for FERMI GeV γ-ray Excess, *JCAP* **1602** (2016) 011, [1504.03908].

[287] P. Ko, W.-I. Park and Y. Tang, Higgs-Portal Dark Matter for GeV Gamma-Ray Excess, in *2nd Toyama International Workshop on Higgs as*

a Probe of New Physics (HPNP2015) Toyama, Japan, February 11-15, 2015, 2015. 1504.06944.

[288] M. Cirelli, D. Gaggero, G. Giesen, M. Taoso and A. Urbano, Antiproton constraints on the GeV gamma-ray excess: a comprehensive analysis, *JCAP* **1412** (2014) 045, [1407.2173].

[289] D. Hooper, T. Linden and P. Mertsch, What Does The PAMELA Antiproton Spectrum Tell Us About Dark Matter?, *JCAP* **1503** (2015) 021, [1410.1527].

[290] T. Bringmann, M. Vollmann and C. Weniger, Updated cosmic-ray and radio constraints on light dark matter: Implications for the GeV gamma-ray excess at the Galactic center, *Phys. Rev.* **D90** (2014) 123001, [1406.6027].

[291] Fermi-LAT collaboration, M. Ackermann et al., Searching for Dark Matter Annihilation from Milky Way Dwarf Spheroidal Galaxies with Six Years of Fermi-LAT Data, 1503.02641.

[292] F. Calore, I. Cholis and C. Weniger, Background model systematics for the Fermi GeV excess, *JCAP* **1503** (2015) 038, [1409.0042].

[293] B. Zhou, Y.-F. Liang, X. Huang, X. Li, Y.-Z. Fan, L. Feng and J. Chang, GeV excess in the Milky Way: The role of diffuse galactic gamma-ray emission templates, *Phys. Rev.* **D91** (2015) 123010, [1406.6948].

[294] I. Cholis, C. Evoli, F. Calore, T. Linden, C. Weniger and D. Hooper, The Galactic Center GeV Excess from a Series of Leptonic Cosmic-Ray Outbursts, *JCAP* **1512** (2015) 005, [1506.05119].

[295] G. L. Case and D. Bhattacharya, A new sigma-d relation and its application to the galactic supernova remnant distribution, *Astrophys. J.* **504** (1998) 761, [astro-ph/9807162].

[296] D. R. Lorimer et al., The Parkes multibeam pulsar survey: VI. Discovery and timing of 142 pulsars and a Galactic population analysis, *Mon. Not. Roy. Astron. Soc.* **372** (2006) 777–800, [astro-ph/0607640].

[297] I. Yusifov and I. Kucuk, Revisiting the radial distribution of pulsars in the galaxy, *Astron. Astrophys.* **422** (2004) 545–553, [astro-ph/0405559].

[298] E. Carlson and S. Profumo, Cosmic Ray Protons in the Inner

Galaxy and the Galactic Center Gamma-Ray Excess, *Phys. Rev.* **D90** (2014) 023015, [1405.7685].

[299] R. M. Crocker, D. I. Jones, F. Melia, J. Ott and R. J. Protheroe, A lower limit of 50 microgauss for the magnetic field near the Galactic Centre, *Nature* **463** (Jan., 2010) 65–67, [1001.1275].

[300] R. M. Crocker, D. I. Jones, F. Aharonian, C. J. Law, F. Melia and J. Ott, γ-rays and the far-infrared-radio continuum correlation reveal a powerful Galactic Centre wind, *MNRAS* **411** (Feb., 2011) L11–L15, [1009.4340].

[301] R. M. Crocker, D. I. Jones, F. Aharonian, C. J. Law, F. Melia, T. Oka and J. Ott, Wild at Heart: the particle astrophysics of the Galactic Centre, *MNRAS* **413** (May, 2011) 763–788, [1011.0206].

[302] J. Ott, A. Weiß, L. Staveley-Smith, C. Henkel and D. S. Meier, ATCA Survey of Ammonia in the Galactic Center: The Temperatures of Dense Gas Clumps between Sgr A* and Sgr B2, *The Astrophysical Journal* **785** (Apr., 2014) 55, [1402.4531].

[303] D. F. Figer, R. M. Rich, S. S. Kim, M. Morris and E. Serabyn, An extended star formation history for the Galactic Center from Hubble Space Telescope / NICMOS observations, *Astrophys. J.* **601** (2004) 319–339, [astro-ph/0309757].

[304] D. F. Figer et al., Massive stars in the arches cluster, *Astrophys. J.* **581** (2002) 258–275, [astro-ph/0208145].

[305] D. F. Figer, Massive Star Formation in the Galactic Center, 0803.1619.

[306] J. C. Mauerhan, A. Cotera, H. Dong, M. R. Morris, Q. D. Wang, S. R. Stolovy and C. Lang, Isolated Wolf-Rayet Stars and O Supergiants in the Galactic Center Region Identified Via Paschen-α Excess, *The Astrophysical Journal* **725** (Dec., 2010) 188–199, [1009.2769].

[307] Fermi-LAT collaboration, M. Ackermann et al., The spectrum of isotropic diffuse gamma-ray emission between 100 MeV and 820 GeV, *Astrophys. J.* **799** (2015) 86, [1410.3696].

[308] K. M. Gorski, E. Hivon, A. J. Banday, B. D. Wandelt, F. K. Hansen, M. Reinecke and M. Bartelman, HEALPix - A Framework for high resolution discretization, and fast analysis of data distributed on the sphere, *Astrophys. J.* **622** (2005) 759–771, [astro-ph/0409513].

[309] "ASTROGAM: a space mission dedicated to the observation of the universe with unprecedented sensitivity in the mostly unexplored energy range 0.3 MeV - 100 MeV (extending up to GeV energies)." http://astrogam.iaps.inaf.it/index.html.

[310] N. P. Topchiev, A. M. Galper, V. Bonvicini, O. Adriani, R. L. Aptekar, I. V. Arkhangelskaja, A. I. Arkhangelskiy et al., The gamma-400 experiment: Status and prospects, *Bulletin of the Russian Academy of Sciences: Physics* **79** (2015) 417–420.

[311] E. Carlson, T. Linden and S. Profumo, Putting Things Back Where They Belong: Tracing Cosmic-Ray Injection with H2, 1510.04698.

[312] E. Carlson, T. Linden and S. Profumo, Improved Cosmic-Ray Injection Models and the Galactic Center Gamma-Ray Excess, 1603.06584.

[313] M. Pohl, P. Englmaier and N. Bissantz, Three-dimensional distribution of molecular gas in the barred milky way, *The Astrophysical Journal* **677** (2008) 283.

[314] M. Schmidt, The Rate of Star Formation., *The Astrophysical Journal* **129** (Mar., 1959) 243.

[315] R. M. Crocker, G. V. Bicknell, A. M. Taylor and E. Carretti, A Unified Model of the Fermi Bubbles, Microwave Haze, and Polarized Radio Lobes: Reverse Shocks in the Galactic Center's Giant Outflows, *Astrophys. J.* **808** (2015) 107, [1412.7510].

[316] Fermi-LAT collaboration, M. Ajello et al., Fermi-LAT Observations of High-Energy γ-Ray Emission Toward the Galactic Center, *Astrophys. J.* **819** (2016) 44, [1511.02938].

[317] F. Yusef-Zadeh, J. W. Hewitt, M. Wardle, V. Tatischeff, D. A. Roberts, W. Cotton, H. Uchiyama et al., Interacting Cosmic Rays with Molecular Clouds: A Bremsstrahlung Origin of Diffuse High-energy Emission from the Inner 2deg $\times$ 1deg of the Galactic Center, *The Astrophysical Journal* **762** (Jan., 2013) 33, [1206.6882].

[318] O. Macias and C. Gordon, Contribution of cosmic rays interacting with molecular clouds to the Galactic Center gamma-ray excess, *Phys. Rev.* **D89** (2014) 063515, [1312.6671].

[319] T. Linden, E. Lovegrove and S. Profumo, The Morphology of Hadronic Emission Models for the Gamma-Ray Source at the Galactic Center, *Astrophys. J.* **753** (2012) 41, [1203.3539].

[320] J. Petrović, P. D. Serpico and G. Zaharijaš, Galactic Center gamma-ray "excess" from an active past of the Galactic Centre?, *JCAP* **1410** (2014) 052, [1405.7928].

[321] W. Wang, Z. J. Jiang and K. S. Cheng, Contribution to diffuse gamma-rays in the Galactic Center region from unresolved millisecond pulsars, *Mon. Not. Roy. Astron. Soc.* **358** (2005) 263–269, [astro-ph/0501245].

[322] K. N. Abazajian, The Consistency of Fermi-LAT Observations of the Galactic Center with a Millisecond Pulsar Population in the Central Stellar Cluster, *JCAP* **1103** (2011) 010, [1011.4275].

[323] Q. Yuan and B. Zhang, Millisecond pulsar interpretation of the Galactic center gamma-ray excess, *JHEAp* **3-4** (2014) 1–8, [1404.2318].

[324] T. D. Brandt and B. Kocsis, Disrupted Globular Clusters Can Explain the Galactic Center Gamma Ray Excess, *Astrophys. J.* **812** (2015) 15, [1507.05616].

[325] D. Hooper, I. Cholis, T. Linden, J. Siegal-Gaskins and T. Slatyer, Pulsars Cannot Account for the Inner Galaxy's GeV Excess, *Phys. Rev.* **D88** (2013) 083009, [1305.0830].

[326] I. Cholis, D. Hooper and T. Linden, Challenges in Explaining the Galactic Center Gamma-Ray Excess with Millisecond Pulsars, *JCAP* **1506** (2015) 043, [1407.5625].

[327] J. Petrović, P. D. Serpico and G. Zaharijaš, Millisecond pulsars and the Galactic Center gamma-ray excess: the importance of luminosity function and secondary emission, *JCAP* **1502** (2015) 023, [1411.2980].

[328] R. Bartels, S. Krishnamurthy and C. Weniger, Strong support for the millisecond pulsar origin of the Galactic center GeV excess, *Phys. Rev. Lett.* **116** (2016) 051102, [1506.05104].

[329] S. K. Lee, M. Lisanti, B. R. Safdi, T. R. Slatyer and W. Xue, Evidence for Unresolved γ-Ray Point Sources in the Inner Galaxy, *Phys. Rev. Lett.* **116** (2016) 051103, [1506.05124].

[330] S. Horiuchi, M. Kaplinghat and A. Kwa, Investigating the Uniformity of the Excess Gamma rays towards the Galactic Center Region, 1604.01402.

[331] D. Hooper and G. Mohlabeng, The Gamma-Ray Luminosity Function of Millisecond Pulsars and Implications for the GeV Excess, *JCAP* **1603** (2016) 049, [1512.04966].

[332] D. Hooper and T. Linden, The Gamma-Ray Pulsar Population of Globular Clusters: Implications for the GeV Excess, *Submitted to: JCAP* (2016) , [1606.09250].

[333] T. Lacroix, O. Macias, C. Gordon, P. Panci, C. Bœhm and J. Silk, Spatial morphology of the secondary emission in the Galactic Center gamma-ray excess, *Phys. Rev.* **D93** (2016) 103004, [1512.01846].

[334] T. Linden, N. L. Rodd, B. R. Safdi and T. R. Slatyer, The High-Energy Tail of the Galactic Center Gamma-Ray Excess, 1604.01026.

[335] L. E. Strigari, S. M. Koushiappas, J. S. Bullock and M. Kaplinghat, Precise constraints on the dark matter content of Milky Way dwarf galaxies for gamma-ray experiments, *Phys. Rev.* **D75** (2007) 083526, [astro-ph/0611925].

[336] L. E. Strigari, S. M. Koushiappas, J. S. Bullock, M. Kaplinghat, J. D. Simon et al., The Most Dark Matter Dominated Galaxies: Predicted Gamma-ray Signals from the Faintest Milky Way Dwarfs, 0709.1510.

[337] G. Lake, Detectability of gamma-rays from clumps of dark matter, *Nature* **346** (July, 1990) 39.

[338] N. W. Evans, F. Ferrer and S. Sarkar, A 'Baedecker' for the dark matter annihilation signal, *Phys. Rev.* **D69** (2004) 123501, [astro-ph/0311145].

[339] E. L. Łokas, Dark matter distribution in dwarf spheroidal galaxies, *MNRAS* **333** (July, 2002) 697–708, [astro-ph/0112023].

[340] G. Battaglia, A. Helmi and M. Breddels, Internal kinematics and dynamical models of dwarf spheroidal galaxies around the Milky Way, *New Astron. Rev.* **57** (2013) 52–79, [1305.5965].

[341] M. Walker, *Dark Matter in the Galactic Dwarf Spheroidal Satellites*, p. 1039. 2013. 10.1007/978-94-007-5612-020.

[342] M. Mateo, Dwarf galaxies of the Local Group, *Ann. Rev. Astron. Astrophys.* **36** (1998) 435–506, [astro-ph/9810070].

[343] A. W. McConnachie, The Observed Properties of Dwarf Galaxies in and around the Local Group, *Astronomic. J.* **144** (July, 2012) 4, [1204.1562].

[344] Fermi-LAT, MAGIC collaboration, M. L. Ahnen et al., Limits to dark matter annihilation cross-section from a combined analysis of MAGIC and Fermi-LAT observations of dwarf satellite galaxies, *JCAP* **1602** (2016) 039, [1601.06590].

[345] G. D. Martinez, J. S. Bullock, M. Kaplinghat, L. E. Strigari and R. Trotta, Indirect Dark Matter Detection from Dwarf Satellites: Joint Expectations from Astrophysics and Supersymmetry, *JCAP* **0906** (2009) 014, [0902.4715].

[346] M. Cirelli, T. Hambye, P. Panci, F. Sala and M. Taoso, Gamma ray tests of Minimal Dark Matter, *JCAP* **1510** (2015) 026, [1507.05519].

[347] S. Liem, G. Bertone, F. Calore, R. R. de Austri, T. M. P. Tait, R. Trotta and C. Weniger, Effective Field Theory of Dark Matter: a Global Analysis, 1603.05994.

[348] K. Bechtol, A. Drlica-Wagner, E. Balbinot, A. Pieres, J. D. Simon, B. Yanny, B. Santiago et al., Eight New Milky Way Companions Discovered in First-year Dark Energy Survey Data, *The Astrophysical Journal* **807** (July, 2015) 50, [1503.02584].

[349] Fermi-LAT collaboration collaboration, M. Ackermann et al., Constraining Dark Matter Models from a Combined Analysis of Milky Way Satellites with the Fermi Large Area Telescope, *Phys.Rev.Lett.* **107** (2011) 241302, [1108.3546].

[350] Fermi-LAT collaboration, M. Ackermann et al., Dark matter constraints from observations of 25 Milky Way satellite galaxies with the Fermi Large Area Telescope, *Phys. Rev.* **D89** (2014) 042001, [1310.0828].

[351] G. D. Martinez, A Robust Determination of Milky Way Satellite Properties using Hierarchical Mass Modeling, 1309.2641.

[352] V. Bonnivard, C. Combet, D. Maurin and M. G. Walker, Spherical Jeans analysis for dark matter indirect detection in dwarf spheroidal galaxies - Impact of physical parameters and triaxiality, *Mon. Not. Roy. Astron. Soc.* **446** (2015) 3002–3021, [1407.7822].

[353] K. Hayashi and M. Chiba, Probing non-spherical dark halos in the Galactic dwarf galaxies, *Astrophys.J.* **755** (2012) 145, [1206.3888].

[354] K. Hayashi and M. Chiba, Structural properties of non-spherical dark halos in Milky Way and Andromeda dwarf spheroidal galaxies, *Astrophys. J.* **810** (2015) 22, [1507.07620].

[355] K. Hayashi, K. Ichikawa, S. Matsumoto, M. Ibe, M. N. Ishigaki and H. Sugai, Dark matter annihilation and decay from non-spherical dark halos in galactic dwarf satellites, *MNRAS* **461** (Sept., 2016) 2914–2928, [1603.08046].

[356] A. Geringer-Sameth, S. M. Koushiappas and M. G. Walker, Comprehensive search for dark matter annihilation in dwarf galaxies, *Phys. Rev.* **D91** (2015) 083535, [1410.2242].

[357] V. Bonnivard, C. Combet, M. Daniel, S. Funk, A. Geringer-Sameth, J. A. Hinton, D. Maurin et al., Dark matter annihilation and decay in dwarf spheroidal galaxies: the classical and ultrafaint dSphs, *MNRAS* **453** (Oct., 2015) 849–867, [1504.02048].

[358] M. G. Walker, C. Combet, J. A. Hinton, D. Maurin and M. I. Wilkinson, Dark matter in the classical dwarf spheroidal galaxies: a robust constraint on the astrophysical factor for gamma-ray flux calculations, *Astrophys. J.* **733** (2011) L46, [1104.0411].

[359] A. Charbonnier et al., Dark matter profiles and annihilation in dwarf spheroidal galaxies: prospectives for present and future gamma-ray observatories - I. The classical dSphs, *Mon. Not. Roy. Astron. Soc.* **418** (2011) 1526–1556, [1104.0412].

[360] A. Geringer-Sameth and S. M. Koushiappas, Exclusion of canonical WIMPs by the joint analysis of Milky Way dwarfs with Fermi, *Phys. Rev. Lett.* **107** (2011) 241303, [1108.2914].

[361] M. N. Mazziotta, F. Loparco, F. de Palma and N. Giglietto, A model-independent analysis of the Fermi Large Area Telescope gamma-ray data from the Milky Way dwarf galaxies and halo to constrain dark matter scenarios, *Astropart. Phys.* **37** (2012) 26–39, [1203.6731].

[362] A. Geringer-Sameth, S. M. Koushiappas and M. Walker, Dwarf galaxy annihilation and decay emission profiles for dark matter experiments, *Astrophys.J.* **801** (2015) 74, [1408.0002].

[363] G. A. Mamon and G. Boué, Kinematic deprojection and mass inversion of spherical systems of known velocity anisotropy, *MNRAS* **401** (Feb., 2010) 2433–2450, [0906.4971].

[364] J. Wolf, G. D. Martinez, J. S. Bullock, M. Kaplinghat, M. Geha et al., Accurate Masses for Dispersion-supported Galaxies, *Mon.Not.Roy.Astron.Soc.* **406** (2010) 1220, [0908.2995].

[365] H. Dejonghe and D. Merritt, Inferring the mass of spherical stellar systems from velocity moments, *The Astrophysical Journal* **391** (June, 1992) 531–549.

[366] J. Binney and S. Tremaine, *Galactic Dynamics: Second Edition*. Princeton University Press, 2008.

[367] L. E. Strigari, Galactic Searches for Dark Matter, *Phys. Rept.* **531** (2013) 1–88, [1211.7090].

[368] M. Irwin and D. Hatzidimitriou, Structural parameters for the Galactic dwarf spheroidals, *MNRAS* **277** (Dec., 1995) 1354–1378.

[369] J. Binney and G. A. Mamon, M/L and velocity anisotropy from observations of spherical galaxies, or must M87 have a massive black hole, *MNRAS* **200** (July, 1982) 361–375.

[370] H. C. Plummer, On the problem of distribution in globular star clusters, *MNRAS* **71** (Mar., 1911) 460–470.

[371] I. King, The structure of star clusters. I. an empirical density law, *Astronomic. J.* **67** (Oct., 1962) 471.

[372] J. L. Sersic, *Atlas de galaxias australes*. 1968.

[373] J. F. Navarro, C. S. Frenk and S. D. M. White, The Structure of cold dark matter halos, *Astrophys. J.* **462** (1996) 563–575, [astro-ph/9508025].

[374] J. F. Navarro, C. S. Frenk and S. D. M. White, A Universal density profile from hierarchical clustering, *Astrophys. J.* **490** (1997) 493–508, [astro-ph/9611107].

[375] P. Salucci and A. Burkert, Dark matter scaling relations, *Astrophys. J.* **537** (2000) L9–L12, [astro-ph/0004397].

[376] P. Salucci, M. I. Wilkinson, M. G. Walker, G. F. Gilmore, E. K. Grebel, A. Koch, C. F. Martins et al., Dwarf spheroidal galaxy kinematics and spiral galaxy scaling laws, *Mon. Not. Roy. Astron. Soc.* **420** (2012) 2034, [1111.1165].

[377] A. Burkert, The Structure of Dark Matter Halos in Dwarf Galaxies, *The Astrophysical Journal Letters* **447** (July, 1995) L25, [astro-ph/9504041].

[378] L. P. Osipkov, Spherical systems of gravitating bodies with an ellipsoidal velocity distribution, *Pisma v Astronomicheskii Zhurnal* **5** (Feb., 1979) 77–80.

[379] D. Merritt, Spherical stellar systems with spheroidal velocity distributions, *Astronomic. J.* **90** (June, 1985) 1027–1037.

[380] M. Baes and E. Van Hese, Dynamical models with a general anisotropy profile, *Astron. Astrophys.* **471** (2007) 419, [0705.4109].

[381] M. R. Merrifield and S. M. Kent, Fourth moments and the dynamics of spherical systems, *Astronomic. J.* **99** (May, 1990) 1548–1557.

[382] E. L. Lokas, G. A. Mamon and F. Prada, Dark matter distribution in the Draco dwarf from velocity moments, *Mon. Not. Roy. Astron. Soc.* **363** (2005) 918, [astro-ph/0411694].

[383] E. L. Łokas, The mass and velocity anisotropy of the Carina, Fornax, Sculptor and Sextans dwarf spheroidal galaxies, *MNRAS* **394** (Mar., 2009) L102–L106, [0901.0715].

[384] T. Richardson and M. Fairbairn, Analytical Solutions to the Mass-Anisotropy Degeneracy with Higher Order Jeans Analysis: A General Method, *Mon. Not. Roy. Astron. Soc.* **432** (2013) 3361–3380, [1207.1709].

[385] T. Richardson and M. Fairbairn, Cores in Classical Dwarf Spheroidal Galaxies? A Dispersion-Kurtosis Jeans Analysis Without Restricted Anisotropy, 1305.0670.

[386] M. G. Walker and J. Penarrubia, A Method for Measuring (Slopes of) the Mass Profiles of Dwarf Spheroidal Galaxies, *Astrophys. J.* **742** (2011) 20, [1108.2404].

[387] N. C. Amorisco and N. W. Evans, Dark Matter Cores and Cusps: The Case of Multiple Stellar Populations in Dwarf Spheroidals, *Mon. Not. Roy. Astron. Soc.* **419** (2012) 184–196, [1106.1062].

[388] L. E. Strigari, C. S. Frenk and S. D. M. White, Dynamical models for the Sculptor dwarf spheroidal in a Lambda CDM universe, 1406.6079.

[389] A. Fattahi, J. F. Navarro, T. Sawala, C. S. Frenk, K. A. Oman, R. A. Crain, M. Furlong et al., The APOSTLE project: Local Group kinematic mass constraints and simulation candidate selection, *MNRAS* **457** (Mar., 2016) 844–856, [1507.03643].

[390] T. Sawala, C. S. Frenk, A. Fattahi, J. F. Navarro, R. G. Bower, R. A. Crain, C. Dalla Vecchia et al., The APOSTLE simulations: solutions to the Local Group's cosmic puzzles, *MNRAS* **457** (Apr., 2016) 1931–1943, [1511.01098].

[391] A. R. Wetzel, P. F. Hopkins, J.-h. Kim, C.-A. Faucher-Giguere, D. Keres and E. Quataert, Reconciling dwarf galaxies with LCDM cosmology: Simulating a realistic population of satellites around a Milky Way-mass galaxy, *ArXiv e-prints* (Feb., 2016) , [1602.05957].

[392] T. Richardson, D. Spolyar and M. Lehnert, Plan β: Core or Cusp?, *Mon.Not.Roy.Astron.Soc.* **440** (2014) 1680–1689, [1311.1522].

[393] L. E. Strigari, J. S. Bullock, M. Kaplinghat, J. Diemand, M. Kuhlen and P. Madau, Redefining the Missing Satellites Problem, *The Astrophysical Journal* **669** (Nov., 2007) 676–683, [0704.1817].

[394] L. E. Strigari, J. S. Bullock, M. Kaplinghat, J. D. Simon, M. Geha, B. Willman and M. G. Walker, A common mass scale for satellite galaxies of the Milky Way, *Nature* **454** (2008) 1096–1097, [0808.3772].

[395] J. Peñarrubia, A. W. McConnachie and J. F. Navarro, The Cold Dark Matter Halos of Local Group Dwarf Spheroidals, *The Astrophysical Journal* **672** (Jan., 2008) 904–913, [astro-ph/0701780].

[396] J. Peñarrubia, A. W. McConnachie and J. F. Navarro, Erratum: "The Cold Dark Matter Halos of Local Group Dwarf Spheroidals" (ApJ, 672, 904 [2008]), *The Astrophysical Journal* **687** (Nov., 2008) 1460.

[397] M. G. Walker, M. Mateo, E. W. Olszewski, J. Peñarrubia, N. Wyn Evans and G. Gilmore, A Universal Mass Profile for Dwarf Spheroidal Galaxies?, *The Astrophysical Journal* **704** (Oct., 2009) 1274–1287, [0906.0341].

[398] M. G. Walker, M. Mateo, E. W. Olszewski, J. Peñarrubia, N. Wyn Evans and G. Gilmore, Erratum: "A Universal Mass Profile For Dwarf Spheroidal Galaxies?", *The Astrophysical Journal* **710** (Feb., 2010) 886–890.

[399] N. C. Amorisco and N. W. Evans, Phase-space models of the dwarf spheroidals, *Mon. Not. Roy. Astron. Soc.* **411** (2011) 2118–2136, [1009.1813].

[400] D. J. R. Campbell, C. S. Frenk, A. Jenkins, V. R. Eke, J. F. Navarro, T. Sawala, M. Schaller et al., Knowing the unknowns: uncertainties in simple estimators of dynamical masses, 1603.04443.

[401] L. Ciotti and L. Morganti, How general is the global density slope-anisotropy inequality?, *MNRAS* **408** (Oct., 2010) 1070–1074, [1006.2344].

[402] E. Van Hese, M. Baes and H. Dejonghe, On the Universality of the Global Density Slope-Anisotropy Inequality, *The Astrophysical Journal* **726** (Jan., 2011) 80, [1010.4301].

[403] J. H. An and N. W. Evans, A cusp slope-central anisotropy theorem, *Astrophys. J.* **642** (2006) 752–758, [astro-ph/0511686].

[404] H. Zhao, Analytical models for galactic nuclei, *Mon. Not. Roy. Astron. Soc.* **278** (1996) 488–496, [astro-ph/9509122].

[405] N. W. Evans, J. An and M. G. Walker, Cores and Cusps in the Dwarf Spheroidals, *Mon. Not. Roy. Astron. Soc.* **393** (2009) 50, [0811.1488].

[406] E. C. Moran, K. Shahinyan, H. R. Sugarman, D. O. Vélez and M. Eracleous, Black Holes At the Centers of Nearby Dwarf Galaxies, *Astronomic. J.* **148** (Dec., 2014) 136, [1408.4451].

[407] A. A. Nucita, L. Manni, F. De Paolis, G. Ingrosso and D. Vetrugno, The high energy search for IMBHs in close dSph Milky Way satellites., *Memorie della Societa Astronomica Italiana* **84** (2013) 645.

[408] A. X. Gonzalez-Morales, S. Profumo and F. S. Queiroz, Effect of Black Holes in Local Dwarf Spheroidal Galaxies on Gamma-Ray Constraints on Dark Matter Annihilation, *Phys. Rev.* **D90** (2014) 103508, [1406.2424].

[409] M. Wanders, G. Bertone, M. Volonteri and C. Weniger, No WIMP Mini-Spikes in Dwarf Spheroidal Galaxies, *JCAP* **1504** (2015) 004, [1409.5797].

[410] I. Cholis and P. Salucci, Extracting limits on Dark Matter annihilation from gamma-ray observations towards dwarf spheroidal galaxies, *Phys.Rev.* **D86** (2012) 023528, [1203.2954].

[411] R. Carrera, A. Aparicio, D. Martínez-Delgado and J. Alonso-García, The Star Formation History and Spatial Distribution of Stellar

Populations in the Ursa Minor Dwarf Spheroidal Galaxy, *Astronomic. J.* **123** (June, 2002) 3199–3209, [astro-ph/0203300].

[412] M. Bellazzini, F. R. Ferraro, L. Origlia, E. Pancino, L. Monaco and E. Oliva, The Draco and Ursa Minor Dwarf Spheroidal Galaxies: A Comparative Study, *Astronomic. J.* **124** (Dec., 2002) 3222–3240, [astro-ph/0209391].

[413] E. W. Olszewski and M. Aaronson, The URSA Minor dwarf galaxy - Still an old stellar system, *Astronomic. J.* **90** (Nov., 1985) 2221–2238.

[414] K. M. Cudworth, E. W. Olszewski and R. A. Schommer, Proper motions and bright-star photometry in the Ursa Minor dwarf galaxy, *Astronomic. J.* **92** (Oct., 1986) 766–776.

[415] S. Piatek, C. Pryor, P. Bristow, E. W. Olszewski, H. C. Harris, M. Mateo, D. Minniti et al., Proper Motions of Dwarf Spheroidal Galaxies from Hubble Space Telescope Imaging. III. Measurement for Ursa Minor, *Astronomic. J.* **130** (July, 2005) 95–115, [astro-ph/0503620].

[416] J. M. Nemec, A. Wehlau and C. Mendes de Oliveira, Variable stars in the Ursa Minor dwarf galaxy, *Astronomic. J.* **96** (Aug., 1988) 528–559.

[417] K. J. Mighell and C. J. Burke, WFPC2 Observations of the Ursa Minor Dwarf Spheroidal Galaxy, *Astronomic. J.* **118** (July, 1999) 366–380, [astro-ph/9903065].

[418] F. James and M. Roos, Minuit: A System for Function Minimization and Analysis of the Parameter Errors and Correlations, *Comput. Phys. Commun.* **10** (1975) 343–367.

[419] W. H. Press, S. A. Teukolsky, W. T. Vetterling and B. P. Flannery, *Numerical Recipes in FORTRAN: The Art of Scientific Computing*. 1992.

[420] P. Ullio, H. Zhao and M. Kamionkowski, A Dark matter spike at the galactic center?, *Phys. Rev.* **D64** (2001) 043504, [astro-ph/0101481].

[421] V. Lora, F. J. Sánchez-Salcedo, A. C. Raga and A. Esquivel, An Upper Limit on the Mass of the Black Hole in Ursa Minor Dwarf Galaxy, *The Astrophysical Journal Letters* **699** (July, 2009) L113–L117, [0906.0951].

[422] A. A. Nucita, F. De Paolis, L. Manni and G. Ingrosso, Hint for a faint

intermediate mass black hole in the Ursa Minor dwarf galaxy, *New Astronomy* **23** (Oct., 2013) 107–112.

[423] A. Caldwell, D. Kollar and K. Kroninger, BAT: The Bayesian Analysis Toolkit, *Comput. Phys. Commun.* **180** (2009) 2197–2209, [0808.2552].

[424] Fermi-LAT collaboration, E. Charles et al., Sensitivity Projections for Dark Matter Searches with the Fermi Large Area Telescope, *Phys. Rept.* **636** (2016) 1–46, [1605.02016].

[425] V. Lefranc, P. Panci and G. A. Mamon, Prospects for annihilating Dark Matter towards Milky Way's dwarf galaxies by the Cherenkov Telescope Array, 1605.02793.

[426] V. Lefranc, E. Moulin, P. Panci, F. Sala and J. Silk, Dark Matter in γ lines: Galactic Center vs dwarf galaxies, 1608.00786.

[427] V. Springel, J. Wang, M. Vogelsberger, A. Ludlow, A. Jenkins, A. Helmi, J. F. Navarro et al., The Aquarius Project: the subhalos of galactic halos, *Mon. Not. Roy. Astron. Soc.* **391** (2008) 1685–1711, [0809.0898].

[428] J. S. Bullock, Notes on the Missing Satellites Problem, *ArXiv e-prints* (Sept., 2010) , [1009.4505].

[429] W. J. G. de Blok, The Core-Cusp Problem, *Advances in Astronomy* **2010** (2010) 789293, [0910.3538].

[430] M. R. Lovell, V. Eke, C. S. Frenk, L. Gao, A. Jenkins, T. Theuns, J. Wang et al., The haloes of bright satellite galaxies in a warm dark matter universe, *MNRAS* **420** (Mar., 2012) 2318–2324, [1104.2929].

[431] M. Kaplinghat, S. Tulin and H.-B. Yu, Dark Matter Halos as Particle Colliders: Unified Solution to Small-Scale Structure Puzzles from Dwarfs to Clusters, *Phys. Rev. Lett.* **116** (2016) 041302, [1508.03339].

[432] A. Fattahi, J. F. Navarro, T. Sawala, C. S. Frenk, L. V. Sales, K. Oman, M. Schaller et al., The cold dark matter content of Galactic dwarf spheroidals: no cores, no failures, no problem, 1607.06479.

[433] M. G. Baring, T. Ghosh, F. S. Queiroz and K. Sinha, New Limits on the Dark Matter Lifetime from Dwarf Spheroidal Galaxies using Fermi-LAT, 1510.00389.

[434] A. J. Buras, Climbing NLO and NNLO Summits of Weak Decays, 1102.5650.